

DEVELOPMENT OF A ROBOTIC MOBILE MAPPING SYSTEM BY VISION-AIDED INERTIAL NAVIGATION: A GEOMATICS APPROACH

THÈSE N° 3440 (2005)

PRÉSENTÉE À LA FACULTÉ ENVIRONNEMENT NATUREL, ARCHITECTURAL ET CONSTRUIT

Laboratoire de topométrie

SECTION DES SCIENCES ET INGÉNIERIE DE L'ENVIRONNEMENT

ÉCOLE POLYTECHNIQUE FÉDÉRALE DE LAUSANNE

POUR L'OBTENTION DU GRADE DE DOCTEUR ÈS SCIENCES

PAR

Fadi Atef BAYOUD

M.Sc. in Geomatics Engineering, University of Calgary, Canada
et de nationalité libanaise

acceptée sur proposition du jury:

Prof. A. Mermoud, président du jury
Prof. B. Merminod, directeur de thèse
Prof. H. Bleuler, rapporteur
Prof. N. El-Sheimy, rapporteur
Prof. P.-A. Farine, rapporteur
Dr A. Martinelli, rapporteur



ÉCOLE POLYTECHNIQUE
FÉDÉRALE DE LAUSANNE

Lausanne, EPFL
2006

Summary

Vision-based inertial-aided navigation is gaining ground due to its many potential applications. In previous decades, the integration of vision and inertial sensors was monopolised by the defence industry due to its complexity and unrealistic economic burden. After the technology advancement, high-quality hardware and computing power became reachable for the investigation and realisation of various applications.

In this thesis, a mapping system by vision-aided inertial navigation was developed for areas where GNSS signals are unreachable, for example, indoors, tunnels, city canyons, forests, etc. In this framework, a methodology on the integration of vision and inertial sensors was presented, analysed and tested when the only available information at the beginning is a number of features with known location/coordinates (with no GNSS signals accessibility), thus employing the method of “SLAM: Simultaneous Localisation And Mapping”. SLAM is a term used in the robotics community to describe the problem of mapping the environment and at the same time using this map to determine (or to help in determining) the location of the mapping device.

In addition to this, a link between the robotics and geomatics community was established where briefly the similarities and differences were outlined in terms of handling the navigation and mapping problem. Albeit many differences, the goal is common: developing a “navigation and mapping system” that is not bounded to the limits imposed by the used sensors.

Classically, terrestrial robotics SLAM is approached using LASER scanners to locate the robot relative to a structured environment and to map this environment at the same time. However, outdoors robotics SLAM is not feasible with LASER scanners alone due to the environment’s roughness and absence of simple geometric features. Recently in the robotics community, the use of visual methods, integrated with inertial sensors, has gained an interest. These visual methods rely on one or more cameras (or video) and make use of a single Kalman Filter with a state vector containing the map and the robot coordinates. This concept introduces high non-linearity and complications to the filter, which then needs to run at high rates (more than 20 Hz) with simplified navigation and mapping models.

In this study, SLAM is developed using the Geomatics Engineering approach. Two filters are used in parallel: the Least-Squares Adjustment (LSA) for feature coordinates determination and the Kalman Filter (KF) for navigation correction. For this, a mobile mapping system (independent of GPS) is introduced by employing two CCD cameras (one metre apart) and one IMU. Conceptually, the outputs of the LSA photogrammetric resection (position and orientation) are used as the external measurements for the inertial KF. The filtered position

and orientation are subsequently employed in the Photogrammetric intersection to map the surrounding features that are used as control points for the resection in the next epoch. In this manner, the KF takes the form of a navigation only filter, with a state vector containing the corrections to the navigation parameters. This way, the mapping and localisation can be updated at low rates (1 to 2 Hz) and use more complete modelling.

Results show that this method is feasible with limitation induced from the quality of the images and the number of used features. Although simulation showed that (depending on the image geometry) determining the features' coordinates with an accuracy of 5-10 cm for objects at distances of up to 10 metres is possible, in practice this is not achieved with the employed hardware and pixel measurement techniques.

Navigational accuracies depend as well on the quality of the images and the number and accuracy of the points used in the resection. While more than 25 points are needed to achieve centimetre accuracy from resection, they have to be within a distance of 10 metres from the cameras; otherwise, the resulting resection output will be of insufficient accuracy and further integration quality deteriorates. The initial conditions highly affect SLAM performance; these are the method of IMU initialisation and the a-priori assumptions on error distribution. The geometry of the system will furthermore have a consequence on possible applications.

To conclude, the development consisted in establishing a mathematical framework, as well as implementing methods and algorithms for a novel integration methodology between vision and inertial sensors. The implementation and validation of the software have presented the main challenges, and it can be considered the first of a kind where all components were developed from scratch, with no pre-existing modules. Finally, simulations and practical tests were carried out, from which initial conclusions and recommendations were drawn to build upon.

It is the author's hope that this work will stimulate others to investigate further this interesting problem taking into account the conclusions and recommendations sketched herein.

Résumé

La navigation inertielle assistée par l'imagerie progresse grâce à ses nombreuses applications potentielles. Au cours des dernières décennies, l'intégration de capteurs inertiels et vidéo fut le monopole de l'industrie militaire, en raison de sa complexité et de son coût élevé. Avec les avancées technologiques, davantage de moyens devinrent accessibles pour la recherche et pour la réalisation d'applications variées.

Dans cette thèse, un système de cartographie par navigation inertielle assistée par imagerie fut développé pour des zones où les signaux satellitaires sont hors de portée, par exemple : à l'intérieur de bâtiments, dans des tunnels, des canyons urbains, des forêts, etc... Dans ce cadre, une méthodologie sur l'intégration de capteurs inertiels et vidéo fut présentée, analysée et testée lorsque la seule information disponible au départ est un ensemble de points connus en coordonnées (sans disponibilité de signaux satellitaires), en utilisant la méthode de la localisation et de la cartographie simultanées (SLAM). Cet acronyme est utilisé dans le domaine de la robotique pour décrire la problématique de la cartographie de l'environnement en utilisant cette carte pour déterminer (ou tout au moins aider à déterminer) la position de la plateforme cartographique.

En outre, un lien entre les communautés de la géomatique et de la robotique fut établi tout en soulignant les similarités et les différences avec lesquelles les dites communautés traitent le problème de la cartographie et de la navigation. En dépit de nombreuses divergences, leur but est unique : le développement d'un système de navigation et de cartographie qui n'est pas limité par des contraintes imposées par les capteurs utilisés. Traditionnellement, l'implémentation du SLAM en robotique terrestre implique l'utilisation de scanners laser pour localiser un robot dans un environnement construit, et pour cartographier cet environnement en même temps. Cependant, le SLAM de la robotique n'est pas réalisable en extérieur avec les seuls scanners laser, en raison de la complexité de cet environnement et de l'absence d'éléments géométriques simples. Dans la communauté de la robotique, l'utilisation de l'imagerie, intégrée avec des capteurs inertiels, a récemment connu un regain d'intérêt. Ces méthodes visuelles reposent sur (au moins un) appareil photo numérique ou une caméra vidéo, et utilisent un seul filtre de Kalman dont le vecteur d'état contient les coordonnées de la carte et du robot. Ce concept introduit une forte non-linéarité et complique le filtre, qui doit être exécuté à une fréquence élevée (plus de 20 Hz) avec des modèles de navigation et de carte simplifiés.

Dans cette étude, le SLAM est implémenté selon la stratégie de l'ingénierie géomatique. Deux filtres sont déployés en parallèle : l'ajustement par moindres carrés pour la détermination des coordonnées des éléments d'intérêt, et le filtre de Kalman pour la

navigation. Pour ce faire, on introduit un système de cartographie mobile (indépendant de GPS) qui emploie deux caméras CCD (distantes de 1 m) et une plateforme inertielle. Du point de vue conceptuel, les résultats d'un relèvement photogrammétrique à l'issue d'un ajustement par moindres carrés (position et orientation) sont utilisés comme mesures externes du filtre de Kalman. Les position et orientation filtrées sont ensuite utilisées dans une intersection stéréoscopique compensée pour cartographier les éléments environnants qui sont utilisés comme points de contrôle pour le relèvement à la prochaine époque. De cette manière, le filtre de Kalman est uniquement dédié à la navigation, avec un vecteur d'état contenant les corrections des paramètres de navigation. Ainsi, la localisation et la cartographie peuvent être mises à jour à des fréquences moindres (1 à 2 Hz) et reposer sur une modélisation plus aboutie.

Les résultats obtenus démontrent que cette méthode est exploitable sans subir les limitations liées à la qualité des images et au nombre d'éléments utilisés. Bien que la simulation montre la possibilité de déterminer (en fonction de la géométrie de l'image) les coordonnées d'éléments d'intérêt avec une précision de 5 à 10 cm pour des objets distants d'au plus 10 m, en pratique, cela n'est pas réalisé avec le matériel et la technique de mesure pixellaire employés. La précision de la navigation dépend aussi bien de la qualité des images que du nombre et de la précision des points utilisés dans le relèvement. Plus de 25 points sont nécessaires pour atteindre une précision centimétrique par relèvement, et ils doivent être choisis dans une zone de 10 m autour des caméras ; sinon, les résultats du relèvement auront une précision insuffisante et l'intégration ultérieure se détériorera rapidement. Les conditions initiales surtout affectent significativement les performances du SLAM ; ces sont les méthodes d'initialisation de la plateforme inertielle et les hypothèses sur la distribution des erreurs. La géométrie du système aura en outre une conséquence sur les applications possibles.

Pour conclure, le développement a consisté en la définition d'un cadre mathématique, de méthodes d'implémentation et d'algorithmes concernant une technologie d'intégration novatrice entre des capteurs inertiels et vidéo. Les principaux défis résidèrent dans l'implémentation et la validation du logiciel développé. Ce dernier peut être considéré comme le précurseur d'une nouvelle catégorie : il fut écrit à l'aide d'un code totalement original, sans recours à des modules préexistants. Finalement, la réalisation de simulations et de tests pratiques a conduit à l'émission de conclusions liminaires et de recommandations.

L'auteur souhaite vraiment que ce travail stimule une recherche approfondie dans cette problématique intéressante, tenant compte des conclusions et des recommandations ébauchées ici.

Acknowledgments

It is not fair to go ahead in our lives without thanking the people that have made a difference in one way or another. Of these people, I like to name a few that played a role during this work and during the last three years and 9 months of my life.

Primarily, I want to thank the One who made me a part of His harmonic world. When I acknowledged God in my M.Sc. thesis, I had written: “I want to thank God for all the things He has blessed and is still blessing me with, without which I would not be able to pursue knowledge, or even life.” Here, I add that I thank Him for blessing me with a Free Spirit, which is a grace I am learning to develop.

My mother **Georgette**, my two sisters **Samar** and **Shatha**, and my nephew **Eddy** and niece **Zeina** are the most important people of my life; no words are enough to express my feeling towards them and thus no words are enough to thank them for their love, care, smile and trust. Although he is not with us anymore, I remember my father, **Atef**, for teaching me how to be a good man and for all the great things he has left for me; I wish he were with us enjoying what he has created.

I thank Professor **Bertrand Merminod** for giving me the chance to be a part of his TOPO team and for the financial aid. Thank you, Bertrand, for your nice and smart advices on how to handle and manage things. In addition, I thank you for advising me on how to overcome some hard moments.

Dr. **Jan Skaloud**. Briefly: without him, this work would not have been realised in its current form, or maybe never realised. I cannot remember how many times I bothered him with my questions, concerns, frustrations and worries. Not a single time, however, I had left his office without being satisfied and cooled down. In addition to the moral and technical support, Jan has written the image acquisition code. Jan, the phrase “Thank you” is not enough for what you have done.

The TOPO team is thanked for making it a wonderful ambiance to work with. However, namely, I acknowledge **Pierre-Yves Gillieron** who opened my eyes to the world of robotics navigation and mapping. I acknowledge **Hervé Gontran** for being the best team player I have ever met. No matter how much busy he was, he was always ready to help me figuring out the problems I faced with my computer; I also thank him for assisting me in carrying out some tests. In addition, I thank Dr. **Klaus Legat** for sharing his brilliant mind and smart scientific discussions. **Véronique Boillat Kireev**, TOPO’s secretary, is acknowledged for her high professionalism; without her, things would have been very difficult in the Lab.

I thank Dr. **Julien Vallet** for the seminal discussions on Photogrammetry and for his assistance in carrying out some tests.

Dr. **Quentin Ladetto**. Thank you for telling me about the EPFL and for being the one who first worked on bringing me to Switzerland; without that email 4 years ago, I would not have been here right now; it is because of you that I am here. In addition, thank you for *all* ... I mean *ALL* ... this *ALL* is so much that cannot fit in few lines ...

I thank Prof. Dr. Naser El-Sheimy for his technical help and for his brilliant suggestions and comments as a member of my thesis committee. In addition, I acknowledge the other thesis committee members: Prof. H. Bleuler, Prof. P.-A. Farine, and Dr. A. Martinelli.

I see it fair as well to acknowledge my professors in Greece (Aristotle University of Thessaloniki) and Canada (University of Calgary) who have taught me the first letters of Geomatics.

Last but definitely not least, I thank the unknown (but known for me) soldiers, with whom I shared my first trials of the true meaning of free spirit and truth seeking ... however, it is just the beginning

“Great minds discuss ideas; Average minds discuss events; Small minds discuss people”

Eleanor Roosevelt

إلى كُلِّ مَنْ رَأَى النُّورَ وَلَمْ يُعَمَّ
 إلى كُلِّ مَنْ نَظَرَ الشَّمْسَ وَلَمْ يَحْتَرِقْ
 إلى كُلِّ مَنْ بَحَثَ الحَقَّ وَلَمْ يَخَفْ
 إلى كُلِّ مَنْ قَرَأَ التَّارِيخَ وَلَمْ يَهْرُبْ، بَلْ تَعَلَّمَ
 إلى كُلِّ مَنْ حَلِمَ المُسْتَقْبَلَ وَلَمْ يَتَوَانَ التَّنْفِيذُ
 إلى كُلِّ مَنْ أَرَادَ الحَيَاةَ وَلَمْ يَأْبَ المَوْتَ
 إلى كُلِّ مَنْ حَارَبَ لِلحُرِّيَّةِ وَاسْتَشْهَدَ
 إلى كُلِّ حُرٍّ خَيْرَ نَشْوَةِ الحُرِّيَّةِ وَعَلَّمَهَا

20 كانون الأول 2005

To love and beauty

To honesty, openness and loyalty

To courage and tolerance

To freedom, self-discipline and duty

To history, present and future

Table of contents

Summary	I
Résumé	III
Acknowledgments	V
Table of contents	IX
Acronyms	XII
Symbols.....	XIV
1 - Introduction.....	1
1.1 - Problem statement	1
1.2 - Geomatics and Robotics – The First Link	3
1.3 - Navigation and Mapping System in Geomatics.....	4
1.4 - Navigation and Mapping Systems in Robotics	7
1.5 - Geomatics and Robotics – The Second Link	8
1.6 - Behaviours, Sensors and Application Themes	10
1.7 - Photogrammetry Alone Solving SLAM	12
1.8 - Thesis Contribution	14
1.9 - Thesis Outline	14
2 - Close-Range Photogrammetry Solving SLAM.....	17
2.1 - Introduction	17
2.2 - Definition of Photogrammetry.....	17
2.3 - Mathematical Model in Photogrammetry.....	18
2.4 - Resection	21
2.4.1 - Resection by Least-Squares Adjustment	21
2.4.2 - Resection Accuracy.....	24
2.5 - Intersection.....	26
2.5.1 - Intersection by Least-Squares Adjustment.....	27
2.5.2 - Intersection Accuracy	31
2.6 - Solving SLAM Trajectory by Photogrammetry	35
3 - Choice of Mapping Instrumentation	43
3.1 - The Focal Length “c”	43
3.2 - The Stereo-Base “b”	45
3.3 - Charged Couple Device Camera	47
3.4 - Frame Grabber.....	49

3.5 - Camera Calibration	50
3.6 - Bundle Least-Squares Adjustment with Self-Calibration.....	51
4 - Strapdown Inertial System Supporting SLAM	55
4.1 - Introduction	55
4.2 - Inertial Navigation System Concept.....	56
4.3 - Mechanisation Equations for the Strapdown INS.....	56
4.3.1 - Earth-Centred-Earth-Fixed Frame.....	58
4.4 - Dynamic Modelling of System Errors	62
4.4.1 - State Space Formulation.....	62
4.4.2 - Error Equations in the Earth-Fixed Frame.....	63
4.5 - Kalman Filter as an Estimation Method	65
4.6 - The IMU in this work	70
4.6.1 - Performance of LN-200.....	70
4.6.2 - Gyro-Compassing by LN200	71
5 - Integration Methodology and System Calibration.....	77
5.1 - Integration Methodology.....	77
5.2 - Kalman Filter External Measurements	81
5.2.1 - The Average of the Two EOP Sets	81
5.2.2 - The Two EOP Sets as Two Independent Updates.....	84
5.3 - System Calibration	86
5.4 - Angle Transformation.....	86
5.4.1 - From Resection to IMU	87
5.4.2 - From IMU to Intersection.....	88
5.4.3 - Rotation between the Mapping and Earth-Fixed Frames.....	88
5.4.4 - Mounting Rotation	89
5.5 - Boresight Estimation	91
5.6 - Leverarm Estimation	93
5.6.1 - Leverarm application from Resection to IMU	95
5.6.2 - Leverarm application from IMU to Intersection.....	96
5.7 - Leverarm and Boresight Numerical Determination	97
6 - Numerical Application.....	103
6.1 - Indoor Test – Control of Concept	105
6.2 - Outdoor Test – Control of Resection and Boresight.....	106
6.3 - Outdoor Test of SLAM	109
6.3.1 - Initialisation and Navigation.....	112

6.3.2 - Modification of the Kalman Filter	117
6.3.3 - Mapping.....	117
7 - Summary, Conclusions and Recommendations	121
7.1 - Summary.....	121
7.2 - Conclusions.....	122
7.3 - Recommendations	123
Appendix A: Photogrammetry Solution with Quaternions	127
Appendix B: Cameras' Calibration	139
Appendix C: Outdoor Images	145
Appendix D: Detailed Tables.....	147
References	151
Curriculum Vitae.....	154

Acronyms

3-D	Three Dimensional
arcmin	arc-minute
arcs	arc-second
AT	Aero Triangulation
AUPT	Attitude Update
CCD	Charged Couple Device
CHP	Checkpoint
CUPT	Coordinates Update
deg	Degree
ECEF	Earth-Centred-Earth-Fixed frame
ENU	East-North-Up reference frame
FOG	Fibre Optic Gyroscope
EOP	Exterior Orientation Parameters
FOV	Field-Of-Vision
EPFL	Ecole Polytechnique Fédérale de Lausanne - Suisse
GARW	Gyro Angular Random Walk
GCP	Ground Control Point
GNSS	Global Navigation Satellite System
GPS	Global Positioning System
H	Horizontal
H-camera	High-Definition camera
hr	Hour
Hz	Hertz (1/s)
IEEE	The Institute of Electrical and Electronics Engineers
IMU	Inertial Measurement Unit
INS	Inertial Navigation System
IOP	Interior Orientation Parameters

IROS	International Conference on Intelligent Robots and Systems
ISPRS	International Society of Photogrammetry and Remote Sensing
L	Left
LASER	Light Amplification by Stimulated Emission of Radiation
LSA	Least Squares Adjustment
KF	Kalman Filter
MEMS	Microelectromechanical Sensor
MMS	Mobile Mapping System
mgals	Milli-Gal
min	min
NED	North-East-Down reference frame
OEEPE	Organisation Européenne d'Etudes Photogrammetriques Expérimentales
R	Right
s	second
SiAc	Silicon Accelerometer
SINS	Strapdown Inertial Navigation System
SLAM	Simultaneous Localisation And Mapping
STD	Standard Deviation
TOPO	Laboratoire de Topométrie - EPFL
V	Vertical
WGS84	World Geodetic System 1984
ZUPT	Zero-Velocity Update
μ	Micro

Symbols

Sub- & superscripts

b	Body frame
c	CCD camera frame
e	Earth-Centred-Earth-Fixed frame
H	High-definition camera frame
i	Inertial frame
l	local-level frame
L	Left
R	Right
m	Mapping frame

\mathbf{R}_a^b Transformation matrix between reference systems a and b

$$\mathbf{R}_1(\chi) = \begin{bmatrix} 1 & 0 & 0 \\ 0 & \cos \chi & \sin \chi \\ 0 & -\sin \chi & \cos \chi \end{bmatrix} \quad \text{Rotation about the x-axis of an angle } \chi$$

$$\mathbf{R}_2(\chi) = \begin{bmatrix} \cos \chi & 0 & -\sin \chi \\ 0 & 1 & 0 \\ \sin \chi & 0 & \cos \chi \end{bmatrix} \quad \text{Rotation about the y-axis of an angle } \chi$$

$$\mathbf{R}_3(\chi) = \begin{bmatrix} \cos \chi & \sin \chi & 0 \\ -\sin \chi & \cos \chi & 0 \\ 0 & 0 & 1 \end{bmatrix} \quad \text{Rotation about the z-axis of an angle } \chi$$

$\mathbf{\Omega}_{ab}^c$ Skew-symmetric matrix of the rotation vector of frame *a* and relative to frame *b* expressed in frame *c*

Chapter 2

k	Time epoch
x, y	Photo-coordinates in the image frame
X, Y, Z	Coordinates in the object frame
c	Focal length of the camera
X_0, Y_0, Z_0	Coordinates of the perspective centre in the object frame
x_0, y_0	Photo-coordinates of the perspective centre in the image frame
R_{ij}	Elements of the rotation matrix R
ω	Roll
α	Azimuth
κ	Pitch
λ	Scale of transformation
\mathbf{x}'	Vector of the unknowns in the resection LSA
$\overset{\circ}{\mathbf{x}'}$	Vector of the approximate values of \mathbf{x}'
$\delta\mathbf{x}'$	Vector of corrections for $\overset{\circ}{\mathbf{x}'}$
\mathbf{y}'	Vector of measurements
$\overset{\circ}{\mathbf{y}'}$	Approximate values of the measurements \mathbf{y}'
\mathbf{w}'	Misclosure vector in the resection LSA
\mathbf{N}'	Normal matrix in the resection LSA
\mathbf{C}'_y	Covariance matrix of the measurements in the resection LSA
\mathbf{A}'	First design matrix in the resection LSA
\mathbf{B}'	Second design matrix in the resection LSA
\mathbf{v}'	LSA error in the resection LSA
$\mathbf{C}'_{\hat{\mathbf{x}}}$	Covariance matrix of $\hat{\mathbf{x}}$
\mathbf{C}'_v	Covariance matrix of the residuals in the resection LSA

$\mathbf{C}'_{\hat{\mathbf{y}}}$	Covariance matrix of the adjusted measurements
\mathbf{x}''	Vector of the unknowns in the intersection LSA
$\overset{\circ}{\mathbf{x}}''$	Vector of the approximate values of \mathbf{x}''
$\delta\mathbf{x}''$	Computed vector of corrections for $\overset{\circ}{\mathbf{x}}''$
\mathbf{y}''	Vector of measurements in the intersection LSA
$\overset{\circ}{\mathbf{y}}''$	Approximate values of the measurements \mathbf{y}''
\mathbf{w}''	Misclosure vector in the intersection LSA
\mathbf{N}''	Normal matrix in the intersection LSA
$\mathbf{C}''_{\mathbf{y}}$	Measurements covariance matrix in the intersection LSA
$\mathbf{C}''_{L/Ry}$	Measurements covariance matrix of the L or R image
\mathbf{C}''_{LRy}	Measurements covariance matrix between the L and R image
\mathbf{A}''	First design matrix in the intersection LSA
$\mathbf{A}''_{L/R}$	First design matrix of L/R image in the intersection LSA
\mathbf{B}''	Second design matrix in the intersection LSA
$\mathbf{B}''_{L/R}$	Second design matrix of L/R image in the intersection LSA
\mathbf{v}''	Residuals in the intersection LSA
$\mathbf{C}''_{\hat{\mathbf{x}}}$	Covariance matrix of adjusted parameters
$\mathbf{C}''_{\mathbf{v}}$	Covariance matrix of the residuals in the intersection LSA
$\mathbf{C}''_{\hat{\mathbf{y}}}$	Covariance matrix of the adjusted measurements \mathbf{y}''
σ^2_{χ}	Variance of variable χ
$\sigma_{\chi\psi}$	Covariance between variables χ and ψ
P_x	Parallax along the x-axis
b	Base between Left and Right CCD's
Σ_i^{photo}	Covariance matrix of the photo-coordinates

$\Sigma_i' \Big _k^{\text{object}}$	Covariance matrix of i -th feature at epoch k
$\Sigma_i' \Sigma_j' \Big _k^{\text{object}}$	Covariance matrix between the i -th and j -th features at epoch k
$\Sigma_{L/R_EOP}'' \Big _k$	Measurement Covariance matrix of the Left and Right EOP at epoch k
$\hat{\sigma}_0^2$	Aposteriori variance of an observable with unit weight

Chapter 3

d	Size of the object's image
D	Actual size of the object
Z	Distance of the object from the image
Δx & Δy	Correction terms due to the CCD lens distortions
$\bar{\delta}x_0, \bar{\delta}y_0, \bar{\delta}c$	Correction to x_0, y_0, c
$a_1, a_2, a_3, \dots, a_n$	Parameters of the lens radial, symmetric and decentring distortions
D	Design matrix that depends on the lens calibration model

Chapter 4

t	Time
$\mathbf{r}^e = (x^e, y^e, z^e)$	Three position components in the Earth frame e
$\mathbf{v}^e = (v_x^e, v_y^e, v_z^e)$	Three velocity components in the Earth frame e
$\mathbf{f}^b = (f_x^b, f_y^b, f_z^b)$	Measured specific forces in body frame b
\mathbf{g}^e	Earth's gravity vector expressed in the Earth frame e
\mathbf{g}^l	Earth's gravity vector expressed in the local frame l
a	Semi-major axis of the reference ellipsoid
e	Eccentricity of the reference ellipsoid
ϕ	Latitude

λ	Longitude
ω_e	Earth rotation rate
$ g $	Value of the gravitational acceleration
γ	Normal gravitational acceleration
h	Ellipsoidal height
$\Delta \mathbf{v}_f^e$	Velocity increments in the e frame
$\Delta \mathbf{v}^b$	Measured velocity increments
$\mathbf{I} + \mathbf{S}^b$	Transformation matrix in the b frame between time t_{k-1} & t_k
θ_i^b	Angular increments of the body rotation with respect to the e frame expressed in the b frame
$\Delta \theta_{ib}^b$	Vector of gyroscopes' measurements $\boldsymbol{\omega}_{ib}^b = (\omega_x, \omega_y, \omega_z)$ expressed in the b -frame multiplied by the time increment, $\Delta t = t_k - t_{k-1}$
$d\theta_{ie}^b$	Earth rotation vector relative to the i frame expressed in the b frame
\mathbf{a}^e	Coriolis correction
φ	Roll
ϑ	Pitch
ψ	Yaw
$\delta \mathbf{x}(t)$	State vector
$\Gamma(t)$	Dynamic matrix
$\mathbf{G} \mathbf{w}(t)$	Vector of the zero-mean white noise process
\mathbf{G}	Shaping matrix
$\delta \mathbf{x}_1$	Position, velocity, and misalignment errors of the inertial system
$\delta \mathbf{x}_2$	Accelerometer and gyro errors
$\delta x^e, \delta y^e \text{ \& } \delta z^e$	Error states in the position vector
$\delta v_x^e, \delta v_y^e \text{ \& } \delta v_z^e$	Error states in the velocity vector

$\delta\epsilon_x, \delta\epsilon_y$ & $\delta\epsilon_z$	Misalignments' error states
$\delta g_x, \delta g_y$ & δg_z	Gyroscopes' drift error states, and
$\delta b_x, \delta b_z$ & δb_z	Accelerometers' drift error states
\mathbf{F}^e	Skew-symmetric matrix of measured specific force vector in e frame
α & β	Diagonal matrices of the reciprocals of time correlation parameters
\mathbf{w}_d & \mathbf{w}_b	Vectors containing white noise
K	Gravitational Constant
M	Earth Mass
δA	Accuracy of the azimuth affected by the x-gyro drift and the latitude
\mathbf{H}_k	Measurement design matrix in the KF
\mathbf{v}_k	White noise sequence corrupting the observations in the KF
\mathbf{z}_k	Measurement vector sampled at time t_k in the KF
$E\{\chi\}$	Expectation of variable χ
\mathbf{P}	Covariance matrix of the state vector \mathbf{x} in the KF
$\Phi_{k-1,k}$	Transition matrix in the KF
\mathbf{Q}_k	Uncertainty of the state vector resulting from the white noise input in the KF
\mathbf{Q}	Spectral density matrix in the KF
σ_{ai}^2 & σ_{gi}^2	Variances of the accelerometers and gyroscopes if the i -axis
\mathbf{K}_k	Kalman gain matrix
\mathbf{R}_k	Covariance matrix of the measurement noise vector \mathbf{v}_k
\mathbf{r}_k	Innovation sequence in the KF

Chapter 5

$X_{0L/R}, Y_{0L/R}, Z_{0L/R}$	Coordinates of the left/right camera including its leverarm with the IMU
$\epsilon_{x_{L/R}}, \epsilon_{y_{L/R}}, \epsilon_{z_{L/R}}$	Attitude of the left/right camera including its boresight angles with the IMU
$\epsilon_{x_{IMU}}, \epsilon_{y_{IMU}}, \epsilon_{z_{IMU}}$	Attitude angles between the body and Earth frames determined from the mechanisation equations
$b_{L/R}$	Leverarm of camera L/R and the IMU
$\alpha_{L/R}$	Boresight between of camera L/R and the IMU
(ϕ_m, λ_m)	Latitude and longitude of the mapping system's origin
ϵ_i	Misalignment angle along the i – axis
$I = (I_x, I_y, I_z)$	Leverarm between the camera and the IMU
X_{cam}^c	Coordinates of the camera in the camera frame
X_{cam}^m	Coordinates of the camera in the mapping frame
X_{IMU}^m	Coordinates of the IMU in the mapping frame
X_{IMU}^e	Coordinates of the IMU in the e frame
X_{IMU}^c	Coordinates of the IMU in the camera frame
I_j^c	Leverarm in the camera frame
I_j^m	Leverarm in the mapping frame
$R_{c/j}^m$	Transformation matrix between camera & mapping frame for camera j
$X_{cam/j}^m$	Coordinates of j camera in the mapping frame (from resection),
$X_{IMU/j}^m$	IMU coordinates in the mapping frame.
$X_{IMU/j}^e$	Coordinates of the IMU in the e frame computed from j camera.
X_{IMU}^e	Kalman filtered (KF-ed) coordinates of the IMU in the ECEF frame,

\mathbf{X}^e	Coordinates of the IMU in the e frame
$\text{KF}(\mathbf{X}^e, \mathbf{X}_{\text{IMU/L}}^e, \mathbf{X}_{\text{IMU/R}}^e)$	Kalman filter with update \mathbf{X}^e and CUPTs $\mathbf{X}_{\text{IMU/L}}^e$ and $\mathbf{X}_{\text{IMU/R}}^e$
I_j^b	Leverarm in the body frame
I_j^e	Leverarm in the e frame
$\mathbf{X}_{\text{IMU}}^e$	IMU position in the e frame determined by KF
$\mathbf{X}_{\text{CAM/j}}^e$	Coordinates of j camera position in the e frame
$\mathbf{X}_{\text{CAM/j}}^m$	KF-ed position of j camera in the mapping frame
$\mathbf{R}_b^{b^*c}$	Sought boresight between the IMU and CCD
\mathbf{T}_H^c	Rotation matrix between the H and CCD cameras
$\mathbf{R}_H^H^*$	Boresight between H and CCD cameras
\mathbf{T}_b^H	Rotation matrix between H and IMU frames
$\mathbf{R}_b^{b^*H}$	Boresight between the H and IMU frames
I_c^b	Leverarm between the CCD and the IMU in the c frame
I_H^b	Leverarm between H and the IMU in the H frame
I_c^H	Leverarm between H and CCD
$\Sigma_{I_H^b}$	Covariance matrix of the components of the leverarm I_H^b
$\Sigma_{I_c^H}$	Covariance matrix of the components of the leverarm I_c^H

1 - INTRODUCTION

في البدء كان نورٌ، والنور كان مع
المعرفة. والنور هو المعرفة

*In the beginning was the Light, and the Light was
with Knowledge, and the Light was Knowledge ...*

This thesis aims at two different communities: Geomatics and Robotics. Despite the apparent differences between these two disciplines, they have nevertheless many aspects in common when mobile robots are involved. Mobile robots are machines that – autonomously – move to complete a task. In a typical challenging situation, when a robot works in an unknown environment, it ought to know its own location (to navigate), and the locations of the surroundings (to map). While Robotics is about designing smart machines, Geomatics Engineering is, among other things, the science of map-making, which includes positioning and navigation. The complementarities and common aspects between the two disciplines are the motivation for this thesis. It is hard to please two distinct communities, and it is even harder if these communities are scientific. Therefore, some parts of this thesis may look familiar to one community but novel to the other. Yet, the author hopes that this is essential to set collaboration between two important disciplines (that have so much in common) for an advance in both.

1.1 - Problem statement

The aim of this work is to develop a localisation methodology for mobile mapping systems ***based on the fusion of inertial and image data.***

To perform this task, a terminology from the robotics community is borrowed: ***SLAM*** – ***Simultaneous Localisation And Mapping***. SLAM is a task for a mobile robot that draws a map and simultaneously uses the map to locate itself. However, to draw a map, the position of the robot has to be known and (usually) for the robot to know its position it has to have a map. Thus, positioning is solved by sequential localisation and mapping that take place simultaneously.

The concept of SLAM is shown in Figure (1-1) for the case of a pair of cameras. At epoch k , the vehicle localises itself by knowing the relative displacement with respect to the “crossed” targets; consequently, when this is done, the vehicle can determine the position of the

assigned “circular” targets. At epoch $k+1$, the vehicle moves to another position and it uses the already determined targets at epoch k to locate itself and then in turn to determine the positions of the “circular” targets. This procedure continues with epoch $k+2$ and so on.

SLAM (or CML: Concurrent Mapping and Localisation) was first introduced by Smith, Self, and Cheeseman (Smith and Cheeseman, 1985; Smith et al., 1990) through seminal papers that presented a statistical framework for simultaneously solving the mapping problem and the induced problem of localising the robot relative to its growing map (Thrun, 2002).

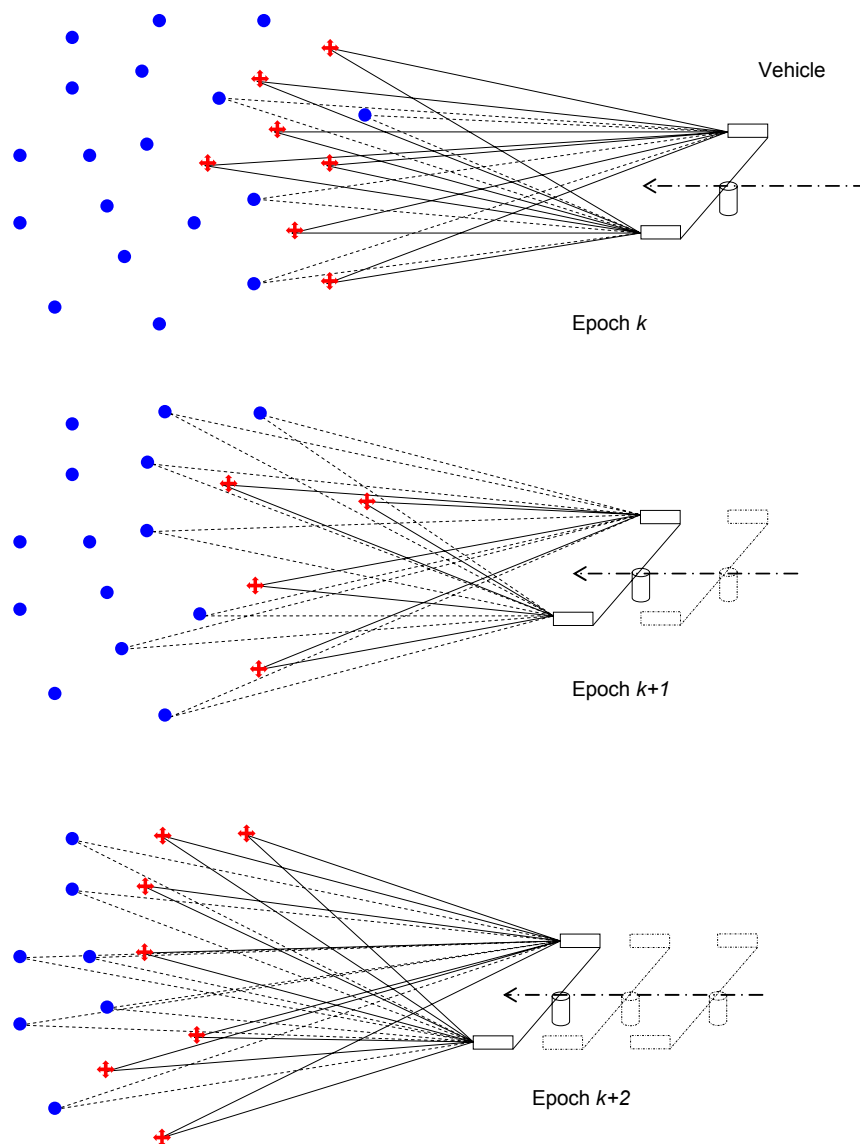


Figure 1-1: SLAM concept

Theoretically, this task can be solved by passive vision as conceptually depicted. However, this is often practically difficult to achieve, and therefore additional sensors need to be employed. An Inertial Measurement Unit will accompany the vision sensors in this work.

In this research, the localisation aspect of SLAM is studied and solved using Geomatics Engineering modus operandi. To understand the methodology followed in this work, it will be helpful to comprehend the differences in methods and technologies used in these two distinct (albeit complementary) scientific fields: Geomatics and Robotics.

1.2 - Geomatics and Robotics – The First Link

Geomatics Engineering is an interdisciplinary field with many branches ranging from Earth sciences on a global scale to the determination of boundaries on a local scale, passing through other engineering disciplines like electronics, mechanics, communication, and information technology.

The most important product of Geomatics Engineering is a map. There are different approaches to map-making and among the many, the one that makes use of accurate navigation and positioning is the focus of this research.

In such map-making, the knowledge of the mathematical and physical characteristics of the planet Earth is vital, such as its shape, size, weight, rotation rate as well as gravitational and magnetic fields. These factors directly affect accurate navigation and positioning, and therefore their accurate knowledge is essential.

In navigation and positioning, electronic and optical-mechanical instruments are used. These could be any, or a combination of: artificial satellites, cameras, laser scanners, gyroscopes and accelerometers, odometer, total-station, compass, mobile-phone networks, etc.

Navigation is the science of planning and management of moving subjects and objects that answers the following subsections: Where? When? How?

The answer to the first question lies in localisation, i.e., in 3-D coordinates and orientation. The answer to the second is found in timing. The 3-D coordinates, the orientation, the time and a map are the answer to the third question, because these variables can draw the path of the movement. Therefore, the core elements of localisation are: three coordinates in a 3-D reference frame (X, Y, Z or φ, λ, h), three angular rotations (roll, pitch and yaw) and the time (t). Moreover, the core of navigation is the interaction between the localisation and the map.

Navigation (and positioning) has been of interest to mankind since it had first set to move. In the course of history, navigation passed through an ample of forms and methods: from navigating oneself and locating other subjects and objects, to training a machine to localise itself and to navigate in known and/or unknown environments via an artificially intelligent design.

First navigators used landmarks as topological means to navigate. Celestial methods followed. The combination of celestial methods and the magnetic compass ruled the navigation arena for several centuries until time was incorporated with the marine chronometer developed by John Harrison (Sobel, 1996) in the sixteenth century. In the twentieth century, ground-based radio navigation was developed along with deduced reckoning and inertial methods. Currently, space-based radio navigation achieves a monopoly over ground-based radio navigation in many situations, although aviation still relies also on ground-based radio navigation. Nevertheless, due to the limits in the space-based radio navigation, its integration with deduced reckoning and inertial methods is inevitable in some applications.

Maps, on the other hand, are graphical/digital representations of the features of the environment in some datum and projection. Depending on the type and size of the environment and on the required map, a mapping method is chosen. In this study, terrestrial close range photogrammetry is the mapping method used.

Mapping System is the term used to describe a set of tools and methods that perform mapping. Mobile Mapping Systems are those systems that equip navigation systems that allow mapping while moving.

Navigation and mapping systems are of a great importance for mobile robots, without which an autonomous exploring robot cannot do its job. The applications of a mobile robot are abundant, but one of the most important is: going to and exploring places where no man is safe to do. These robots do not reach the perfection by only having a good navigation and mapping system. The navigation and mapping system is only a part of an integrated system that combines control, artificial intelligence, dynamics, sensing, vision, learning, estimation methods, etc. It is even hard to tell which of these is more important since they all work as a team, benefiting from each other's contribution. Yet, it can be said that a navigation and mapping system is a core element to these robots. The extraterrestrial missions to Mars and the placement of rovers on its surface are good examples of the use of these robots. A map of the surrounding environment of the robot is essential for the robot to perform manoeuvres and in turn to complete its scientific mission

1.3 - Navigation and Mapping System in Geomatics

Navigation involves the above-mentioned processes in real time, but in this work, it will refer to trajectory determination in an off-line mode. In the geomatics literature, this is called "Kinematic Geodesy".

The navigation systems usually consist in a Global Positioning System (GPS) receiver – and antenna – integrated with an Inertial Measurement Unit (IMU) to determine the position and attitude of the mapping system. The research conducted in Geomatics Engineering in GPS/IMU navigation is enormous, where it started in the late seventies when GPS was first realised (for example see, Cox, 1980). Publications in this field are vast and they cover every aspect of this integration; to name a very few: Grewal and Weill, 2002; Schwarz, 1986; Skaloud, 1999; Shin, 2005. The GPS/IMU is not only used for navigation, but also for the determination of the Earth's gravity field (Knickmeyer, 1990, Schwarz, 2000; Bruton, 2001; Bayoud, 2002).

The GPS/IMU integration provides the position and attitude of the moving vehicle. The IMU consists of a triad of accelerometers and gyroscopes that measure the vehicle's accelerations and rotation rates, respectively. The accelerations are integrated twice and the rotation rates are integrated once to provide the displacement of the vehicle. The rotation rates are also used to determine the attitude of the vehicle with respect to a reference system. Since these systems suffer from biases and drifts in their accelerations and rotation rates, their solution degrades fast with time. To control this degradation, GPS is integrated with an IMU in a Kalman Filter to determine an optimal position and attitude and to provide a better knowledge on the biases and drifts of the IMU.

The accuracy achieved from this integration depends on the quality of the IMU used. IMUs are classified into Navigation, strategic, tactical, and automotive grade. Currently, the tactical-grade IMUs are widely used in navigation and mapping (Skaloud and Vallet, 2005; Vallet and Skaloud, 2004; Tomé, 2002; Petovello, 2002; to name a few), where it guarantees an accuracy of few centimetres in position and half an arc-minute to an arc-minute in attitude. In case of GPS signal loss, the tactical-grade IMU can run for a couple of minutes without degrading the navigation solution to an unacceptable level. Automotive grade IMU are also used in a few mapping systems; the disadvantage of these systems is that their solution degrades very fast when GPS is not available, and their error can reach several tens of metres within a couple of minutes (Shin, 2001).

Mapping can be done by photogrammetry, where images taken from at least one camera are geometrically analysed. (LASER scanners are also used, but are still in the testing stage.) When the scene is pictured by a stereo-pair of photographs, the mapping process involves three phases:

- *Localisation and Orientation by Resection*: the position and attitude (exterior orientation parameters, EOP) of an image are determined by having at least three

points with known coordinates (Ground Control Points, GCP) in the object frame as well as in the image frame;

- *Transfer of homologous points by intersection*: two images with known exterior orientations parameters are used to determine the coordinates in the object frame of points found on both images simultaneously, employing the principle of stereovision.
- *Restitution*: where the actual mapping takes place by drawing the features, contour line, borders, surfaces, etc.

Thus, resection is used for localisation and orientation, and intersection is used for determining features' coordinates; by combining these two problems aero-triangulation (AT) is accomplished. Before the realisation of the GPS/IMU integration for the direct georeferencing (Skaloud 1999, Colomina, 1999), the mapping industry relied mainly on the AT and Bundle Adjustment (Triggs et al., 2000) by making use of GCPs.

Mapping systems are employed in aircrafts as well as in land vehicles. *Airborne systems* usually employ a high quality camera and/or a LASER scanner for mapping, and IMU/GPS integration for the determination of the location and orientation (georeferencing) of the images. An example of the *airborne systems* is an innovative hand-held system that was developed at the Swiss Federal Institute of Technology in Lausanne that utilises a tactical-grade IMU, a GPS, a high-definition camera, and a laser scanner (Skaloud et al., 2005).

Terrestrial systems are similar to their airborne counterparts with a difference that more than one camera might be used (El-Sheimy, 1996); these systems are the standard ones used now in the mapping industry.

The sensors used for the location and orientation can be a combination of IMU/GPS, odometers, compasses, etc. Another example of terrestrial mapping systems is a hand-held system consisting of a GPS, compass, and a camera was developed in 2001, with which small and quick surveys are accomplished (Ellum, 2001).

The estimation methods in Geomatics are mainly the Kalman Filter (Kalman, 1960) and the Least Squares Adjustment (Bjerhammar, 1973; Mikhail, 1976). Kalman Filter has been the focus of research in Geomatics Engineering in the 1980's and 1990's, where centralised, decentralised, federated, adaptive filters were analysed and compared (Wei and Schwarz, 1990; Gao et al., 1993).

LSA has been the monopolistic estimation method for Geomatics Engineers for more than 200 years. LSA usage ranged from adjusting simple geodetic networks to computing the orbits of satellites (e.g., see Moritz, 1980).

In mobile mapping system, the two filters go along each other. The navigation parameters are determined by Kalman and LSA and are then used for feature coordinates determination by LSA.

Newly, other estimation and filtering methods have been surfacing, for example, neural networks (Chiang, 2005) and wavelets (Nassar, 2003). These investigations are still in their infancy and their effectiveness is still under scrutiny.

As in the case of this work, positioning/localisation can be done by vision employing the method of resection. Chaplin and Chapman (1998) and Chaplin (1999) studied the possibility of using the position of known features to estimate the position of the camera. Their attempt stopped at that stage without going further to exploit any integration with other sensors. Recently, other studies start to surface using images to position the mapping vehicles. Two of these studies were presented in the latest conference on Optical 3-D Measurement Techniques held in Vienna. The first (Forlani et al., 2005) uses a sequence of images to georeference the mapping van for 15 s (300m) trajectory, where they concentrated on feature automated extraction and robust removal of mismatches; however, they have not used the information from the IMU. The intersection-resection problem is solved by taking the relative orientation between the two cameras into account. Although this aids in the automation of finding the targets, it will render the system useless when one of the cameras malfunctions.

The second study (Horemuz and Gajdamowicz, 2005) is similar to what this thesis is about, yet they are using a single camera and the system seems to be handheld. Nevertheless, from the paper and later discussion with one of the authors no clear picture could be extracted on their methodology of integration in Kalman Filter. In this paper also, feature extraction was done in an automated procedure.

Other studies used photogrammetric localisation in industry, but this was limited in using one stationary camera to localise moving objects (El-Hakim et al., 1997; Blais et al., 2001; Böhm et al., 2001). Hofmann-Wellenhof et al. (2002) describes briefly the use of photogrammetry as a navigation method, but no further discussion was made.

1.4 - Navigation and Mapping Systems in Robotics

There is a plethora of navigation and mapping systems in the robotics community. The reader can consult Thrun (2002) for a general survey on robotic mapping.

Classically, terrestrial robotics SLAM is approached using LASER scanners to locate the robot relative to a structured environment and to map this environment at the same time.

LASER scanners have shown to be very good tools where the accuracy of localisation is within the centimetre level. However, outdoors robotics SLAM is not feasible with LASER scanners alone due to the environment's roughness and absence of simple geometric features. Recently, the use of cameras (and videos) has gained an interest.

Inertial systems, IMU, GPS, compasses and odometers are widely used in the robotics community as navigation sensors; however, mostly localisation is solved in 2-D space.

A survey of recent publications shows an augmented interest in the use of cameras and inertial sensors; this is due to the advancement in the hardware and software. It is hard to choose a list of publications due to the huge amount of production; for this, reference will be made on journal papers and theses. Concerning proceeding papers, one can consult the IROS conferences and the IEEE publications.

A quick look can classify these systems into two categories:

- Indoors: the indoor robots are supported by laser scanners, odometers, MEMS, and recently cameras.
- Outdoors: the outdoors robots can be classified as terrestrial, airborne, and underwater. Mainly, these robots are supported by cameras, IMU and GPS.

In the robotics community, lots of effort is directed towards full automation; and thus one can see many publications on the possibility of automated pixel tracking on images and real time navigation and mapping (Jung, 2004). As for the estimation methods, Kalman Filter is widely used and it will be discussed in the next Section.

The interested reader can go through the following list of publications: Masson et. al (2003); Nebot and Durrant-Whyte (1999); Sukkarieh (2000); Huster (2003); Davison (1998); Wheeler (1996); Rönnbäck (2000); Guivant (2002); Knight (2002); Bosse (1997); Csorba (1997); Newman (1999); Mächler (1998); Majumder (2001); Williams (2001); Jung (2004); Bailey (2002); Tomatis (2001); Lemon (2005); Groves et al. (2004); Martinelli (2002). The reader can also look at the two special issues of the Journal of Robotic Systems (Volume 21, issues 1 and 2, 2004) that is devoted to the topic of "Integration of Visual and Inertial Sensors".

The differences with the Geomatics methodology of mapping and navigation will be pointed out in the next Sections.

1.5 - Geomatics and Robotics – The Second Link

The difference between Robotics versus Geomatics Engineering arise from the global understanding of Geomatics Engineers about localisation and mapping, where the

applications are not limited to indoors and/or to small areas, but rather the whole planet is concerned. For Geomatics Engineers, coordinates are meaningless if they are not linked to a global reference frame and maps are useless if they only represent an area without the possibility of linking it to other areas. Three-dimensional perception is very essential for the Geomatics community, where the vertical component is as important as the other two horizontal components (not to mention the fourth dimension of Geomatics, time).

Mapping in the Geomatics community has to give a clear image of the surrounding. It is important to know if the object is a tree, a power column or a traffic post, or whether the other object is a fence or a house wall, or if this structure is a house, a building, or a factory, etc.

For Geomatics Engineers, a geographically referenced object does not mean much if it is not associated with information about its nature. Therefore, Geomatics Engineers do not only navigate and map to accomplish a certain task, but also acquire information about the mapped objects to determine spatially referenced databases for many needs.

From what is revealed from the publications done by the robotics community, the solution is usually simplified by forcing some postulations that apply to small scale SLAM, e.g., 2-D localisation, ignoring offsets and angle transformations and not contributing for different reference systems. It is clear that these simplifications do not affect the 2-D SLAM; however, this is not the case when working on 3-D SLAM. If one takes for example the study done by Kim and Sukkarieh (2003) – which is very close to this work – it can be argued that the navigation modelling is not complete for large scale 3-D SLAM; moreover, the mapping modelling is correct for LASER scanning and not for frame images.

In addition to this, SLAM solutions compute the features coordinates using Kalman Filter (Thrun, 2002). Conceptually this is an interesting problem, but practically it is problematic due to the simplification forced on the models; in addition, if estimation methods other than the Kalman Filter are used, the correlations between the location of the vehicle and the map cannot be taken into account. Moreover, as more features are mapped, the state vectors becomes bigger and bigger thus increasing the possibility of the filter divergence. Despite the fact that this concept contributes for the important correlations between the features' coordinates and the mapping device coordinates, these contributions do not affect the overall results as was shown in Martenilli and Siegwart (2005).

The methodology proposed here to solve the SLAM is by using the Photogrammetric resection outputs – computed by LSA – as the INS Kalman Filter external measurements to compute a filtered position that is used in the photogrammetric intersection to determine the feature coordinates by LSA.

The Kalman Filter (KF) used here is similar to that of navigation applications where traditionally the IMU provides data for the prediction and the GPS (and other positioning and orientation sensors) are used for the update. Nevertheless, instead of using the GPS, the outputs from photogrammetric resection (EOP) will be used as updates. In this way – contrary to the robotics SLAM KF – the SLAM navigation KF proposed here:

- Operates at the frequency of the update (e.g., 1 or 2 Hz), and
- Its state vector size is kept constant and small (e.g., 15 states) with homogeneous states that guarantee rapid convergence.

In addition, by separating the two filters a rigorous integration is achieved between the vision and inertial sensors using complete modelling.

1.6 - Behaviours, Sensors and Application Themes

Figures (1-2) to (1-4) show the pipelines that define Application Themes of the system, used Sensors and system's Behaviours.

The system is for localisation/navigation using an unknown metric map that can be run on-line and off-line. The system is as well a mapping system that uses the photogrammetry either with one or two cameras employing the property of stereovision (Fig. 1-2).

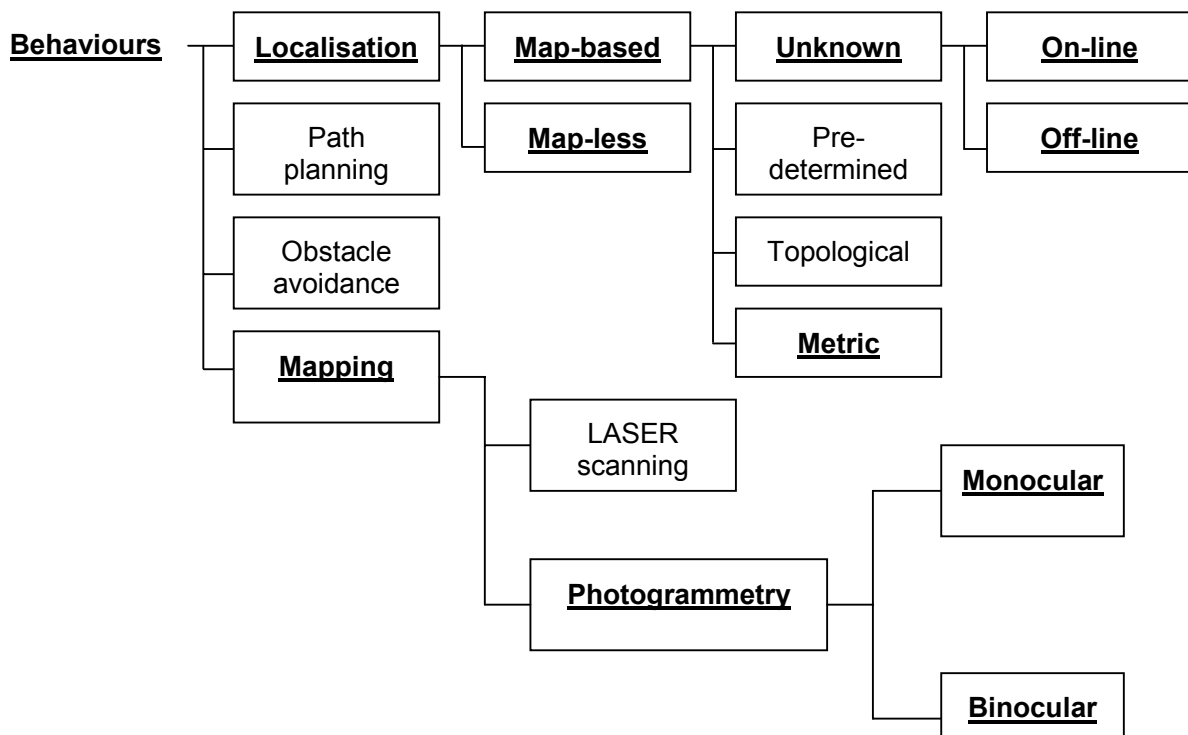


Figure 1-2: Behaviours of the system

In the navigation and mapping systems, there is a plethora of choices of sensors; but mainly they are classified according to Figure (1-3). Of these, the system in this work uses vision and inertial.

Sensors

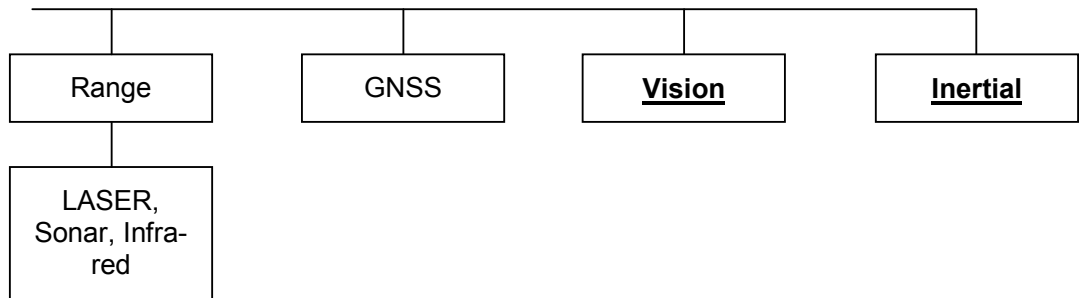


Figure 1-3: Used sensors

As for the applications envisaged for this system, they are mainly concerned with Mobile Mapping Systems (MMS) and robotics. Figure (1-4) shows explicitly the different applications' branches.

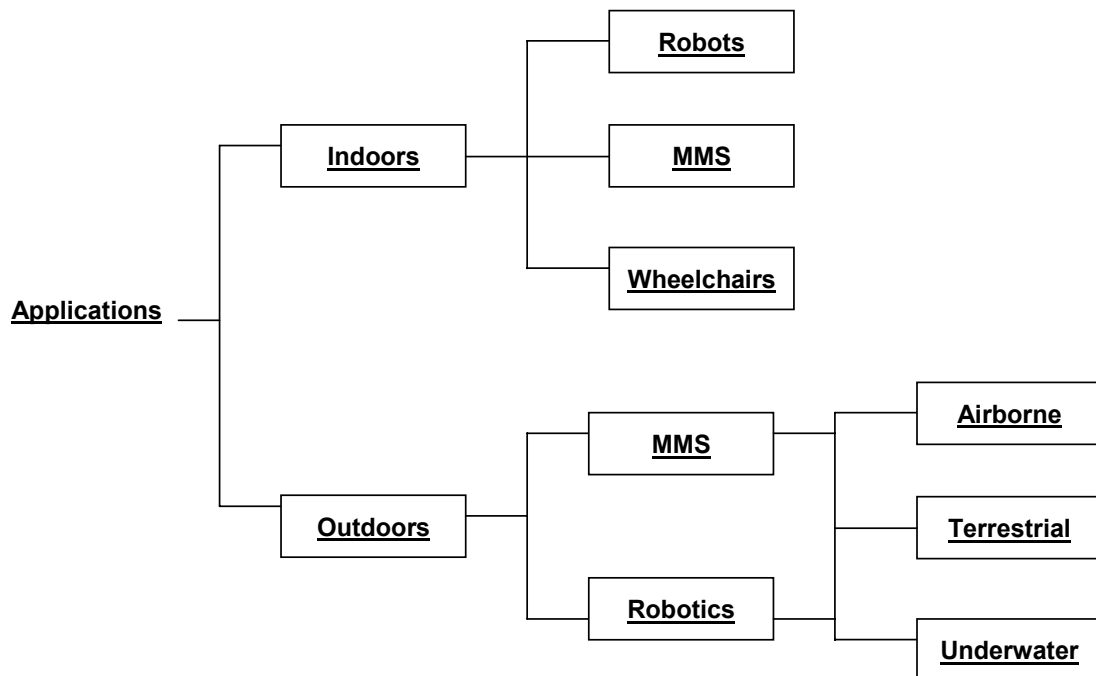


Figure 1-4: Applications of the system

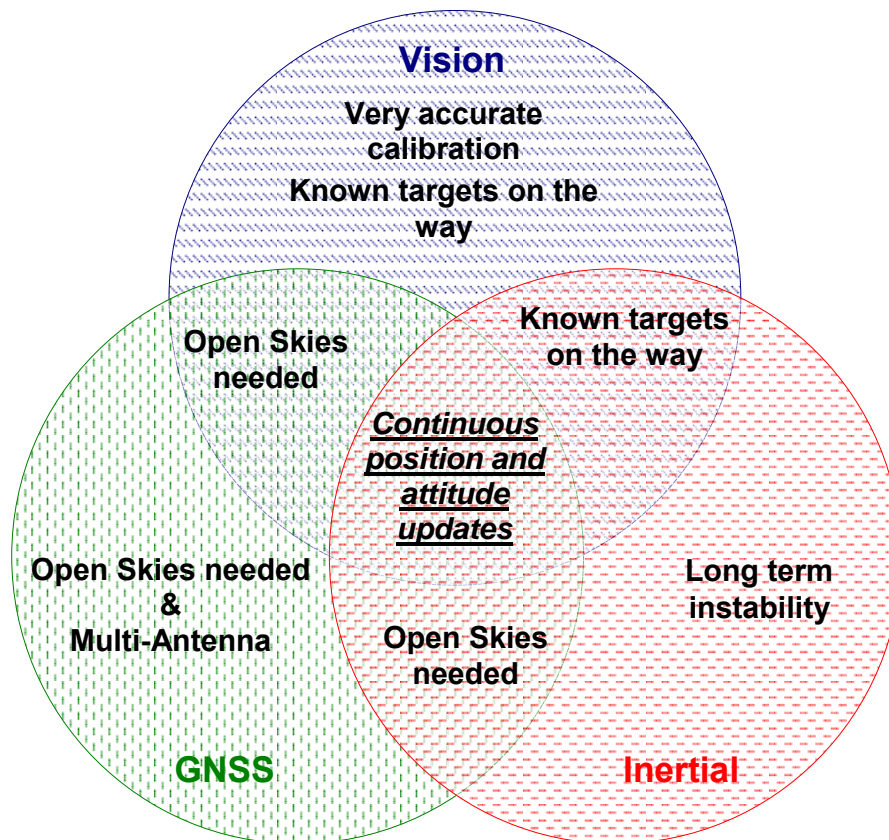


Figure 1-5: Navigation methods

Figure (1-5) shows the disadvantages of each of the navigation methods that could be used and the advantages of integrating them. (In Figure (1-5), ranging sensors are considered as vision sensors.) This figure is self-explanatory, where it is obvious that integrating two or three of these navigation methods will provide with the best-case scenario.

Automated feature extraction and object recognition are two essential parts of any MMS, which are so far considered to be the main obstacles in mobile mapping. Yet, these issues are not discussed in this work due to the complexity and huge effort that they require, where they merit an independent study.

1.7 - Photogrammetry Alone Solving SLAM

By looking at the phases of map-making, one can observe that photogrammetry by itself is a SLAM solution. An obvious question is: why an IMU is needed?

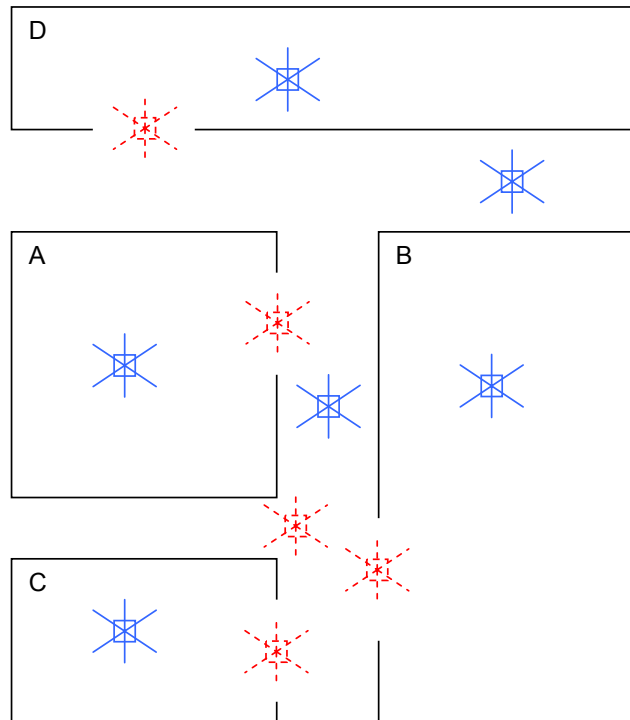


Figure 1-6: A possible environment where an IMU is needed

Consider Figure (1-6). This is a typical environment, where the robot manoeuvres between rooms A, B, C and D. As long as the robot takes the positions depicted in the solid symbol, an IMU might be considered as superfluous. However, when the vehicle is located in situations similar to those depicted in the dashed symbol:

- The field of vision of the cameras is too narrow, or
- The number of known points is insufficient.

If the cameras were to take images with a high frequency, e.g., greater than 20 Hz, the two points above might be obsolete; however, would the solution be reliable considering the narrow field of vision that would be created? In addition, depending on the geometry of the system, images at 20 Hz will not guarantee a problem-free solution, especially when objects are far away from the cameras.

Nevertheless, Chapter 2 will contain a derived solution of SLAM by photogrammetry, where this procedure requires certain points to consider:

- Recursive LSA: the LSA solution of the epoch $k-1$ is used as observations for epoch k ,
- Correlations between measurements and unknowns are carried from one epoch to the other.

In addition to this, the IMU-derived position is likely to facilitate the connection between the photographs so that the search region in the different images for feature pixel tracking is minimised. This is important when the same feature needs to be tracked on different images.

1.8 - Thesis Contribution

In this thesis, a vision-based inertial navigation system was developed for a mobile mapping system. Although such systems already exist in the robotics community, the contribution of this thesis lies in proposing and testing a novel methodology for a rigorous integration between vision and inertial sensors by using complete modelling.

Image-based bridging techniques were proposed in geomatics engineering at the end of the last decade; however, these techniques did not go as far as the integration with IMU in a Kalman Filter.

In addition to the novel concept of this integration, a detailed derivation of recursive LSA through interchanging resection and intersection was presented to solve SLAM by photogrammetry alone. To the knowledge of the author, this derivation is introduced for the first time.

Extensive and from-scratch programming was necessary for this work. Although SLAM codes are abundant in the robotics community, they were inadequate for this work. To test the methodology, a SLAM program was written (in MATLAB®) using the following modules, in addition to the main program: INS mechanisation equations, LSA resection, LSA intersection, Kalman Filter and Boresight and leverarm computation. Planning, writing and testing the main program and its accompanying modules took a large portion of the time dedicated for this thesis because no modules pre-existed beforehand and thus everything had to start from the scratch. (The image acquisition and synchronisation codes were appreciatively written by Dr. Jan Skaloud.)

1.9 - Thesis Outline

The thesis is organised as follows.

The Second Chapter covers Photogrammetry and its positioning solution for SLAM. The mathematical models and the least-squares adjustment of resection and intersection are shown along with their error analyses.

The Third Chapter discusses the instrumentation used for photogrammetry. The design of the system by analysing the choice of the focal length and stereo-base is examined. The last Section of this chapter studies the camera calibration.

The Fourth Chapter analyses the Inertial Navigation Systems (INS). The mechanisation equations are presented and the INS system errors are analysed, which is later used in the Kalman Filter. The last Section treats the quality of the IMU used in this work and the possibility of auto-initialisation (gyro-compassing).

In the Fifth Chapter, the positioning methodology via integrating vision and inertial sensors is presented. In this Chapter, the different reference systems transformations and system calibration are introduced and the appropriate equations are derived.

In Chapter 6, the methodology is tested and results are discussed.

Chapter 7 draws conclusions and suggests recommendation for future work.

Finally, Appendix A shows the full solution of the two photogrammetric problems in terms of quaternions, Appendix B has the calibration solution of the two CCDs, Appendix C shows the photos that are used in the test and Appendix D has detailed tables determined in Chapter 6.

2 - CLOSE-RANGE PHOTOGRAMMETRY SOLVING SLAM

... being a Photogrammetrist, I am trained to have a 3-D vision and to map new opportunities ...

2.1 - Introduction

The link between photogrammetry and SLAM is established in this chapter. This relation has not gained much attention until lately due to the fact that SLAM, among other things, requires automation, which is far from reality in photogrammetry. Many attempts are directed towards the full automation of photogrammetry, but still falling short due to the need of a high level of artificial intelligence.

Having in mind that it is only a matter of time to reach full automation, an investigation on SLAM from the Geomatics point of view is essential.

This chapter covers the functional mathematical model and formulation of photogrammetry, by which the two main problems of photogrammetry – namely Resection and Intersection – are solved in a Least-Square Adjustment frame. The last Section concentrates on the recursive mode for solving SLAM trajectory using resection and intersection.

2.2 - Definition of Photogrammetry

According to the International Society of Photogrammetry and Remote Sensing (ISPRS): “Photogrammetry and Remote Sensing is the art, science, and technology of obtaining reliable information about physical objects and the environment through the processes of recording, measuring, and interpreting imagery and digital representations thereof derived from non-contact sensor systems.”

The two terms, Photogrammetry and Remote Sensing, passed through many stages of controversial definitions and connotation until the ISPRS in 1992 gave the definition stated above.

Reliable information here is defined by its geographical location, so that it can be correctly represented on a geographic information medium, i.e., a map. For the Geomatics community, photogrammetry is a mapping technique, by which images of the real world are analysed mathematically – after being recorded, processed, and interpreted – and coordinates of physical objects and of the environment, found on the images, are determined in a reference frame.

There is a broad range of categories in photogrammetry: airborne, terrestrial and close-range with vertical, nearly vertical, oblique and horizontal exposures. Close-range terrestrial photogrammetry and horizontal exposures are dealt with in this work. The mathematical principles of photogrammetry are known and in general, they apply to all previously mentioned categories.

2.3 - Mathematical Model in Photogrammetry

The relation between the image and the objects are derived from the physical assumption that the perspective centre, the object and its image are collinear (Figure 2-1). This relation gives the following functional model per point (ASPRS, 2004):

$$\begin{aligned} F(x) &\equiv -x + x_0 - c \frac{R_{11}(X - X_0) + R_{12}(Y - Y_0) + R_{13}(Z - Z_0)}{R_{31}(X - X_0) + R_{32}(Y - Y_0) + R_{33}(Z - Z_0)} = -x + x_0 - c \frac{U}{W} = 0 \\ F(y) &\equiv -y + y_0 - c \frac{R_{21}(X - X_0) + R_{22}(Y - Y_0) + R_{23}(Z - Z_0)}{R_{31}(X - X_0) + R_{32}(Y - Y_0) + R_{33}(Z - Z_0)} = -y + y_0 - c \frac{V}{W} = 0 \end{aligned} \quad (2.1)$$

where

x, y are the photo-coordinates in the image frame

X, Y, Z are the coordinates in the object frame

c is the focal length of the camera

X_0, Y_0, Z_0 are the coordinates of the perspective centre in the object frame

x_0, y_0 are the photo-coordinates of the principal point that is the projection of the perspective centre to the image plane. Theoretically, it has to coincide with the centre of the image frame, but in reality it does not

R_{ij} 's are the elements of the rotation matrix between the image and object frames, based on Euler angles: roll ω , azimuth α , and pitch κ

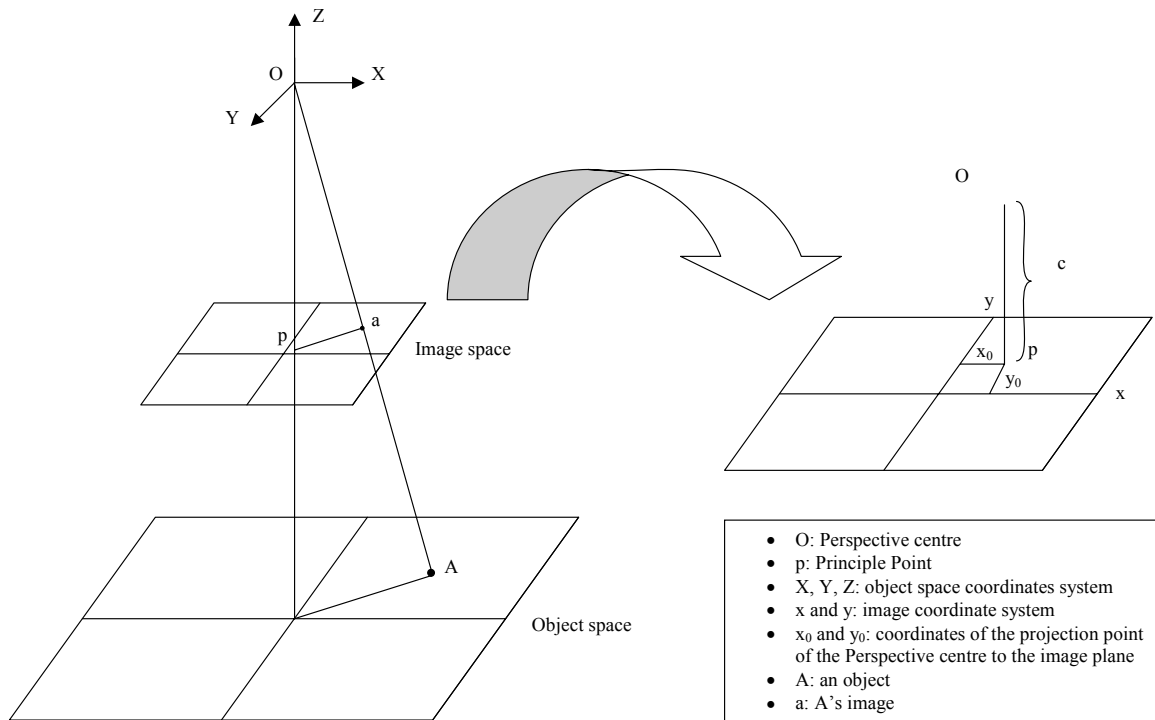


Figure 2-1: General Image Geometry

The rotation matrix \mathbf{R}_m^c links the image coordinate system to the mapping reference system, which is chosen to be an East-North-Up (ENU) system, as follows (λ being the scale):

$$\begin{bmatrix} x - x_0 \\ y - y_0 \\ -c \end{bmatrix} = \lambda^{-1} \mathbf{R}_m^c \begin{bmatrix} X - X_0 \\ Y - Y_0 \\ Z - Z_0 \end{bmatrix}$$

To go from ENU to the image coordinate system (Figure 2-2), a sequence of rotations is carried out as follows (Dermanis, 1990; P. 233):

- A rotation of 90° around the X-axis: $\mathbf{R}_1(90^\circ)$
- A rotation of $-\alpha$ around the Y-axis: $\mathbf{R}_2(-\alpha)$
- A rotation of ω around the X-axis: $\mathbf{R}_1(\omega)$
- A rotation of κ around the Z-axis: $\mathbf{R}_3(\kappa)$

Thus, the overall rotation is:

$$\mathbf{R}_m^c = \mathbf{R}_3(\kappa) \mathbf{R}_1(\omega) \mathbf{R}_2(-\alpha) \mathbf{R}_1(90^\circ)$$

$$\mathbf{R}_m^c = \begin{bmatrix} \cos\kappa \cos\alpha + \sin\kappa \sin\omega \sin\alpha & \cos\kappa \sin\alpha - \sin\kappa \sin\omega \cos\alpha & \sin\kappa \cos\omega \\ -\sin\kappa \cos\alpha + \cos\kappa \sin\omega \sin\alpha & -\sin\kappa \sin\alpha - \cos\kappa \sin\omega \cos\alpha & \cos\kappa \cos\omega \\ \cos\omega \sin\alpha & -\cos\omega \cos\alpha & -\sin\omega \end{bmatrix}$$

Of course there are other rotation sequences that can be followed, and there is really no central reason why to choose one among the other as long as no singularity is produced.

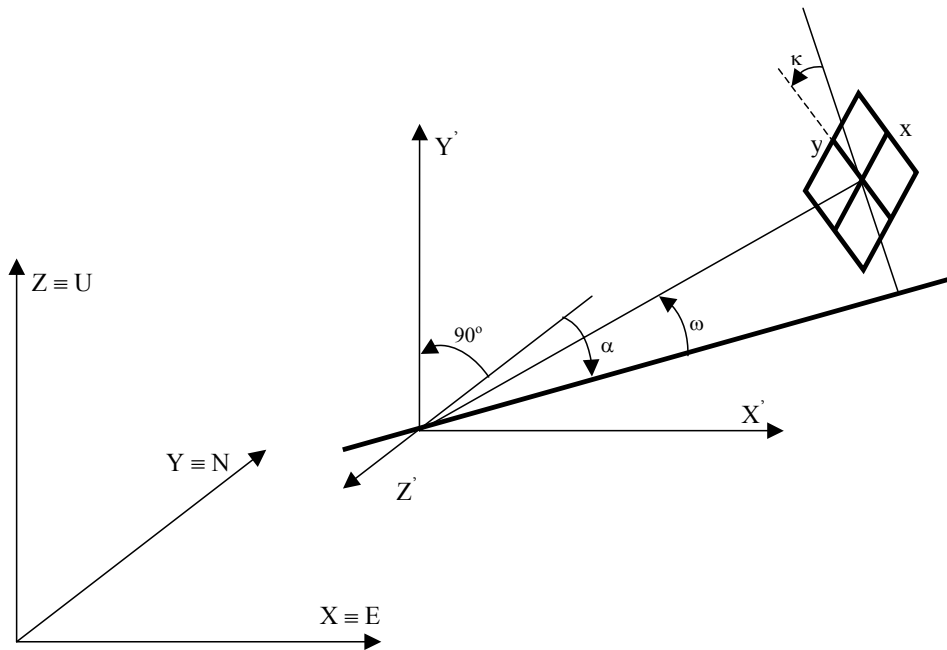


Figure 2-2: Transformation sequence between ENU and image systems

To avoid singularities in computing the rotation angles from \mathbf{R}_m^c , a quaternion solution can be suggested. Appendix A shows the development of this chapter in terms of quaternions.

In photogrammetry, two terms are distinguished: interior and exterior orientation. The first term embraces the focal length and the coordinates of the projection of the perspective centre to the image plane: c, x_0, y_0 . The Exterior Orientation Parameters (EOP), on the other hand, is the set of the coordinates of the perspective centre in the object frame and the three rotation angles: $X_0, Y_0, Z_0, \omega, \alpha, \kappa$.

In this chapter, all the vectors and matrices (**Bold**) headed by a prime (e.g., \mathbf{X}') refer to the resection and all those headed by two primes (e.g., \mathbf{X}'') refer to the intersection.

2.4 - Resection

Equation (2.1) is the fundamental mathematical model of photogrammetry describing the relationship between the image and the object coordinate systems. With this model, one can solve the basic problems of photogrammetric mapping, namely: the resection and the intersection, which when merged together form the photogrammetric triangulation.

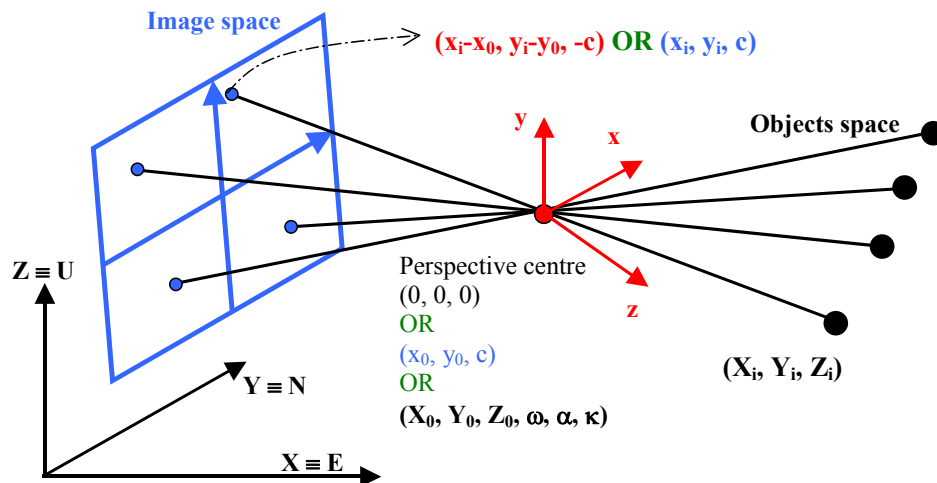


Figure 2-3: Resection Problem

With the problem of resection (Figure 2-3), the EOP of an image are determined by having at least a set of three points whose coordinates are known in the object frame as well as in the image frame; these points are called Ground Control Points (GCP). Therefore, in the problem of resection the known, unknowns and measurements are:

Measurements: $X_i, Y_i, Z_i, x_i, y_i \quad i = 1 \dots n$; **Unknowns:** $X_0, Y_0, Z_0, \omega, \alpha, \kappa$

In the resection, there are six unknowns; for the system of equation to be solved, at least six equations are needed. A minimum set of six equations is used through measuring the photo-coordinates, (x_i, y_i) , of three GCPs. When over determined, which is the case all the time, the resection is handled in the frame of LSA.

2.4.1 - Resection by Least-Squares Adjustment

To solve the resection, we consider the following vectors. The vector of the unknowns:

$$\mathbf{x}' = [X_0 \quad Y_0 \quad Z_0 \quad \omega \quad \alpha \quad \kappa]^T$$

is computed by:

$$\mathbf{x}' = \overset{\circ}{\mathbf{x}'} + \delta\mathbf{x}' \quad (2.2)$$

where $\overset{\circ}{\mathbf{x}'}$ is the vector of the approximate values of \mathbf{x}' (computed with a minimum of 3 GCPs):

$$\overset{\circ}{\mathbf{x}'} = \left[\overset{\circ}{X}_0 \quad \overset{\circ}{Y}_0 \quad \overset{\circ}{Z}_0 \quad \overset{\circ}{\omega} \quad \overset{\circ}{\alpha} \quad \overset{\circ}{\kappa} \right]^T$$

and $\delta\mathbf{x}'$ is the computed vector of corrections by LSA:

$$\delta\mathbf{x}' = [\delta X_0 \quad \delta Y_0 \quad \delta Z_0 \quad \delta\omega \quad \delta\alpha \quad \delta\kappa]^T$$

The vector of observables is:

$$\mathbf{y}' = [x_1 \quad y_1 \quad X_1 \quad Y_1 \quad Z_1 \quad \cdots \quad x_n \quad y_n \quad X_n \quad Y_n \quad Z_n]^T$$

Having the above vectors, $\delta\mathbf{x}'$ is computed through solving the following linear equation:

$$\mathbf{A}'\delta\mathbf{x}' + \mathbf{B}'\mathbf{v}' + \mathbf{w}' = \mathbf{0} \quad (2.3)$$

\mathbf{v}' is the vector of errors. The misclosure vector $\mathbf{w}' = F\left(\overset{\circ}{\mathbf{x}'}, \mathbf{y}'\right)$. The LSA solution of Equation (2.3) is:

$$\delta\mathbf{x}' = \mathbf{N}'^{-1}\mathbf{U}', \quad (2.4)$$

$$\text{with } \mathbf{N}' = \mathbf{A}'^T \mathbf{M}'^{-1} \mathbf{A}', \quad \mathbf{U}' = \mathbf{A}'^T \mathbf{M}'^{-1} \mathbf{w}', \quad \mathbf{M}' = \mathbf{B}' \mathbf{C}'_y \mathbf{B}'^T$$

\mathbf{C}'_y is the variance-covariance matrix of the observables that takes the following form:

$$\mathbf{C}'_y = \begin{bmatrix}
 \sigma_{x_1}^2 & 0 & 0 & 0 & 0 & \dots & 0 & 0 & 0 & 0 & 0 \\
 & \sigma_{y_1}^2 & 0 & 0 & 0 & \dots & 0 & 0 & 0 & 0 & 0 \\
 & & \sigma_{x_1}^2 & \sigma_{x_1 y_1} & \sigma_{x_1 z_1} & \dots & 0 & 0 & \sigma_{x_1 x_n} & \sigma_{x_1 y_n} & \sigma_{x_1 z_n} \\
 & & & \sigma_{y_1}^2 & \sigma_{y_1 z_1} & \dots & 0 & 0 & \sigma_{y_1 x_n} & \sigma_{y_1 y_n} & \sigma_{y_1 z_n} \\
 & & & & \sigma_{z_1}^2 & \dots & 0 & 0 & \sigma_{z_1 x_n} & \sigma_{z_1 y_n} & \sigma_{z_1 z_n} \\
 & & & & & \dots & \vdots & \vdots & \vdots & \vdots & \vdots \\
 & & & & & & \sigma_{x_n}^2 & 0 & 0 & 0 & 0 \\
 & & & & & & & \sigma_{y_n}^2 & 0 & 0 & 0 \\
 & & & & & & & & \sigma_{x_n}^2 & \sigma_{x_n y_n} & \sigma_{x_n z_n} \\
 & & & & & & & & & \sigma_{y_n}^2 & \sigma_{y_n z_n} \\
 & & & & & & & & & & \sigma_{z_n}^2
 \end{bmatrix}_{5n \times 5n}$$

Matrix \mathbf{A}' is the first design matrix (Jacobi matrix) and it contains the derivatives of the measurement model (Eq. 2.1) with respect to the Unknowns. Matrix \mathbf{B}' is the second design matrix and it contains the derivatives of the measurement model with respect to the observables.

$$\mathbf{A}' = \begin{bmatrix}
 \frac{\partial F(x)_1}{\partial X_0} & \frac{\partial F(x)_1}{\partial Y_0} & \frac{\partial F(x)_1}{\partial Z_0} & \frac{\partial F(x)_1}{\partial \omega} & \frac{\partial F(x)_1}{\partial \alpha} & \frac{\partial F(x)_1}{\partial \kappa} \\
 \frac{\partial F(y)_1}{\partial X_0} & \frac{\partial F(y)_1}{\partial Y_0} & \frac{\partial F(y)_1}{\partial Z_0} & \frac{\partial F(y)_1}{\partial \omega} & \frac{\partial F(y)_1}{\partial \alpha} & \frac{\partial F(y)_1}{\partial \kappa} \\
 \vdots & \vdots & \vdots & \vdots & \vdots & \vdots \\
 \frac{\partial F(x)_n}{\partial X_0} & \frac{\partial F(x)_n}{\partial Y_0} & \frac{\partial F(x)_n}{\partial Z_0} & \frac{\partial F(x)_n}{\partial \omega} & \frac{\partial F(x)_n}{\partial \alpha} & \frac{\partial F(x)_n}{\partial \kappa} \\
 \frac{\partial F(y)_n}{\partial X_0} & \frac{\partial F(y)_n}{\partial Y_0} & \frac{\partial F(y)_n}{\partial Z_0} & \frac{\partial F(y)_n}{\partial \omega} & \frac{\partial F(y)_n}{\partial \alpha} & \frac{\partial F(y)_n}{\partial \kappa}
 \end{bmatrix}_{2n \times 6}$$

$$\mathbf{B}' = \begin{bmatrix}
 \frac{\partial F(x)_1}{\partial x_1} & \frac{\partial F(x)_1}{\partial y_1} & \frac{\partial F(x)_1}{\partial X_1} & \frac{\partial F(x)_1}{\partial Y_1} & \frac{\partial F(x)_1}{\partial Z_1} & \dots & 0 & 0 & 0 & 0 & 0 \\
 \frac{\partial F(y)_1}{\partial x_1} & \frac{\partial F(y)_1}{\partial y_1} & \frac{\partial F(y)_1}{\partial X_1} & \frac{\partial F(y)_1}{\partial Y_1} & \frac{\partial F(y)_1}{\partial Z_1} & \dots & 0 & 0 & 0 & 0 & 0 \\
 \vdots & \vdots & \vdots & \vdots & \vdots & \ddots & \vdots & \vdots & \vdots & \vdots & \vdots \\
 0 & 0 & 0 & 0 & 0 & \dots & \frac{\partial F(x)_n}{\partial x_n} & \frac{\partial F(x)_n}{\partial y_n} & \frac{\partial F(x)_n}{\partial X_n} & \frac{\partial F(x)_n}{\partial Y_n} & \frac{\partial F(x)_n}{\partial Z_n} \\
 0 & 0 & 0 & 0 & 0 & \dots & \frac{\partial F(y)_n}{\partial x_n} & \frac{\partial F(y)_n}{\partial y_n} & \frac{\partial F(y)_n}{\partial X_n} & \frac{\partial F(y)_n}{\partial Y_n} & \frac{\partial F(y)_n}{\partial Z_n}
 \end{bmatrix}$$

$$= \begin{bmatrix} -1 & 0 & \frac{\partial F(x)_1}{\partial X_1} & \frac{\partial F(x)_1}{\partial Y_1} & \frac{\partial F(x)_1}{\partial Z_1} & \dots & 0 & 0 & 0 & 0 & 0 \\ 0 & -1 & \frac{\partial F(y)_1}{\partial X_1} & \frac{\partial F(y)_1}{\partial Y_1} & \frac{\partial F(y)_1}{\partial Z_1} & \dots & 0 & 0 & 0 & 0 & 0 \\ \vdots & \vdots & \vdots & \vdots & \vdots & \ddots & \vdots & \vdots & \vdots & \vdots & \vdots \\ 0 & 0 & 0 & 0 & 0 & \dots & -1 & 0 & \frac{\partial F(x)_n}{\partial X_n} & \frac{\partial F(x)_n}{\partial Y_n} & \frac{\partial F(x)_n}{\partial Z_n} \\ 0 & 0 & 0 & 0 & 0 & \dots & 0 & -1 & \frac{\partial F(y)_n}{\partial X_n} & \frac{\partial F(y)_n}{\partial Y_n} & \frac{\partial F(y)_n}{\partial Z_n} \end{bmatrix}_{2n \times 5n}$$

The approximate values of the parameters are used to compute the matrices \mathbf{A}' and \mathbf{B}' .

The precision estimation of the parameters, residuals and observables are computed, respectively, as:

$$\mathbf{C}'_{\hat{x}} = \mathbf{N}'^{-1} \quad (2.6)$$

$$\mathbf{C}'_v = \mathbf{C}'_y \mathbf{B}'^T \mathbf{M}'^{-1} \mathbf{B}' \mathbf{C}'_y - \mathbf{C}'_y \mathbf{B}'^T \mathbf{M}'^{-1} \mathbf{A}' \mathbf{N}'^{-1} \mathbf{A}'^T \mathbf{M}'^{-1} \mathbf{B}' \mathbf{C}'_y \quad (2.7)$$

$$\mathbf{C}'_{\hat{y}} = \mathbf{C}'_y - \mathbf{C}'_v \quad (2.8)$$

The a-posteriori variance factor is:

$$\hat{\sigma}_0^2 = \frac{\mathbf{v}^T \mathbf{P} \mathbf{v}}{2n - 6}$$

where $2n$ is the number of observables, 6 is the number of the unknowns.

2.4.2 - Resection Accuracy

The accuracy of the resection increases as the number of measured points increases. In order to determine the accuracy of the resection, the design matrices \mathbf{A}' and \mathbf{B}' have to be determined by substituting the approximate values (shown below) of the unknowns, from which the normal matrix \mathbf{N}' is computed by $\mathbf{N}' = \mathbf{A}'^T \mathbf{M}'^{-1} \mathbf{A}'$. The accuracy estimates of resection outputs are calculated by $\mathbf{C}'_{\hat{x}} = \mathbf{N}'^{-1}$. For this task, a simulation was performed. To begin with, consider that the approximate values of the EOP to be as follows:

$$\overset{\circ}{X}_0 = \overset{\circ}{Y}_0 = \overset{\circ}{Z}_0 = 0 \quad , \quad \overset{\circ}{\omega} = \overset{\circ}{\alpha} = \overset{\circ}{\kappa} = 0$$

This means that a reference system is considered with its axes approximately parallel to their corresponding image axes, and that the principal point approximately coincides with the origin of the reference system. In addition to this, a grid of GCPs (with known error information) of size $q \times q$ with each node located at a different distance "h" from the camera, (Figure 2-4) was designed. In this way, one would be able to compute the elements of the design matrices. Four simulations were conducted:

- Four points were used with $q \times q = 6 \times 6$ metres,
- Nine points were used with $q \times q = 3 \times 3$ metres,
- Twenty five points were used with $q \times q = 1.5 \times 1.5$ metres, and
- Hundred points were used with $q \times q \approx 0.7 \times 0.7$ metres.

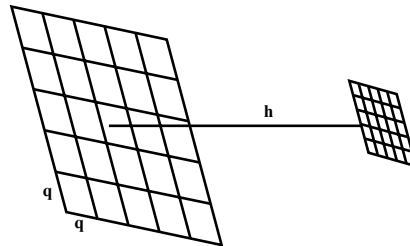


Figure 2-4

The coordinates of the GCPs in the object frame can be easily simulated because they belong to a grid with different depths. The error estimates of the GCPs were chosen to be 2.5 cm and that of the photo-coordinates to be $5\mu\text{m}$. The focal length was taken to be 6 mm and considered fixed in the LSA. The results of the simulations are shown in Table (2-1). As expected, the more the GCPs, the more accurate is the determination of the EOP. In real applications, a homogenous distribution of the GCPs all over the image is very important to attain good geometry to determine accurate EOP. Twenty-five points homogeneously distributed on the image allow locating the camera within a few centimetres.

Table 2-1: Estimated accuracies of Resection (Simulated)

	σ_{X_o} (m)	σ_{Y_o} (m)	σ_{Z_o} (m)	ω (arcmin)	α (arcmin)	κ (arcmin)
1 st test (4 pts.)	0.239	0.224	0.148	38.45	27.42	41.311
2 nd test (9 pts.)	0.145	0.132	0.097	6.51	8.38	9.24
3 rd test (25 pts.)	0.062	0.059	0.061	4.34	4.05	4.22
4 th test (100 pts.)	0.016	0.016	0.030	2.96	2.37	2.94

2.5 - Intersection

With the problem of intersection (Figure 2-5), two images, whose EOP are known, are used to determine the coordinates in the object frame of features found on both of them, employing the principle of stereovision. The known, unknowns and measurements (R and L designate the Right and Left camera/image) of this problem are:

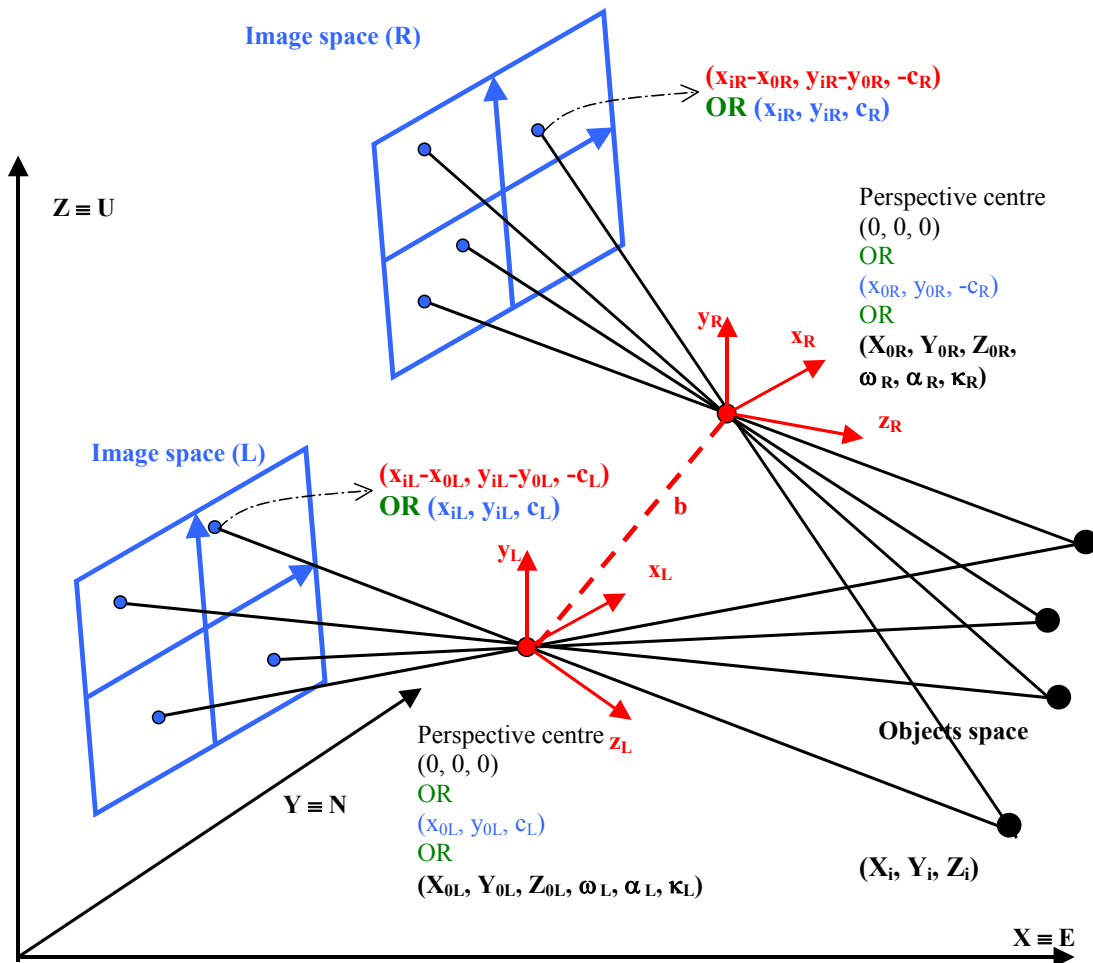


Figure 2-5: Intersection Problem

Measurements: $X_{0L/R}, Y_{0L/R}, Z_{0L/R}, \omega_{L/R}, \alpha_{L/R}, \kappa_{L/R}$ x_{ij}, y_{ij} ; **Unknowns:** X_i, Y_i, Z_i
 $i = 1 \dots n, j = R, L$

Intersection is always handled in the frame of LSA because there are always more measurements ($4n$) than unknowns ($3n$).

2.5.1 - Intersection by Least-Squares Adjustment

To solve the intersection, we consider the following vectors. The vector of the unknowns:

$$\mathbf{x}'' = [X_1 \ Y_1 \ Z_1 \ \cdots \ X_n \ Y_n \ Z_n]^T$$

is computed by:

$$\mathbf{x}'' = \overset{\circ}{\mathbf{x}}'' + \delta\mathbf{x}'' \quad (2.9)$$

where $\overset{\circ}{\mathbf{x}}''$ is the vector of the approximate values of the unknowns:

$$\overset{\circ}{\mathbf{x}}'' = \left[\overset{\circ}{X}_1 \ \overset{\circ}{Y}_1 \ \overset{\circ}{Z}_1 \ \cdots \ \overset{\circ}{X}_n \ \overset{\circ}{Y}_n \ \overset{\circ}{Z}_n \right]^T$$

and $\delta\mathbf{x}''$ is the computed vector of corrections by LSA:

$$\delta\mathbf{x}'' = [\delta X_1 \ \delta Y_1 \ \delta Z_1 \ \cdots \ \delta X_n \ \delta Y_n \ \delta Z_n]^T$$

The vector of observables is:

$$\mathbf{y}'' = \left[x_{L1} \ y_{L1} \ \cdots \ x_{Ln} \ y_{Ln} \ x_{L0} \ y_{L0} \ z_{L0} \ \omega_L \ \alpha_L \ \kappa_L \right. \\ \left. x_{R1} \ y_{R1} \ \cdots \ x_{Rn} \ y_{Rn} \ x_{R0} \ y_{R0} \ z_{R0} \ \omega_R \ \alpha_R \ \kappa_R \right]^T$$

Having the above vectors, $\delta\mathbf{x}''$ is computed through solving the following equation:

$$\mathbf{A}''\delta\mathbf{x}'' + \mathbf{B}''\mathbf{v}'' + \mathbf{w}'' = \mathbf{0} \quad (2.10)$$

\mathbf{v}'' is the vector of errors. The misclosure vector $\mathbf{w}'' = F\left(\overset{\circ}{\mathbf{x}}'', \mathbf{y}''\right)$. The LSA solution of

Equation (2.10) is, (similarly to (2.4)):

$$\delta\mathbf{x}'' = \mathbf{N}''^{-1}\mathbf{U}'' \quad (2.11)$$

where $\mathbf{N}'' = \mathbf{A}''^T \mathbf{M}''^{-1} \mathbf{A}''$, $\mathbf{U}'' = \mathbf{A}''^T \mathbf{M}''^{-1} \mathbf{w}''$, $\mathbf{M}'' = \mathbf{B}'' \mathbf{C}_y'' \mathbf{B}''^T$

The error information of the measurements \mathbf{C}_y'' is included in the variance-covariance matrix (R and L refer to the Right and Left camera/image):

$$\mathbf{C}_y'' = \begin{bmatrix} \mathbf{C}_{Ly}'' & \mathbf{C}_{LRy}'' \\ \mathbf{C}_{LRy}''^T & \mathbf{C}_{Ry}'' \end{bmatrix}_{(4n+14) \times (4n+14)}$$

$$\mathbf{C}_{jy}'' = \begin{bmatrix} \sigma_{x_{j1}}^2 & 0 & 0 & 0 & 0 & 0 & 0 & 0 & 0 & 0 & 0 & 0 \\ & \sigma_{y_{j1}}^2 & 0 & 0 & 0 & 0 & 0 & 0 & 0 & 0 & 0 & 0 \\ & & \ddots & 0 & 0 & 0 & 0 & 0 & 0 & 0 & 0 & 0 \\ & & & \sigma_{x_{jn}}^2 & 0 & 0 & 0 & 0 & 0 & 0 & 0 & 0 \\ & & & & \sigma_{y_{jn}}^2 & 0 & 0 & 0 & 0 & 0 & 0 & 0 \\ \text{---} & & & & & \sigma_{X_{j0}}^2 & \sigma_{X_{j0}Y_{j0}} & \sigma_{X_{j0}Z_{j0}} & \sigma_{X_{j0}\omega_j} & \sigma_{X_{j0}\alpha_j} & \sigma_{X_{j0}K_j} & \\ & & & & & \sigma_{Y_{j0}}^2 & \sigma_{Y_{j0}Z_{j0}} & \sigma_{Y_{j0}\omega_j} & \sigma_{Y_{j0}\alpha_j} & \sigma_{Y_{j0}K_j} & & \\ & & & & & & \sigma_{Z_{j0}}^2 & \sigma_{Z_{j0}\omega_j} & \sigma_{Z_{j0}\alpha_j} & \sigma_{Z_{j0}K_j} & & \\ & & & & & & & \sigma_{\omega_j}^2 & \sigma_{\omega_j\alpha_j} & \sigma_{\omega_jK_j} & & \\ & & & & & & & & \sigma_{\alpha_j}^2 & \sigma_{\alpha_jK_j} & & \\ & & & & & & & & & \sigma_{K_j}^2 & & \\ \text{---} & & & & & & & & & & & \end{bmatrix}$$

SYM.

$$\mathbf{C}_{LRy}'' = \begin{bmatrix} 0 & 0 & 0 & 0 & 0 & 0 & 0 & 0 & 0 & 0 & 0 \\ & 0 & 0 & 0 & 0 & 0 & 0 & 0 & 0 & 0 & 0 \\ & & \ddots & 0 & 0 & 0 & 0 & 0 & 0 & 0 & 0 \\ & & & 0 & 0 & 0 & 0 & 0 & 0 & 0 & 0 \\ & & & & 0 & 0 & 0 & 0 & 0 & 0 & 0 \\ \text{---} & & & & & \sigma_{X_{L0}X_{R0}} & \sigma_{X_{L0}Y_{R0}} & \sigma_{X_{L0}Z_{R0}} & \sigma_{X_{L0}\omega_R} & \sigma_{X_{L0}\alpha_R} & \sigma_{X_{L0}K_R} & \\ & & & & & \sigma_{Y_{L0}Y_{R0}} & \sigma_{Y_{L0}Z_{R0}} & \sigma_{Y_{L0}\omega_R} & \sigma_{Y_{L0}\alpha_R} & \sigma_{Y_{L0}K_R} & & \\ & & & & & & \sigma_{Z_{L0}Z_{R0}} & \sigma_{Z_{L0}\omega_R} & \sigma_{Z_{L0}\alpha_R} & \sigma_{Z_{L0}K_R} & & \\ & & & & & & & \sigma_{\omega_L\omega_R} & \sigma_{\omega_L\alpha_R} & \sigma_{\omega_LK_R} & & \\ & & & & & & & & \sigma_{\alpha_L\alpha_R} & \sigma_{\alpha_LK_R} & & \\ & & & & & & & & & \sigma_{K_LK_R} & & \\ \text{---} & & & & & & & & & & & \end{bmatrix}$$

SYM.

Matrix \mathbf{A}'' is the first design matrix (Jacobi matrix) and it contains the derivatives of the measurement model (Eq. 2.1) with respect to the unknowns.

$$\mathbf{A}'' = \begin{bmatrix} \mathbf{A}''_L \\ \mathbf{A}''_R \end{bmatrix}_{4n \times 3n}$$

With,

$$\mathbf{A}''_{j=(L,R)} = \begin{bmatrix} \frac{\partial F(x)_{j1}}{\partial X_1} & \frac{\partial F(x)_{j1}}{\partial Y_1} & \frac{\partial F(x)_{j1}}{\partial Z_1} & \dots & \frac{\partial F(x)_{j1}}{\partial X_n} & \frac{\partial F(x)_{j1}}{\partial Y_n} & \frac{\partial F(x)_{j1}}{\partial Z_n} \\ \frac{\partial F(y)_{j1}}{\partial X_1} & \frac{\partial F(y)_{j1}}{\partial Y_1} & \frac{\partial F(y)_{j1}}{\partial Z_1} & \dots & \frac{\partial F(y)_{j1}}{\partial X_n} & \frac{\partial F(y)_{j1}}{\partial Y_n} & \frac{\partial F(y)_{j1}}{\partial Z_n} \\ \vdots & \vdots & \vdots & \ddots & \vdots & \vdots & \vdots \\ \frac{\partial F(x)_{jn}}{\partial X_1} & \frac{\partial F(x)_{jn}}{\partial Y_1} & \frac{\partial F(x)_{jn}}{\partial Z_1} & \dots & \frac{\partial F(x)_{jn}}{\partial X_n} & \frac{\partial F(x)_{jn}}{\partial Y_n} & \frac{\partial F(x)_{jn}}{\partial Z_n} \\ \frac{\partial F(y)_{jn}}{\partial X_1} & \frac{\partial F(y)_{jn}}{\partial Y_1} & \frac{\partial F(y)_{jn}}{\partial Z_1} & \dots & \frac{\partial F(y)_{jn}}{\partial X_n} & \frac{\partial F(y)_{jn}}{\partial Y_n} & \frac{\partial F(y)_{jn}}{\partial Z_n} \\ \vdots & \vdots & \vdots & \ddots & \vdots & \vdots & \vdots \end{bmatrix}_{2n \times 3n} =$$

$$= \begin{bmatrix} \frac{\partial F(x)_{j1}}{\partial X_1} & \frac{\partial F(x)_{j1}}{\partial Y_1} & \frac{\partial F(x)_{j1}}{\partial Z_1} & \dots & 0 & 0 & 0 \\ \frac{\partial F(y)_{j1}}{\partial X_1} & \frac{\partial F(y)_{j1}}{\partial Y_1} & \frac{\partial F(y)_{j1}}{\partial Z_1} & \dots & 0 & 0 & 0 \\ \vdots & \vdots & \vdots & \ddots & \vdots & \vdots & \vdots \\ 0 & 0 & 0 & \dots & \frac{\partial F(x)_{jn}}{\partial X_n} & \frac{\partial F(x)_{jn}}{\partial Y_n} & \frac{\partial F(x)_{jn}}{\partial Z_n} \\ 0 & 0 & 0 & \dots & \frac{\partial F(y)_{jn}}{\partial X_n} & \frac{\partial F(y)_{jn}}{\partial Y_n} & \frac{\partial F(y)_{jn}}{\partial Z_n} \end{bmatrix}_{2n \times 3n}$$

Matrix \mathbf{B}'' is the second design matrix and it contains the derivatives of the measurement model (Eq. 2.1) with respect to the vector of measurements. It has the following form:

$$\mathbf{B}'' = \begin{bmatrix} \mathbf{B}''_L & \mathbf{B}''_{LR} \\ \mathbf{B}''_{LR}^T & \mathbf{B}''_R \end{bmatrix}_{4n \times 4n+14} \quad ; \quad \mathbf{B}''_{LR} = \mathbf{0} \quad \text{and,}$$

$$\mathbf{B}'_j = \begin{matrix} \begin{matrix} \frac{\partial F(x)_{j1}}{\partial x_{j1}} & \frac{\partial F(x)_{j1}}{\partial y_{j1}} & \dots & \frac{\partial F(x)_{j1}}{\partial x_{jn}} & \frac{\partial F(x)_{j1}}{\partial y_{jn}} \\ \frac{\partial F(y)_{L1}}{\partial x_{j1}} & \frac{\partial F(y)_{L1}}{\partial y_{j1}} & \dots & \frac{\partial F(y)_{L1}}{\partial x_{jn}} & \frac{\partial F(y)_{L1}}{\partial y_{jn}} \\ \vdots & \vdots & \ddots & \vdots & \vdots \\ \frac{\partial F(x)_{jn}}{\partial x_{j1}} & \frac{\partial F(x)_{jn}}{\partial y_{j1}} & \dots & \frac{\partial F(x)_{jn}}{\partial x_{jn}} & \frac{\partial F(x)_{jn}}{\partial y_{jn}} \\ \frac{\partial F(y)_{j1}}{\partial x_{j1}} & \frac{\partial F(y)_{j1}}{\partial y_{j1}} & \dots & \frac{\partial F(y)_{Ln}}{\partial x_{jn}} & \frac{\partial F(y)_{jn}}{\partial y_{jn}} \\ \frac{\partial F(x)_{j1}}{\partial x_{j1}} & \frac{\partial F(x)_{j1}}{\partial y_{j1}} & \dots & \frac{\partial F(x)_{j1}}{\partial x_{jn}} & \frac{\partial F(x)_{j1}}{\partial y_{jn}} \end{matrix} \\ \left[\begin{matrix} \frac{\partial F(x)_{j1}}{\partial X_{j0}} & \frac{\partial F(x)_{j1}}{\partial Y_{j0}} & \frac{\partial F(x)_{j1}}{\partial Z_{j0}} & \frac{\partial F(x)_{j1}}{\partial \omega_j} & \frac{\partial F(x)_{j1}}{\partial \alpha_j} & \frac{\partial F(x)_{j1}}{\partial \kappa_j} \\ \frac{\partial F(y)_{j1}}{\partial X_{j0}} & \frac{\partial F(y)_{j1}}{\partial Y_{j0}} & \frac{\partial F(y)_{j1}}{\partial Z_{j0}} & \frac{\partial F(y)_{j1}}{\partial \omega_j} & \frac{\partial F(y)_{j1}}{\partial \alpha_j} & \frac{\partial F(y)_{j1}}{\partial \kappa_j} \\ \vdots & \vdots & \vdots & \vdots & \vdots & \vdots \\ \frac{\partial F(x)_{jn}}{\partial X_{j0}} & \frac{\partial F(x)_{jn}}{\partial Y_{j0}} & \frac{\partial F(x)_{jn}}{\partial Z_{j0}} & \frac{\partial F(x)_{jn}}{\partial \omega_j} & \frac{\partial F(x)_{jn}}{\partial \alpha_j} & \frac{\partial F(x)_{jn}}{\partial \kappa_j} \\ \frac{\partial F(y)_{jn}}{\partial X_{j0}} & \frac{\partial F(y)_{jn}}{\partial Y_{j0}} & \frac{\partial F(y)_{jn}}{\partial Z_{j0}} & \frac{\partial F(y)_{jn}}{\partial \omega_j} & \frac{\partial F(y)_{jn}}{\partial \alpha_j} & \frac{\partial F(y)_{jn}}{\partial \kappa_j} \\ \frac{\partial F(x)_{j1}}{\partial X_{j0}} & \frac{\partial F(x)_{j1}}{\partial Y_{j0}} & \frac{\partial F(x)_{j1}}{\partial Z_{j0}} & \frac{\partial F(x)_{j1}}{\partial \omega_j} & \frac{\partial F(x)_{j1}}{\partial \alpha_j} & \frac{\partial F(x)_{j1}}{\partial \kappa_j} \end{matrix} \right]_{2n \times 2n+6} \end{matrix}$$

$$= \begin{matrix} \begin{bmatrix} -1 & 0 & \dots & 0 & 0 \\ 0 & -1 & \dots & 0 & 0 \\ \vdots & \vdots & \ddots & \vdots & \vdots \\ 0 & 0 & \dots & -1 & 0 \\ 0 & 0 & \dots & 0 & -1 \end{bmatrix} \\ \left[\begin{matrix} \frac{\partial F(x)_{j1}}{\partial X_{j0}} & \frac{\partial F(x)_{j1}}{\partial Y_{j0}} & \frac{\partial F(x)_{j1}}{\partial Z_{j0}} & \frac{\partial F(x)_{j1}}{\partial \omega_j} & \frac{\partial F(x)_{j1}}{\partial \alpha_j} & \frac{\partial F(x)_{j1}}{\partial \kappa_j} \\ \frac{\partial F(y)_{j1}}{\partial X_{j0}} & \frac{\partial F(y)_{j1}}{\partial Y_{j0}} & \frac{\partial F(y)_{j1}}{\partial Z_{j0}} & \frac{\partial F(y)_{j1}}{\partial \omega_j} & \frac{\partial F(y)_{j1}}{\partial \alpha_j} & \frac{\partial F(y)_{j1}}{\partial \kappa_j} \\ \vdots & \vdots & \vdots & \vdots & \vdots & \vdots \\ \frac{\partial F(x)_{jn}}{\partial X_{j0}} & \frac{\partial F(x)_{jn}}{\partial Y_{j0}} & \frac{\partial F(x)_{jn}}{\partial Z_{j0}} & \frac{\partial F(x)_{jn}}{\partial \omega_j} & \frac{\partial F(x)_{jn}}{\partial \alpha_j} & \frac{\partial F(x)_{jn}}{\partial \kappa_j} \\ \frac{\partial F(y)_{jn}}{\partial X_{j0}} & \frac{\partial F(y)_{jn}}{\partial Y_{j0}} & \frac{\partial F(y)_{jn}}{\partial Z_{j0}} & \frac{\partial F(y)_{jn}}{\partial \omega_j} & \frac{\partial F(y)_{jn}}{\partial \alpha_j} & \frac{\partial F(y)_{jn}}{\partial \kappa_j} \\ \frac{\partial F(x)_{j1}}{\partial X_{j0}} & \frac{\partial F(x)_{j1}}{\partial Y_{j0}} & \frac{\partial F(x)_{j1}}{\partial Z_{j0}} & \frac{\partial F(x)_{j1}}{\partial \omega_j} & \frac{\partial F(x)_{j1}}{\partial \alpha_j} & \frac{\partial F(x)_{j1}}{\partial \kappa_j} \end{matrix} \right]_{2n \times 2n+6} \end{matrix}$$

The approximate values are used to compute the matrices \mathbf{A}' and \mathbf{B}' . In the LSA adjustment of intersection, each point is solved independently using a stereo-model. The equation of combined case LSA takes the form:

$$\mathbf{A}_{ji}'' \delta \mathbf{x}_i'' + \mathbf{B}_{ji}'' \mathbf{v}_{ji}'' + \mathbf{w}_{ji}'' = 0 \quad (2.12)$$

where the subscript i denotes feature i , and j indicates Left or Right images (camera). The solution of $\delta \mathbf{x}_i''$ is:

$$\delta \mathbf{x}_i'' = (\mathbf{N}_{Li}'' + \mathbf{N}_{Ri}'')^{-1} (\mathbf{U}_{Li}'' + \mathbf{U}_{Ri}'') \quad (2.13)$$

$$\begin{aligned} \text{with} \quad \mathbf{N}_{Li}'' &= \mathbf{A}_{Li}''^T (\mathbf{B}_{Li}'' \mathbf{C}_{Ly}'' \mathbf{B}_{Li}''^T)^{-1} \mathbf{A}_{Li}'' & \mathbf{N}_{Ri}'' &= \mathbf{A}_{Ri}''^T (\mathbf{B}_{Ri}'' \mathbf{C}_{Ry}'' \mathbf{B}_{Ri}''^T)^{-1} \mathbf{A}_{Ri}'' \\ \mathbf{U}_{Li}'' &= \mathbf{A}_{Li}''^T (\mathbf{B}_{Li}'' \mathbf{C}_{Ly}'' \mathbf{B}_{Li}''^T)^{-1} \mathbf{w}_{Li}'' & \mathbf{U}_{Ri}'' &= \mathbf{A}_{Ri}''^T (\mathbf{B}_{Ri}'' \mathbf{C}_{Ry}'' \mathbf{B}_{Ri}''^T)^{-1} \mathbf{w}_{Ri}'' \end{aligned}$$

The precision estimation of the parameters, residuals and measurements are:

$$\mathbf{C}_{\hat{\mathbf{x}}}'' = \mathbf{N}''^{-1} \quad (2.14)$$

$$\mathbf{C}_{\mathbf{v}}'' = \mathbf{C}_{\mathbf{y}}''^T \mathbf{M}''^{-1} \mathbf{B}'' \mathbf{C}_{\mathbf{y}}'' - \mathbf{C}_{\mathbf{y}}''^T \mathbf{M}''^{-1} \mathbf{A}'' \mathbf{N}''^{-1} \mathbf{A}''^T \mathbf{M}''^{-1} \mathbf{B}'' \mathbf{C}_{\mathbf{y}}'' \quad (2.15)$$

$$\mathbf{C}_{\mathbf{y}}'' = \mathbf{C}_{\mathbf{y}}'' - \mathbf{C}_{\mathbf{v}}'' \quad (2.16)$$

2.5.2 - Intersection Accuracy

To analyse the accuracy of the intersection problem, a simplified relation between the images and object frames can be used. The following conditions for Equations (2.1) are considered:

$$X_{0R} = Y_{0R} = Y_{0L} = Z_{0R} = Z_{0L} = 0$$

$$X_{0L} = -b$$

$$\omega_R = \omega_L = \alpha_R = \alpha_L = \kappa_R = \kappa_L = 0$$

$$x_{0R} = x_{0L} = y_{0R} = y_{0L} = 0$$

b refers to the distance between the two cameras. These conditions mean that the origin of the right camera coincides with the origin of the reference system, the pitch and tilt of the two cameras are zero and their azimuth is also zero. This means that the origin of the left camera is located at an abscissa of $-b$ (Fig. 2-6).

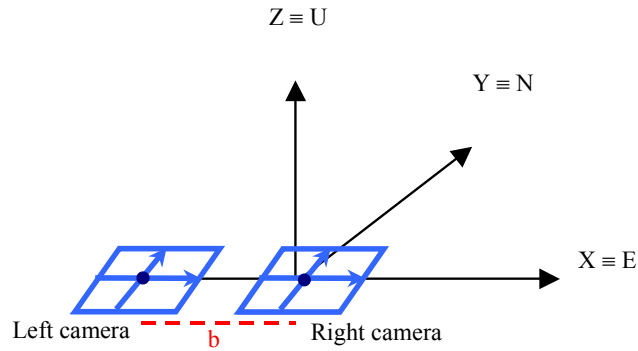


Figure 2-6: The simplified assumptions illustrated in a figure

Substituting these conditions into Equations (2.1), the following is obtained:

Right image (R):

$$X = Y \frac{x_R}{c}, \quad Z = Y \frac{y_R}{c} \quad (2.17)$$

Left image (L):

$$X = -b + Y \frac{x_L}{c}, \quad Z = Y \frac{y_L}{c} \quad (2.18)$$

From equations (2.17) and (2.18) the following equalities are obtained:

$$X = Y \frac{x_R}{c}, \quad Z = Y \frac{y_R}{c} = Y \frac{y_L}{c}, \quad Y = -\frac{cb}{x_R - x_L} = \frac{cb}{x_L - x_R} = \frac{cb}{p_x} \quad (2.19)$$

p_x is the parallax along the x-axis of the images. After applying the theory of error propagation, the error estimate equations are:

$$\sigma_Y = \frac{Y}{p_x} \sigma_{p_x} = \frac{Y^2}{bc} \sigma_{p_x} \quad (2.20)$$

$$\sigma_X = \sqrt{\left(\frac{x}{c} \sigma_Y\right)^2 + \left(\frac{Y}{c} \sigma_x\right)^2} \quad (2.21)$$

$$\sigma_Z = \sqrt{\left(\frac{y}{c} \sigma_Y\right)^2 + \left(\frac{Y}{c} \sigma_y\right)^2} \quad (2.22)$$

The photo-coordinates of point P are x and y , and Y is the distance from the image to the object. $\sigma_x, \sigma_y, \sigma_z$ are the accuracy of the feature's X, Y, Z coordinates obtained from the restriction of the base b , focal length c , observation accuracy of the measured x and y (σ_x, σ_y) on the images, and the accuracy of the parallax measurement, $\sigma_{p_x} = \sqrt{2}\sigma_x$. As can be seen in the above equations, the stereo-base b , and the focal length c , put constraints on the possible accuracy achieved from intersection. The choice of b and c is discussed in Chapter 3.

Figure (2-7) shows the accuracy plot of the Y-axis computed from Equation (2.20). A base of 1 metre can guarantee a Y measuring accuracy of less than 15 cm for an object 10 metres away from the cameras. Pixel size is $7.4 \mu\text{m}$ and pixel measurement accuracy is $5 \mu\text{m}$; focal length is 6 mm.

Figure (2-8) shows the accuracy plot of X and Z-axes computed from equations (2.21) and (2.22), respectively, which demonstrate that it is possible to use points all over the image, and still achieve measuring accuracy, due to the geometry constrained by a base of 1 metre, of less than 15 cm for object 20 metres away. Pixel size, pixel measurement accuracy, and focal length are the same as above.

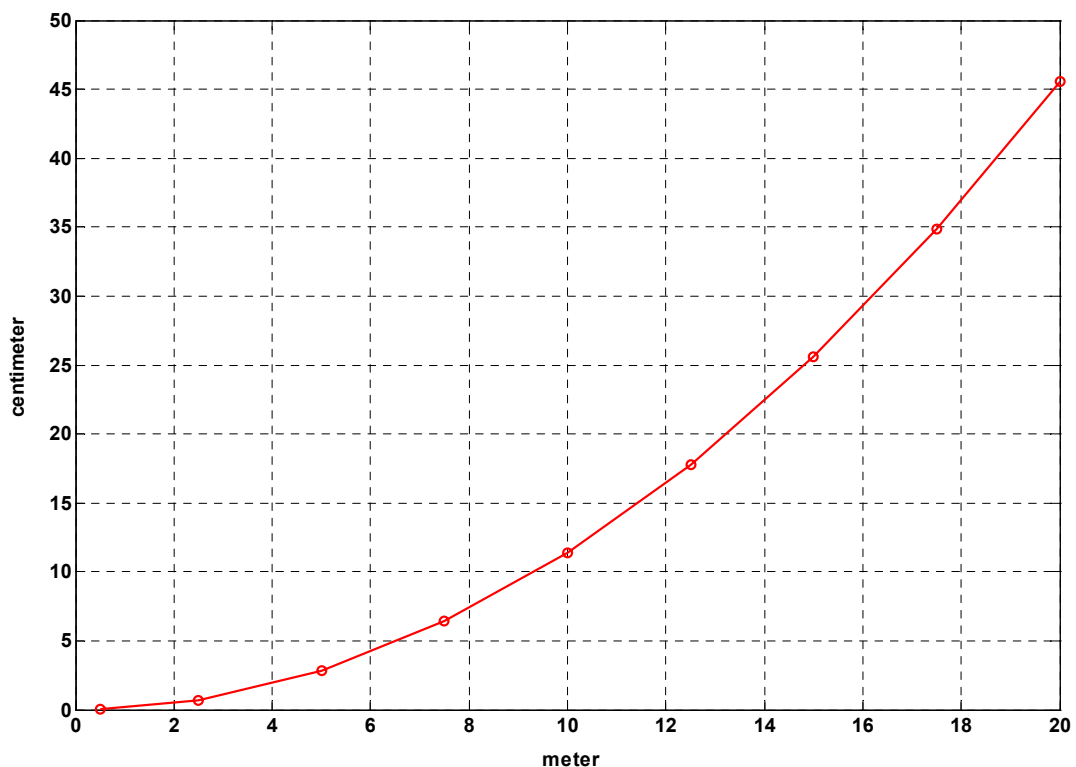


Figure 2-7: Simulated accuracy in Y-axis using $b = 1 \text{ m}$, $c = 6 \text{ mm}$

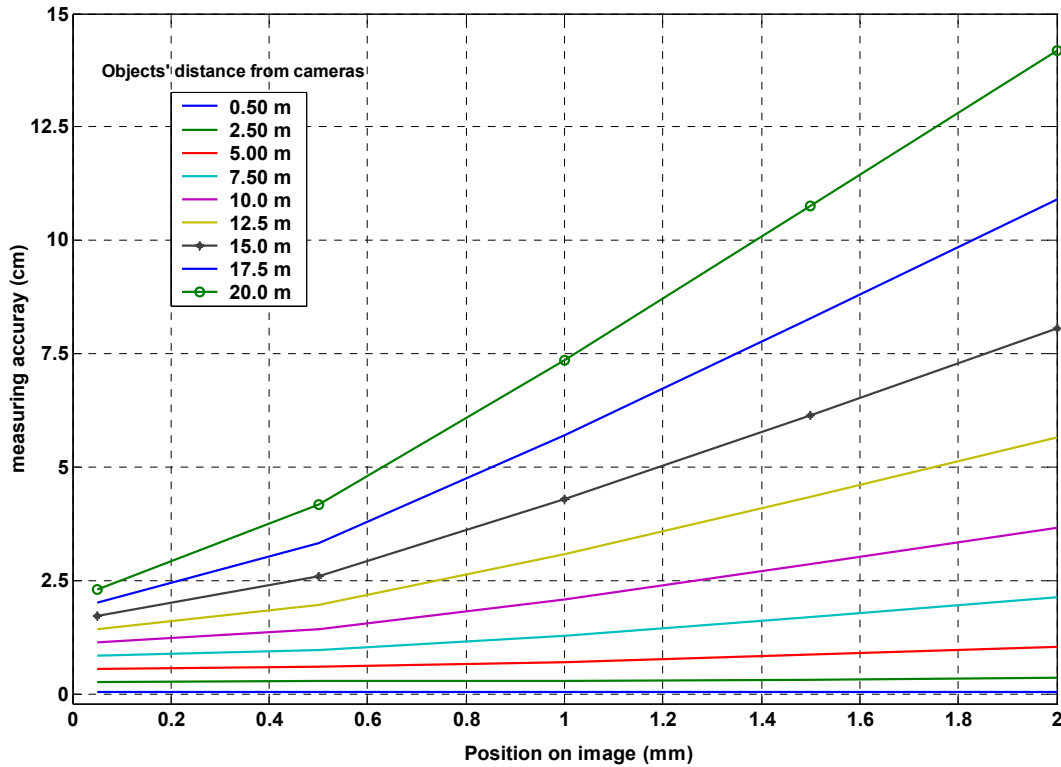


Figure 2-8: Simulated accuracy in X and Z-axis using $b = 1$ m, $c = 6$ mm

Thus, the geometry of the images constrains the accuracy to about 15 cm for objects 10 metres away for the Y value but a much better accuracy for the X and Z coordinates. This accuracy size is standard for many application requirements. However, this is a simulation and simulations do not usually reflect the reality, but rather an approximation.

The X and Y accuracies change according to the initial conditions; if the azimuth was changed from 0 to 90, the accuracy information between X and Y will swap based on the following equations ($Y_{0L} = -b$):

Right image (R):

$$Y = -X \frac{x_R}{c}, \quad Z = -X \frac{y_R}{c} \quad (2.23)$$

Left image (L):

$$Y = -b - X \frac{x_L}{c}, \quad Z = -X \frac{y_L}{c} \quad (2.24)$$

From Equations (2.23) and (2.24), the following equalities are obtained:

$$Y = -X \frac{x_R}{c}, \quad Z = -X \frac{y_R}{c} = -X \frac{y_L}{c}, \quad X = \frac{cb}{x_L - x_R} = \frac{cb}{p_x} \quad (2.25)$$

Comparing Equations (2.25) with those of (2.19), it can be clearly seen that X and Y are swapped.

From this simple simulation, it is expected that the weakest components will be X and Y depending on the orientation of the system and in all cases the Z-component will always be the strongest.

In real applications, this accuracy is somewhat optimistic because conceptually the EOP of the two images are not perfectly known and the measurements accuracies of the photo-coordinates depend on the quality of the images and might be lower than 5µm.

2.6 - Solving SLAM Trajectory by Photogrammetry

Figure (2-9) explains the procedure of SLAM by photogrammetry without image scene restitution; it is similar to Figure (1-1). The previously described resection and intersection are combined in a common process that evolves in time. Considering the initial position as known, intersection is used to map a number of features that will be considered as GCPs – or alternatively Controlled Homologous Points, CHOP – (i.e., of known position) when the vehicle moves and captures new images. This procedure goes on through the whole survey.

This procedure requires considering certain points:

- Recursive LSA: the LSA solution of the epoch $k - 1$ is used as observations for epoch k ,
- Correlations are carried from one epoch to the other.

Furthermore, the procedure requires homologous point determination on the image stereo-pair and between epochs. This problem is a part of an automated SLAM and is not considered in this thesis.

This Section illustrates the operation of SLAM with resection and intersection in a recursive approach, with the embedding of the time index k . To start with, the initialisation has to be performed by determining the initial EOP of the two cameras. The initialisation can be done in three ways:

- Initialisation with GPS/INS, which demands good GPS signal reception,

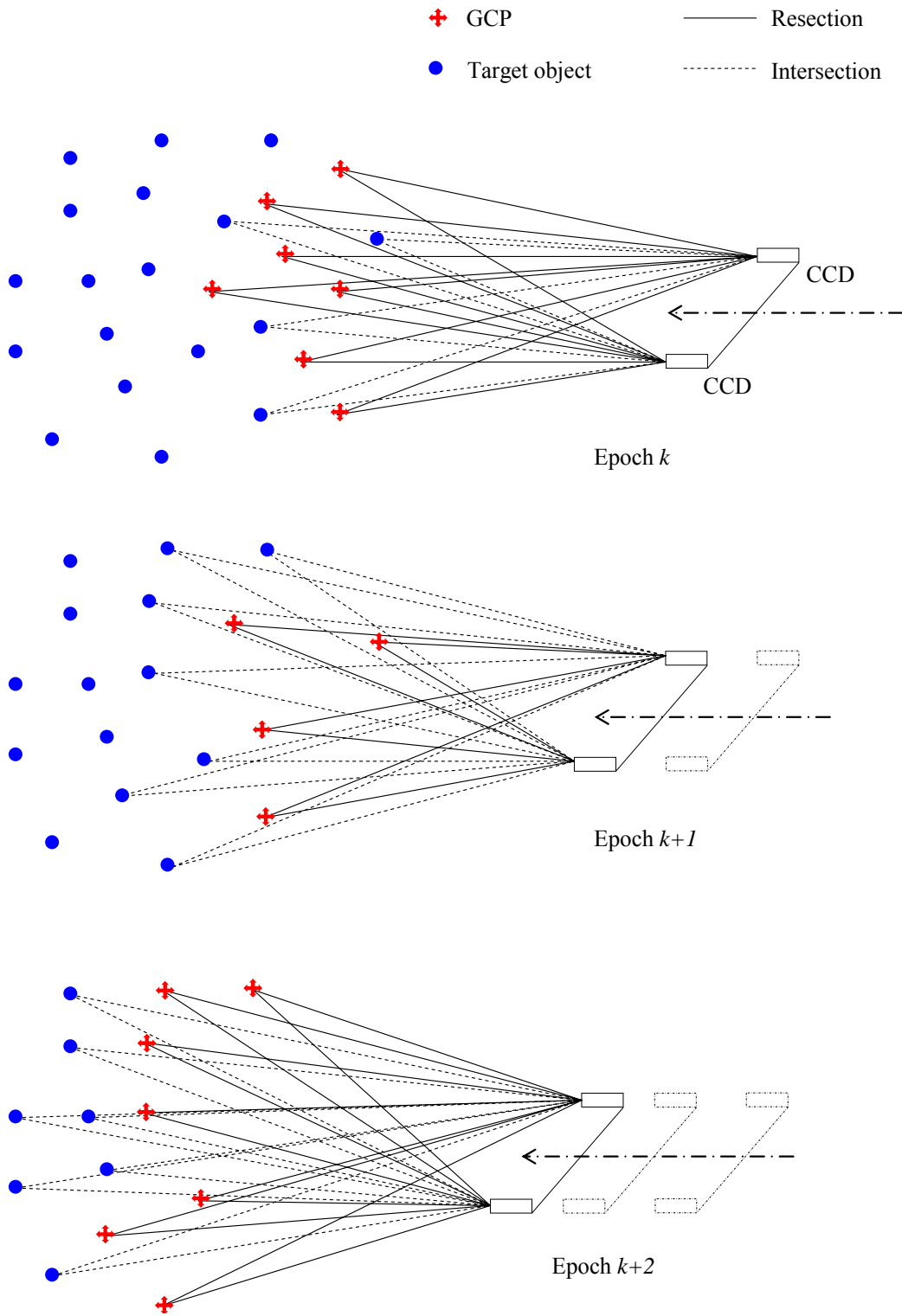


Figure 2-9: SLAM by photogrammetry

- Initialisation with resection, which demands the existence of sufficient GCPs at the beginning of the survey, or
- Initialisation by standing on known position and performing initial alignment by gyro compassing; depending on the IMU quality, this can be an approximate solution.

In the first case, GPS signal reception is vital. The GPS/INS gives us the position and attitude of the IMU (or GPS, or the vehicle, etc.), which after applying the leverarm and boresight correction yield the EOP of the two cameras (Chapter 6). Thus, initialisation is achieved.

As for the second case, at least three GCPs are required for the determination of the position and attitude of each camera by resection. However, it is always preferable to use as many GCPs as possible.

The third initialisation requires the existence of a benchmark for the localisation and depending on the used IMU, enough time to perform static alignment by gyro-compassing. Another alignment procedure can be performed approximately by using a compass to determine the initial orientation, and an inclinometer to determine the initial roll and pitch.

After the initialisation, intersection starts to determine feature coordinates. The vehicle moves and captures two images; moves again, capture images, etc. The flowchart of this procedure is laid out in Figure (2-10).

The algorithm will be discussed now considering that the initialisation is properly done, i.e., the initial EOP and their covariances of the two cameras are supplied.

To simplify the notation, at each given epoch k , n features are mapped. In this way, the dimensions of the different matrices are:

$$\begin{array}{ll}
 \delta \mathbf{x}'_{(L,R)} : 6 \times 1 & \delta \mathbf{x}'' : 3n \times 1 \\
 \mathbf{y}'_{(L,R)} : 5n \times 1 & \mathbf{y}'' : (4n + 12) \times 1 \\
 \mathbf{A}'_{(L,R)} : 2n \times 6 & \mathbf{A}'' : 4n \times 3n \\
 \mathbf{B}'_{(L,R)} : 2n \times 5n & \mathbf{B}'' : 4n \times (4n + 12) \\
 \mathbf{N}'_{(L,R)} : 6 \times 6 & \mathbf{N}'' : 3n \times 3n
 \end{array}$$

$$\begin{aligned} \mathbf{U}_{(L,R)} &: 6 \times 1 & \mathbf{U}'' &: 3n \times 1 \\ \mathbf{C}'_{(L,R)y} &: 5n \times 5n & \mathbf{C}''_y &: (4n + 12) \times (4n + 12) \\ \mathbf{C}'_{(L,R)x} &: 6 \times 6 & \mathbf{C}''_x &: 3n \times 3n \end{aligned}$$

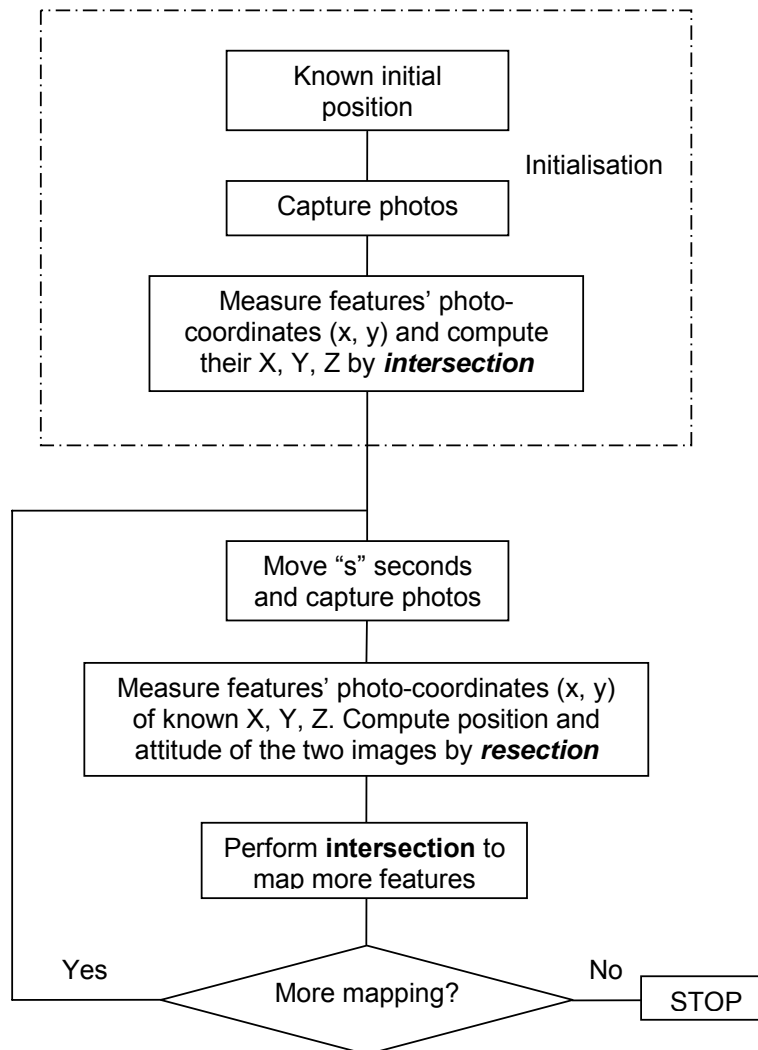


Figure 2-10: Flowchart of Photogrammetric SLAM

(It should be noted that in practice the number of features n changes from one epoch to the other, but it is assumed constant here to facilitate the derivations.)

Intersection at epoch k :

$$\delta \mathbf{x}_k'' = \mathbf{N}_k''^{-1} \mathbf{U}_k'', \quad \mathbf{N}_k'' = \mathbf{A}_k''^T \left(\mathbf{B}_k'' \mathbf{C}_{y/k}'' \mathbf{B}_k''^T \right)^{-1} \mathbf{A}_k'', \quad \mathbf{U}_k'' = \mathbf{A}_k''^T \left(\mathbf{B}_k'' \mathbf{C}_{y/k}'' \mathbf{B}_k''^T \right)^{-1} \mathbf{w}_k''$$

where

$$\delta \mathbf{x}_k'' = [\delta X_1 \ \delta Y_1 \ \delta Z_1 \ \dots \ \delta X_n \ \delta Y_n \ \delta Z_n]^T$$

and the solution of intersection at epoch k is: $\mathbf{x}_k'' = \overset{\circ}{\mathbf{x}}_k'' + \delta \mathbf{x}_k''$.

The elements of \mathbf{x}_k'' are used as GCPs (CHOP) at epoch $k+1$ when resection is solved:

$$\delta \mathbf{x}'_{k+1} = \mathbf{N}'_{k+1} \mathbf{U}'_{k+1} \Big|_{(L,R)},$$

with

$$\mathbf{N}'_{k+1} = \mathbf{A}'_{k+1}{}^T (\mathbf{B}'_{k+1} \mathbf{C}'_{y/k+1} \mathbf{B}'_{k+1}{}^T)^{-1} \mathbf{A}'_{k+1} \Big|_{(L,R)}, \quad \mathbf{U}'_{k+1} = \mathbf{A}'_{k+1}{}^T (\mathbf{B}'_{k+1} \mathbf{C}'_{y/k+1} \mathbf{B}'_{k+1}{}^T)^{-1} \mathbf{w}'_{k+1} \Big|_{(L,R)}$$

where

$$\delta \mathbf{x}'_{k+1} = [\delta X_0 \ \delta Y_0 \ \delta Z_0 \ \delta \omega \ \delta \alpha \ \delta \kappa]^T \Big|_{(L,R)}$$

and the final solution of resection of epoch $k+1$ is: $\mathbf{x}'_{k+1} = \overset{\circ}{\mathbf{x}}'_{k+1} + \delta \mathbf{x}'_{k+1} \Big|_{(L,R)}$.

The elements of $\mathbf{x}'_{k+1} \Big|_{(L,R)}$ are used in a stereo-model at epoch $k+1$ to map n new features, \mathbf{x}''_{k+1} . These n new features at epoch $k+1$, \mathbf{x}''_{k+1} , are used at epoch $k+2$ to compute \mathbf{x}''_{k+2} . The procedure continues until the end of the survey.

It is important to note that not only \mathbf{x}' and \mathbf{x}'' are used from one epoch to the next, but also the Covariances via the matrices \mathbf{C}'_y , \mathbf{C}''_y , \mathbf{C}'_x , and \mathbf{C}''_x . The $\mathbf{C}''_{y/k=0}$ is given along with the information about the initial camera's position at epoch $k=0$. (It is used to find the object coordinates of n new features by intersection in order to compute the EOP of the two cameras at epoch $k+1=1$.) The $\mathbf{C}'_{y/k+1}$ is computed as:

$$\mathbf{C}'_{y/k+1} = \begin{bmatrix} \Sigma_1 \Big|_{\text{photo}} & \mathbf{0} & \dots & \mathbf{0} & \mathbf{0} \\ \mathbf{0} & \Sigma'_1 \Big|_{\text{object}} & \dots & \mathbf{0} & \Sigma'_1 \Sigma'_n \Big|_{\text{object}} \\ \vdots & \vdots & \ddots & \vdots & \vdots \\ \mathbf{0} & \mathbf{0} & \dots & \Sigma_n \Big|_{\text{photo}} & \mathbf{0} \\ \mathbf{0} & \Sigma'_n \Sigma'_1 \Big|_{\text{object}} & \dots & \mathbf{0} & \Sigma'_n \Big|_{\text{object}} \end{bmatrix}$$

where Σ_i^{photo} is a 2×2 Covariance matrix of the photo-coordinates, which is always given and depends on image quality. $\Sigma_i^{\text{object}}|_{k+1}$ and $\Sigma_i' \Sigma_j^{\text{object}}|_{k+1}$, on the other hand, are 3×3 Covariance matrix of feature i -th and j -th object coordinates. These will be taken from the output of the intersection of epoch k , specifically from matrix $\mathbf{C}_{x/k}''$ that is equal to:

$$\mathbf{C}_{x/k}'' = \mathbf{N}_k''^{-1} = \left(\mathbf{A}_k''^T \mathbf{M}''^{-1} \mathbf{A}_k'' \right)^{-1} = \begin{bmatrix} \Sigma_1''^{\text{object}}|_k & \dots & \Sigma_1'' \Sigma_n''^{\text{object}}|_k \\ \vdots & \ddots & \vdots \\ \Sigma_n'' \Sigma_1^{\text{object}}|_k & \dots & \Sigma_n''^{\text{object}}|_k \end{bmatrix}$$

$$\text{with } \Sigma_i^{\text{object}}|_{k+1} = \Sigma_i''^{\text{object}}|_k = \begin{bmatrix} \sigma_{X_i}^2 & \sigma_{X_i} \sigma_{Y_i} & \sigma_{X_i} \sigma_{Z_i} \\ \sigma_{Y_i} \sigma_{X_i} & \sigma_{Y_i}^2 & \sigma_{Y_i} \sigma_{Z_i} \\ \sigma_{Z_i} \sigma_{X_i} & \sigma_{Z_i} \sigma_{Y_i} & \sigma_{Z_i}^2 \end{bmatrix}$$

$$\text{and } \Sigma_i' \Sigma_j^{\text{object}}|_{k+1} = \Sigma_i' \Sigma_j''^{\text{object}}|_k = \begin{bmatrix} \sigma_{X_i} \sigma_{X_j} & \sigma_{X_i} \sigma_{Y_j} & \sigma_{X_i} \sigma_{Z_j} \\ \sigma_{Y_i} \sigma_{X_j} & \sigma_{Z_i} \sigma_{Z_j} & \sigma_{Y_i} \sigma_{Z_j} \\ \sigma_{Z_i} \sigma_{X_j} & \sigma_{Z_i} \sigma_{Y_j} & \sigma_{Z_i} \sigma_{Z_j} \end{bmatrix}$$

As for $\mathbf{C}_{y/k+1}''$ (measurements covariance used in the intersection), it is computed in a similar way as follows:

$$\mathbf{C}_{Ly/k+1}'' = \begin{bmatrix} \Sigma_i^{\text{photo}} & \mathbf{0} \\ \mathbf{0} & \Sigma_{L_EOP}''|_{k+1} \end{bmatrix}, \quad \mathbf{C}_{Ry/k+1}'' = \begin{bmatrix} \Sigma_i^{\text{photo}} & \mathbf{0} \\ \mathbf{0} & \Sigma_{R_EOP}''|_{k+1} \end{bmatrix}$$

$\Sigma_{L_EOP}''|_{k+1}$ and $\Sigma_{R_EOP}''|_{k+1}$ are the measurement covariance matrices of the Left and Right EOP that are needed to compute new n features at epoch $k+1$. These are found from the output of the resection epoch $k+1$ as follows ($j=L,R$):

$$\Sigma_{j_EOP}''|_{k+1} = \mathbf{C}_{\hat{x}/k+1}' = \mathbf{N}_{k+1}'^{-1} = \left(\mathbf{A}_{k+1}'^T \left(\mathbf{B}_{k+1}' \mathbf{C}_{y/k+1}' \mathbf{B}_{k+1}'^T \right)^{-1} \mathbf{A}_{k+1}' \right)^{-1}$$

$$= \begin{bmatrix} \sigma_{X_{j0}}^2 & \sigma_{X_{j0}Y_{j0}} & \sigma_{X_{j0}Z_{j0}} & \sigma_{X_{j0}\omega_j} & \sigma_{X_{j0}\alpha_j} & \sigma_{X_{j0}\kappa_j} \\ & \sigma_{Y_{j0}}^2 & \sigma_{Y_{j0}Z_{j0}} & \sigma_{Y_{j0}\omega_j} & \sigma_{Y_{j0}\alpha_j} & \sigma_{Y_{j0}\kappa_j} \\ & & \sigma_{Z_{j0}}^2 & \sigma_{Z_{j0}\omega_j} & \sigma_{Z_{j0}\alpha_j} & \sigma_{Z_{j0}\kappa_j} \\ & & & \sigma_{\omega_j}^2 & \sigma_{\omega_j\alpha_j} & \sigma_{\omega_j\kappa_j} \\ & \text{SYM.} & & & \sigma_{\alpha_j}^2 & \sigma_{\alpha_j\kappa_j} \\ & & & & & \sigma_{\kappa_j}^2 \end{bmatrix}_{k+1}$$

Summarising, the procedure explained above can be put as in Table (2-2).

Table 2-2: SLAM Procedure for taking information from one epoch o the other

Epoch	0	1	2	...	K-1	K	K+1	...
Intersection (X_i, Y_i, Z_i)	y'_0 $C'_{y/0}$ x'_0 $C'_{\hat{x}/0}$	y'_1 $C'_{y/1}$ x'_1 $C'_{\hat{x}/1}$	y'_2 $C'_{y/2}$ x'_2 $C'_{\hat{x}/2}$...	y'_{k-1} $C'_{y/k-1}$ x'_{k-1} $C'_{\hat{x}/k-1}$	y'_k $C'_{y/k}$ x'_k $C'_{\hat{x}/k}$	y'_{k+1} $C'_{y/k+1}$ x'_{k+1} $C'_{\hat{x}/k+1}$...
Resection ($X_0, Y_0, Z_0,$ ω, α, κ)	y''_0 $C''_{y/0}$ x''_0 $C''_{\hat{x}/0}$	y''_1 $C''_{y/1}$ x''_1 $C''_{\hat{x}/1}$	y''_2 $C''_{y/2}$ x''_2 $C''_{\hat{x}/2}$...	y''_{k-1} $C''_{y/k-1}$ x''_{k-1} $C''_{\hat{x}/k-1}$	y''_k $C''_{y/k}$ x''_k $C''_{\hat{x}/k}$	y''_{k+1} $C''_{y/k+1}$ x''_{k+1} $C''_{\hat{x}/k+1}$...

Alternatively and to abridge more, the covariance transportability:

$C'_{y/k+1} \equiv$ Given accuracies of the GCPs $\equiv C''_{\hat{x}/k}$

$C'_{\hat{x}/k+1} \equiv$ Computed accuracies of the EOP

$C''_{y/k+1} \equiv$ Given accuracies of the EOP $\equiv C'_{\hat{x}/k+1}$

$C''_{\hat{x}/k+1} \equiv$ Computed accuracies of the next epoch's (k+2) GCPs

The above analysis can be put in a one-step approach called recursive "Bundle Adjustment". The one-step approach is followed when there is no other technique to determine the EOP, which is not the case here. In addition to the two cameras, an IMU will also provide the EOP.

After incorporating the IMU, the analysis above changes as follows. The output of the resection at the epoch k will become external measurements for the INS Kalman Filter (KF). After obtaining the navigation parameters corrections from the KF, intersection is carried out at the same epoch k . As a consequence, instead of using the $\mathbf{C}'_{\hat{x}/k}$ to build up $\mathbf{C}'_{y/k}$, the variance-covariance matrix output of KF is used (discussed in Chapter Five).

3 - CHOICE OF MAPPING INSTRUMENTATION

... being a Surveyor, I am trained to have the precise orientation and locate strategic targets ...

This Chapter focuses on the selection of the photogrammetric instruments. The choice will be guided by simulations and stochastic analysis as well as the practicality of the equipment.

Cameras are “*acquisition instruments*” in photogrammetry. Traditionally, metric cameras are used for applications requiring high accuracy; but lately, the new advancement in optics and the development of mature calibration models gave the non-metric cameras an advantage over the metric ones in certain close-range photogrammetry applications due to their lower cost.

First, the choice of the focal length and stereo-base is made in Section 3.1 and 3.2. In Section 3.3, a brief description about the cameras used in this work is shown. To link the camera to the computer for data acquisition, a frame grabber is needed, which is described briefly in Section 3.4. Camera calibration and its general mathematical model with the LSA solution are studied in Section 3.5.

3.1 - The Focal Length “c”

When building a photogrammetric system the size and resolution of the cameras and the lens are two important issues.

To choose the focal length, one needs to study the size of the object’s image and Field-Of-Vision (FOV) with relation to the image resolution and size. A feasibility study was made for this task.

The capability of seeing an object, with a certain size, on the image depends on the focal length of the lens and the pixel size. The pixel size of the used CCD cameras is 7.4 μm (See Section 3.3). The size of the object’s image d (possibility of seeing its image), consequently,

depends on the focal length c , its actual size D , and its distance Z from the image through the relation of Figure (3-1).

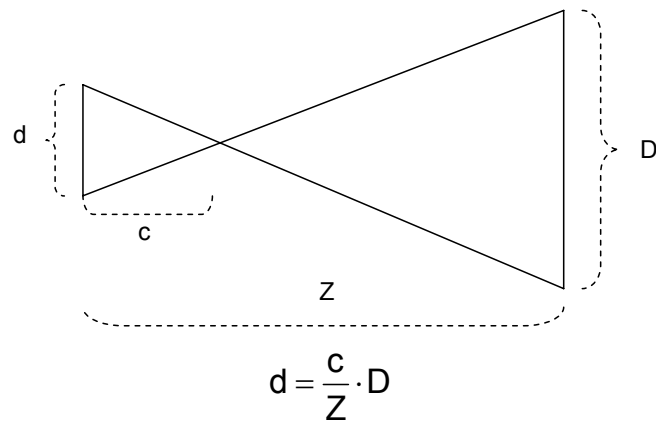


Figure 3-1: The relationship between focal length, object distance, and its size

Figure (3-2) shows the relation between different focal lengths and the image of an object of size 5 cm located at different distances from the lens. If this object is 15 m away, a lens of 6 mm can present it with a size of around 0.022 mm; thus, with a pixel size of 0.0074 mm this object's image can be viewed.

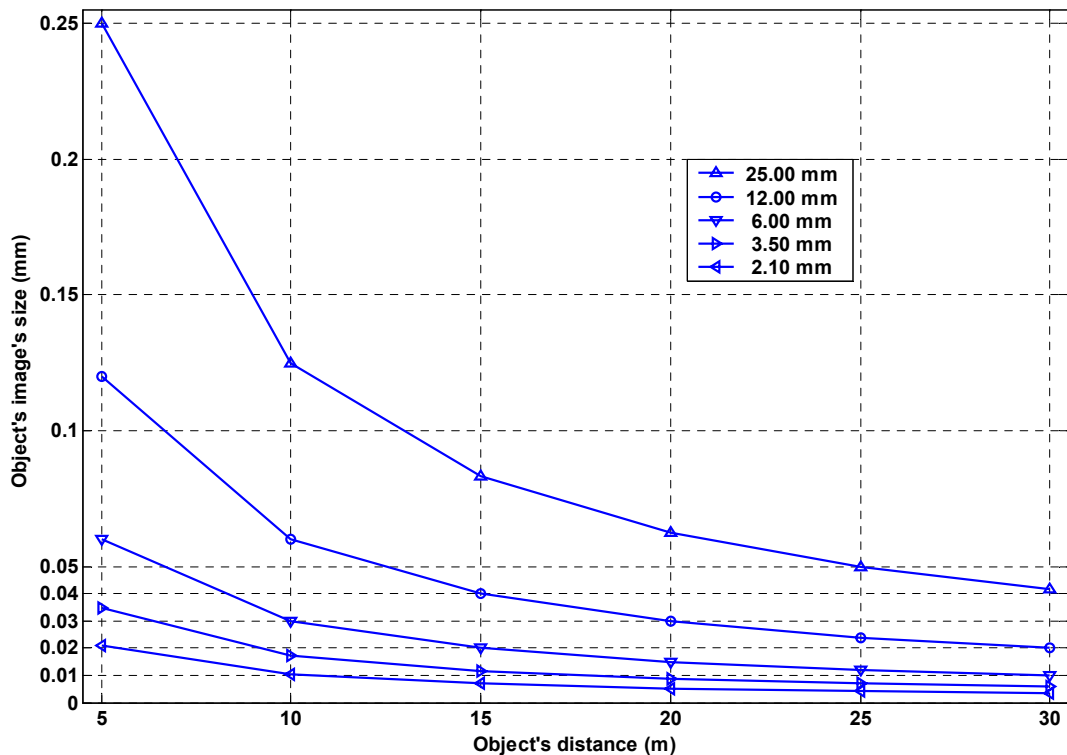


Figure 3-2: Relation between object distance and its image size with different focal lengths

Figure (3-3), on the other hand, shows the relation between objects with different sizes and their respective sizes on the image for fixed focal length. For example, with focal length of 6 mm, an object size of 2 cm and 15 m away has an image size of around 0.010 mm; taking into account that the pixel size is 0.0074 mm, it is difficult to see this object clearly and, therefore to map it.

As for the FOV, the longer the focal length the smaller the FOV is. Having a focal length of 6 mm, guarantees a FOV of $40.8^\circ \times 31.2^\circ$. Considering Figure (3-1) and with the CCDs chip size of around $4.9(H) \times 3.7(V)$ mm, the FOV at a distance of 15 m is around $11.3(H) \times 8.5(V)$ m. As a compromise, a focal length of 6 mm was chosen for acceptable FOV and good mapping resolution.

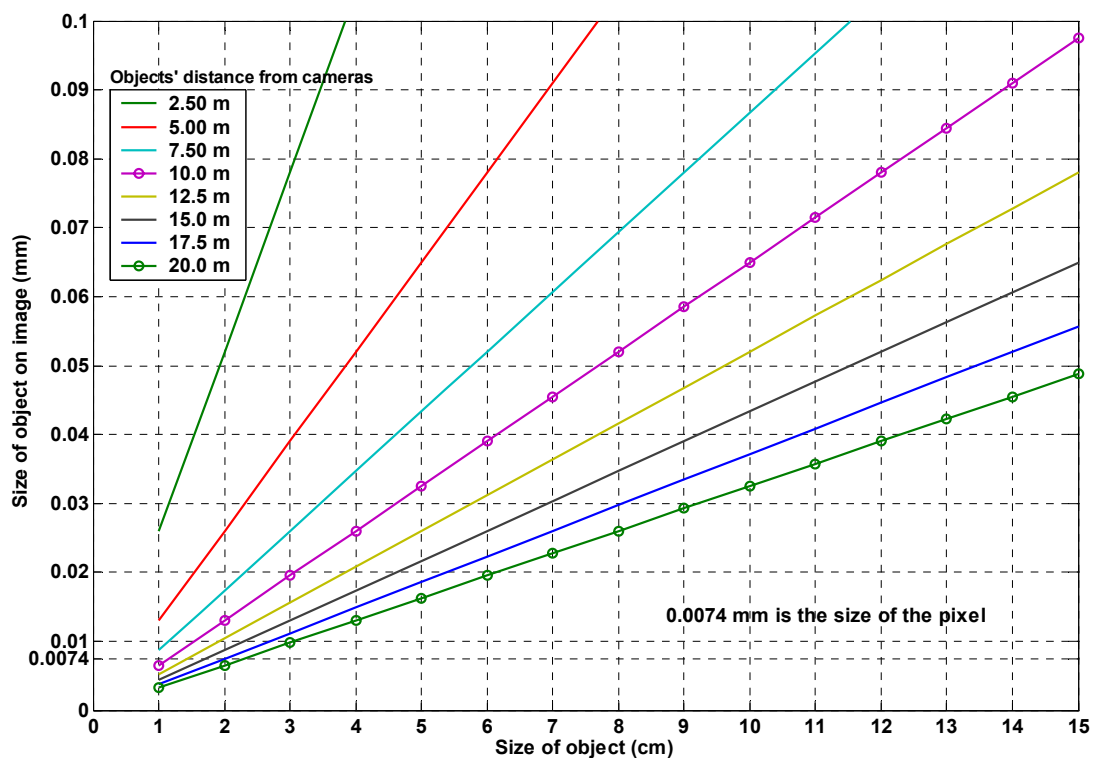


Figure 3-3: Relation between object size, its distance and its image size ($c = 6\text{mm}$)

3.2 - The Stereo-Base “b”

In terrestrial applications more than one camera can be used, the knowledge of the distance between the cameras is crucial; this distance is called the stereo-base. (In airborne applications, the stereo-base is the distance between two exposures.)

Usually, the ratio between the length of the stereo-base and the distance of the objects is preferably (ASPRS, 2004):

$$\frac{1}{15} < \frac{b}{Z} < \frac{1}{4}$$

Depending on a particular application in close-range photogrammetry, this ratio may be difficult to achieve. Here, we chose a base of one metre due to the restrictions in the size of the vehicle. This short base will affect the intersection accuracy as was seen in Section 2.5.2. Alternatively, this handicap could be mitigated by a lateral movement of the vehicle that acts as a baseline extension.

The focal length and the stereo-base are both in the denominator of Equation (2.19). So, they can be chosen in a way that keeps the accuracy of intersection within certain limits. (A small focal length obliges the stereo-base to be larger to keep a defined accuracy.) Therefore, a compromise between the two must be found.

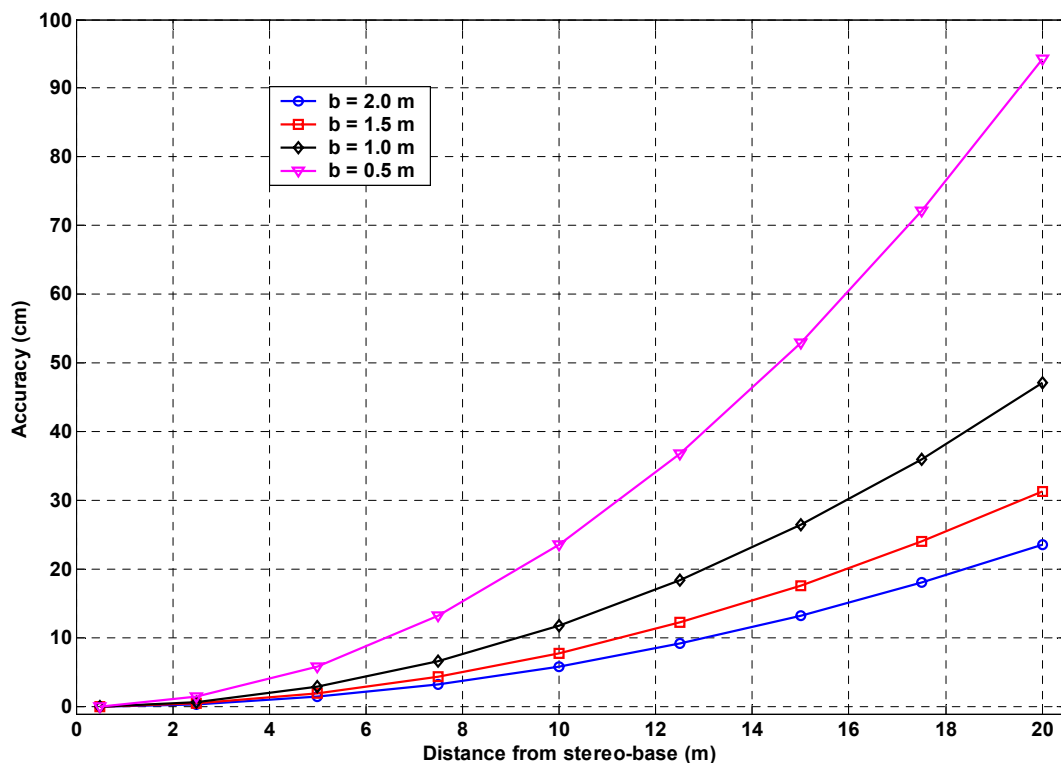


Figure 3-4: Effect of the stereo-base length on mapping accuracy on the depth components

After choosing a focal length of 6 mm, the effect of different stereo-bases on the depth accuracy is demonstrated in Figure (3-4), where it shows that long stereo-bases guarantee

more accurate mapping. This is reflected also on the other two components as shown in Figure (3-5) computed by Equations (2.21) and (2.22); to plot Figures (3-4) and (3-5), an object at a distance of 15 m was chosen.

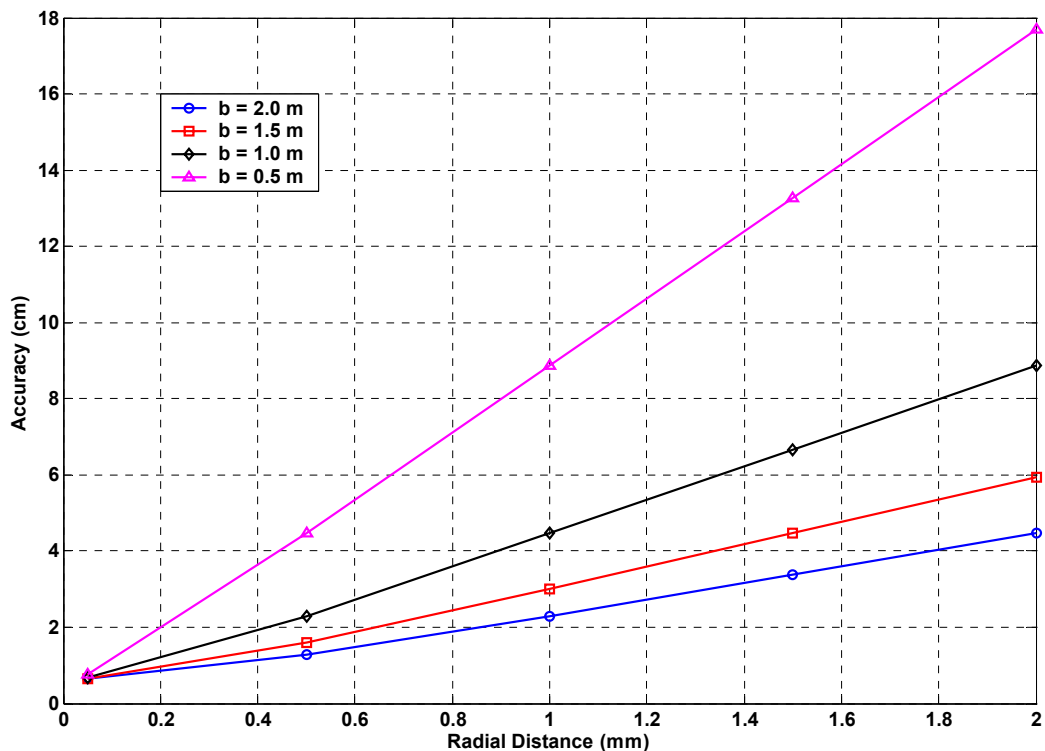


Figure 3-5: Effect of the stereo-base length on mapping accuracy of the X- and Z-component for an object at a distance of 15 m

3.3 - Charged Couple Device Camera

Charge Coupled Devices are classified under the Solid-State Cameras category, where the film is replaced with a solid-state sensor. Figure (3-6) shows a cross-Section of such cameras.

The following part is taken after (Atkinson, 2001), Section 3.2.5, page 57.

A Charge Coupled Device (CCD) is the most commonly used device for recording the amount of light falling on to a surface for photogrammetric arrays. CCDs are arranged in linear arrays or in two-dimensional arrays. Linear arrays are used to scan a scene and this introduces time-dependent geometry. Two-dimensional arrays, as in a CCD camera, provide a complete record of light falling onto a two-dimensional surface at a particular instant of time.

The CCD works by converting photons, which fall onto the sensor surface into electrons. These are accumulated in capacitors and converted into digital form for output. The size of the array and the pixel size are the most important characteristics of a camera for photogrammetric use. Other important features are the dynamic range, the geometric characteristics (particularly lens distortion), the transfer of data from sensor and the time taken to record an image. Seitz et al. (1995) give a full description of these characteristics.

The size of the array is limited by technology. However, for aerial application, 2-dimensional arrays of 7168×4096 $12 \mu\text{m}$ pixels are possible (DMC from Z/I).

For terrestrial applications, a low-cost (e.g., the CS 3910BH < 2K Euro) CCD with a 1392×1040 array of $6.4 \mu\text{m}$ pixel size is readily available. More expensive cameras (e.g., the Hasselblad H2 > 25K Euro) are available with an array of 5448×4080 and a pixel size of $9 \mu\text{m}$.

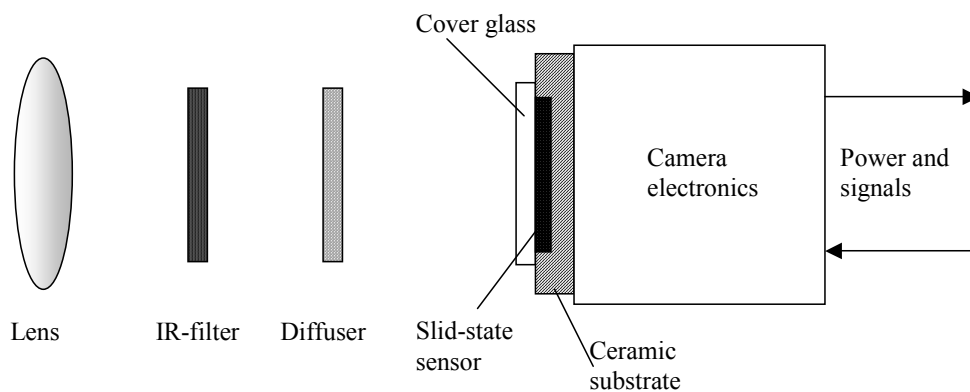


Figure 3-6: Solid-State Camera (Courtesy Beyer, 1992)

The amount of data needed to store an image in digital form is obviously related to the array size. A simple off-the-shelf camera with a 752×480 array will need 360 Kbytes and a 3000×2000 array will need 6 Mbytes.

The CCD we chose to work with is a Sony XC-55 Figure (3-7). We employ two analogue Sony CCDs (commonly used in the photogrammetry and robotics) that are linked via one cable to a frame grabber. The image data are synchronised with the data of an Inertial Measurement Unit (IMU). The interval between subsequent exposures is programmed to 0.5 or 1 s. As mentioned above, due to the limitations in the size of the vehicle, a base of one metre is chosen to separate the two cameras. Table (1) shows some specifications of these CCDs.

Table 3-1: Specifications of the CCD cameras

Effective picture elements	659(H) x 494(V)
Cell size	7.4 μm x 7.4 μm
Lens mount	C mount
Focal length	6 mm
Filed of vision	40.8° x 31.2°

3.4 - Frame Grabber

Following Atkinson (2001), Section 5.5.2, page 143, a frame grabber is typically a printed circuit board, which is designed to reside in a host computer. The purpose of a frame grabber is to instantaneously sample the output from a solid-state sensor, which is transmitting standard analogue video. The standard video signal is output continuously on the basis that it will be broadcast, shown on a video monitor or perhaps recorded continuously. The sample collected by the frame grabber is loaded into onboard solid-state memory, which can then be accessed by a host computer. Stored as a contiguous array of intensity values, the fields or frame are assembled into a digital image composed of pixels. Depending on the application, the frame grabber may be required to intermittently sample and store individual frames, collect short sequences of frames, or perhaps continuously read the video image and carry out a real time processing task.

In this work, the frame grabber will be used to sample individual frames of two cameras simultaneously and make them accessible by a host computer.

The Matrox Meteor-II/Multi-Channel frame grabber is used in this work. It is part of the Matrox family of high performance frame grabbers for cost sensitive applications. The grabber is hosted by a compact Matrox 4-Sight industrial PC with windows NT-Embedded operating system. The acquisition and synchronisation program (written by J. Skaloud) makes use of Matrox Image Library (MIL) that facilitates image acquisition and control of the grabber. Designed to capture from standard or variable analogue monochrome or component RGB frame scan sources, it specifically supports acquisition from interlaced or progressive scan component RGB cameras and single or dual-channel progressive scan monochrome cameras.

Figure (3-7) shows the two Sony XC-55 cameras connected via one cable to the Matrox Meteor-II PC hosting Multi-Channel frame grabber.

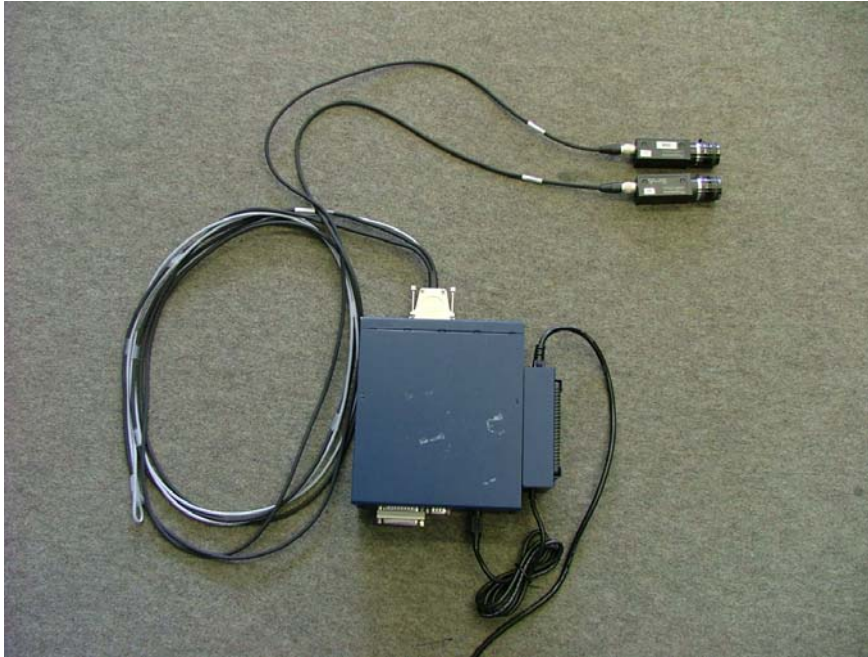


Figure 3-7: The two CCD connected to the frame grabber inside the Matrox4-Sight PC

3.5 - Camera Calibration

Cameras need calibration in order to be adapted for photogrammetry due to imperfections, especially in their lenses. Camera calibration involves (Ziemann and El-Hakim, 1982):

- Evaluation of the performance of a lens,
- Evaluation of the stability of a lens,
- Determination of the optical and geometric parameters of a lens,
- Determination of the optical and geometric parameters of a lens-camera systems,
- Determination of the optical and geometric parameters of a data acquisition system.

Only the geometric parameters of the lenses will be evaluated here. This means the interior orientation parameters and the radial symmetric and decentring distortion caused by the lens. The choice to perform this calibration only stems from the fact that other corrections will not affect the accuracy of the system under development.

Thus, camera calibration here aims at determining the interior orientation (x_0, y_0, c) of the camera and the radial symmetric and decentring distortion caused by the lens. Every camera

requires an independent calibration process. The results of the calibration of the two CCDs are shown in Appendix B.

Camera calibration is done in the context of LSA using the following mathematical model:

$$\begin{aligned} x &= x_0 - c \frac{U}{W} + \Delta x \\ y &= y_0 - c \frac{V}{W} + \Delta y \end{aligned} \quad (4.1)$$

U and V are the numerators and W is the denominator of Equation (2.1). This model is based on the co-linearity condition used in the intersection and resection with the addition of Δx and Δy , which are the correction terms due to the distortions. There are many models to determine these parameters; to name a few: El-Hakim and Faig, Ebner, Brown, Grun, etc.

As shown in Beyer (1992), radial symmetric lens distortion is the largest systematic error source when using solid-state cameras with low cost lenses and short focal lengths (5 to 20 mm).

The determination of Δx and Δy is achieved via a bundle adjustment with self-calibration.

3.6 - Bundle Least-Squares Adjustment with Self-Calibration

Camera self-calibration is usually done within the bundle adjustment to circumvent the effect of the change of the interior orientation during exposures. This process combines the processes of resection, intersection, and calibration into a single adjustment. Photo-coordinates of known and unknown (GCPs and homologous) points are measured and put into the model of Equation (4.1), then a LSA is performed. To define the datum and avoid the singularity in the matrix of normal equations, the corrections of some of the known points are forced to zero and the rows and columns that represent these known points are excluded from the normal matrix.

The mathematical model for the bundle adjustment with self-calibration is:

$$\begin{aligned} F(x) &\equiv -x + x_0 - c \frac{U}{W} + \Delta x(\delta x_0, \delta y_0, \delta c, a_1, a_2, a_3, \dots, a_h) \\ F(y) &\equiv -y + y_0 - c \frac{V}{W} + \Delta y(\delta x_0, \delta y_0, \delta c, a_1, a_2, a_3, \dots, a_h) \end{aligned} \quad (4.5)$$

where $\delta x_0, \delta y_0, \delta c$ are the correction to x_0, y_0, c and $a_1, a_2, a_3, \dots, a_h$ are the polynomial coefficients that contribute for the lens radial symmetric and decentring distortions.

The linearised observation equation for each photograph is:

$$\mathbf{w}_{ji} = \mathbf{A}'_{ji} \delta \mathbf{x}'_j + \mathbf{A}''_{ji} \delta \mathbf{x}''_i + \mathbf{D}_{ji} \delta \mathbf{y} + \mathbf{v}_{ji} \quad (4.6)$$

Where

\mathbf{A}' is the design matrix of resection, with dimensions $2n \times 7$; $j = L, R$

\mathbf{A}'' is the design matrix of intersection, with dimensions $2n \times 3n$, and

\mathbf{D} is the design matrix, with dimensions $2n \times (3+h)$, of the calibration equations and $\delta \mathbf{y}$ is the vector of the interior orientation correction and polynomial parameters: $\delta \mathbf{y} = [\delta x_0 \quad \delta y_0 \quad \delta c \quad a_1 \quad a_2 \quad \dots \quad a_h]^T$.

The solution of this LSA problem is:

$$\begin{bmatrix} \delta \mathbf{x} \\ \delta \mathbf{y} \end{bmatrix} = \begin{bmatrix} \mathbf{N}_{xx} & \mathbf{N}_{xy} \\ \mathbf{N}_{xy} & \mathbf{N}_{yy} \end{bmatrix}^{-1} \begin{bmatrix} \mathbf{U}_x \\ \mathbf{U}_y \end{bmatrix} \quad (4.7)$$

More explicitly, having n points, 2 images (L and R) and $h+3$ unknown calibration parameters, the above matrix becomes:

$$\begin{bmatrix} \delta x'_L \\ \delta x'_R \\ \delta x''_1 \\ \vdots \\ \delta x''_n \\ \delta \mathbf{y} \end{bmatrix} = \begin{bmatrix} \mathbf{N}'_L & \mathbf{0} & \overline{\mathbf{N}}_{L1} & \dots & \overline{\mathbf{N}}_{Ln} & \mathbf{N}_{yL} \\ \mathbf{0} & \mathbf{N}'_R & \overline{\mathbf{N}}_{R1} & \dots & \overline{\mathbf{N}}_{Rn} & \mathbf{N}_{yR} \\ \overline{\mathbf{N}}_{L1}^T & \overline{\mathbf{N}}_{R1}^T & \mathbf{N}''_1 & \mathbf{0} & \mathbf{0} & \mathbf{N}_{y1} \\ \vdots & \vdots & \mathbf{0} & \ddots & \mathbf{0} & \vdots \\ \overline{\mathbf{N}}_{Ln}^T & \overline{\mathbf{N}}_{Rn}^T & \mathbf{0} & \mathbf{0} & \mathbf{N}''_n & \mathbf{N}_{yn} \\ \overline{\mathbf{N}}_{yL}^T & \overline{\mathbf{N}}_{yR}^T & \mathbf{N}_{y1} & \dots & \mathbf{N}_{yn} & \mathbf{N}_{yy} \end{bmatrix}^{-1} \begin{bmatrix} \mathbf{U}'_L \\ \mathbf{U}'_R \\ \mathbf{U}''_1 \\ \vdots \\ \mathbf{U}''_n \\ \mathbf{U}_y \end{bmatrix} \quad (4.8)$$

With

$$\mathbf{N}'_L = \sum_{i=1}^n \mathbf{A}'_{Li}{}^T \cdot \mathbf{P}_{Li} \cdot \mathbf{A}'_{Li}$$

$$\mathbf{N}'_R = \sum_{i=1}^n \mathbf{A}'_{Ri}{}^T \cdot \mathbf{P}_{Ri} \cdot \mathbf{A}'_{Ri}$$

$$\mathbf{U}'_L = \sum_{i=1}^n \mathbf{A}'_{Li}{}^T \cdot \mathbf{P}_{Li} \cdot \mathbf{b}_{Li}$$

$$\mathbf{U}'_R = \sum_{i=1}^n \mathbf{A}'_{Ri}{}^T \cdot \mathbf{P}_{Ri} \cdot \mathbf{b}_{Ri}$$

$$\overline{\mathbf{N}}_{Li} = \mathbf{A}'_{Li}{}^T \cdot \mathbf{P}_{Li} \cdot \mathbf{A}''_{Li}$$

$$\overline{\mathbf{N}}_{Ri} = \mathbf{A}'_{Ri}{}^T \cdot \mathbf{P}_{Ri} \cdot \mathbf{A}''_{Ri}$$

$$\mathbf{N}_i'' = \mathbf{A}_{Li}''^T \cdot \mathbf{P}_{Li} \cdot \mathbf{A}_{Li}'' + \mathbf{A}_{Ri}''^T \cdot \mathbf{P}_{Ri} \cdot \mathbf{A}_{Ri}''$$

 3×3

$$\mathbf{U}_i'' = \mathbf{A}_{Li}''^T \cdot \mathbf{P}_{Li} \cdot \mathbf{b}_{Li} + \mathbf{A}_{Ri}''^T \cdot \mathbf{P}_{Ri} \cdot \mathbf{b}_{Ri}$$

 3×1

The computation of the other matrices is:

$$\mathbf{N}_{xy} = \begin{bmatrix} \mathbf{N}_{yL} \\ \mathbf{N}_{yR} \\ \mathbf{N}_{y1} \\ \vdots \\ \mathbf{N}_{yn} \end{bmatrix} = \begin{bmatrix} \sum_{i=1}^n \mathbf{A}_{Li}''^T \cdot \mathbf{P}_{Li} \cdot \mathbf{D}_{Li} \\ \sum_{i=1}^n \mathbf{A}_{Ri}''^T \cdot \mathbf{P}_{Ri} \cdot \mathbf{D}_{Ri} \\ \mathbf{A}_{L1}''^T \cdot \mathbf{P}_{L1} \cdot \mathbf{D}_{L1} + \mathbf{A}_{R1}''^T \cdot \mathbf{P}_{R1} \cdot \mathbf{D}_{R1} \\ \vdots \\ \mathbf{A}_{Ln}''^T \cdot \mathbf{P}_{Ln} \cdot \mathbf{D}_{Ln} + \mathbf{A}_{Rn}''^T \cdot \mathbf{P}_{Rn} \cdot \mathbf{D}_{Rn} \end{bmatrix} \quad (4.9)$$

and

$$\mathbf{N}_{yy} = \sum_{i=1}^n \mathbf{D}_{Li}^T \cdot \mathbf{P}_{Li} \cdot \mathbf{D}_{Li} + \sum_{i=1}^n \mathbf{D}_{Ri}^T \cdot \mathbf{P}_{Ri} \cdot \mathbf{D}_{Ri}$$

 $(h+3) \times (h+3)$

$$\mathbf{U}_y = \sum_{i=1}^n \mathbf{D}_{Li}^T \cdot \mathbf{P}_{Li} \cdot \mathbf{b}_{Li} + \sum_{i=1}^n \mathbf{D}_{Ri}^T \cdot \mathbf{P}_{Ri} \cdot \mathbf{b}_{Ri}$$

 $(h+3) \times 1$

The explicit form of the Jacobi matrix \mathbf{D} is not shown here because its size and shape are dictated by the calibration model.

The calibration of the two cameras, that were used in this work, was done by the Software BINGO-F®, whose model is not published; however, the theoretical development shown above remains the same regardless of the model used.

4 - STRAPDOWN INERTIAL SYSTEM SUPPORTING SLAM

... being a Geodesist, I am trained to have a global view and to aim at the stars ...

... being a Navigator, I am trained to have the curiosity to explore and to go beyond the horizon ...

4.1 - Introduction

With about 60 years-long history, Inertial Navigation Systems (INS) developed mainly as a military technology. Nowadays, they are used not only in the navigation arena, but also in other fields that require estimation of motion by autonomous measurements.

The Inertial Measurement Units (IMU) are usually classified into:

- Strategic-Grade IMU (Space shuttles, Submarines, ballistic missiles, etc.)
- Navigation-Grade IMU (air transport and military air and surface vehicles, etc.)
- Tactical-Grade IMU (missiles, mapping system, land navigation, etc.), and
- Automotive-Grade IMU (robots, machine control, etc.)

An informative discussion about class characteristics can be found in Greenspan (1995).

In general, the quality of a Strapdown INS (SINS) is correlated with its acquisition cost. All IMUs are subject to systematic errors that translate to position time dependent error growth. While the magnitude of the sensor errors changes with the “accuracy class”, the inherent principles of transforming sensor measurements into change in position and attitude are common to all SINS.

In what follows, a brief overview about the INS concept is presented and the mechanisation equations of the SINS are shown. The common SINS error analysis for a tactical-grade IMU and Kalman Filter presentation follow. In the last Section, the IMU used in this research is introduced.

4.2 - Inertial Navigation System Concept

Inertial Navigation Systems belong to the deduced-reckoning category, where a current position of a vehicle is deduced from its previous position.

An INS utilises the inertial properties of sensors mounted aboard a vehicle to execute the navigation function through appropriate processing of data obtained from specific force and inertial angular velocity measurements.

All INSs must perform the following functions, (Schwarz, 1986):

- Instrument a reference frame
- Measure specific force and angular rates
- Have knowledge of the gravitational field
- Time-integrate the force and rate data to obtain change in position and attitude information

An IMU consists of the following items:

- Three gyroscopes
- Three accelerometers with known orientation with respect to the gyroscopes
- A data processor
- An accurate time recorder.

The gyroscopes can be used to either measure or control orientation changes from the initially defined reference. The measuring of the specific force is achieved by the accelerometers. The processor (computer) and the time measurements accomplish the time integration. The knowledge of the gravitational field is accomplished by the knowledge of the position of the sensor with respect to an associated model.

4.3 - Mechanisation Equations for the Strapdown INS

To derive the mechanisation Equations of SINS, the modelling Equations have to be formulated first. Following the derivation of Schwarz and Wei (2000), the first-order differential equations for vehicle motion in the *Earth-Centred-Earth-Fixed (ECEF)* frame is written as:

$$\dot{\mathbf{x}}^e = \begin{pmatrix} \dot{\mathbf{r}}^e \\ \dot{\mathbf{v}}^e \\ \dot{\mathbf{R}}_b^e \end{pmatrix} = \begin{pmatrix} \mathbf{v}^e \\ \mathbf{R}_b^e \mathbf{f}^b - 2\boldsymbol{\Omega}_{ie}^e \mathbf{v}^e + \mathbf{g}^e \\ \mathbf{R}_b^e (\boldsymbol{\Omega}_{ei}^b + \boldsymbol{\Omega}_{ib}^b) \end{pmatrix} \quad (4.1)$$

where

$\mathbf{r}^e = (x^e, y^e, z^e)$ are the three position components in the Earth frame e

$\mathbf{v}^e = (v_x^e, v_y^e, v_z^e)$ is the vector of the three velocity components in the Earth frame e

$\mathbf{f}^b = (f_x^b, f_y^b, f_z^b)$ is the vector of the measured specific forces in body frame b

\mathbf{R}_b^e is the transformation matrix between the body frame b and Earth frame e

$\boldsymbol{\Omega}_{ie}^e$ is the skew-symmetric matrix of the rotation vector of the Earth frame e and relative to the inertial frame i in the e frame

$\boldsymbol{\Omega}_{ei}^b$ is the skew-symmetric matrix of the rotation vector of the inertial frame i and relative to the Earth frame e in the body frame b

$\boldsymbol{\Omega}_{ib}^b$ is the skew-symmetric matrix of the rotation vector of the body frame b and relative to the inertial frame i in the b frame sensed by the gyroscopes

\mathbf{g}^e is the Earth's gravity vector expressed in the Earth frame e and is computed by:

$\mathbf{g}^e = \bar{\mathbf{g}}^e - \boldsymbol{\Omega}_{ie}^e \boldsymbol{\Omega}_{ie}^e \mathbf{r}^e$, where the first term is the gravitation and the second term is the centripetal acceleration.

The dot (\cdot) represents derivation with respect to time.

In the above Equations, the gravity vector \mathbf{g}^e is computed as follows:

$$\mathbf{g}^e = \begin{bmatrix} |g| \cos \phi \cos \lambda \\ |g| \cos \phi \sin \lambda \\ |g| \sin \phi \end{bmatrix} + \begin{bmatrix} \omega_e^2 x^e \\ \omega_e^2 y^e \\ 0 \end{bmatrix} \quad (4.2)$$

where ϕ is the latitude of the computation point (note the notation distinction between the latitude ϕ and the pitch φ), ω_e ($= 7.292115 \times 10^{-5}$ rad/sec) is the Earth rotation rate, λ is the longitude of the computation point, and $|g|$ is the value of the gravitational acceleration

usually approximated by the normal gravitational acceleration, γ (with h being the geometric height – in metres – above the reference ellipsoid):

$$\gamma = \gamma_1(1 + \gamma_2 \sin^2 \phi + \gamma_3 \sin^4 \phi) + (\gamma_4 + \gamma_5 \sin^2 \phi)h + \gamma_6 h^2 \quad (4.3)$$

$$\begin{aligned} \gamma_1 &= 9.7803267715 \text{ m/sec}^2 & ; & & \gamma_2 &= 0.0052790414 \\ \gamma_3 &= 0.0000232718 & ; & & \gamma_4 &= -0.000003087691089 \text{ 1/sec}^2 \\ \gamma_5 &= 0.000000004397731 \text{ 1/sec}^2 & ; & & \gamma_6 &= 0.000000000000721 \text{ 1/msec}^2 \end{aligned}$$

From these differential equations, one can derive the mechanisation equations. Following Schwarz and Wei (2000), the detailed **ECEF** frame mechanisation equations, used to compute the spatial translation, are shown below.

4.3.1 - Earth-Centred-Earth-Fixed Frame

The vehicle velocity increments are computed as:

$$\Delta \mathbf{v}^e = \Delta \mathbf{v}_f^e - \mathbf{a}^e \Delta t + \boldsymbol{\gamma}^e \Delta t \quad (4.4)$$

The process of solving the above Equations is recursive. Therefore, the parameters of epoch k are derived from those of epoch $k - 1$.

The first two terms on the right-hand side of the above equality are computed from the measurements.

$\Delta \mathbf{v}_f^e$ is the velocity increments derived from: $\mathbf{f}^e = \mathbf{R}_b^e \mathbf{f}^b$, and at epoch k is equal to:

$$\Delta \mathbf{v}_f^e = \mathbf{R}_b^e(t_{k-1}) \left(\mathbf{I} + \frac{1}{2} \mathbf{S}^b \right) \Delta \mathbf{v}^b \quad (4.5)$$

Where

$\Delta \mathbf{v}^b$ is the vector of measured velocity increments – accelerations,

$\mathbf{I} + \mathbf{S}^b$ is the orthogonal transformation matrix between the body frame at time t_{k-1} and current time t_k , and is equal to (\mathbf{I} is a 3×3 identity matrix):

$$\mathbf{I} + \mathbf{S}^b = \begin{bmatrix} 1 & -\theta_z^b & \theta_y^b \\ \theta_z^b & 1 & -\theta_x^b \\ -\theta_y^b & \theta_x^b & 1 \end{bmatrix} \quad (4.6)$$

where the angles θ_i^b are the angular increments of the body rotation with respect to the e -frame expressed in the b -frame and computed from $\boldsymbol{\theta}_{eb}^b = \Delta\boldsymbol{\theta}_{ib}^b - \mathbf{d}\boldsymbol{\theta}_{ie}^b$ as:

$$\begin{bmatrix} \theta_x^b & \theta_y^b & \theta_z^b \end{bmatrix}^T = \begin{bmatrix} \Delta\theta_x^b & \Delta\theta_y^b & \Delta\theta_z^b \end{bmatrix}^T - \begin{bmatrix} d\theta_x^b & d\theta_y^b & d\theta_z^b \end{bmatrix}^T$$

$\Delta\boldsymbol{\theta}_{ib}^b$ is the vector of gyroscopes' measurements $\boldsymbol{\omega}_{ib}^b$ expressed in the b -frame multiplied by the time increment, $\Delta t = t_k - t_{k-1}$

$\mathbf{d}\boldsymbol{\theta}_{ie}^b$ is the Earth rotation vector relative to the inertial frame expressed in the b -frame and equal to $\boldsymbol{\omega}_{ie}^b \Delta t$, where

$$\boldsymbol{\omega}_{ie}^b = \mathbf{R}_e^b \boldsymbol{\omega}_e = \mathbf{R}_e^b \begin{bmatrix} 0 \\ 0 \\ \omega_e \end{bmatrix} = \begin{bmatrix} R_{31}\omega_e & R_{32}\omega_e & R_{33}\omega_e \end{bmatrix}^T \quad (4.7)$$

\mathbf{R}_e^b is derived from the quaternions:

$$\begin{bmatrix} R_{11} & R_{12} & R_{13} \\ R_{21} & R_{22} & R_{23} \\ R_{31} & R_{32} & R_{33} \end{bmatrix} = \begin{bmatrix} (q_1^2 - q_2^2 - q_3^2 + q_4^2) & 2(q_1q_2 - q_3q_4) & 2(q_1q_3 + q_2q_4) \\ 2(q_1q_2 + q_3q_4) & (q_2^2 - q_1^2 - q_3^2 + q_4^2) & 2(q_2q_3 - q_1q_4) \\ 2(q_1q_3 - q_2q_4) & 2(q_2q_3 + q_1q_4) & (q_3^2 - q_1^2 - q_2^2 + q_4^2) \end{bmatrix}$$

The quaternion update Equation can be written in terms of the angular increments $\boldsymbol{\theta}_{eb}^b$ (see Schwarz and Wei (2000), Chapter 5, for more details):

$$\begin{bmatrix} q_1 \\ q_2 \\ q_3 \\ q_4 \end{bmatrix}_k = \begin{bmatrix} q_1 \\ q_2 \\ q_3 \\ q_4 \end{bmatrix}_{k-1} + \frac{1}{2} \begin{bmatrix} c & s\theta_z^b & -s\theta_y^b & s\theta_x^b \\ -s\theta_z^b & c & s\theta_x^b & s\theta_y^b \\ s\theta_y^b & -s\theta_x^b & c & s\theta_z^b \\ -s\theta_x^b & -s\theta_y^b & -s\theta_z^b & c \end{bmatrix}_k \cdot \begin{bmatrix} q_1 \\ q_2 \\ q_3 \\ q_4 \end{bmatrix}_{k-1} \quad (4.8)$$

In the equality above, the terms c and s are equal to:

$$c = 2 \left(\cos \frac{\theta}{2} - 1 \right) \quad \text{and} \quad s = \frac{2}{\theta} \sin \frac{\theta}{2}$$

$$\text{with} \quad \theta = \sqrt{(\theta_x^b)^2 + (\theta_y^b)^2 + (\theta_z^b)^2}.$$

Going back to Equation (4.4), \mathbf{a}^e is the Coriolis correction and is calculated by:

$$\mathbf{a}^e = 2\boldsymbol{\Omega}_{ie}^e \mathbf{v}^e = [-2\omega_e v_y \quad 2\omega_e v_x \quad 0]^T \tag{4.9}$$

After computing $\Delta \mathbf{v}^e$, the velocity $\mathbf{v}^e = (v_x^e, v_y^e, v_z^e)$ at epoch k is computed as:

$$\mathbf{v}_k^e = \mathbf{v}_{k-1}^e + \frac{1}{2}(\Delta \mathbf{v}_k^e + \Delta \mathbf{v}_{k-1}^e) \tag{4.10}$$

and the ECEF coordinates $\mathbf{r}^e = (x^e, y^e, z^e)$ are determined by:

$$\mathbf{r}_k^e = \mathbf{r}_{k-1}^e + \frac{\Delta t}{2}(\mathbf{v}_k^e + \mathbf{v}_{k-1}^e). \tag{4.11}$$

The flowchart of the mechanisation equations in the ECEF is shown in Figure (4-1).

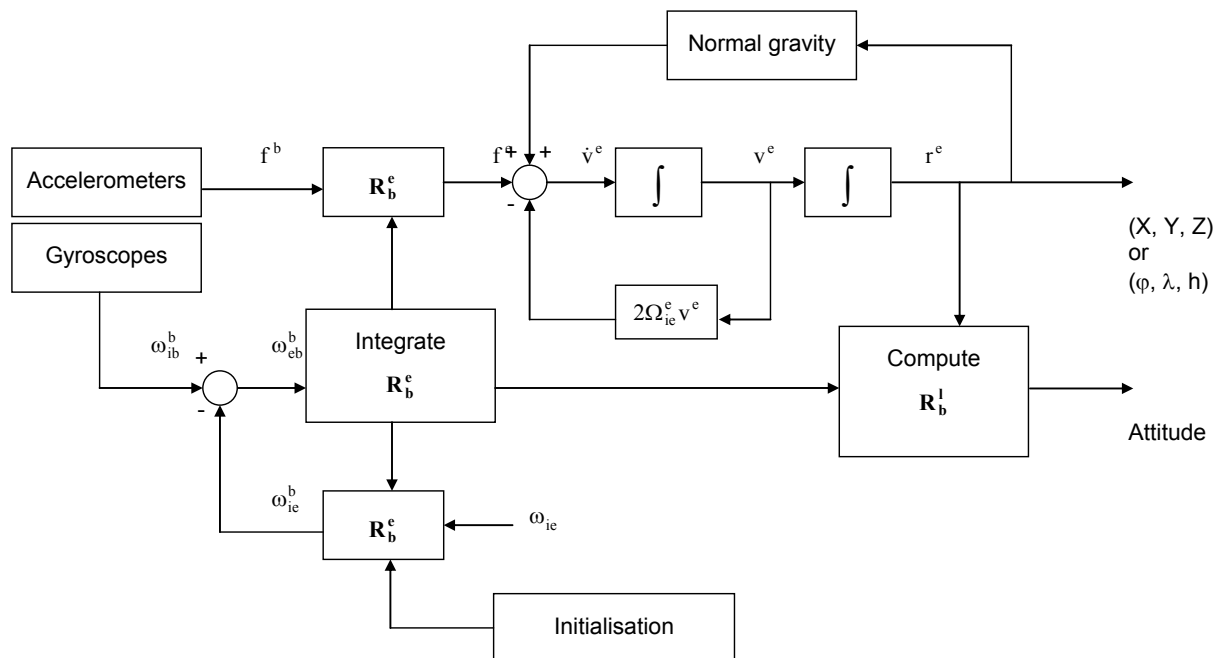


Figure 4-1: Mechanisation Equations in the Earth-fixed frame

From the Earth-fixed Cartesian coordinates, $\mathbf{r}^e = (x^e, y^e, z^e)$, one can compute the geodetic coordinates, (ϕ, λ, h) :

$$\lambda = \arctan\left(\frac{y^e}{x^e}\right) \quad (4.12)$$

$$\phi = \bar{\Psi} + D \quad (4.13)$$

$$h = \frac{\sqrt{(x^e)^2 + (y^e)^2}}{\cos \phi} - N \quad (4.14)$$

$$\text{where} \quad \bar{\Psi} = \arcsin\left(\frac{z^e}{r}\right) \quad D = \frac{\arcsin\left(k \sin 2\bar{\Psi} / \sqrt{1 - e^2 \sin^2 \bar{\Psi}}\right)}{1 - 2k \cos 2\bar{\Psi} + 2k^2 \sin^2 \bar{\Psi}}$$

$$k = 0.5e^2 \frac{a}{r} \quad r = \sqrt{(x^e)^2 + (y^e)^2 + (z^e)^2}$$

As for the attitude angles – roll φ , pitch ϑ , and yaw ψ – they are computed from the matrix:

$$\mathbf{R}_b^I = \mathbf{R}_e^I \cdot \mathbf{R}_b^e \quad (4.15)$$

where

$$\mathbf{R}_b^I = \begin{bmatrix} \cos \varphi \cos \psi - \sin \varphi \sin \vartheta \sin \psi & -\cos \vartheta \sin \psi & \sin \varphi \cos \psi + \cos \varphi \sin \vartheta \sin \psi \\ \cos \varphi \sin \psi + \sin \varphi \sin \vartheta \cos \psi & \cos \vartheta \cos \psi & \sin \varphi \sin \psi - \cos \varphi \sin \vartheta \cos \psi \\ -\sin \varphi \cos \vartheta & \sin \vartheta & \cos \varphi \cos \vartheta \end{bmatrix}$$

$$\mathbf{R}_I^e = \begin{bmatrix} -\sin \lambda & -\sin \phi \cos \lambda & \cos \phi \cos \lambda \\ \cos \lambda & -\sin \phi \sin \lambda & \cos \phi \sin \lambda \\ 0 & \cos \phi & \sin \phi \end{bmatrix}$$

Thus,

$$\varphi = \arctan\left(\frac{R_b^I(3,1)}{R_b^I(3,3)}\right) \quad (4.16)$$

$$\psi = \arctan\left(-\frac{R_b^l(1,2)}{R_b^l(2,2)}\right) \quad (4.17)$$

$$\vartheta = \arcsin(R_b^l(3,2)) \quad (4.18)$$

4.4 - Dynamic Modelling of System Errors

The coordinates provided by direct integration of the system output suffer from systematic errors. The error sources can be grouped in two distinct categories. First, there are errors induced by the erroneous initial conditions; these errors are called initial system errors. Second, there are errors due to the imperfections in the gyros and accelerometers, and they are called sensor errors.

Constant system errors can be accurately removed by regular calibrations. The systematic errors that changes from mission to mission or vary throughout a mission are known as state errors. These errors affect the sensors output and are usually modelled by a set of linear differential equations that express the errors rate of change in time.

4.4.1 - State Space Formulation

A dynamic system can be described by ordinary differential Equations in which time is the independent variable. Using matrix notation, an n th-order differential equation may be expressed by n first-order differential equations, where n becomes the number of state variables necessary to describe the dynamics of a system completely. Using state-space formulation, the error behaviour of the system errors can be described by the following system of differential Equations (Gelb, 1974):

$$\dot{\mathbf{x}}(t) = \mathbf{\Gamma}(t)\mathbf{x}(t) + \mathbf{G}\mathbf{w}(t) \quad (4.19)$$

$\mathbf{x}(t)$ is the state vector and $\mathbf{\Gamma}(t)$ is the dynamic matrix. The vector $\mathbf{w}(t)$ is a zero-mean white noise process representing the random disturbances in the system and \mathbf{G} is a shaping matrix. The state vector $\mathbf{x}(t)$ can be partitioned into two vectors of lower dimensions:

$$\mathbf{x} = [\mathbf{x}_1 \quad \mathbf{x}_2]^T \quad (4.20)$$

Where the error state \mathbf{x}_1 describes the behaviour of the position, velocity and misalignment errors of the inertial system, while \mathbf{x}_2 is used to model time varying accelerometer and gyro errors. Using matrix notation, Equation (4.19) takes the following form:

$$\dot{\mathbf{x}} = \begin{bmatrix} \Gamma_1 & \Gamma_{12} \\ \mathbf{0} & \Gamma_2 \end{bmatrix} \begin{bmatrix} \mathbf{x}_1 \\ \mathbf{x}_2 \end{bmatrix} + \begin{bmatrix} \mathbf{0} \\ \mathbf{G}\mathbf{u}_2 \end{bmatrix} \quad (4.21)$$

The matrix Γ_{12} describes the manner in which accelerometer and gyro errors affect the position, velocity and misalignment errors.

4.4.2 - Error Equations in the Earth-Fixed Frame

Choosing a 15 elements error state vector for the ECEF frame mechanisation equations gives the following form:

$$\begin{aligned} \mathbf{x}^e &= \begin{bmatrix} \mathbf{x}_1^e & \mathbf{x}_2^e \end{bmatrix}^T = \begin{bmatrix} \delta\mathbf{r}^e & \delta\mathbf{v}^e & \boldsymbol{\varepsilon}^e & \mathbf{d} & \mathbf{b} \end{bmatrix}^T \\ &= \begin{bmatrix} \delta x^e & \delta y^e & \delta z^e & \delta v_x^e & \delta v_y^e & \delta v_z^e & \delta\varepsilon_x & \delta\varepsilon_y & \delta\varepsilon_z & \delta g_x & \delta g_y & \delta g_z & \delta b_x & \delta b_y & \delta b_z \end{bmatrix}^T \end{aligned} \quad (4.22)$$

Where

δx^e , δy^e and δz^e are the error states in the position vector

δv_x^e , δv_y^e and δv_z^e are the error states in the velocity vector

$\delta\varepsilon_x$, $\delta\varepsilon_y$ and $\delta\varepsilon_z$ are the misalignments' error states

δg_x , δg_y and δg_z are the gyroscopes' drift error states, and

δb_x , δb_y and δb_z are the accelerometers' drift error states

The state vector usually contains many other states than those shown above, such as scale factors, non-orthogonalities, random effects, etc. Only the sensors drifts were used in this work due to the minimal effect of the other types of errors when functioning in low dynamics.

Following the linearisation shown in Schwarz and Wei (2000), the differential Equations of the error model of the dynamic system in the Earth-fixed frame takes the form:

$$\dot{\mathbf{x}}^e(t) = \begin{bmatrix} \delta \mathbf{r}^e \\ \delta \dot{\mathbf{v}}^e \\ \dot{\mathbf{\epsilon}}^e \\ \dot{\mathbf{d}} \\ \dot{\mathbf{b}} \end{bmatrix} = \begin{bmatrix} \delta \mathbf{v}^e \\ -\mathbf{F}^e \boldsymbol{\epsilon}^e + \boldsymbol{\Xi}^e \delta \mathbf{r}^e - 2\boldsymbol{\Omega}_{ie}^e \delta \mathbf{v}^e + \mathbf{R}_b^e \mathbf{b} \\ -\boldsymbol{\Omega}_{ie}^e \boldsymbol{\epsilon}^e + \mathbf{R}_b^e \mathbf{d} \\ -\boldsymbol{\alpha} \mathbf{d} + \mathbf{w}_d \\ -\boldsymbol{\beta} \mathbf{b} + \mathbf{w}_b \end{bmatrix} \quad (4.23)$$

where \mathbf{F}^e is the skew-symmetric matrix of the measured specific force vector in the Earth-fixed frame \mathbf{f}^b , $\boldsymbol{\alpha}$ and $\boldsymbol{\beta}$ are the diagonal matrices containing reciprocals of the time correlation parameters of the Gauss-Markov process used to form the stochastic model of the gyroscopes' drift residual \mathbf{d} and the accelerometers' bias residual \mathbf{b} , and \mathbf{w}_d and \mathbf{w}_b are vectors containing white noise. Other terms were already defined.

Equation (4.23) can be re-written in the form of Equation (4.19):

$$\dot{\mathbf{x}}^e(t) = \boldsymbol{\Gamma}^e(t) \mathbf{x}^e(t) + \mathbf{G}^e \mathbf{w}(t) \quad (4.24)$$

with

$$\boldsymbol{\Gamma}^e(t) = \begin{bmatrix} 0 & 0 & 0 & 1 & 0 & 0 & 0 & 0 & 0 & 0 & 0 & 0 & 0 & 0 & 0 \\ 0 & 0 & 0 & 0 & 1 & 0 & 0 & 0 & 0 & 0 & 0 & 0 & 0 & 0 & 0 \\ 0 & 0 & 0 & 0 & 0 & 1 & 0 & 0 & 0 & 0 & 0 & 0 & 0 & 0 & 0 \\ \Xi_{11} & \Xi_{12} & \Xi_{13} & 0 & 0 & 0 & 0 & f_z^e & -f_y^e & 0 & 0 & 0 & R_{11} & R_{12} & R_{13} \\ \Xi_{21} & \Xi_{22} & \Xi_{23} & 0 & 0 & 0 & -f_z^e & 0 & f_x^e & 0 & 0 & 0 & R_{21} & R_{22} & R_{23} \\ \Xi_{31} & \Xi_{32} & \Xi_{33} & 0 & 0 & 0 & f_y^e & -f_x^e & 0 & 0 & 0 & 0 & R_{31} & R_{32} & R_{33} \\ 0 & 0 & 0 & 0 & 0 & 0 & 0 & 0 & 0 & R_{11} & R_{12} & R_{13} & 0 & 0 & 0 \\ 0 & 0 & 0 & 0 & 0 & 0 & 0 & 0 & 0 & R_{21} & R_{22} & R_{23} & 0 & 0 & 0 \\ 0 & 0 & 0 & 0 & 0 & 0 & 0 & 0 & 0 & R_{31} & R_{32} & R_{33} & 0 & 0 & 0 \\ 0 & 0 & 0 & 0 & 0 & 0 & 0 & 0 & 0 & -\alpha & 0 & 0 & 0 & 0 & 0 \\ 0 & 0 & 0 & 0 & 0 & 0 & 0 & 0 & 0 & 0 & -\alpha & 0 & 0 & 0 & 0 \\ 0 & 0 & 0 & 0 & 0 & 0 & 0 & 0 & 0 & 0 & 0 & -\alpha & 0 & 0 & 0 \\ 0 & 0 & 0 & 0 & 0 & 0 & 0 & 0 & 0 & 0 & 0 & 0 & -\beta & 0 & 0 \\ 0 & 0 & 0 & 0 & 0 & 0 & 0 & 0 & 0 & 0 & 0 & 0 & 0 & -\beta & 0 \\ 0 & 0 & 0 & 0 & 0 & 0 & 0 & 0 & 0 & 0 & 0 & 0 & 0 & 0 & -\beta \end{bmatrix}$$

The elements R_{ij} are those of the rotation matrix \mathbf{R}_b^e . In addition, the elements Ξ 's are computed as:

$$\Xi = \frac{KM}{r^3} \begin{bmatrix} -1 + \frac{3(x^e)^2}{r} & \frac{3x^e y^e}{r^2} & \frac{3x^e z^e}{r^2} \\ \frac{3x^e y^e}{r^2} & -1 + \frac{3y^2}{r} & \frac{3y^e z^e}{r^2} \\ \frac{3x^e z^e}{r^2} & \frac{3y^e z^e}{r^2} & -1 + \frac{3(z^e)^2}{r} \end{bmatrix} + \begin{bmatrix} \omega_e^2 & 0 & 0 \\ 0 & \omega_e^2 & 0 \\ 0 & 0 & 0 \end{bmatrix} \quad (4.25)$$

where K is the gravitational constant and M is the Earth's mass. The central term in the "KM" is known with much higher accuracy than either 'K' or 'M'. The refined value of the WGS84 GM parameter, along with its 1σ uncertainty is: $KM = 3986004.418 \times 10^8 \pm 0.008 \text{ m}^3/\text{sec}^2$. This value includes the mass of the atmosphere and is based on several types of space measurements; for more details, see <http://www.wgs84.com>.

4.5 - Kalman Filter as an Estimation Method

Estimation is the process of extracting information from data – data which can be used to infer the desired information and may contain errors (Gelb, 1974). Since the INS can give us real-time results, optimal real-time estimation methods techniques are required here. These techniques are based on error modelling, which take the dynamics of the system errors into account, as well as the statistics associated with those errors. Optimal estimation deals with three distinct problems: prediction, filtering, and smoothing. The prediction and filtering algorithms are combined to provide real-time estimates of the state vector of a linear system. Kalman (1960) has developed one of the most common forms of optimal filtering. The smoothing algorithm, on the other hand, calculates improved estimates of the state vector backward in time.

The basic problem to be solved here is the optimal estimation of a time varying state vector \mathbf{x} from a set of observations linearly related to the state vector. The dynamics of the state vector is described by the matrix $\mathbf{\Gamma}$. The control measurements are related to the state vector by the following equation:

$$\mathbf{z}_k = \mathbf{H}_k \mathbf{x}_k + \mathbf{v}_k \quad (4.26)$$

where \mathbf{z}_k is the vector of observations and \mathbf{H}_k is the measurement design matrix defining the relationship between the observations and the error state vector. \mathbf{v}_k is a white noise sequence corrupting the observations.

Let us define a set of measurements of the form:

$$\mathbf{Z} = \{\mathbf{z}_0, \dots, \mathbf{z}_k, \dots, \mathbf{z}_n\} \quad (4.27)$$

where \mathbf{z}_k corresponds to the measurement vector sampled at time t_k . The prediction problem is to find an estimate of the state vector \mathbf{x} at time t_i based upon the set of measurements \mathbf{z}_k where $i > k$. The *predicted* estimate is denoted by

$$\mathbf{x}_{i,k} = E\{\mathbf{x}_i \mid \mathbf{Z}_k\} \quad i > k \quad (4.28)$$

where $E\{\mathbf{A} \mid \mathbf{B}\}$ represents the expected value of the estimate \mathbf{A} , given the set of data \mathbf{B} .

The *filtering* problem occurs when the time at which the estimate is desired coincides with the last variable set of measurements.

$$\mathbf{x}_{i,k} = E\{\mathbf{x}_i \mid \mathbf{Z}_k\} \quad i = k \quad (4.29)$$

The *smoothing* algorithm uses all measurements between $t = t_0$ and $t = t_n$ to estimate the state of the system at certain time t_k where $t_0 \leq t_k \leq t_n$.

$$\mathbf{x}_{i,k} = E\{\mathbf{x}_i \mid \mathbf{Z}_n\} \quad k \leq n \quad (4.30)$$

The time t_n corresponds to the last epoch of the measurement update. Smoothing uses the set of measurements done after time t_k , $\{\mathbf{z}_{k+1}, \mathbf{z}_{k+2}, \dots, \mathbf{z}_n\}$, which contains additional information about the state vector. This implies that optimal smoothing is a post mission procedure and can be done only after the complete set of measurements has been collected over a defined time interval.

Kalman Filtering provides the optimal real-time estimate of the state vector \mathbf{x} and, at the same time, a continuous measure of the estimation accuracy of the state vector.

Denoting the covariance matrix of the state vector by \mathbf{P} :

$$\mathbf{P}(t) = E\{\mathbf{x}(t) \mathbf{x}(t)^T\} \quad (4.31)$$

the KF algorithm can be applied to a continuous process with measurements taken at discrete points in time. Between observations, the prediction of \mathbf{x} and \mathbf{P} over the interval $[t_{k-1}, t_k]$ is obtained from:

$$\mathbf{x}_k(-) = \Phi_{k-1,k} \mathbf{x}_{k-1}(+) \quad (4.32)$$

$$\mathbf{P}_k(-) = \Phi_{k-1,k} \cdot \mathbf{P}_{k-1}(+) \cdot \Phi_{k-1,k}^T + \mathbf{Q}_{k-1} \quad (4.33)$$

The matrix $\Phi_{k-1,k}$, called the transition matrix, is the solution of the set of differential equations (Section 4.4):

$$\dot{\mathbf{x}} = \Gamma \mathbf{x} \quad (4.34)$$

And, \mathbf{x}_{k-1} and \mathbf{x}_k represent the state vector at time t_{k-1} and t_k respectively. Provided Δt is small enough, so that the matrix Γ can be considered constant over this interval, Φ can be computed using:

$$\Phi(\Delta t) = \mathbf{I} + \sum_{n=1}^{n=\infty} \Gamma^n (\Delta t)^n \quad (4.35)$$

For practical real-time implementation, the integration interval can be chosen small enough so that a truncated series of the previous equation can be used in the calculation of the matrix Φ . In the absence of high dynamics, the following approximation is sufficient:

$$\Phi(\Delta t) = \mathbf{I} + \Gamma(\Delta t) \quad (4.36)$$

The matrix \mathbf{Q}_k in Equation (4.33) represents the uncertainty of the state vector resulting from the white noise input acting over the interval $[t_{k-1}, t_k]$. Provided the dynamics matrix Γ is constant over the interval Δt , a numerical solution of matrix \mathbf{Q}_k can be computed using:

$$\mathbf{Q}_k = \mathbf{Q}_{k-1} + \Gamma \cdot \mathbf{Q} \cdot \Gamma^T \quad (4.37)$$

Where \mathbf{Q} is the spectral density matrix; in the numerical applications of this work it was chosen to take the following form:

$$\mathbf{Q} = \text{diag}(\sigma_{ax}^2, \sigma_{ay}^2, \sigma_{az}^2, \sigma_{gx}^2, \sigma_{gy}^2, \sigma_{gz}^2)$$

With σ_{ai}^2 and σ_{gi}^2 being the variances of the accelerometers and gyroscopes of the i -axis.

When the measurements become available, the state vector \mathbf{x} and the matrix \mathbf{P} are updated using the following set of equations:

$$\mathbf{x}_k(+)=\mathbf{x}_k(-)+\mathbf{K}_k\cdot(\mathbf{z}_k-\mathbf{H}_k\mathbf{x}_k(-)) \quad (4.38)$$

$$\mathbf{P}_k(+)=\left(\mathbf{I}-\mathbf{K}_k\mathbf{H}_k\right)\mathbf{P}_k(-) \quad (4.39)$$

The difference between the measurement \mathbf{z}_k and a prediction of the measurements based on all past observations is denoted by:

$$\mathbf{r}_k=\mathbf{z}_k-\mathbf{H}_k\mathbf{x}_k(-) \quad (4.40)$$

\mathbf{r}_k can be regarded as reflecting the new information provided by the measurement vector \mathbf{z}_k to \mathbf{x}_k . For this reason, \mathbf{r}_k is called the innovation sequence. It can be shown that for an adequate modelling of the system, the innovation sequence will tend to have the characteristics of a white noise process, i.e.,

$$E\{\mathbf{r}_k\}=0 \quad E\{\mathbf{r}_{k-1} \quad \mathbf{r}_k\}=0 \quad (4.41)$$

The covariance matrix of the vector \mathbf{r}_k is represented by the matrix \mathbf{D}_k , where:

$$E\left\{\begin{matrix} \mathbf{r}_k \\ \mathbf{r}_k^T \end{matrix}\right\}=\mathbf{D}_k=\mathbf{H}_k\cdot\mathbf{P}(-)\cdot\mathbf{H}_k^T+\mathbf{R}_k \quad (4.42)$$

The matrix \mathbf{K}_k is the Kalman gain matrix and is computed using:

$$\mathbf{K}_k=\mathbf{P}_k(-)\mathbf{H}_k^T\left[\mathbf{H}_k\mathbf{P}_k(-)\mathbf{H}_k^T+\mathbf{R}_k\right]^{-1} \quad (4.43)$$

The signs $(-)$ and $(+)$ define quantities before and after update respectively while \mathbf{R}_k is the variance of the measurement noise vector \mathbf{v}_k .

While the dimensions of the matrices \mathbf{H}_k and \mathbf{P}_k do not change – because they depend on the state vector – the dimension of \mathbf{R}_k depends on the external measurements. This matrix can be either defined once for all at the beginning or changed at each update. In our case, this matrix is constructed from the output Covariance matrix of the photogrammetric resection, where its elements are the Covariances of the EOPs.

The statistical properties of the innovation sequence given in Equation (4.41) and (4.42) provide information, which can be used effectively to edit the incoming measurements. This suggests that poor measurements can be detected by testing the residual sequence against its theoretical statistical properties. Based on the predicted covariance matrix \mathbf{D}_k , a

confidence test can be defined so that a measurement will be rejected if it falls outside the limits of the confidence interval. Table (4-1) summarises the process of KF in terms of equations and Figure (4-2) shows the classical flowchart of the KF process.

Table 4-1: Kalman Filter equations

Prediction
<i>Predicted state vector:</i> $\mathbf{x}_k(-) = \Phi_{k-1,k} \mathbf{x}_{k-1}(+)$
<i>Predicted covariance matrix:</i> $\mathbf{P}_k(-) = \Phi_{k-1,k} \mathbf{P}_{k-1}(+) \Phi_{k-1,k}^T + \mathbf{Q}_{k-1}$
Update
<i>Updated state estimate:</i> $\mathbf{x}_k(+) = \mathbf{x}_k(-) + \mathbf{K}_k (\mathbf{z}_k - \mathbf{H}_k \mathbf{x}_k(-))$
<i>Updated covariance matrix:</i> $\mathbf{P}_k(+) = (\mathbf{I} - \mathbf{K}_k \mathbf{H}_k) \mathbf{P}_k(-)$
<i>Kalman Gain:</i> $\mathbf{K}_k = \mathbf{P}_k(-) \mathbf{H}_k^T [\mathbf{H}_k \mathbf{P}_k(-) \mathbf{H}_k^T + \mathbf{R}_k]^{-1}$

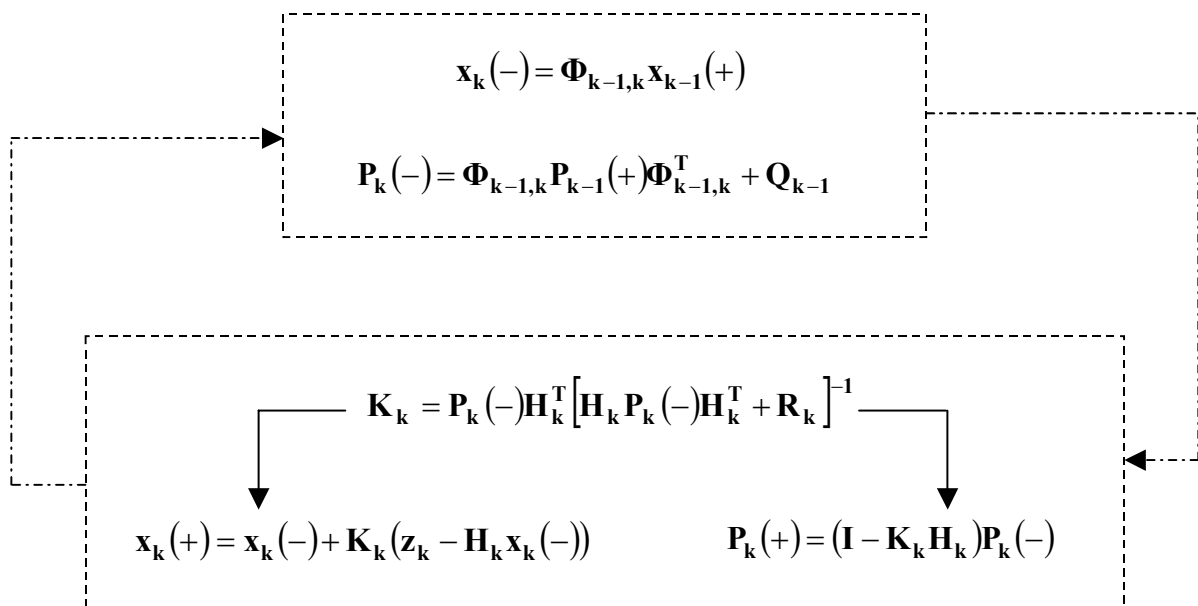


Figure 4-2: Kalman Filter process flowchart

4.6 - The IMU in this work

For this research, a Tactical-Grade IMU from Northrop Grumman, namely the LN-200, is used, which combines three Fibre Optic Gyroscopes (FOG) and three silicon accelerometers (SiAc). The specifications of LN-200 are listed in Table (4-2).

Table 4-2: Specification of LN-200 (Courtesy Northrop Grumman web page)

Physical	
Weight	700 grams
Size	8.9cm diameter by 8.5 cm high
Power	10 watts steady-state (nominal)
Activation Time	0.8 s (5 s to full accuracy)
Performance – Gyroscope	
Bias Repeatability	1deg/hr to 10deg/hr 1σ
Random Walk	0.04 to 0.1deg/(hr) ^{1/2} PSD level
Scale Factor Stability	100 ppm 1σ
Bias Variation	0.35deg/hr 1σ w/ 100-s correlation time
Non-orthogonality	20 arcs 1σ
Bandwidth	> 500 Hz
Performance - Accelerometer	
Bias Repeatability	200 μ g to 1 milli-g, 1σ
Scale Factor Stability	300 ppm 1σ
Vibration Sensitivity	50 μ g/g ² 1σ
Bias Variation	50 μ g 1σ w/ 60-s correlation time
Non-orthogonality	20 arcs 1σ
White Noise	50 μ g(Hz) ^{1/2} PSD level
Bandwidth	100 Hz

4.6.1 - Performance of LN-200

The mapping industries prefer the tactical grade IMUs due to their reasonable price-to-quality ratio. (Its price is around 15KEuro ~25k\$). The acquisition toolbox used in this research was developed at TOPO-EPFL.

To study the quality of this IMU, three surveys in a running vehicle were carried out upon which 12 GPS outages were forced. These simulated outages were done so that the first outage lasted for 5 seconds, the second for 10 seconds, the third for 15 seconds, until the twelfth outage that lasted for an entire minute. These tests are shown in Figures (4-3) to (4-5).

Similar test can be made with stationary data, but the dynamic of motion gives a more realistic image on system behaviour.

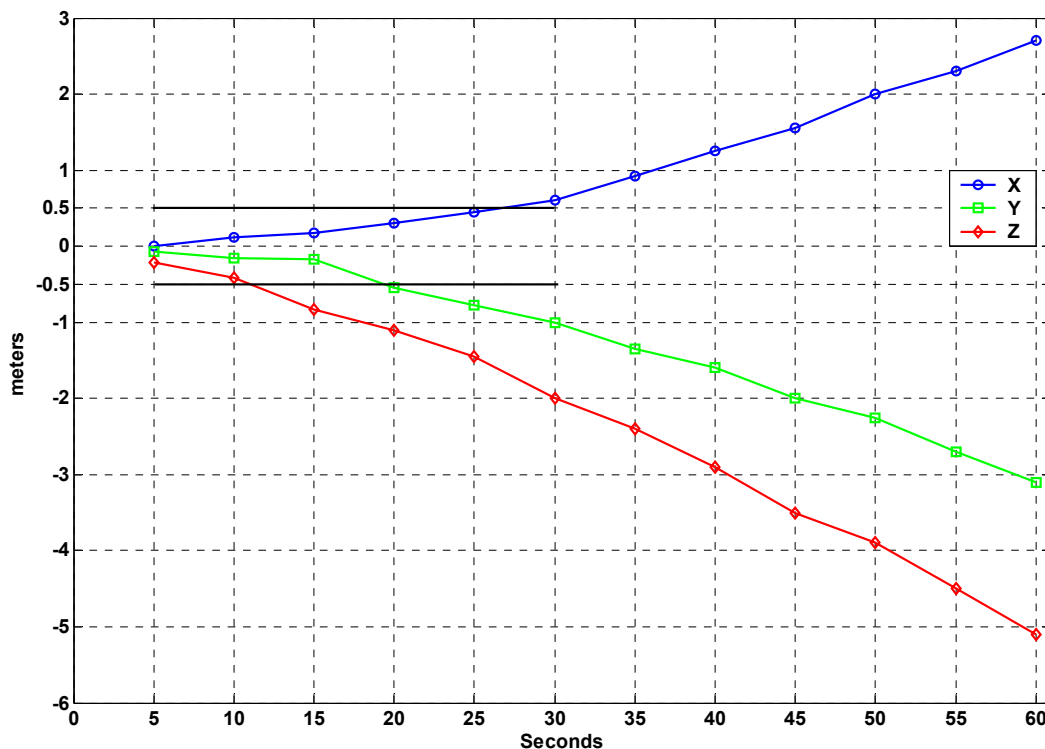


Figure 4-3: IMU positioning quality: first test

4.6.2 - Gyro-Compassing by LN200

When performing SLAM, in certain cases the INS needs to determine its initial orientation without external information. Gyro-compassing is a technique used to determine the initial orientation of an IMU. Any error committed in finding the correct orientation is generally called *misalignment*. There are other techniques for finding the initial orientation and the interested reader can refer to Britting (1971), Savage (1978), Liu (1992), Scherzinger (1996), Titterton and Weston (1997).

Gyro-compassing is a technique applied when the IMU is stationary. The accuracy of this process depends on the sensor quality and duration of the time record of data used.

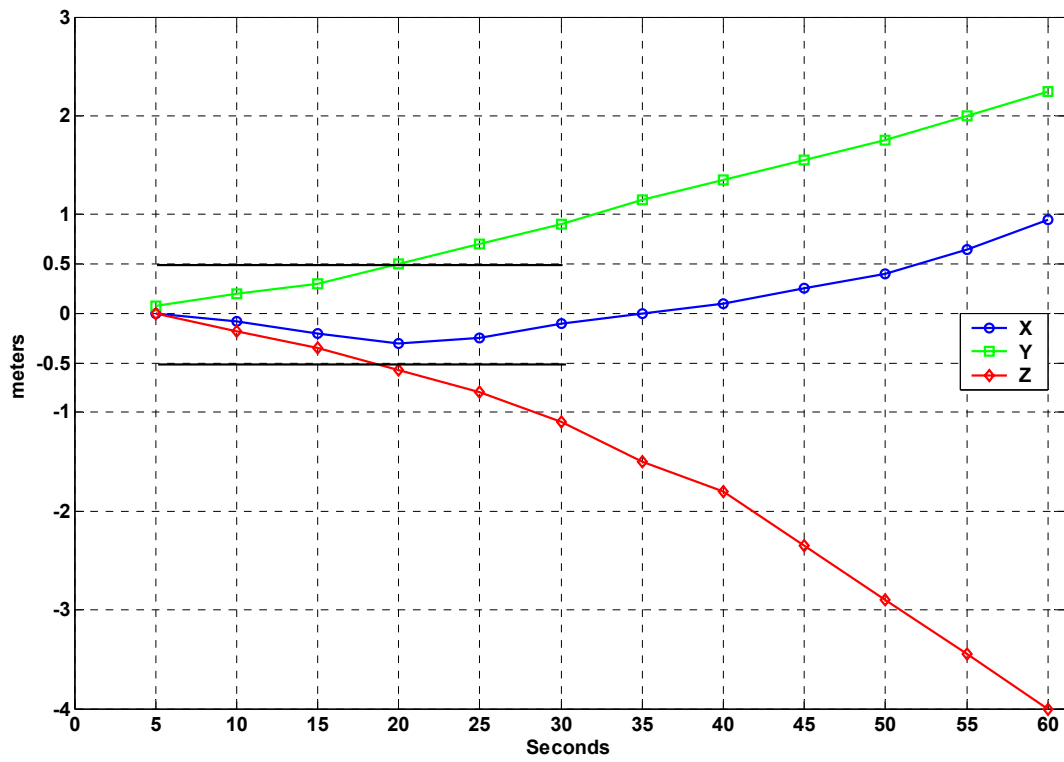


Figure 4-4: IMU positioning quality: second test

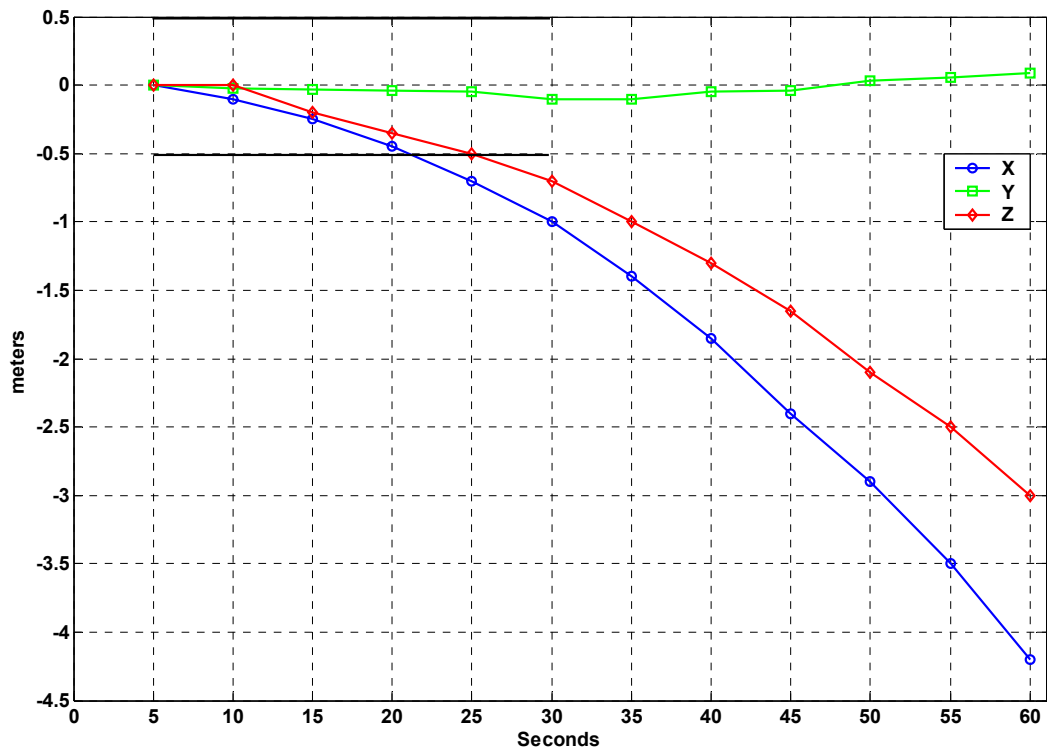


Figure 4-5: IMU positioning quality: third test

In an error free environment supposing the body frame of an IMU gets perfectly aligned with the local-level frame, i.e., the axes of the vertical sensors are perfectly aligned with the Earth's gravity and the y-axis is absolutely directed towards the geographic north (ENU configuration), the six sensors would sense the following input:

Gyroscopes:

$$\omega_x = 0 \qquad \omega_y = \omega_e \cos \phi \qquad \omega_z = \omega_e \sin \phi \qquad (4.44)$$

Accelerometers:

$$a_x = 0 \qquad a_y = 0 \qquad a_z = -g \qquad (4.45)$$

(It will be sufficient to know the latitude to within a degree, i.e., about 100 km.)

The deviation of the sensors from these values may have two reasons: one is that the IMU axes are not aligned as was described above, the second is that the sensor input is different from its expected output, i.e., errors in the measurements.

Considering the first reason, any misalignment from the geographic north with an angle A (Azimuth) is sensed by x and y gyroscopes and thus these sensors will measure:

$$\omega_x = \omega_e \cos \phi \cos A \qquad \omega_y = \omega_e \cos \phi \sin A \qquad (4.46)$$

Thus, the azimuth is computed by dividing the above two terms:

$$A = \arctan 2 \left(\frac{\omega_y}{\omega_x} \right) \qquad (4.47)$$

In addition to a misalignment from the geographic north, the IMU's vertical axis may not be perfectly aligned with the gravity vector and this causes the horizontal accelerometers to output:

$$a_x = g \sin \theta_x \qquad a_y = g \sin \theta_y \qquad (4.48)$$

Due to this, the x and y gyroscopes will measure part of the vertical component, rendering them imperfect in Azimuth determination; thus, a transformation from the body frame to a levelled frame is needed.

However, roll (θ_x) and pitch (θ_y) can be estimated from this signal as angles between the body and local-level frames,

$$\theta_x = \arcsin\left(\frac{a_x}{g}\right) \quad \theta_y = \arcsin\left(\frac{a_y}{g}\right) \quad (4.49)$$

To compute the azimuth from the outputs of the gyroscopes, one needs first to transform the measurements from the body frame to the frame that has a misalignment from the local-level frame with an angle equal to the Azimuth; the transformation is:

$$\begin{bmatrix} \omega'_x \\ \omega'_y \\ \omega'_z \end{bmatrix} = R_1(\theta_x) \cdot R_2(\theta_y) \cdot \begin{bmatrix} \omega_x \\ \omega_y \\ \omega_z \end{bmatrix} \quad (4.50)$$

From Equation (4.50), the azimuth is computed as:

$$A = \arctan 2\left(\frac{\omega'_y}{\omega'_x}\right) \quad (4.51)$$

The errors due to sensors imperfection do not change this procedure, but it introduces misalignments in the initial orientation. Finally, depending on the quality of the sensors, the gyro-compassing can be inadequate if the size of the sensor systematic error is bigger than the input (mainly that of the Earth rotation).

Whereas the LN-200 accelerometer errors can be considered stable during the period of gyro-compassing, the gyroscopes time-dependent errors are the limiting factor of the theoretically achievable accuracy.

The turn-on-turn-off bias of the LN200 accelerometer of $200 \mu\text{g}$ ($=200 \text{ mgals} = 0.002 \text{ m/s}^2$) will cause a roll/pitch error of 40 arcs. Thus, this will not affect the gyro-compassing significantly.

The dominant factors that limit the determination of the Azimuth by gyro-compassing are x-gyro drift, the latitude (i.e., amplitude of the Earth angular rate), gyro angular random walk, and the alignment time.

The accuracy of the azimuth is affected by the x-gyro drift and the latitude as follows:

$$\delta A = \frac{d_x}{\omega_e \cos \phi} \quad (4.52)$$

Hence, a LN 200 with the gyro drift is in the range of 1 deg/hr can achieve an accuracy of around 5 degrees at latitude of 45 degrees.

On the other hand, gyro angular random walk (GARW) and the alignment time t influence the azimuth computation according to:

$$\delta A = \frac{\text{GARW}}{\omega_e \cos \phi \sqrt{t}} \quad (4.53)$$

The LN 200 has a GARW of around $0.05 \text{ deg}/\sqrt{\text{hr}}$, accordingly an alignment time of 25 minutes will guarantee an accuracy of 0.4 degrees.

In two separate tests, the gyro-compassing results were better than the theoretical claim. In the first test, the azimuth determined after fine alignment (determined using professional software – Applanix Posproc®) was compared with the gyro-compassed azimuth, where the two values were within a few arcmin after a record of 25 minutes. During the second test (with different dataset), the engine of the vehicle were on and after the same time record of the first test the difference between the azimuths determined from gyro-compassing and fine alignment was significantly higher, at few degrees level.

5 - INTEGRATION METHODOLOGY AND SYSTEM CALIBRATION

... being a Scientist, I am trained to the commitment to solve challenging problems and to uncover innovative solutions ...

5.1 - Integration Methodology

Although SLAM can be solved by entirely photogrammetric means, practically this is difficult to achieve. The homogeneity of the texture in the scene and insufficient stereoscopic cover are just two examples that can break the principle of visual positioning. As it will be demonstrated in this chapter, integrating an IMU into the concept adds to the system and makes SLAM more achievable.

As described in Section 2.6, at the beginning, there is a need to initialise the system by defining its position and orientation with respect to a mathematical reference frame that can be linked with other systems because this is important when the SLAM is solved on a global scale. The initialisation is similar to that described in Chapter 2.

The need for an initialisation is essential for two main reasons:

- For the INS to function properly it must be provided with an initialisation in a defined reference system
- For the map to have a useful meaning, it must be able to be connected with other maps and databases.

For the different scenarios of initialisation, refer to Section 2.6.

The integration will be carried out on the system level where the positioning and orientation knowledge of one system will be passed on to the other and vice-versa. Figure (5-1) shows the SLAM methodology when incorporating the IMU.

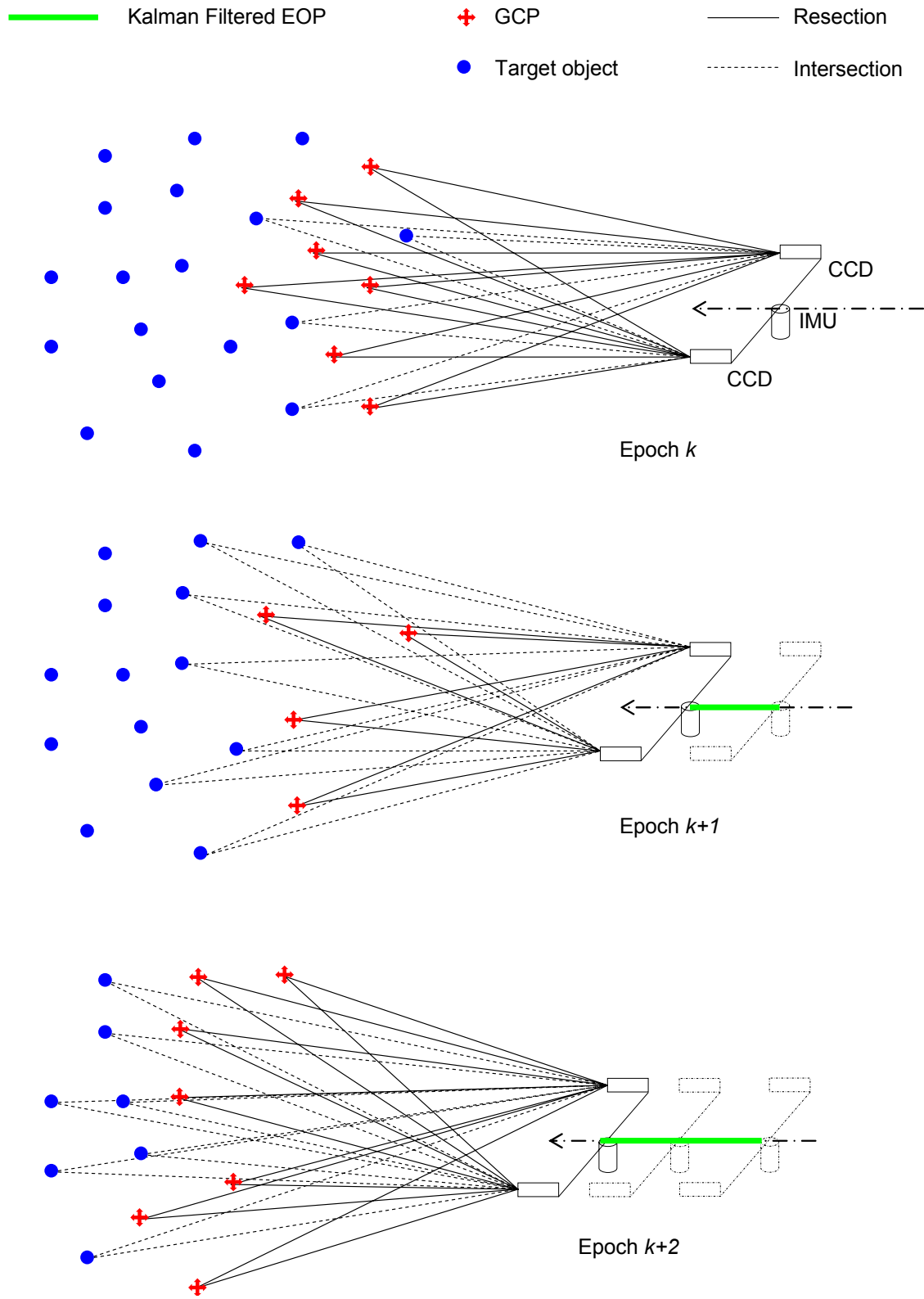


Figure 5-1: SLAM procedure integrating photogrammetry and INS

The algorithm can be depicted as follows:

Initial map:

- Position and attitude of the two cameras considered as known (from the initialisation)
- Intersection is employed to determine objects coordinates (i.e., to map)

After mapping enough objects:

- Vehicle moves and new stereo-pair of images is taken
- On these images, resection computes the cameras' EOP by LSA using the features determined from the previous cameras' location. (IMU predicted EOP could be used for feature extraction or in extreme cases to bridge EOP if there is not sufficient stereo-cover between successive images.)
- Leverarm and angles transformation (and boresight) are applied to the EOP to form external observations for the IMU
- The Kalman Filter is updated by the transformed EOP to compute filtered position and attitude of the current location
- Leverarm and attitude transformation (and boresight) are applied to the filtered position and attitude to determine the filtered EOP of the cameras
- Intersection is used to map more objects by LSA from the current location
- Algorithm repeats

The above methodology is pursued in this work. It differs from that of the classical mobile mapping systems in the fact that the map is used to determine the external measurements for the INS Kalman Filter. In addition, it differs from the conventional robotics SLAM in the new mapping method used and in the Kalman Filter utilised as well as in the rigorous modelling and transformations from one system to the other.

The flowchart is depicted in Figure (5-2)

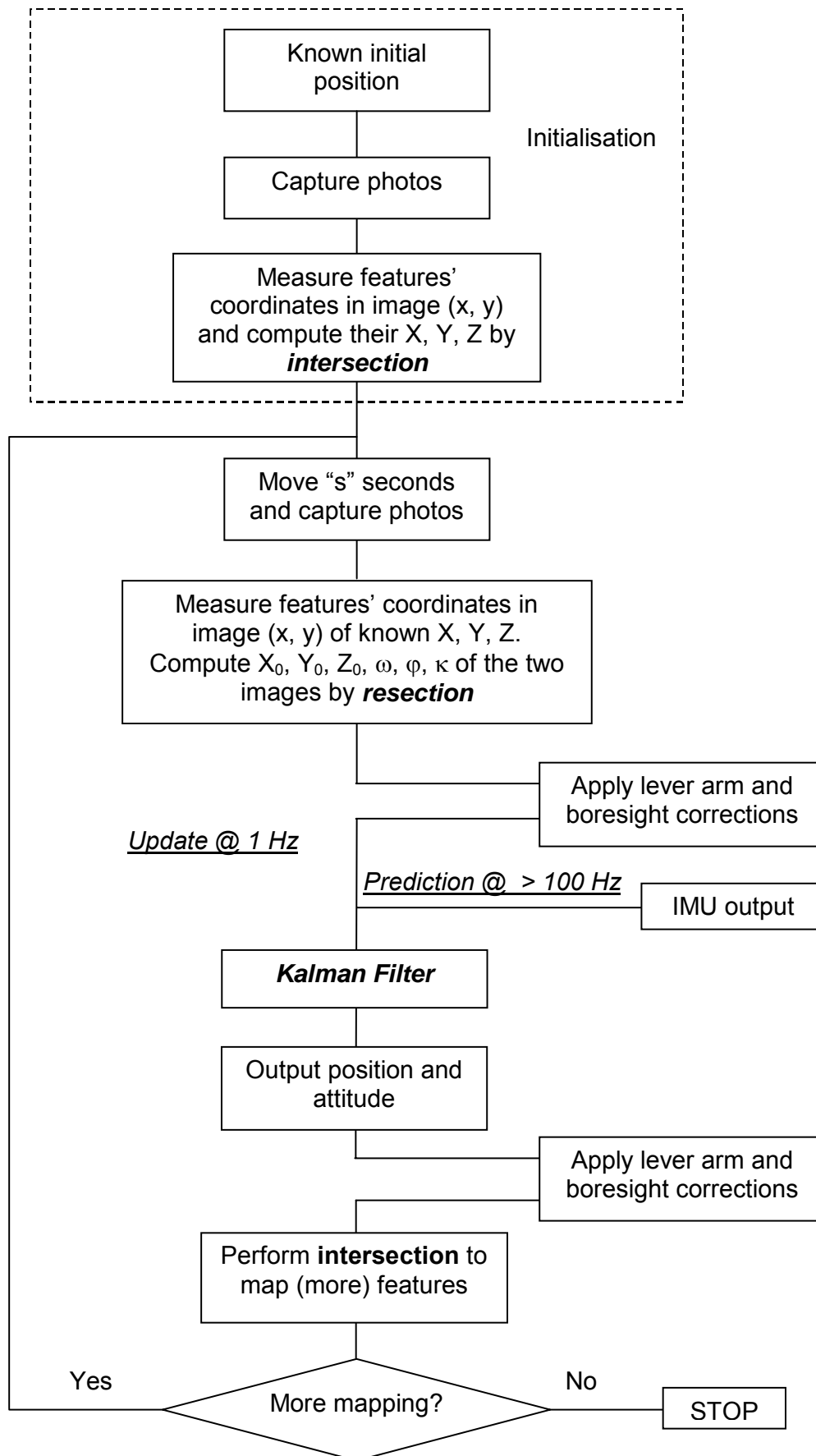


Figure 5-2: Flowchart of the Photogrammetric and INS integration

5.2 - Kalman Filter External Measurements

The external measurements for the Kalman Filter in navigation can be linked functionally with either the IMU outputs (orientation rates and accelerations) or with the final product (coordinates, velocity, orientation), or both.

In open spaces, GPS measurements play the role of external measurements (during the past two decades). In areas with limited GPS signal, these are augmented with other sensors, like odometer, compass, barometer, etc. (No discussion will be invested here on these measurements; the navigation and Geomatics literatures are abundant on this topic.)

The external measurements in this work are the photogrammetric resection outputs; these provide the Coordinates Update (CUPT) and Attitude Update (AUPT); in addition, Zero-Velocity Updates (ZUPT) will be used as measurements when the system is stationary.

Since there are two cameras, two sets of external measurements are available; one is the EOP of the left camera and the other is the EOP of the right camera. There are three possibilities to use them after applying the leverarm and the boresight parameters.

The first possibility is to take the average of the two EOP sets and to update the IMU with this result. The second is considering the two EOP sets as two independent non-correlated updates. The third is considering the two EOP sets as two correlated updates (not studied in this work). First, we will show the vectors and matrices used for the first possibility and then those used for the second possibility.

All the measurements are contained in $\mathbf{r}_k = \mathbf{z}_k - \mathbf{H}_k \mathbf{x}_k(-)$. Since the filter will be reset after every update, $\mathbf{x}_k(-)$ is forced to zero; in this way, $\mathbf{r}_k = \mathbf{z}_k$. The size and elements of \mathbf{r}_k can be defined with the help of Section 4.4 and the following discussion.

5.2.1 - The Average of the Two EOP Sets

When the average of the two EOP is considered, \mathbf{z}_k is:

$$\mathbf{z}_k = \left[\bar{X}_{0b} - x^e \quad \bar{Y}_{0b} - y^e \quad \bar{Z}_{0b} - z^e \quad 0 \quad 0 \quad 0 \quad \bar{\epsilon}_x - \epsilon_{x_{IMU}} \quad \bar{\epsilon}_y - \epsilon_{y_{IMU}} \quad \bar{\epsilon}_z - \epsilon_{z_{IMU}} \right]^T \quad (5.1)$$

where

$$\bar{X}_{0b} = \frac{X_{0LbL} + X_{0RbR}}{2} \quad \bar{Y}_{0b} = \frac{Y_{0LbL} + Y_{0RbR}}{2} \quad \bar{Z}_{0b} = \frac{Z_{0LbL} + Z_{0RbR}}{2}$$

where

$$\Delta X = \bar{X}_{0b} - x^e$$

$$\Delta Y = \bar{Y}_{0b} - y^e$$

$$\Delta Z = \bar{Z}_{0b} - z^e$$

$$\Delta \varepsilon_x = \bar{\varepsilon}_x - \varepsilon_{xIMU}$$

$$\Delta \varepsilon_y = \bar{\varepsilon}_y - \varepsilon_{yIMU}$$

$$\Delta \varepsilon_z = \bar{\varepsilon}_z - \varepsilon_{zIMU}$$

With CUPTs, AUPTs and ZUPTs, \mathbf{r}_k and \mathbf{H}_k take the forms:

$$\mathbf{r}_k = [\Delta X \quad \Delta Y \quad \Delta Z \quad \Delta V_x \quad \Delta V_y \quad \Delta V_z \quad \Delta \varepsilon_x \quad \Delta \varepsilon_y \quad \Delta \varepsilon_z]^T \quad (5.4)$$

$$\mathbf{H}_k \mathbf{x}_k(-) = \begin{bmatrix} 1 & 0 & 0 & 0 & 0 & 0 & 0 & 0 & 0 & 0 & 0 & 0 & 0 & 0 & 0 & 0 & 0 & 0 & 0 \\ 0 & 1 & 0 & 0 & 0 & 0 & 0 & 0 & 0 & 0 & 0 & 0 & 0 & 0 & 0 & 0 & 0 & 0 & 0 \\ 0 & 0 & 1 & 0 & 0 & 0 & 0 & 0 & 0 & 0 & 0 & 0 & 0 & 0 & 0 & 0 & 0 & 0 & 0 \\ 0 & 0 & 0 & 1 & 0 & 0 & 0 & 0 & 0 & 0 & 0 & 0 & 0 & 0 & 0 & 0 & 0 & 0 & 0 \\ 0 & 0 & 0 & 0 & 1 & 0 & 0 & 0 & 0 & 0 & 0 & 0 & 0 & 0 & 0 & 0 & 0 & 0 & 0 \\ 0 & 0 & 0 & 0 & 0 & 1 & 0 & 0 & 0 & 0 & 0 & 0 & 0 & 0 & 0 & 0 & 0 & 0 & 0 \\ 0 & 0 & 0 & 0 & 0 & 0 & 1 & 0 & 0 & 0 & 0 & 0 & 0 & 0 & 0 & 0 & 0 & 0 & 0 \\ 0 & 0 & 0 & 0 & 0 & 0 & 0 & 1 & 0 & 0 & 0 & 0 & 0 & 0 & 0 & 0 & 0 & 0 & 0 \\ 0 & 0 & 0 & 0 & 0 & 0 & 0 & 0 & 1 & 0 & 0 & 0 & 0 & 0 & 0 & 0 & 0 & 0 & 0 \end{bmatrix} \begin{bmatrix} \delta x \\ \delta y \\ \delta z \\ \delta v_x \\ \delta v_y \\ \delta v_z \\ \delta \varepsilon_x \\ \delta \varepsilon_y \\ \delta \varepsilon_z \\ \delta g_x \\ \delta g_y \\ \delta g_z \\ \delta b_x \\ \delta b_y \\ \delta b_z \end{bmatrix} \quad (5.5)$$

with

$$\Delta V_x = -v_x^e$$

$$\Delta V_y = -v_y^e$$

$$\Delta V_z = -v_z^e$$

where $\mathbf{v}^e = (v_x^e, v_y^e, v_z^e)$ are computed from Equation (4.10)

The gain matrix \mathbf{K}_k here has the dimensions: 15×9 .

5.2.2 - The Two EOP Sets as Two Independent Updates

The correlation between the two EOP is reflected by non-zero terms outside the main diagonal of the covariance matrices. When the two EOP are taken as two independent updates, \mathbf{z}_k is:

$$\mathbf{z}_k = \begin{bmatrix} X_{0Lb_L} - x^e & Y_{0Lb_L} - y^e & Z_{0Lb_L} - z^e & \varepsilon_{x_L} - \varepsilon_{x_{IMU}} & \varepsilon_{y_L} - \varepsilon_{y_{IMU}} & \varepsilon_{z_L} - \varepsilon_{z_{IMU}} \\ X_{0Rb_R} - x^e & Y_{0Rb_R} - y^e & Z_{0Rb_R} - z^e & \varepsilon_{x_R} - \varepsilon_{x_{IMU}} & \varepsilon_{y_R} - \varepsilon_{y_{IMU}} & \varepsilon_{z_R} - \varepsilon_{z_{IMU}} \\ 0 & 0 & 0 \end{bmatrix}^T \quad (5.6)$$

The zeros indicate that no velocity measurements were considered, and their function here is similar to one explained in the previous Section.

Considering only CUPTs and AUPTs, \mathbf{r}_k and \mathbf{H}_k take the forms:

$$\mathbf{r}_k = \begin{bmatrix} \Delta X_L & \Delta Y_L & \Delta Z_L & \Delta \varepsilon_{x_L} & \Delta \varepsilon_{y_L} & \Delta \varepsilon_{z_L} & \Delta X_R & \Delta Y_R & \Delta Z_R \\ \Delta \varepsilon_{x_R} & \Delta \varepsilon_{y_R} & \Delta \varepsilon_{z_R} & 0 & 0 & 0 \end{bmatrix}^T \quad (5.7)$$

$$\mathbf{H}_k \mathbf{x}_k(-) = \begin{bmatrix} \mathbf{1} & 0 & 0 & 0 & 0 & 0 & 0 & 0 & 0 & 0 & 0 & 0 & 0 & 0 & 0 \\ 0 & \mathbf{1} & 0 & 0 & 0 & 0 & 0 & 0 & 0 & 0 & 0 & 0 & 0 & 0 & 0 \\ 0 & 0 & \mathbf{1} & 0 & 0 & 0 & 0 & 0 & 0 & 0 & 0 & 0 & 0 & 0 & 0 \\ 0 & 0 & 0 & 0 & 0 & 0 & \mathbf{1} & 0 & 0 & 0 & 0 & 0 & 0 & 0 & 0 \\ 0 & 0 & 0 & 0 & 0 & 0 & 0 & \mathbf{1} & 0 & 0 & 0 & 0 & 0 & 0 & 0 \\ 0 & 0 & 0 & 0 & 0 & 0 & 0 & 0 & \mathbf{1} & 0 & 0 & 0 & 0 & 0 & 0 \\ \mathbf{1} & 0 & 0 & 0 & 0 & 0 & 0 & 0 & 0 & 0 & 0 & 0 & 0 & 0 & 0 \\ 0 & \mathbf{1} & 0 & 0 & 0 & 0 & 0 & 0 & 0 & 0 & 0 & 0 & 0 & 0 & 0 \\ 0 & 0 & \mathbf{1} & 0 & 0 & 0 & 0 & 0 & 0 & 0 & 0 & 0 & 0 & 0 & 0 \\ 0 & 0 & 0 & 0 & 0 & 0 & \mathbf{1} & 0 & 0 & 0 & 0 & 0 & 0 & 0 & 0 \\ 0 & 0 & 0 & 0 & 0 & 0 & 0 & \mathbf{1} & 0 & 0 & 0 & 0 & 0 & 0 & 0 \\ 0 & 0 & 0 & 0 & 0 & 0 & 0 & 0 & \mathbf{1} & 0 & 0 & 0 & 0 & 0 & 0 \\ 0 & 0 & 0 & 0 & 0 & 0 & 0 & 0 & 0 & \mathbf{1} & 0 & 0 & 0 & 0 & 0 \\ 0 & 0 & 0 & 0 & 0 & 0 & 0 & 0 & 0 & 0 & \mathbf{1} & 0 & 0 & 0 & 0 \\ 0 & 0 & 0 & 0 & 0 & 0 & 0 & 0 & 0 & 0 & 0 & \mathbf{1} & 0 & 0 & 0 \\ 0 & 0 & 0 & 0 & 0 & 0 & 0 & 0 & 0 & 0 & 0 & 0 & \mathbf{1} & 0 & 0 \\ 0 & 0 & 0 & 0 & 0 & 0 & 0 & 0 & 0 & 0 & 0 & 0 & 0 & \mathbf{1} & 0 \\ 0 & 0 & 0 & 0 & 0 & 0 & 0 & 0 & 0 & 0 & 0 & 0 & 0 & 0 & \mathbf{1} \end{bmatrix} \begin{bmatrix} \delta x \\ \delta y \\ \delta z \\ \delta v_x \\ \delta v_y \\ \delta v_z \\ \delta \varepsilon_x \\ \delta \varepsilon_y \\ \delta \varepsilon_z \\ \delta g_x \\ \delta g_y \\ \delta g_z \\ \delta b_x \\ \delta b_y \\ \delta b_z \end{bmatrix} \quad (5.8)$$

where

$$\Delta X_L = X_{0Lb_L} - x^e$$

$$\Delta Y_L = Y_{0Lb_L} - y^e$$

$$\Delta Z_L = Z_{0Lb_L} - z^e$$

$$\begin{aligned}\Delta X_R &= X_{0RbR} - x^e & \Delta Y_R &= Y_{0RbR} - y^e & \Delta Z_R &= Z_{0RbR} - z^e \\ \Delta \varepsilon_{x_L} &= \varepsilon_{x_L} - \varepsilon_{x_{IMU}} & \Delta \varepsilon_{y_L} &= \varepsilon_{y_L} - \varepsilon_{y_{IMU}} & \Delta \varepsilon_{z_L} &= \varepsilon_{z_L} - \varepsilon_{z_{IMU}} \\ \Delta \varepsilon_{x_R} &= \varepsilon_{x_R} - \varepsilon_{x_{IMU}} & \Delta \varepsilon_{y_R} &= \varepsilon_{y_R} - \varepsilon_{y_{IMU}} & \Delta \varepsilon_{z_R} &= \varepsilon_{z_R} - \varepsilon_{z_{IMU}}\end{aligned}$$

In addition, with ZUPTs, \mathbf{r}_k and \mathbf{H}_k take the forms:

$$\mathbf{r}_k = \begin{bmatrix} \Delta X_L & \Delta Y_L & \Delta Z_L & \Delta \varepsilon_{x_L} & \Delta \varepsilon_{y_L} & \Delta \varepsilon_{z_L} & \Delta X_R & \Delta Y_R & \Delta Z_R \\ \Delta \varepsilon_{x_R} & \Delta \varepsilon_{y_R} & \Delta \varepsilon_{z_R} & \Delta V_x & \Delta V_y & \Delta V_z \end{bmatrix}^T \quad (5.9)$$

$$\mathbf{H}_k \mathbf{x}_k(-) = \begin{bmatrix} \mathbf{1} & 0 & 0 & 0 & 0 & 0 & 0 & 0 & 0 & 0 & 0 & 0 & 0 & 0 & 0 \\ 0 & \mathbf{1} & 0 & 0 & 0 & 0 & 0 & 0 & 0 & 0 & 0 & 0 & 0 & 0 & 0 \\ 0 & 0 & \mathbf{1} & 0 & 0 & 0 & 0 & 0 & 0 & 0 & 0 & 0 & 0 & 0 & 0 \\ 0 & 0 & 0 & 0 & 0 & 0 & \mathbf{1} & 0 & 0 & 0 & 0 & 0 & 0 & 0 & 0 \\ 0 & 0 & 0 & 0 & 0 & 0 & 0 & \mathbf{1} & 0 & 0 & 0 & 0 & 0 & 0 & 0 \\ 0 & 0 & 0 & 0 & 0 & 0 & 0 & 0 & \mathbf{1} & 0 & 0 & 0 & 0 & 0 & 0 \\ \mathbf{1} & 0 & 0 & 0 & 0 & 0 & 0 & 0 & 0 & 0 & 0 & 0 & 0 & 0 & 0 \\ 0 & \mathbf{1} & 0 & 0 & 0 & 0 & 0 & 0 & 0 & 0 & 0 & 0 & 0 & 0 & 0 \\ 0 & 0 & \mathbf{1} & 0 & 0 & 0 & 0 & 0 & 0 & 0 & 0 & 0 & 0 & 0 & 0 \\ 0 & 0 & 0 & 0 & 0 & 0 & \mathbf{1} & 0 & 0 & 0 & 0 & 0 & 0 & 0 & 0 \\ 0 & 0 & 0 & 0 & 0 & 0 & 0 & \mathbf{1} & 0 & 0 & 0 & 0 & 0 & 0 & 0 \\ 0 & 0 & 0 & 0 & 0 & 0 & 0 & 0 & \mathbf{1} & 0 & 0 & 0 & 0 & 0 & 0 \\ 0 & 0 & 0 & \mathbf{1} & 0 & 0 & 0 & 0 & 0 & 0 & 0 & 0 & 0 & 0 & 0 \\ 0 & 0 & 0 & 0 & \mathbf{1} & 0 & 0 & 0 & 0 & 0 & 0 & 0 & 0 & 0 & 0 \\ 0 & 0 & 0 & 0 & 0 & \mathbf{1} & 0 & 0 & 0 & 0 & 0 & 0 & 0 & 0 & 0 \end{bmatrix} \begin{bmatrix} \delta x \\ \delta y \\ \delta z \\ \delta v_x \\ \delta v_y \\ \delta v_z \\ \delta \varepsilon_x \\ \delta \varepsilon_y \\ \delta \varepsilon_z \\ \delta g_x \\ \delta g_y \\ \delta g_z \\ \delta b_x \\ \delta b_y \\ \delta b_z \end{bmatrix} \quad (5.10)$$

The gain matrix \mathbf{K}_k here has the dimensions: 15×15 .

5.3 - System Calibration

So far, no details were given on the compatibility of the IMU and camera reference systems. An IMU and thus the Kalman filter (in this work) functions in the Earth-Fixed reference system and photogrammetry functions in an arbitrary mapping reference system; thus, a way to link these two systems is needed for data fusion in the KF. For the simplicity, we will further consider that the mapping system is some arbitrary Cartesian coordinate system whose rotation and translation with respect to the Earth-Fixed reference system are known.

Although generally there is a difference in the definition between a **reference system** and a **reference frame**, this distinction will not be imposed here. So, the term **frame** will be used for both.

Among the inputs to Kalman Filter are the coordinates in the Earth-fixed frame and the orientation angles between the body and Earth-fixed frames; these have to be provided by the IMU and cameras' outputs. Whereas the mechanisation equations provide this information, the external measurements are in a different frame; the coordinates are in the mapping frame and the orientation angles are between the mapping and the camera frames.

At the same time, the outputs of the KF are the coordinates in the Earth-fixed frame and the orientation angles between the body and Earth-fixed frames. However, to perform the intersection, we need the coordinates in the mapping frame and the orientation angles between the mapping and the camera frames.

To transform coordinates and angles from the cameras to the IMU or vice-versa, the spatial offset called **leverarm** and angular offset called **Boresight** need to be considered.

In what follows, the transformation processes between the different frames are discussed first and then the calibration procedures to attain the **leverarm** and **Boresight** are shown.

5.4 - Angle Transformation

Resection provides attitude angles between the cameras and the mapping frame (Chapter 2). The rotation matrix will be denoted as: \mathbf{R}_m^c .

IMU mechanisation equation in the Earth-Fixed frame provides attitude angles between the IMU body and the Earth-Fixed frames. The rotation matrix will be denoted as: \mathbf{R}_b^e .

The camera frame is depicted in Figure (5-3). The z_c -axis passes through the optical axis. The x_c -axis is directed to the right-hand side. The y_c -axis completes the right-handed system. The Earth-Fixed frame is the conventional Earth-Centred-Earth-Fixed (ECEF) frame (Figure 5-4).

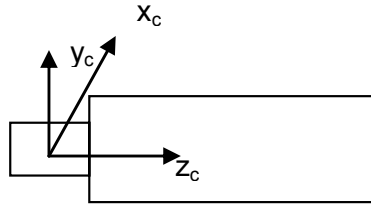


Figure 5-3: Camera body frame

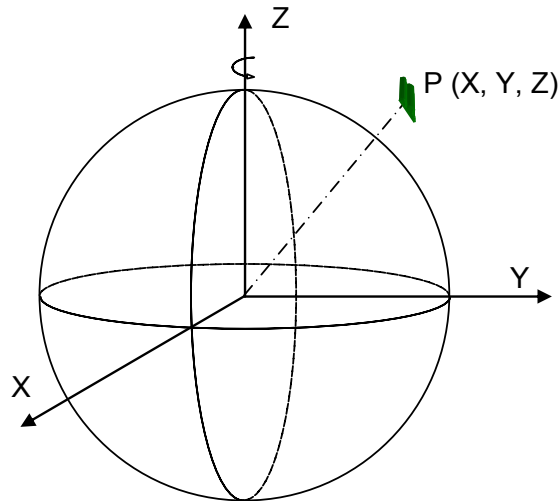


Figure 5-4: Earth-Centred-Earth-Fixed (ECEF) frame

In direct georeferencing, one goes from \mathbf{R}_b^e to \mathbf{R}_m^c . This means that the Kalman filtered outputs are transformed to \mathbf{R}_m^c so intersection can be performed. Here we will need also the inverse transformation from \mathbf{R}_m^c to \mathbf{R}_b^e to use as external attitude measurements in the KF.

5.4.1 - From Resection to IMU

The transformation from \mathbf{R}_m^c and \mathbf{R}_b^e is used to transform the orientation computed from resection to an orientation compatible with the Earth-Fixed frame to use it in the KF as external measurements:

$$\mathbf{R}_b^e = \mathbf{R}_m^e \cdot (\mathbf{R}_m^c)^T \cdot \mathbf{R}_b^c \quad (5.11)$$

where

\mathbf{R}_m^c is the transformation matrix between mapping and camera frames

\mathbf{R}_b^c is the orientation offset due to mounting, i.e., the transformation matrix between IMU and camera frames (depends on the definition of the axes). Later this will be decomposed into \mathbf{T}_b^c and $\mathbf{R}_b^{b^*}$, where \mathbf{T}_b^c is the mounting matrix and $\mathbf{R}_b^{b^*}$ is the boresight.

\mathbf{R}_b^e is the transformation matrix between IMU body and Earth-Fixed frames (KF output)

\mathbf{R}_m^e is the transformation matrix between Earth-Fixed and mapping frames.

5.4.2 - From IMU to Intersection

The transformation from \mathbf{R}_b^e and \mathbf{R}_m^c is used to transform the output of the KF to the camera reference frame to perform the mapping. This is well documented in the relevant literature (Skaloud, 1999; Skaloud and Schaer, 2003). The transformation is:

$$\mathbf{R}_m^c = \mathbf{R}_b^c \cdot (\mathbf{R}_b^e)^T \cdot \mathbf{R}_m^e \quad (5.12)$$

5.4.3 - Rotation between the Mapping and Earth-Fixed Frames

The mapping frame used this work is the right-handed East, North and Up (ENU) tangential plane (Figure 5-5). The transformation between the mapping and ECEF frame is computed as:

$$\mathbf{R}_m^e = \begin{bmatrix} -\sin \lambda_m & -\sin \phi_m \cos \lambda_m & \cos \phi_m \cos \lambda_m \\ \cos \lambda_m & -\sin \phi_m \sin \lambda_m & \cos \phi_m \sin \lambda_m \\ 0 & \cos \phi_m & \sin \phi_m \end{bmatrix} \quad (5.13)$$

(ϕ_m, λ_m) define the latitude and longitude of the origin of the mapping system.

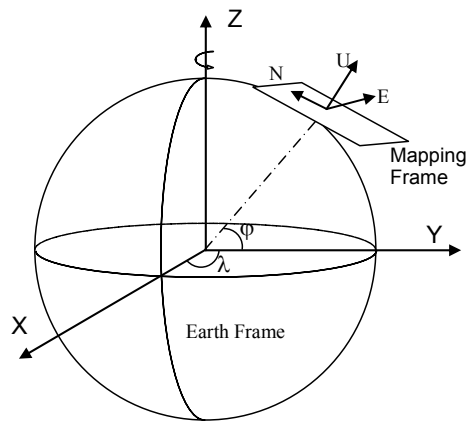


Figure 5-5: Relationship between ECEF and Mapping frames

5.4.4 - Mounting Rotation

The mounting of the camera and IMU defines the matrix \mathbf{T}_b^c . For example, in Figure (5-3) the orientation of the camera frame is shown, and Figure (5-6) demonstrates the orientation of the IMU body frame. The cameras and the IMU are mounted on the vehicle as shown in Figure (5-7).

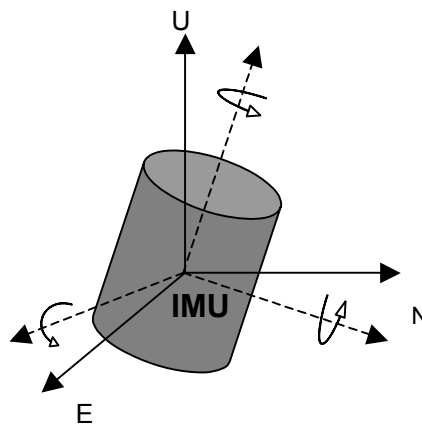


Figure 5-6: Body frame defined by the IMU

So, \mathbf{T}_b^c is:

$$\mathbf{T}_b^c = \mathbf{R}_x\left(\frac{\pi}{2}\right) \cdot \mathbf{R}_z\left(\frac{\pi}{2}\right) = \begin{bmatrix} 0 & 1 & 0 \\ 0 & 0 & 1 \\ 1 & 0 & 0 \end{bmatrix} \quad (5.14)$$

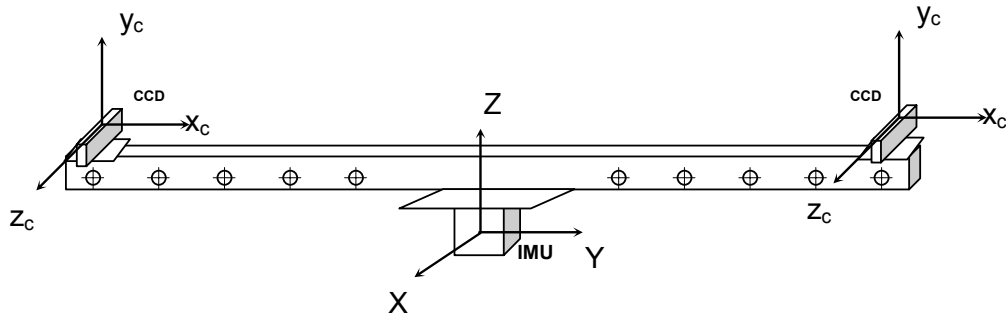
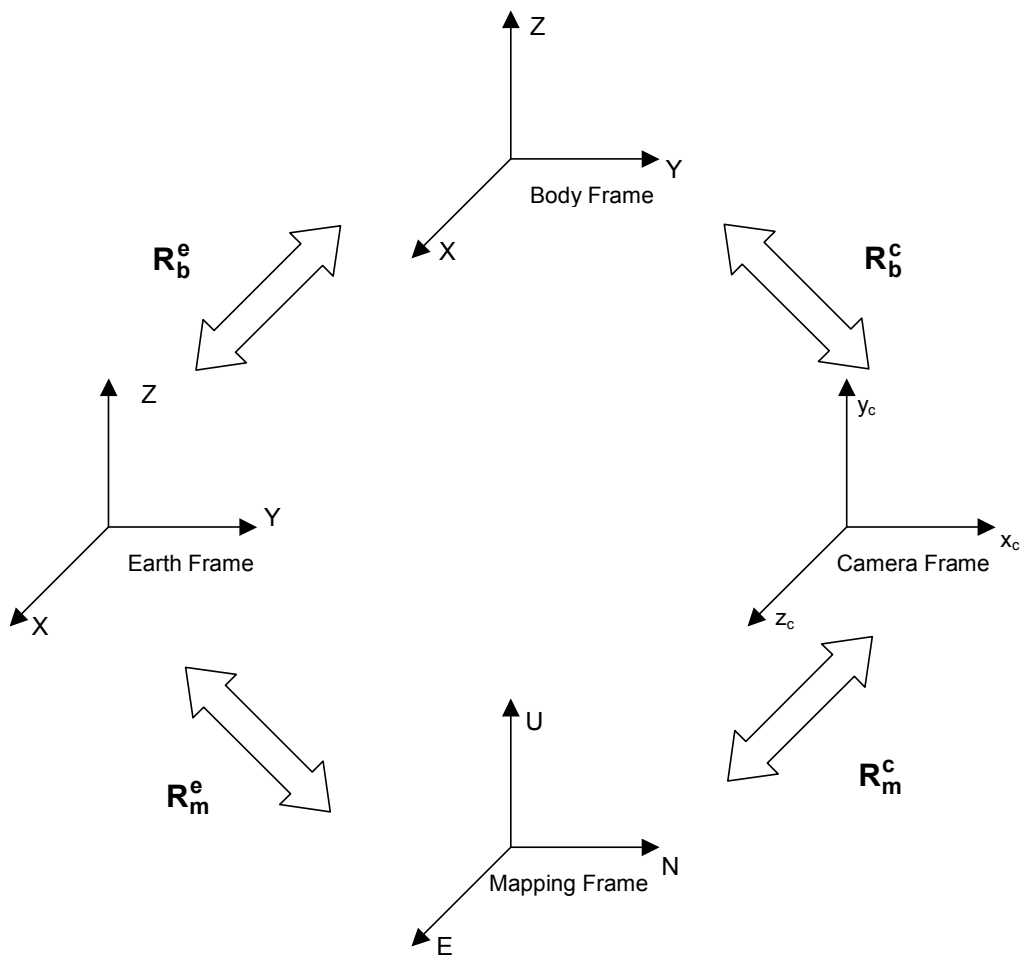


Figure 5-7: Mounting of the cameras and IMU

Finally, Figure (5-8) summarises the relation between the different reference frames.



$$R_m^c = R_b^c (R_b^e)^T R_m^e$$

$$R_b^e = R_m^e (R_m^c)^T R_b^c$$

Figure 5-8: The different frames

5.5 - Boresight Estimation

The IMU and each camera have two offsets; one is a boresight, and the other is the leverarm. This is illustrated in Figure (5-9).

The matrix \mathbf{T}_b^c aligns the axes between the IMU body and the camera just approximately (within few degrees). The additional rotation $\mathbf{R}_b^{b^*}$ is called boresight and it corrects for the mounting misalignment. Thus the \mathbf{T}_b^c computed from Equation (5.14) does not contribute for the misalignment; that is, it does not transform the body to the camera frame, but rather transforms another body frame “ b^* ” that differs from the true body frame “ b ” by a rotation matrix $\mathbf{R}_b^{b^*}$:

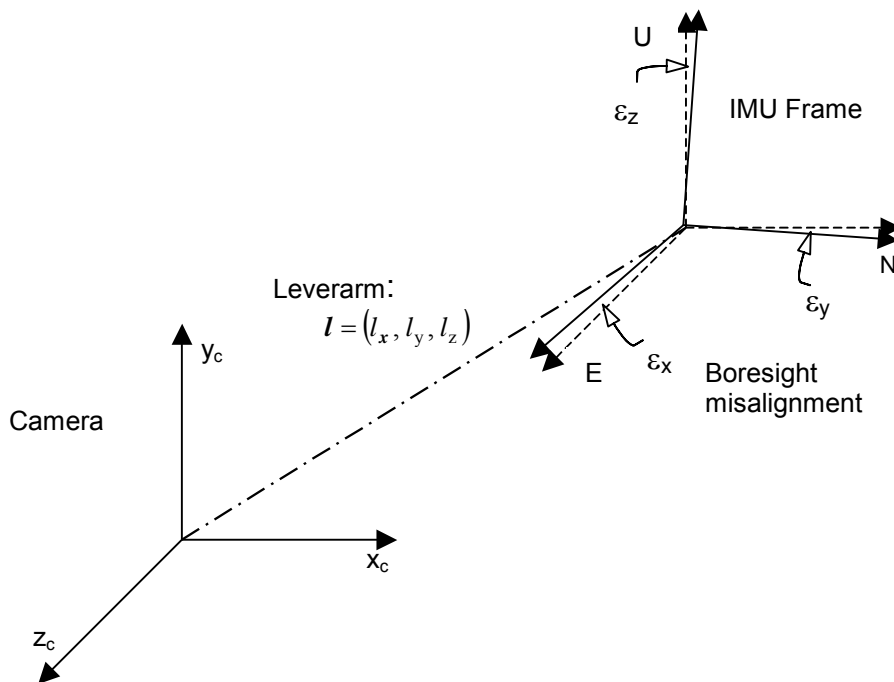


Figure 5-9: Boresight and Leverarm

$$\mathbf{R}_b^{b^*} = \begin{bmatrix} 1 & \epsilon_z & -\epsilon_y \\ -\epsilon_z & 1 & \epsilon_x \\ \epsilon_y & -\epsilon_x & 1 \end{bmatrix} \quad (6.5)$$

where ϵ_i is the misalignment angle along the i -axis. Thus, the correct transformation between the IMU body and camera frame is:

$$\mathbf{R}_b^c = \mathbf{T}_{b^*}^c \cdot \mathbf{R}_b^{b^*} \quad (5.16)$$

While $\mathbf{T}_{b^*}^c$ is the matrix computed from Equation (5.14), matrix $\mathbf{R}_b^{b^*}$ is to be determined.

Therefore, Equations (5.11) and (5.12), respectively, take the form:

$$\mathbf{R}_m^c = \mathbf{T}_{b^*}^c \cdot \mathbf{R}_b^{b^*} \cdot (\mathbf{R}_b^e)^T \cdot \mathbf{R}_m^e \quad (5.17)$$

$$\mathbf{R}_b^e = \mathbf{R}_m^e \cdot (\mathbf{R}_m^c)^T \cdot \mathbf{T}_{b^*}^c \cdot \mathbf{R}_b^{b^*} \quad (5.18)$$

Matrix of Equation (5.15) can be considered constant throughout the survey and is computed with Equation (5.18). The following paragraphs follow the discussion in Bäumker et al. (2001).

The determination of the misalignments can be performed with a specific *on-the-job-calibration* procedure. In this procedure, the complete system with the camera(s) and INS is put in a test flight over a test area with well-surveyed control points. Then, in a bundle adjustment for each photo the angles phi, omega and kappa are determined. These angles are used to estimate the misalignments. The estimation of the misalignments is performed in an adjustment for which the following data of each image are used:

- Inertially derived angles: roll, pitch and yaw (\mathbf{R}_b^e)
- Photogrammetric angles determined by resection: phi, omega and kappa (\mathbf{R}_m^c)
- Rotations between the mapping and ECEF frame (\mathbf{R}_m^e)
- $\mathbf{T}_{b^*}^c$ is a known constant

To formulate the model for adjustment, Equation (5.18) needs to be modified as follows:

$$\mathbf{R}_b^e = \mathbf{R}_m^e \cdot (\mathbf{R}_m^c)^T \cdot \mathbf{T}_{b^*}^c \cdot \mathbf{R}_b^{b^*}$$

$$\mathbf{B} = \mathbf{D} \mathbf{R}_b^{b^*} \quad (5.19)$$

Equation (5.19) can be written as:

$$\begin{bmatrix} \mathbf{b}_{11} & \mathbf{b}_{12} & \mathbf{b}_{13} \\ \mathbf{b}_{21} & \mathbf{b}_{22} & \mathbf{b}_{23} \\ \mathbf{b}_{31} & \mathbf{b}_{32} & \mathbf{b}_{33} \end{bmatrix} = \begin{bmatrix} \mathbf{d}_{11} & \mathbf{d}_{12} & \mathbf{d}_{13} \\ \mathbf{d}_{21} & \mathbf{d}_{22} & \mathbf{d}_{23} \\ \mathbf{d}_{31} & \mathbf{d}_{32} & \mathbf{d}_{33} \end{bmatrix} \cdot \begin{bmatrix} 1 & -\varepsilon_z & \varepsilon_y \\ \varepsilon_z & 1 & -\varepsilon_x \\ -\varepsilon_y & \varepsilon_x & 1 \end{bmatrix}$$

Thus, for each image, the following set of observation equations is solved:

$$\mathbf{b}_{11} = \mathbf{d}_{11} + \mathbf{d}_{12}\varepsilon_z - \mathbf{d}_{13}\varepsilon_y \quad \mathbf{b}_{12} = -\mathbf{d}_{11}\varepsilon_z + \mathbf{d}_{12} + \mathbf{d}_{13}\varepsilon_x \quad \mathbf{b}_{13} = \mathbf{d}_{11}\varepsilon_y - \mathbf{d}_{12}\varepsilon_x + \mathbf{d}_{13}$$

$$\mathbf{b}_{21} = \mathbf{d}_{21} + \mathbf{d}_{22}\varepsilon_z - \mathbf{d}_{23}\varepsilon_y \quad \mathbf{b}_{22} = -\mathbf{d}_{21}\varepsilon_z + \mathbf{d}_{22} + \mathbf{d}_{23}\varepsilon_x \quad \mathbf{b}_{23} = \mathbf{d}_{21}\varepsilon_y - \mathbf{d}_{22}\varepsilon_x + \mathbf{d}_{23}$$

$$\mathbf{b}_{31} = \mathbf{d}_{31} + \mathbf{d}_{32}\varepsilon_z - \mathbf{d}_{33}\varepsilon_y \quad \mathbf{b}_{32} = -\mathbf{d}_{31}\varepsilon_z + \mathbf{d}_{32} + \mathbf{d}_{33}\varepsilon_x \quad \mathbf{b}_{33} = \mathbf{d}_{31}\varepsilon_y - \mathbf{d}_{32}\varepsilon_x + \mathbf{d}_{33}$$

Considering the approximate values of $\begin{pmatrix} \varepsilon_x & \varepsilon_y & \varepsilon_z \end{pmatrix}$ to be zeros:

$$\mathbf{x} = [\varepsilon_x \quad \varepsilon_y \quad \varepsilon_z]^T = \left(\sum_{i=1}^n (\mathbf{A}_i^T \mathbf{A}_i) \right)^{-1} \left(\sum_{i=1}^n (\mathbf{A}_i^T \mathbf{b}_i) \right)$$

where n is the number of photographs used for the calibration, and

$$\mathbf{b}_i = \begin{bmatrix} \mathbf{b}_{11} - \mathbf{d}_{11} \\ \mathbf{b}_{12} - \mathbf{d}_{12} \\ \mathbf{b}_{13} - \mathbf{d}_{13} \\ \mathbf{b}_{21} - \mathbf{d}_{21} \\ \mathbf{b}_{22} - \mathbf{d}_{22} \\ \mathbf{b}_{23} - \mathbf{d}_{23} \\ \mathbf{b}_{31} - \mathbf{d}_{31} \\ \mathbf{b}_{32} - \mathbf{d}_{32} \\ \mathbf{b}_{33} - \mathbf{d}_{33} \end{bmatrix} \quad \mathbf{A}_i = \begin{bmatrix} 0 & -\mathbf{d}_{13} & \mathbf{d}_{12} \\ \mathbf{d}_{13} & 0 & -\mathbf{d}_{11} \\ -\mathbf{d}_{12} & \mathbf{d}_{11} & 0 \\ 0 & -\mathbf{d}_{23} & \mathbf{d}_{22} \\ \mathbf{d}_{23} & 0 & -\mathbf{d}_{21} \\ \mathbf{d}_{22} & \mathbf{d}_{21} & 0 \\ 0 & -\mathbf{d}_{33} & \mathbf{d}_{32} \\ \mathbf{d}_{33} & 0 & -\mathbf{d}_{31} \\ -\mathbf{d}_{32} & \mathbf{d}_{31} & 0 \end{bmatrix}$$

This procedure is done for each camera separately.

5.6 - Leverarm Estimation

The leverarm, $\mathbf{l} = (l_x, l_y, l_z)$, is considered constant and computed once as in the case of the boresight.

To determine this spatial offset, the coordinates of the IMU and cameras have to refer to identical unchangeable frame. The camera frame is a fixed frame, where its axes are always directed as explained in Section 5.4, no matter how the camera is oriented.

To compute the coordinates of the camera and IMU in the same frame, we follow a similar approach as in the previous Section.

The camera coordinates are computed in the mapping frame by resection, along with the orientation angles – EOP. These coordinates are transformed to the camera frame by \mathbf{R}_m^c that is computed from the orientation angles. So,

$$\mathbf{X}_{\text{cam}}^c = \mathbf{R}_m^c \mathbf{X}_{\text{cam}}^m \quad (5.20)$$

where

$\mathbf{X}_{\text{cam}}^c$ are the coordinates of the camera in the camera frame

$\mathbf{X}_{\text{cam}}^m$ are the coordinates of the camera in the mapping frame

Note that there are two cameras: a *Left* and *Right*. Their indices will be introduced later.

The IMU coordinates are computed in the Earth-Fixed frame by employing the mechanisation equations (with the aid of the GPS in a KF).

$$\mathbf{X}_{\text{IMU}}^m = \mathbf{R}_e^m \mathbf{X}_{\text{IMU}}^e \quad (5.21)$$

where

$\mathbf{X}_{\text{IMU}}^m$ are the coordinates of the IMU in the mapping frame

$\mathbf{X}_{\text{IMU}}^e$ are the coordinates of the IMU in the Earth-Fixed frame

To move from the mapping frame to the camera frame, we use again the \mathbf{R}_m^c matrix; thus,

$$\mathbf{X}_{\text{IMU}}^c = \mathbf{R}_m^c \mathbf{X}_{\text{IMU}}^m \quad (5.22)$$

where

$\mathbf{X}_{\text{IMU}}^c$ are the coordinates of the IMU in the camera frame.

Hence, the leverarm is computed by subtracting Equations (5.20) and (5.22):

$$I = \begin{bmatrix} I_x \\ I_y \\ I_z \end{bmatrix} = \mathbf{X}_{\text{cam}}^c - \mathbf{X}_{\text{IMU}}^c \quad (5.23)$$

After determining the leverarm for both cameras, L and R, they apply as follows.

5.6.1 - Leverarm application from Resection to IMU

Resection gives the coordinates of the cameras in the mapping frame. To these the leverarm is added, after transforming it from the camera frame to the mapping frame, to determine the coordinates of the IMU in the mapping frame. After computing the IMU position in the mapping frame, the next step will be transforming it to the Earth-Fixed frame. Having the coordinates of the IMU, computed from resection, in the Earth-Fixed frame, they are added to KF to determine the filtered position of the IMU.

In terms of vectors and matrices, it is done as follows ($j = L, R$).

Step one:

$$I_j^m = \mathbf{R}_{c/j}^m \cdot I_j^c \quad (5.24)$$

where

I_j^c is the leverarm in the camera frame,

I_j^m is the leverarm in the mapping frame,

$\mathbf{R}_{c/j}^m$ is the transformation matrix between the camera and mapping frame for camera j .

Step two:

$$\mathbf{X}_{\text{IMU}j}^m = \mathbf{X}_{\text{cam}j}^m + I_j^m \quad (5.25)$$

Where

$\mathbf{x}_{cam/j}^m$ are j camera coordinates in the mapping frame (from resection),

$\mathbf{X}_{IMU/j}^m$ are IMU coordinates in the mapping frame.

Step three:

$$\mathbf{X}_{IMU/j}^e = \mathbf{R}_m^e \mathbf{X}_{IMU/j}^m \quad (5.26)$$

Where $\mathbf{X}_{IMU/j}^e$ are the coordinates of the IMU in the ECEF frame computed from the j camera.

Step four:

$$\mathbf{X}_{IMU}^e = \text{KF}(\mathbf{X}^e, \mathbf{X}_{IMU/L}^e, \mathbf{X}_{IMU/R}^e) \quad (5.27)$$

where

\mathbf{X}_{IMU}^e are the Kalman filtered (KF-ed) coordinates of the IMU in the ECEF frame,

\mathbf{X}^e are the coordinates of the IMU in the ECEF frame computed from the mechanisation equations,

$\text{KF}(\mathbf{X}^e, \mathbf{X}_{IMU/L}^e, \mathbf{X}_{IMU/R}^e)$ is the Kalman filter with \mathbf{X}^e as update, and $\mathbf{X}_{IMU/L}^e$ and $\mathbf{X}_{IMU/R}^e$ as CUPTs.

5.6.2 - Leverarm application from IMU to Intersection

The KF gives the filtered position of the IMU in the ECEF frame. To apply the intersection, the position of the cameras has to be derived from this filtered position. Inversing the procedure above, this process is done as follows.

Step one:

$$I_j^b = \mathbf{R}_c^b \cdot I_j^c \quad (5.28)$$

Where I_j^b is the leverarm in the body frame.

Step two:

$$I_j^e = R_b^e \cdot I_j^b \quad (5.29)$$

Where I_j^e is the leverarm in the ECEF frame.

Step three:

$$X_{CAM/j}^e = X_{IMU}^e + I_j^e \quad (5.30)$$

Where

X_{IMU}^e is the Kalman Filtered IMU position in the ECEF frame,

$X_{CAM/j}^e$ is the j camera position in the ECEF frame.

Step four:

$$X_{CAM/j}^m = R_e^m X_{CAM/j}^e \quad (5.31)$$

Where

$X_{CAM/j}^m$ is the KF-ed position of the j camera in the mapping frame.

$X_{CAM/L}^m$ and $X_{CAM/R}^m$ are used in intersection to map more features as shown in Chapter 2.

5.7 - Leverarm and Boresight Numerical Determination

In this work, an indirect procedure was followed to determine the two boresight matrices and two leverarm vectors of the left (L) and right (R) cameras. In the frame work of the Geodetic Engineering Laboratory, a mapping system with a high-definition digital camera (named as

“H”) is well calibrated with respect to the IMU with known boresight and leverarm according to the procedure described in Sections 5.5 and 5.6; to this system, the two CCDs were added (Figures 5-10 and 5-11). The boresight and leverarm of the two CCDs were first calibrated with respect to the high-definition digital camera by determining the EOP of the three cameras in three different locations using more than 35 precise GCPs. Then, once the average boresight and leverarm were computed, the link between the two CCDs and the IMU were directly made through the already known boresight and leverarm between the H camera and the IMU. The estimated accuracy of the EOP, boresight and leverarm between three cameras are shown in Tables (5-1) and (5-2).

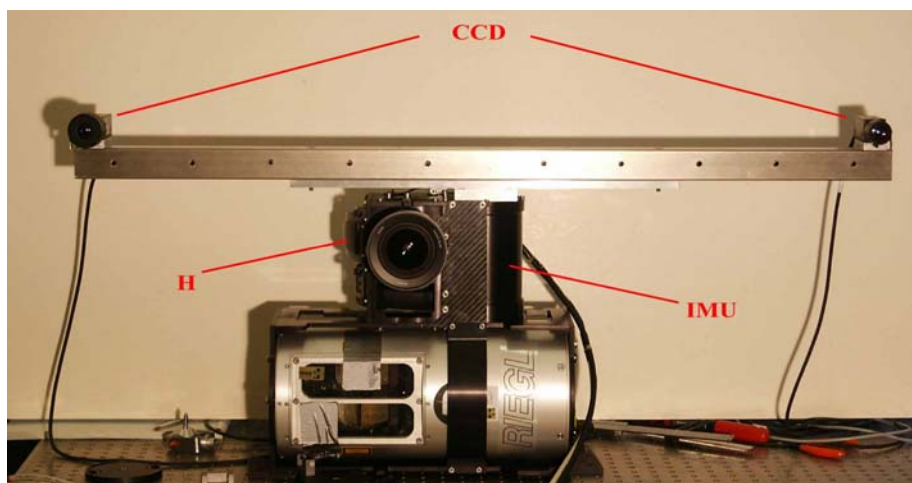


Figure 5-10: The system

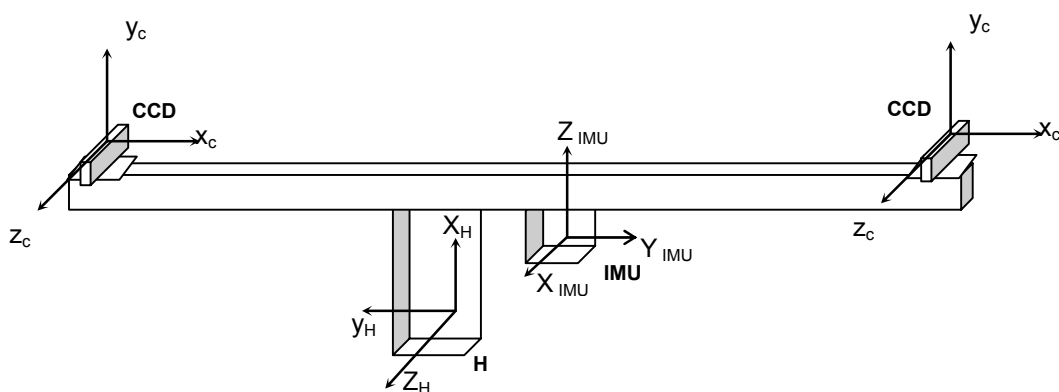


Figure 5-11: The mounting of the system (looking from the back of Figure 5-10)

Table 5-1: Estimated boresight and its accuracy between the CCDs and H (L=Left CCD, R=Right CCD, H=High Definition Camera) - arcmin

		Pitch	Azimuth	Roll
Boresight	L to H	43.37	37.15	-67.73
	R to H	61.43	31.22	20.59
Boresight accuracy	L to H	3.50	6.26	2.84
	R to H	0.91	2.80	3.27

Table 5-2: Estimated leverarm and its accuracy between the CCD and H (cm)

		X	Y	Z
Leverarm	L to H	59.8	-10.0	-23.0
	R to H	-41.5	-11.8	-21.8
Leverarm accuracy	L to H	1.0	1.6	1.0
	R to H	0.6	1.0	0.3

Tables (5-3) and (5-4) show the boresight and leverarm between the CCD and the IMU after contributing for the boresight and leverarm of Tables (5-5) and (5-6) between H and IMU.

Table 5-3: Estimated boresight between the CCDs and IMU (arcmin)

		Pitch	Azimuth	Roll
Boresight	L to H	90.9	35.8	61.6
	R to H	7.3	22.3	79.2

Table 5-4: Estimated leverarm and its accuracy between the CCD and IMU (cm)

		X	Y	Z
Leverarm	L to H	50.0	-17.8	-3.5
	R to H	-51.3	-19.6	-2.3
Leverarm accuracy	L to H	1.0	1.0	0.5
	R to H	1.0	1.0	0.5

Table 5-5: Estimated boresight and its accuracy between the IMU and the H camera (arcmin)

	Pitch	Azimuth	Roll
Boresight	-15	15.9	-18.84
Boresight accuracy	0.66	0.6	0.9

Table 5-6: Estimated leverarm and its accuracy between the IMU and H camera (cm)

	X	Y	Z
Leverarm	7.8	-9.5	9.8
Leverarm accuracy	0.5	0.5	0.5

The mathematical formulas that allow determining the boresight between the CCDs and the IMU via those between the CCD and H, and H and IMU are:

$$\mathbf{T}_{b^*}^c \cdot \mathbf{R}_{b^*}^{b^*c} = \mathbf{R}_b^c = \mathbf{T}_H^c \cdot \mathbf{R}_H^{H^*} \cdot \mathbf{T}_{b^*}^H \cdot \mathbf{R}_{b^*}^{b^*H} = \mathbf{R}_H^c \cdot \mathbf{R}_b^H \quad (5.32)$$

Where

$\mathbf{R}_{b^*}^{b^*c}$ is the sought boresight between the IMU and CCD (c being L or R), which is the same as $\mathbf{R}_b^{b^*}$ of Equation (5.15) but with the addition of superscript “c” to indicate that is between the CCD and the IMU (Table 5-3)

\mathbf{T}_H^c is the rotation matrix between the H and CCD cameras, depending on the mounting (Figure 5-9)

$\mathbf{R}_H^{H^*}$ is the boresight between H and CCD cameras (Table 5-1), computed as mentioned above in this Section

$\mathbf{T}_{b^*}^H$ is the rotation matrix between H and IMU frames, depending on the mounting (Figure 5-9)

$\mathbf{R}_{b^*}^{b^*H}$ is the boresight between the H and IMU frames (Table 5-5), which is the same as $\mathbf{R}_b^{b^*}$ of Equation (5.15), but with the addition of superscript “H” to indicate that is between H camera and the IMU, computed as mentioned in Section 5.5

\mathbf{R}_H^c is the rotation matrix between H and CCD taking into account the boresight and the mounting

\mathbf{R}_b^H is the rotation matrix between H and IMU taking into account the boresight and the mounting.

The leverarm determination is more straightforward. The equation used is:

$$\mathbf{l}_c^b = \mathbf{R}_H^c \cdot \mathbf{l}_H^b + \mathbf{l}_c^H \quad (5.33)$$

Where \mathbf{l}_c^b is the leverarm between the CCD and the IMU in the c frame

\mathbf{l}_H^b is the leverarm between H and the IMU in the H frame computed as shown in Section 5.6

\mathbf{l}_c^H is the leverarm between H and CCD computed as mentioned above in this Section.

Applying the error propagation to Equation (5.33), the covariance matrix of \mathbf{l}_c^b is:

$$\boldsymbol{\Sigma}_{\mathbf{l}_c^b} = \mathbf{R}_H^c{}^T \cdot \boldsymbol{\Sigma}_{\mathbf{l}_H^b} \cdot \mathbf{R}_H^c + \boldsymbol{\Sigma}_{\mathbf{l}_c^H} \quad (5.34)$$

Where $\boldsymbol{\Sigma}_{\mathbf{l}_H^b}$ is the covariance matrix of the components of the leverarm \mathbf{l}_H^b

$\boldsymbol{\Sigma}_{\mathbf{l}_c^H}$ is the covariance matrix of the components of the leverarm \mathbf{l}_c^H

Because of the importance of the boresight (as will be seen in the next chapter), their accurate determination is critical; as for the leverarm, less stringent requirements are possible. Subsequently, the values listed in the tables above fall within the constraints of this work.

6 - NUMERICAL APPLICATION

... tests with patience are a way to perfection ...

Three tests were conducted to validate the methodology and the algorithms described in this thesis:

1. An Indoor test: control of concept
2. An outdoor test: control of resection and boresight
3. An outdoor test of SLAM

The set-up (Figure 7-1) consists of a pair of CCD cameras (progressive scan SONY XC-55, 640*480 square pixels of resolution 7.4 μm , and with a 6 mm c-mount lens) fixed one metre apart and an LN-200 IMU (1 deg/hr). Along, there are a synchronisation pulse, a Matrox Meteor-II/Multi-Channel frame grabber and a screen, IMU data acquisition box developed at the EPFL-TOPO (Skaloud and Viret, 2004), a laptop, and the power supply. The image grabbing was carried out at every second and was properly synchronised with the IMU via a synchronisation pulse (image acquisition program was written by Dr. Jan Skaloud). After several minutes of inertial initialisation, the vehicle moved and started taking images.

In all tests, as many features (homologous points) as possible were selected from the images. Ideally, more than 25 features per stereo-pair have to be selected in order to guarantee resection with sufficient accuracy, but this was not possible all the time. All photo-coordinates were measured manually using professional photogrammetric software.

To provide a consistent geodetic solution, a local mapping reference system shall be established as follows:

- Determine coordinates of two points with GPS (or use existing triangulation points)
- Take one point as the origin of the local mapping system (ENU) and transform the second point according to it
- By a total station determine the coordinates of the GCP and checkpoints in this local mapping frame

This provides a mapping frame that is linked with the other frames as described in Chapter 6.

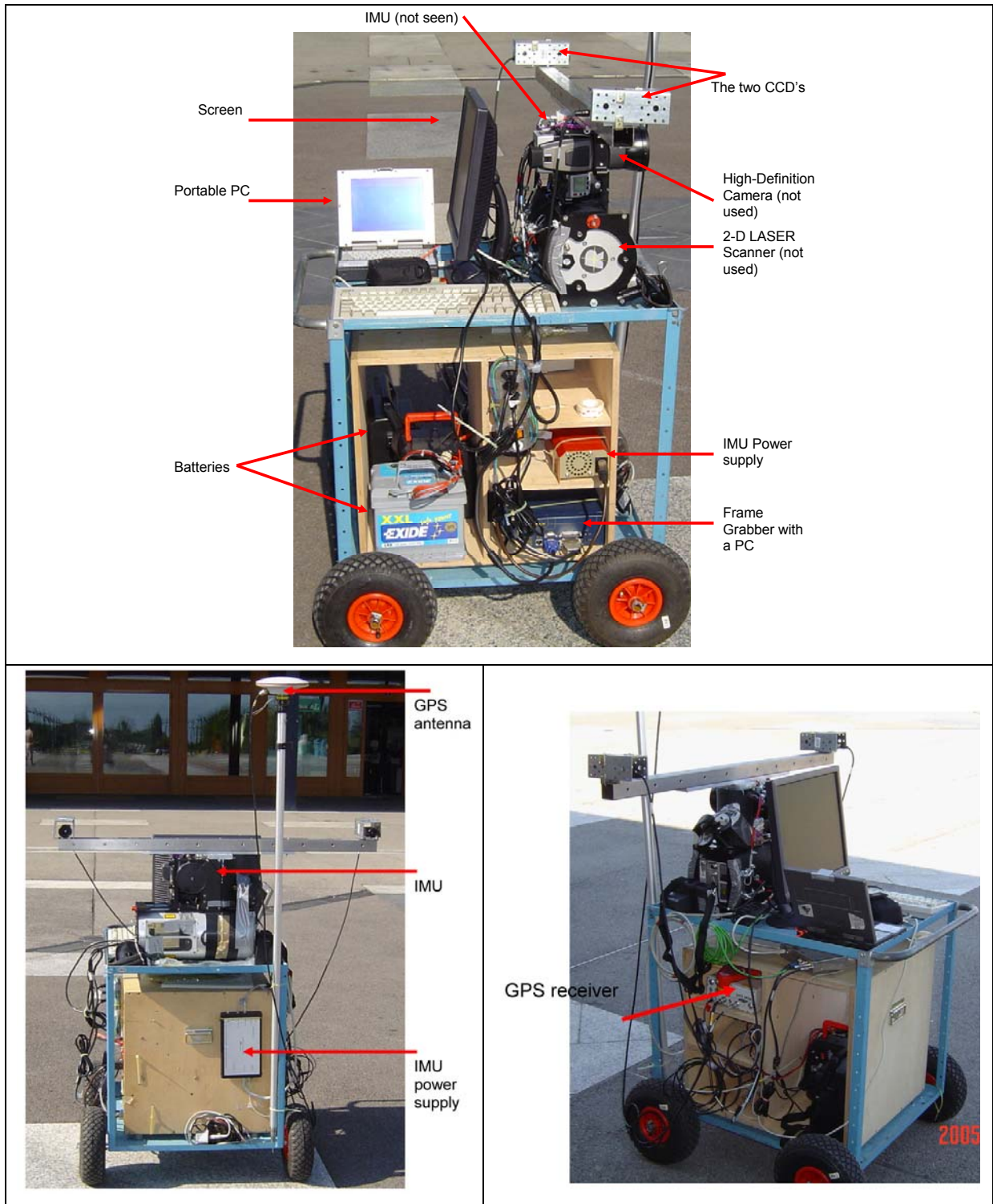


Figure 6-1: The System

6.1 - Indoor Test – Control of Concept

Running the two indoor tests in a controlled environment in terms of special targets and close to optimal lighting, the methodology was tested and the software's were validated. Figures (6-1) and (6-2) show image samples of the two sets.

The analysis and simulations done in previous chapters agree with the findings of this control test. After the initialisation using around 20 GCP, homologous points were determined and the survey continued for 13 seconds for the first test and 20 seconds for the second test using six photos each.

At the end of each test, four checkpoints (CHP) were used to control the mapping accuracy, through which the vehicle localisation accuracy was indirectly controlled. For a direct control of system localisation, an outdoors test with GPS is needed. Tables (6-1) and (6-2) show the differences in the CHP of the two tests, respectively, determined by a theodolite and their SLAM estimated positions. It is obvious that the depth (the X & Y-components) is geometrically weak because of the short stereo base (1m long).

In the first test, the vehicle's azimuth was around the 180 degrees and this is reflected in the poorer accuracy in the Y-axis relative to the X- axis. As for the second test, the azimuth was around the 45 degrees causing the accuracy in the X and Y- axes to agree.

Table 6-1: Validation of the first test, error on control points after 20 seconds and 6 photos (cm)

GCP	X	Y	Z
1	1.9	3.9	-0.5
2	6.7	11.9	0
3	6.2	10.1	-0.8
4	4.4	7.0	-0.4

Table 6-2: Validation of the first test, error on control points after 13 seconds and 6 photos (cm)

GCP	X	Y	Z
1	-4.9	4.5	0.1
2	-1.1	1.1	-1.7
3	-1.8	0.5	-1.4
4	-5.5	7.5	1.3

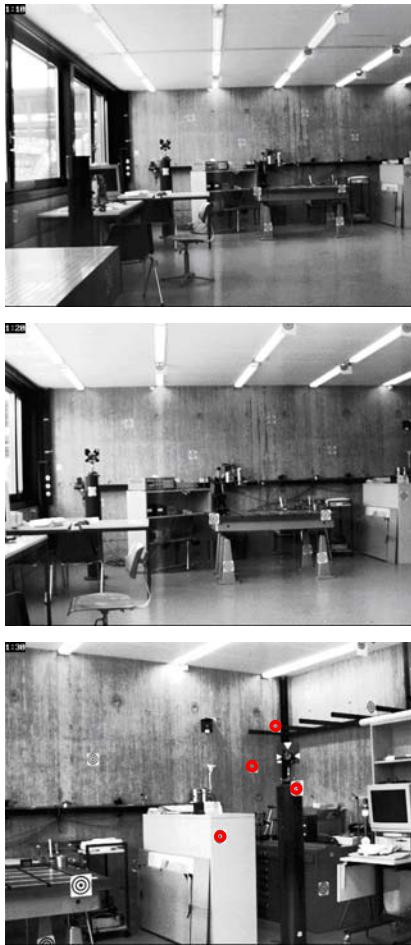


Figure 6-2: First data set

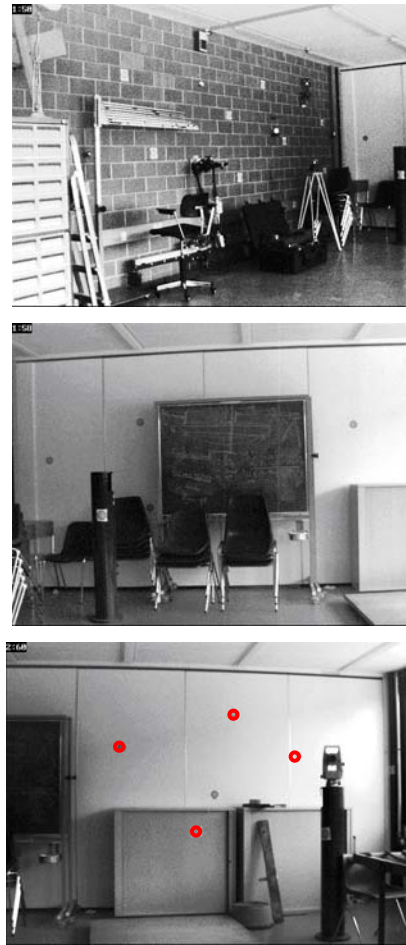


Figure 6-3: Second data set

6.2 - Outdoor Test – Control of Resection and Boresight

It was difficult to find a testing place with open skies and at the same time suitable to perform the photogrammetric processing. Hence, this outdoor test with GPS was used to compare the EOP derived from photogrammetric resection with the GPS/INS position and attitude. Intersection was not performed in this test because its performance was analysed in the other tests. In addition, the boresight correction was re-checked and validated.

This process is similar to the OEEPE's (Heipke et al., 2001) (<http://www.oeepe.org/>) investigations on the accuracy of INS/GPS for direct georeferencing in airborne applications. However, the analysis here differs in terms of the used cameras, sought accuracies and change of resection accuracies due to the use of newly determined homologous points whose accuracies changes in time.

After the initialisation by GPS/INS, photographs were taken repeatedly of a pre-surveyed structure (Figure 6-4). In order to photograph the same structure and create dynamics in

motion, the track followed an “8” shape as seen in Figure (6-5) and the images were used at the loop cross-point. The targets coordinates were measured by a total station and determined in a local reference frame with known transformation from the ECEF reference frame used for IMU integration. Out of more than a hundred image pairs, twelve were used to compare the EOP between resection and carrier phase differential INS/GPS; the test duration was a minute and a half and the separation between stereo-pairs ranges from 2 to 17 seconds.



Figure 6-4: The structure. The depth range that give a stronger geometry for resection

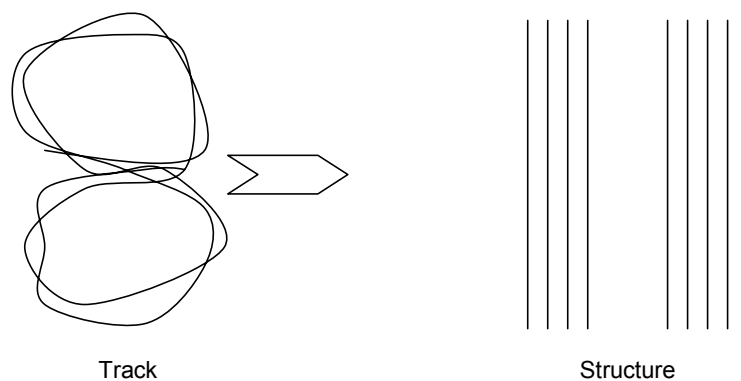


Figure 6-5: Images were taken whenever the cameras could see the structure

The first test here will start by comparing GPS/INS with resection using the measured accuracies of the GCP and then in the next test, noise will be added to the GCP coordinates depending on their distance from the cameras (based on simulations of Chapters 2 and 3). In this way, the intersection is simulated. It should be noted here as well that the accuracy of the photo-coordinates is set to the size of the pixel (7.4 μm) due the poor quality of the cameras.

Table (6-3) lists the differences in position between GPS/INS and resection based on measuring accuracy and simulated accumulated errors of 5, 10 and 15 centimetres. With errors up to 10 centimetres, the differences are kept within the desired accuracies. It should be noted here that the targets are up to 15 metres away from the cameras, and the results in this table validate the simulation done in Chapters 2 and 3. Since the system was always directed towards the east – Azimuth $\sim +90^\circ$ – when the images were taken, the quality of the positions in the X-axis direction is the worse.

From the same tests, the attitude angles were also compared between GPS/INS and resection. However, the boresight effect was also studied here where each simulation was run twice, one with the boresight correction and the other without the contribution of the boresight correction.

In classical georeferencing where the camera position is derived directly from the INS/GPS, the boresight corrections are essential for the determination of the attitude of the camera and their effect on the position is negligible due to their small size.

Table 6-3: Mean differences between EOP determined by resection and GPS/INS based on accumulated error (m)

Accuracy	X-axis		Y-axis		Z-axis	
	L	R	L	R	L	R
Measured ~ 0.01	0.03	-0.02	0.04	0.01	0.01	-0.01
0.05	0.07	0.01	0.05	0.02	0.02	-0.01
0.10	0.19	0.06	0.05	0.02	-0.05	-0.02
0.15	0.24	0.22	-0.03	-0.03	-0.13	-0.12

Tables (D-1), (D-2), (D-3) and (D-4) (Appendix D) list the angles between the body and Earth frame computed from the INS/GPS-derived R_b^e and resection-derived R_b^e matrix with and without boresight corrections for twelve stereo-pairs and with different GCPs accuracies. Table (6-4) on the other hand shows the RMS of the differences between these angles. It is clear that boresight correction has the biggest effect in this analysis.

Table 6-4: RMS of the differences of the R_b^e angles' derived from INS/GPS and resection (angles shown in Appendix D)

GCP Accuracy (m)		Angles accuracy with boresight correction (deg)			Angles accuracy without boresight correction (deg)		
		E_x	E_y	E_z	E_x	E_y	E_z
~ 0.01	L	0.0362	-0.0332	-0.0673	1.5479	0.5383	1.1063
	R	-0.0270	0.0117	-0.0111	0.1455	0.4063	1.3718
0.05	L	0.1080	-0.1158	-0.1208	1.7159	0.5400	1.2877
	R	0.0682	-0.0754	-0.1029	0.3279	0.3967	1.3942
0.10	L	-0.9729	1.6131	1.3870	1.8365	0.9435	0.9601
	R	0.5483	0.5511	0.9206	-0.9629	1.6175	1.4648
0.15	L	-0.3413	0.3994	0.0469	2.8134	-0.3860	-0.6966
	R	-0.4784	0.5253	0.3457	1.2401	-0.6162	-0.2668

From Table (6-3) and (6-4), it is obvious that once the homologous points accuracies are worse than 10 cm, the contribution of the KF attitude update becomes useless, whereas the position update keeps steering the IMU as long as its accuracy is better than 15 cm.

In Figure (2-6), it was shown that to achieve an accuracy of 15 cm in intersection, objects that are 11 metres away from the system should not be used.

6.3 - Outdoor Test of SLAM

In the third test, SLAM was performed. This test shows how critical the cameras' set-up is to the overall performance of the system. When working outdoors, the operator cannot control the scene's visibility quality and its features distance from the cameras. The images can be seen in Appendix C; although they look sharp, once fine targets are sought, problems start to appear. Looking for example at two zoomed out images of the set (Figure (6-6)), one can see the difficulty in finding fine targets to use. This effectively reduces the quality of the whole system. First, the initialisation becomes of poor accuracy and the subsequent positioning and orientation determination by resection are not accurate enough to be considered as valuable updates for the Kalman Filter.

It should be noted that by using linear primitives, i.e., lines, the pixel measurement problems could be overcome and thus leading to better resection/intersection solutions. See, for example, Habib et al., (2004) and Al-Ruzouq (2004).

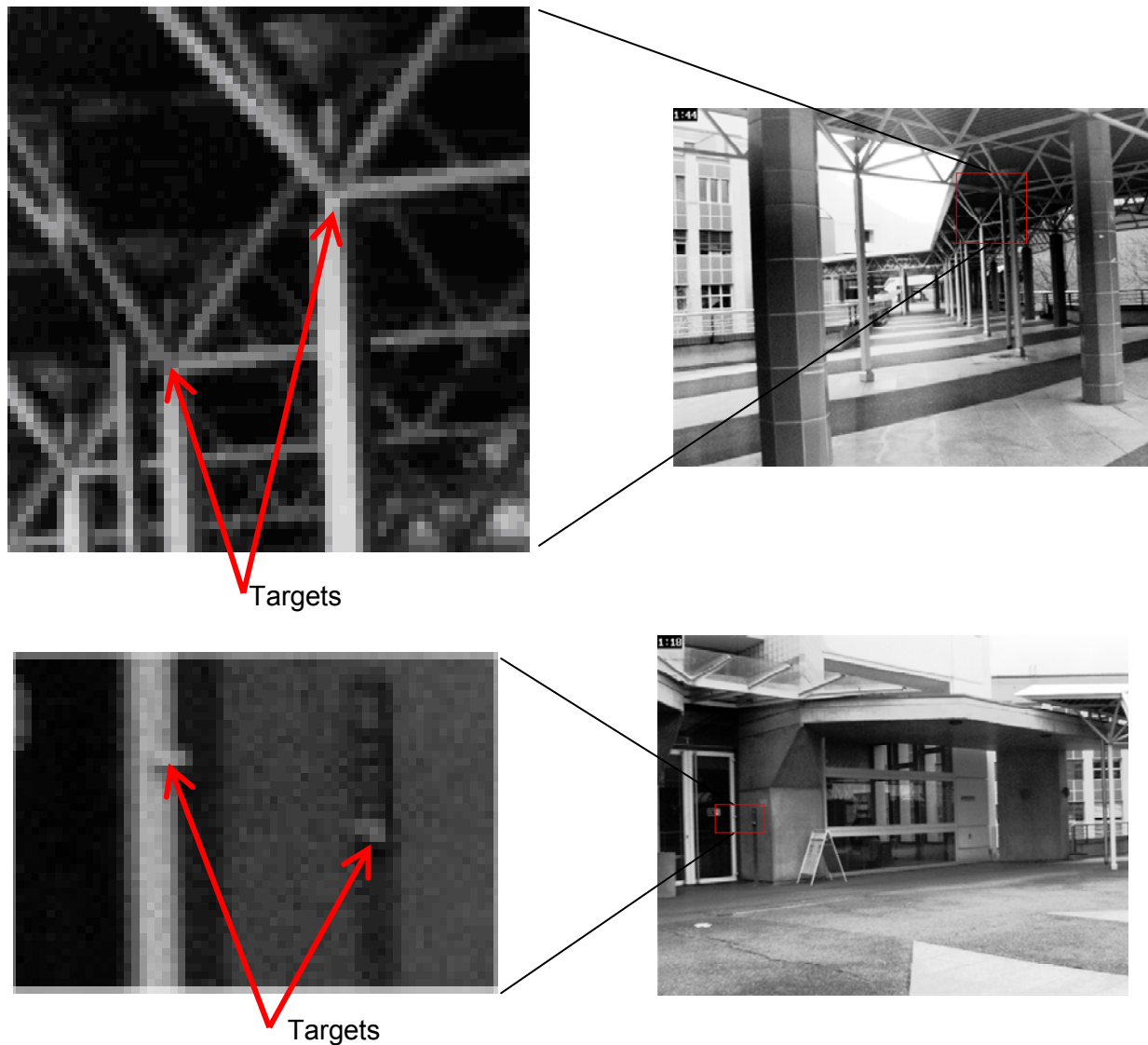


Figure 6-6: An example of the poor quality of the images once they are zoomed to find targets to map

In this test, the initialisation was done using around 30 GCPs on each image. A way to verify the consistency of the LSA solution, one can use the misclosure vector between the measured and the computed photo-coordinates from the resection after the conversion of the LSA solution.

Figures (6-7) and (6-8) show the differences (misclosure) graphically in the GCPs photo-coordinates after the convergence of the LSA of five iterations for the Left and Right images. Although some points can be considered as outliers (see those in the dotted ellipses), they are kept in the adjustment because they reflect the bad quality of the images rather than being considered as outliers.

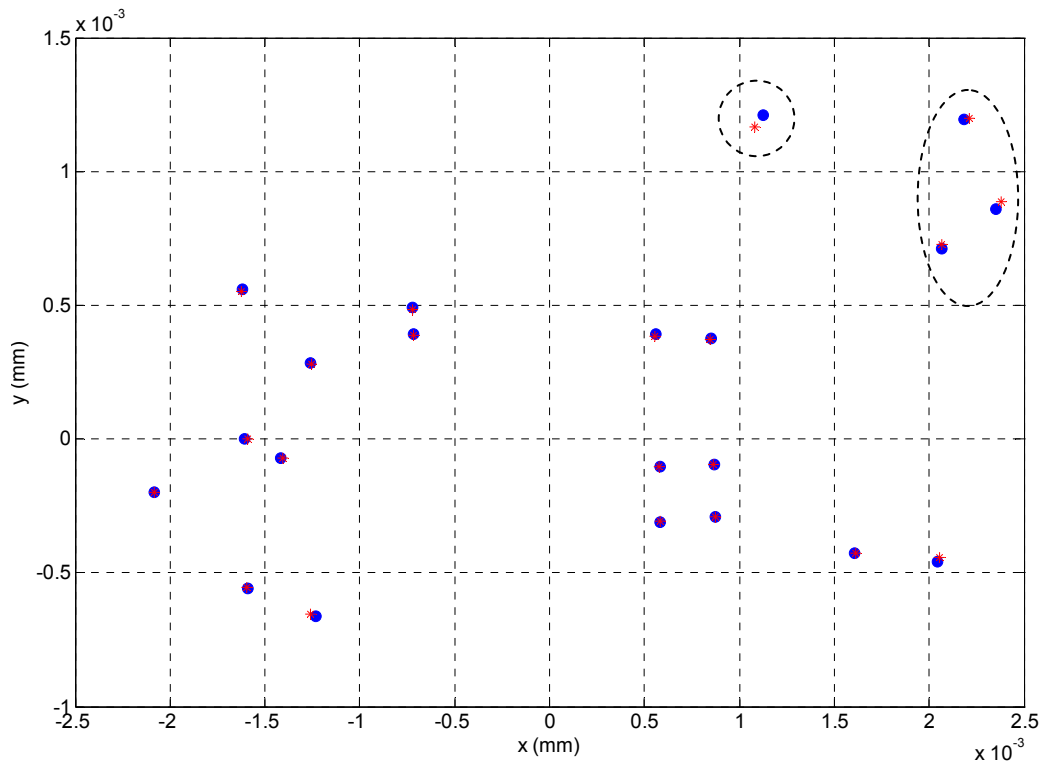


Figure 6-7: Misclosure information in the resection LSA for a Left image (outliers are indicated in the dotted ellipses)

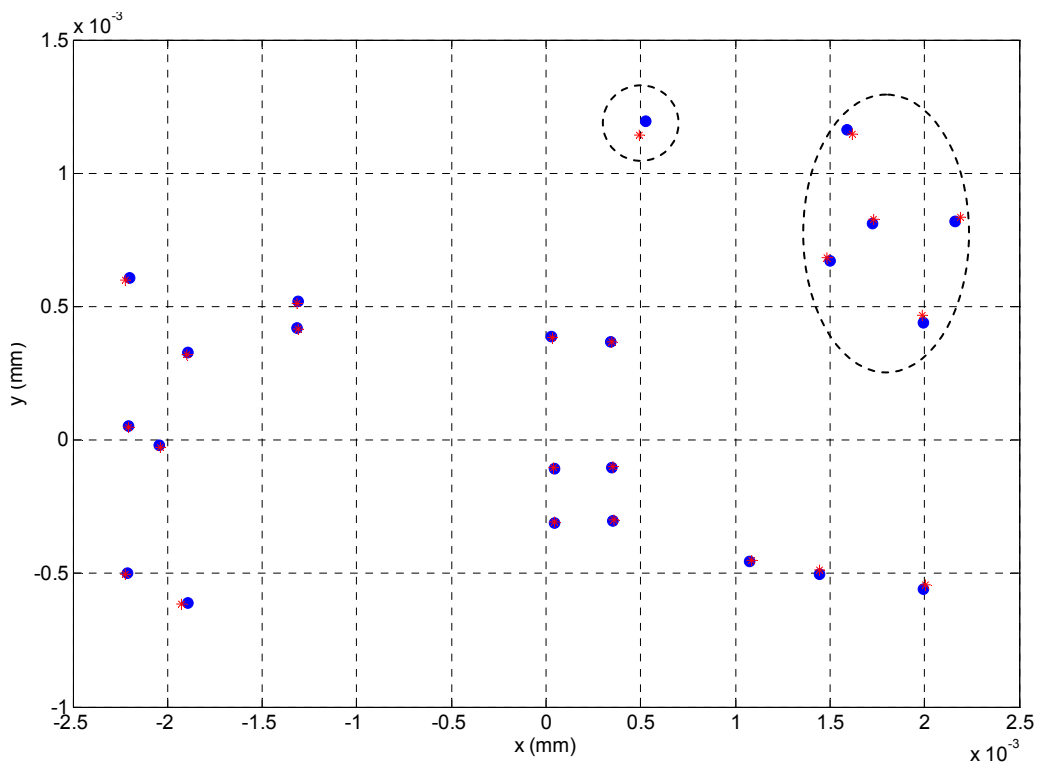


Figure 6-8: Misclosure information in the resection LSA for a Right image (outliers are indicated in the dotted ellipses)

6.3.1 - Initialisation and Navigation

The method of initialisation is important for practical reasons. Considering the small size of the system and its potential uses, one might consider a rigorous solution in terms of initialisation and reference systems consistency as an extra. Therefore, the initialisation method will be an integrated part of the following investigations.

Three initialisation methods were tested:

- Initialisation by resection position and gyro compassing
- Initialisation by resection EOP without boresight corrections
- Initialisation by resection EOP with boresight corrections

Through these initialisation methods, ZUPTs were continuously updating the KF, which drastically improved the initialisation quality.

Although practically gyro compassing can be used, long time is needed for accurate initialisation. This is mainly true for the azimuth, where several minutes are needed to determine an azimuth within few degrees accuracy by a LN-200. Here, the gyro compassing was performed for few minutes, thus leading to insufficient initialisation accuracy as seen in Figure (6-9).

The update at position 2 was made by GCPs as well due to the discontinuity in visibility between images of set 1 and 2 (see Appendix C). After the third update, the Kalman Filter succeeded to estimate the misalignments and position errors; once applied, the navigation solution started to converge to the accuracy of the resection.

In case of initialisation by resection without boresight corrections, the inaccurate initialisation will force the navigation solution to diverge rapidly if no updates are provided, which is clearly seen in Figure (6-10) that shows the IMU navigation solution between the first and second epochs. The alleged convergence of the navigation solution after the third epoch is due to the fact the trajectory is straight and all differences in rotation angles are considered as misalignments. Therefore, once a turn is made, it is expected that the boresight non-contribution (correction) effect will clearly appear as a divergence in the navigation solution.

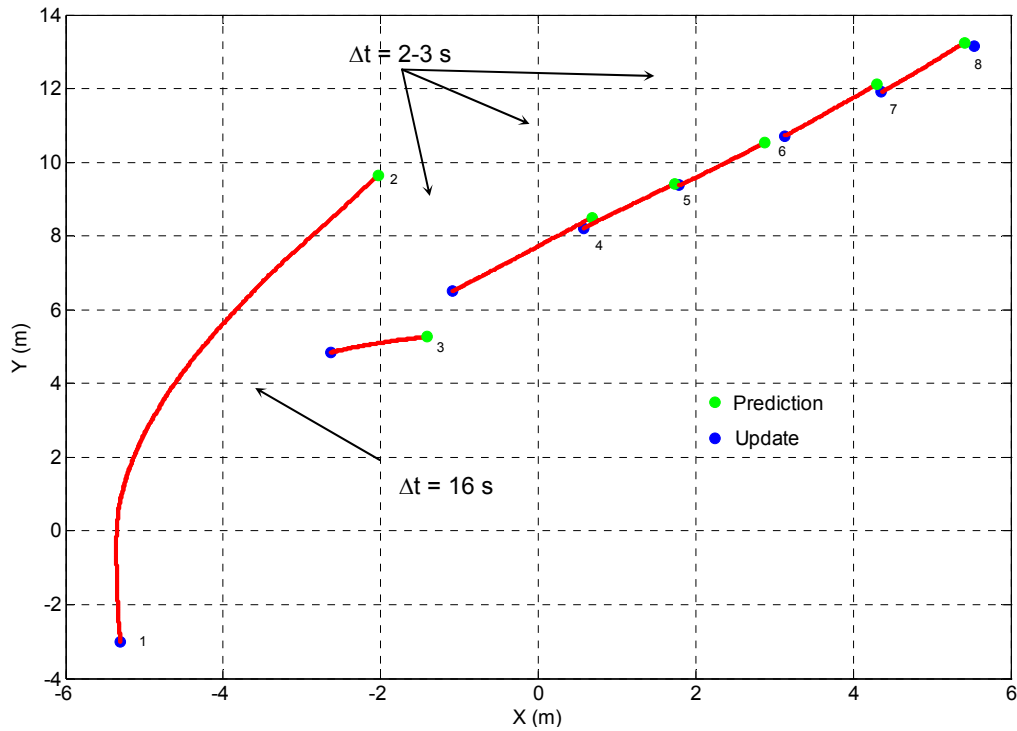


Figure 6-9: Vehicle planimetric trajectory showing the differences between the prediction and update (ground truth) when initialised with gyro-compassing (innovation)

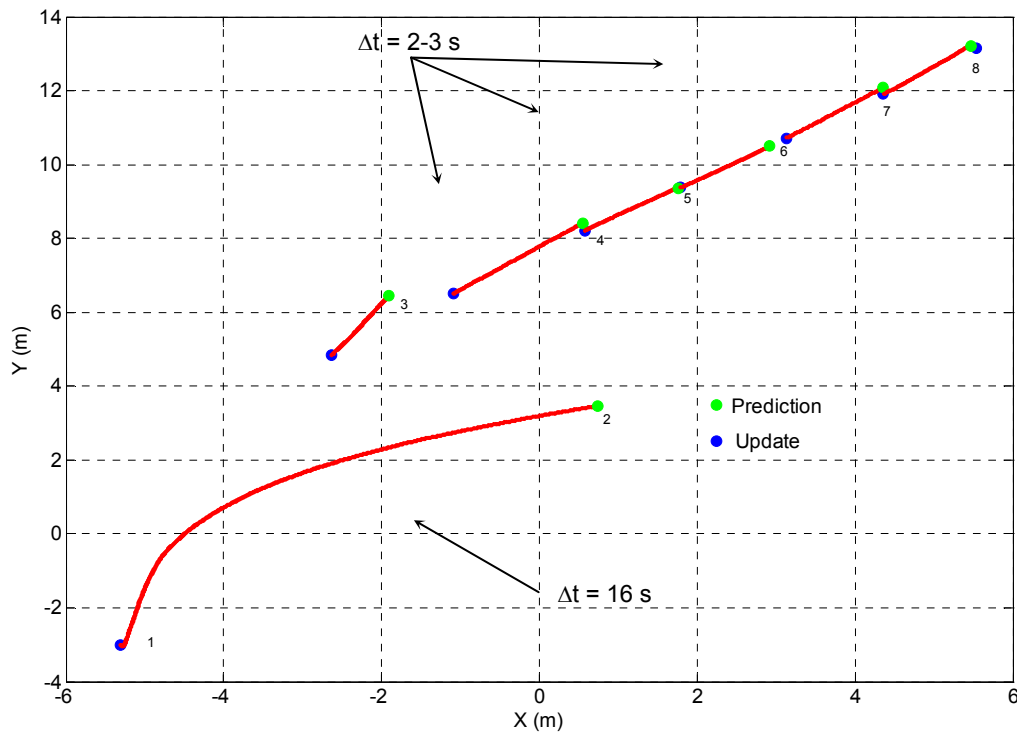


Figure 6-10: Vehicle planimetric trajectory showing the differences between the prediction and update (ground truth) when initialised with photogrammetric resection without boresight corrections (innovation)

When the boresight corrections are considered, the navigation solution (Figure 6-11) is much better at the beginning where the prediction and update are within few centimetres from each other, but later, as can be expected, the two solutions are of a similar quality as in Figure (6-10). However, if a turn was made, the navigation solution with the boresight contribution will not diverge, as would that without the boresight contribution (correction).

The resection will affect the solution in a way that when the planimetric components are not accurate, the Kalman filter will depend more on the IMU solution that if left for several minutes without updates will cause the whole system's quality to degrade in time.

The vertical component, as seen in Figure (6-12), is within the expected accuracy. It is worthwhile to note the stability in the z-channel – with almost the same results regardless of the initialisation method used, images are not shown because of their similarity – where after the third epoch the innovation does not exceed few centimetres. It is a usual case that the innovation of the Z-channel is better than that of the horizontal channels when low dynamics are observed, as in our case. In the particular case herein, the initial misalignment would be the dominant source of errors causing the X and Y components to drift; this analysis comes from the deduction that the Z-component of the IMU (its weak component) is very consistent with the Z-component of resection (the strong photo component).

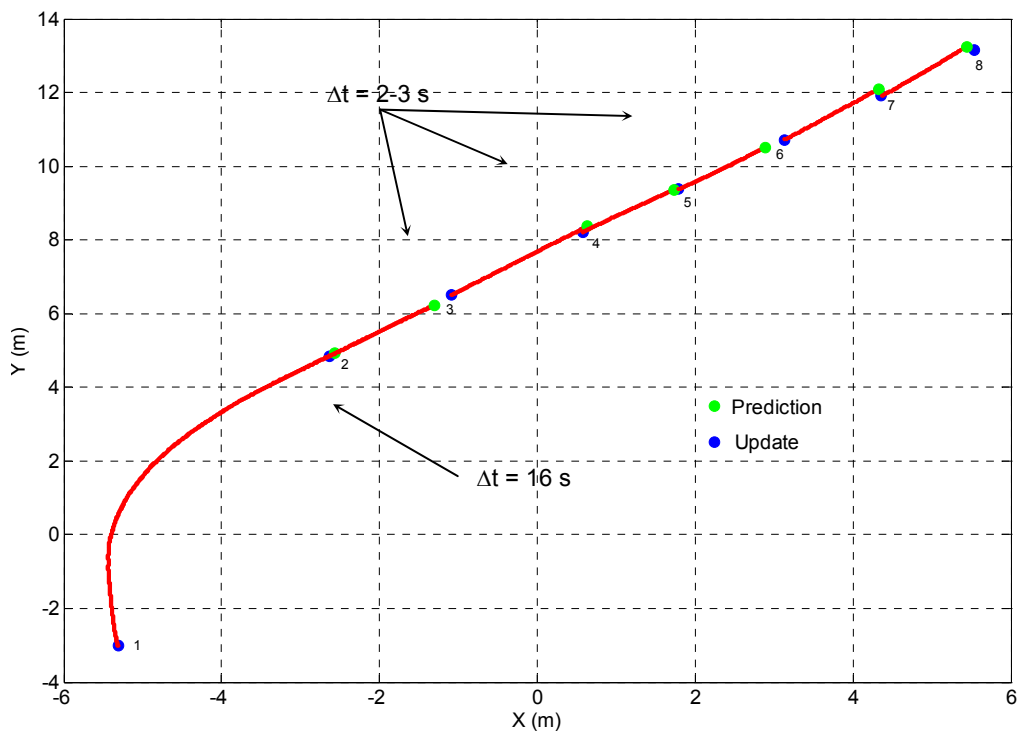


Figure 6-11: Vehicle planimetric trajectory showing the differences between the prediction and update (ground truth) when initialised with photogrammetric resection with boresight corrections (innovation)

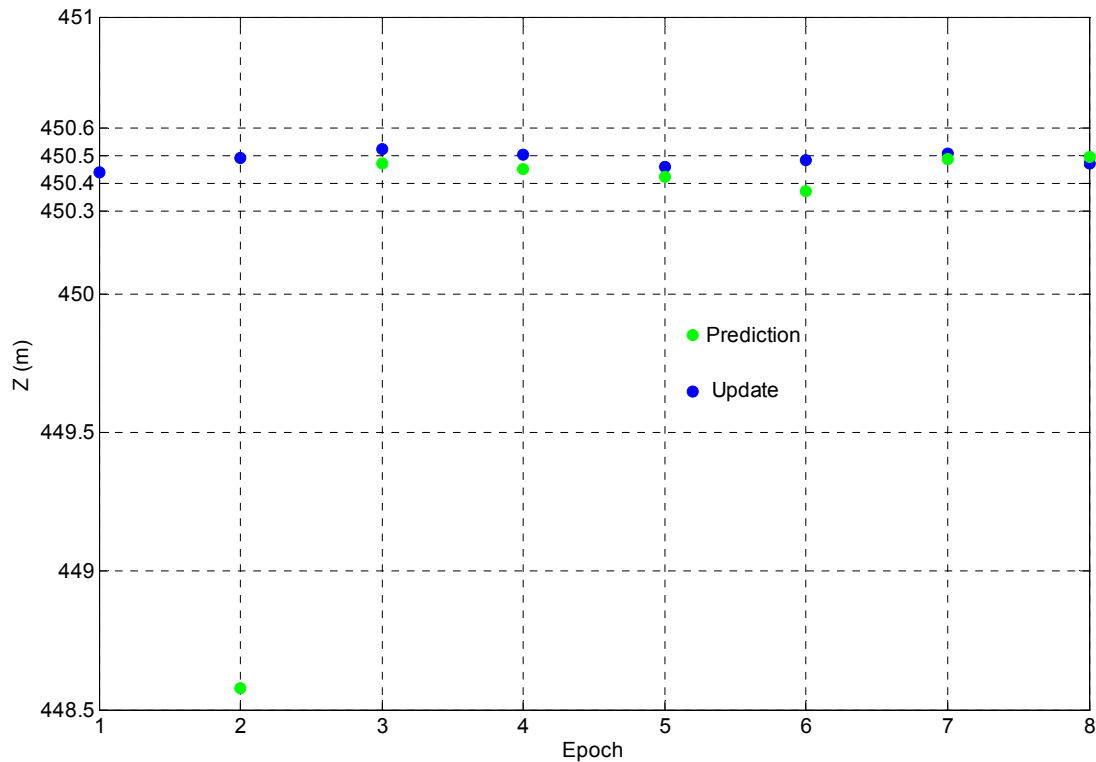


Figure 6-12: Vehicle vertical trajectory showing the differences (innovation) between the prediction and update (ground truth)

The process does not finish by choosing the correct method of initialisation. Through subsequent analysis, it was found that the measurement variance of the photo-coordinates plays an important role in the process. For example, if this variance was chosen to be small (STD $\sim 2.5 \mu\text{m}$), the updates will be accompanied by small variances that will force the Kalman Filter through the gain matrix to trust them more. Whereas when the photo-coordinate variances are chosen to be more realistic according to the quality of the images (STD $\sim 7.5 \mu\text{m}$), the updates, whose values will not change much, will be accompanied with larger variances that will relax the Kalman filter, thus leading to correct estimate and improved navigation solution.

To demonstrate this finding, Figure (6-13) shows the planimetric solution when initialisation was done by resection with boresight correction but with photo-coordinate accuracy of $2.5 \mu\text{m}$.

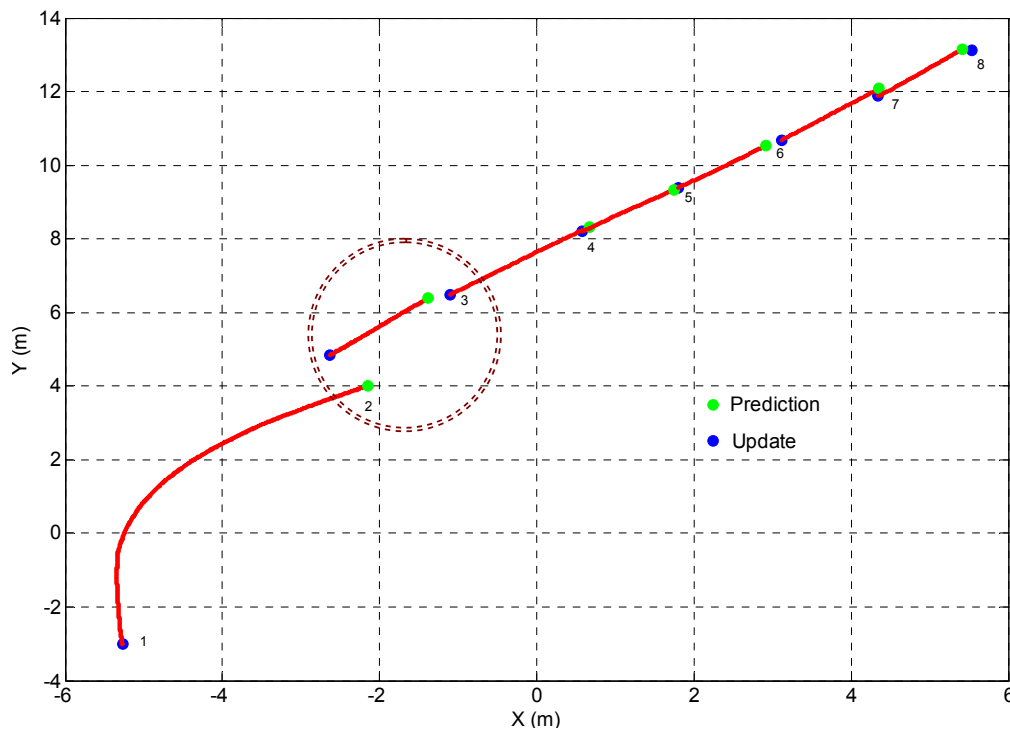


Figure 6-13: Vehicle planimetric trajectory when assigning a $2.5 \mu\text{m}$ STD for the photo-coordinates

The same thing applies to the choice of the initial \mathbf{P}_0 matrix of the Kalman Filter. This matrix defines the initial uncertainties of the initial state vector elements. By altering the uncertainties of the initial misalignment from 2 to 4 arcmin (see chapters 4), the solution changes accordingly as shown in Figure (6-14).

A bank of Parallel Filters with different initialisation parameters can be suggested in order to choose the optimal initial values through a calibration procedure. In this way, the first two epochs of the SLAM need to be initiated by resection and this way the software chooses which of the branches of the bank provides the values closest to the second epoch.

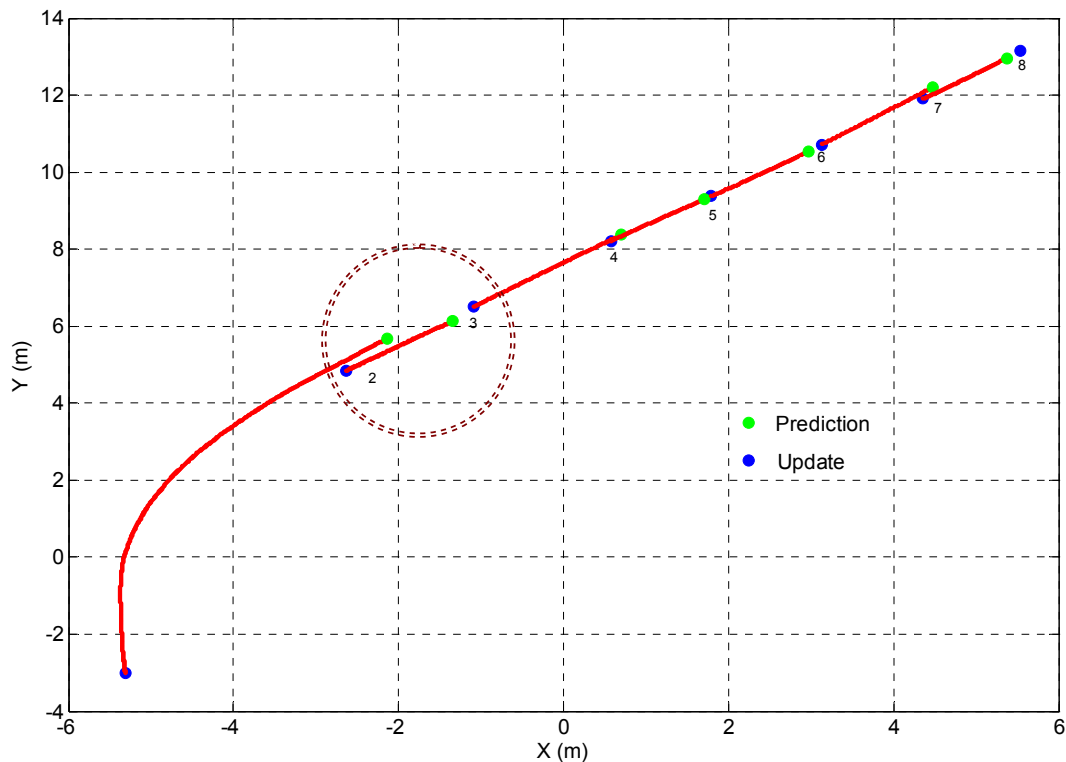


Figure 6-14: Vehicle planimetric trajectory when assigning 4-arcmin attitude uncertainty in the P_0 matrix instead of 2-arcmin

6.3.2 - Modification of the Kalman Filter

In Chapter 5, two scenarios were shown to combine the external measurement in KF; one by using the average of the two cameras' positions and the other by using these two positions as independent uncorrelated measurements. This requires certain modification in the software and its modules. After modifying the software accordingly, it was found that the results from the second scenario were very similar to the first with statistically insignificant differences.

The second scenario can be used when one of the two cameras is malfunctioning and thus the processes shifts to accept measurements from one camera. In this sense, the intersection relies on forming stereo-base between successive images from the camera that would be still properly functioning.

6.3.3 - Mapping

According to the intersection theory and its previous simulations, determining the X and Y components coordinates is geometrically weak. In addition, the accuracy of the image coordinates is limited for relatively low resolution of 640*480 square pixels when

accompanied by short focal length. During this SLAM test, 21 points were used as checkpoints throughout the survey, whose validation and accuracies are shown in Figure (6-15). The large errors belong to those points that are located more than 15 metres away from the stereo-base. Besides, one can see the accurate mapping of the Z-component.

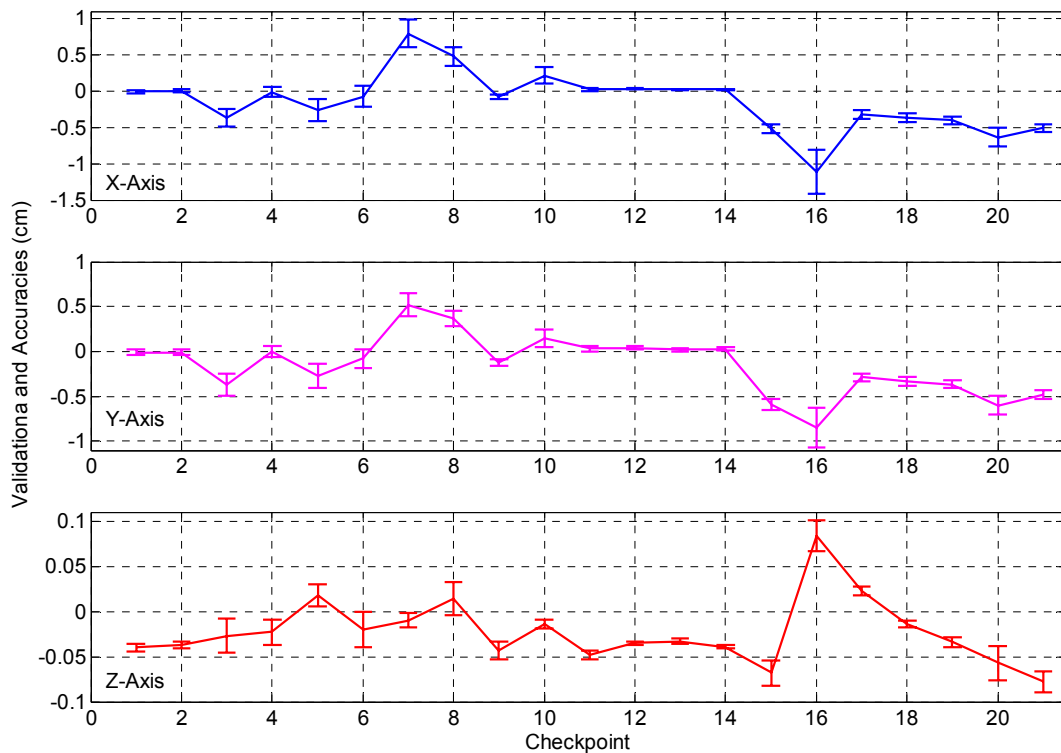


Figure 6-15: Validation and accuracy of newly mapped features

For a best-case scenario, the system designer needs to take into account the different factors that affect the accuracy of the mapping: focal length, CCD's chip size, stereo-base and object's distance from the stereo-base. For example, to achieve an accuracy of less than 10 cm in X and Y with the current system installation (according to Equations (2.20) and (2.22)), the features must not be further than 9 metres away from the cameras in the Y direction when the system is engaged towards north-south and in the X direction when the system is engaged towards east-west.

In different system installation, keeping the CCD's quality but adapting a focal length of 25 mm and stereo-base of 2 m, the maximum distance to achieve 10 cm accuracy would go up to 22 metres. Whereas by choosing a focal length of 12.5 mm and stereo-base of 1.5 m, objects require not be further than 13 m away to achieve an accuracy of 10 cm, as depicted in Figure (6-16).

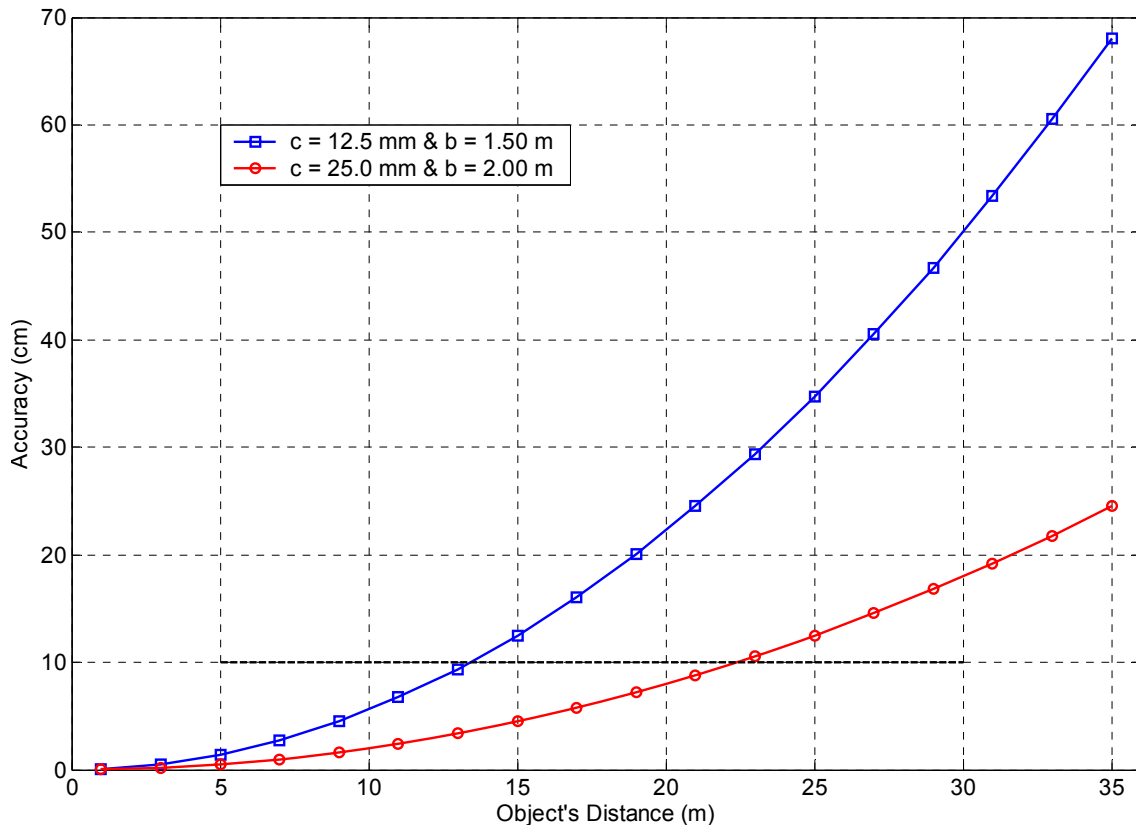


Figure 6-16: Depth accuracy depending on focal length and stereo-base

...perfection cannot be a target, but rather a target can be perfection...

7 - SUMMARY, CONCLUSIONS AND RECOMMENDATIONS

... it is the end, thus the start begins ...

7.1 - Summary

Vision-based inertial-aided navigation is gaining ground due to its many potential applications. In previous decades, the integration of vision and inertial sensors was monopolised by the defence industry due to its complexity and unrealistic economic burden. After the technology advancement, high-quality hardware and computing power became reachable for the investigation and realisation of various applications.

In the 1980's, the robotics community started to localise robots and navigate them according to relative maps made by lasers mounted on the robots; vision cues integrated with inertial sensors gained ground in the late 1990's and beginning of the new century. Simultaneous Localisation And Mapping (SLAM) is a term (conceived in late 1980's) used by the robotics community to describe the problem of locating the robot relative to a map that is made by the robots itself. For many, this was an egg-chicken problem because in order to draw a map the location of the mapping device has to be known, and to know the location of the mapping device a map is usually needed. The mathematical modelling of map-making and localisation of the robot, used in the robotics community, are done in a single Kalman Filter that runs at high frequencies that obliges many approximations to be made upon the models and thus rendering the filter unstable.

In geomatics engineering, precise navigation is a necessity to carry out mapping. In this thesis, mapping turned to be also a necessity to perform navigation, using the concept of SLAM but solving it in a different approach than that of robotics.

The methodology to solve SLAM in this thesis is different from others because:

- Two filters are used: a least-square adjustment filter for map-making and a Kalman Filter for navigation
- No approximations are made to the mapping and navigation models

- The KF runs at low frequency 1/2 or 1/3 Hz, thus the filter stability is guaranteed
- Mapping mathematical model is photogrammetry
- Navigation mathematical model is aeronautical
- A global coordinate frame is used as reference, through which the created map can be linked to other maps by geodetic transformations – such a frame will also allow the INS to exploit the aeronautical navigation model

SLAM has proven to be an interesting yet challenging problem; a blind traverse that depends on two deduced reckoning methods: recursive photogrammetry and inertial navigation. As is the case in many systems, the quality of the sensors that build the system dictates the overall performance of the system.

The system consisted of two CCD cameras (progressive scan SONY XC-55, 640*480 square pixels of resolution 7.4 μm , and with a 6 mm c-mount lens) fixed one metre apart and an LN-200 IMU (1 deg/hr). Along, there are a synchronisation pulse, a Matrox Meteor-II/Multi-Channel frame grabber and a screen, IMU data acquisition box developed at the EPFL-TOPO, a laptop, and the power supply.

7.2 - Conclusions

The major objective of this work was to develop, implement and test a robotic mobile mapping system employing vision-aided inertial navigation. The chief contributions lie in:

- Developing a novel integration methodology between vision and inertial sensors using complete modelling;
- Designing and implementing the SLAM software required to test the methodology;
- Setting a collaboration stage between Geomatics Engineering and Robotics.

To conclude, the quality of vision-based solution dictates the overall quality of the system. The errors in the photogrammetric modelling are governed by:

- Cameras quality and resolution
- The compromise between the focal length, stereo-base and the required field of vision that depend on the envisaged applications of the system
- The method used to measure the features' photo-coordinates

- The number, type, quality and location of used features

Due to the weak geometry and low cameras' quality, it was expected that the map accuracy and navigation quality from intersection and resection would not exceed 15 cm.

The accurate initialisation of the navigation and mapping systems is always important; however, in classical systems it is achieved by GPS and high-dynamics manoeuvring. For the current case, resection-derived EOP provide accurate initialisation, yet they have to be accompanied by accurate boresight corrections. Depending on the quality of the used IMU, gyro compassing can always be an option for attitude initialisation, though several minutes are needed. Regardless of the initialisation method, it was obvious that the use of ZUPT during the initialisation is highly favourable in order to accomplish accurate results.

Although computational consideration is always an issue in robotics SLAM, in this work it was not a concern because the feature coordinates determination filter was completely separated from the navigation filter. This way, in case of on-line performance, the system concentrates on achieving the best possible point matching processing.

In this thesis, the main concern was the *proof-of-concept*. It was shown that the concept of SLAM is naturally possible using this approach and that SLAM can be used in mapping systems when GNSS signals are not available or even in cases where a fast initialisation of the IMU is needed.

7.3 - Recommendations

From the findings in this thesis, the following recommendations can be drawn:

- ∴ Better sensors' quality is needed for an operational system: the system used in this thesis was a prototype. Vibrations in the bar holding the cameras caused a couple of degrees variation in the attitude when the vehicle was moving
- ∴ On-line camera calibration is recommended. In low and medium quality cameras, the lens and chip characteristics might change with time and temperature, so modelling them on-line will improve the photogrammetric products (map and position)
- ∴ When updates are made every one or two seconds, an automotive grade IMU could be used; this lowers the cost of the system
- ∴ Other sensors, although adding to the complexity of the system, can significantly improve the navigation quality in time. Such sensors can be odometer, compass, barometer, etc

- .: For a system oriented towards research, a laser scanner will be an asset for mapping, localisation and scale determination to be used in the photogrammetric problem
- .: The maximum possible number of map features, the better the solution becomes. This requires automated feature recognition algorithms that can match features, not only on a stereo-pair but also on successive images. The predicted position from the IMU will definitely help in narrowing the search area of same features
- .: In this thesis, mapping was made using a stereo-pair of images taken at the same time. It is recommended that more than one stereo-pair be used in order to have more degrees of freedom in the intersection LSA, and thus leading to a higher mapping quality
- .: Features chosen for either resection or intersection must be of a distance that guarantees an accurate solution
- .: Since no absolute reference might be available, performing a ZUPT every couple of minutes is highly recommended to improve the navigation quality of the system

*... I am late, but do not leave without me ...
let us start together, I can catch up ...*

APPENDIX A: PHOTOGRAMMETRY SOLUTION WITH QUATERNIONS

The same functional mathematical model as Equation (2.1) is used:

$$F(x) \equiv -x + x_0 - c \frac{R_{11}(X - X_0) + R_{12}(Y - Y_0) + R_{13}(Z - Z_0)}{R_{31}(X - X_0) + R_{32}(Y - Y_0) + R_{33}(Z - Z_0)} = -x + x_0 - c \frac{U}{W} = 0$$

$$F(y) \equiv -y + y_0 - c \frac{R_{21}(X - X_0) + R_{22}(Y - Y_0) + R_{23}(Z - Z_0)}{R_{31}(X - X_0) + R_{32}(Y - Y_0) + R_{33}(Z - Z_0)} = -y + y_0 - c \frac{V}{W} = 0$$

Due to the known problem of instability caused by using Euler angles, especially when one of these angles takes a value of 90 or 270 degrees, and due to the foreseen integration with the outputs of an IMU the quaternions, $\mathbf{q} = (q_1, q_2, q_3, q_4)$, are used in the rotation matrix.

Quaternions were introduced by Sir W. R. Hamilton (1805-1865) in the mid nineteenth century and they remained a piece of theory without potential usage until the mid twentieth century. Currently, quaternions are used in the areas of computer vision and graphics, virtual reality, theory of relativity, navigation, aerospace, etc. Their main advantage is the singularity-free rotation operations. An important feature of quaternions is that their norm has to be equal to unity; this means: $\|\mathbf{q}\|^2 = q_1^2 + q_2^2 + q_3^2 + q_4^2 = 1$; to achieve this relation, normalisation is usually done. For interested readers, see Kuipers (1984).

The association between the attitude angles and the quaternions does not depend on the parameterisation of rotation. This relation is based on a relationship between the elements of the rotation matrix R and those of the quaternions matrix Q as follows:

$$\begin{bmatrix} R_{11} & R_{12} & R_{13} \\ R_{21} & R_{22} & R_{23} \\ R_{31} & R_{32} & R_{33} \end{bmatrix} = \begin{bmatrix} (q_1^2 - q_2^2 - q_3^2 + q_4^2) & 2(q_1q_2 - q_3q_4) & 2(q_1q_3 + q_2q_4) \\ 2(q_1q_2 + q_3q_4) & (q_2^2 - q_1^2 - q_3^2 + q_4^2) & 2(q_2q_3 - q_1q_4) \\ 2(q_1q_3 - q_2q_4) & 2(q_2q_3 + q_1q_4) & (q_3^2 - q_1^2 - q_2^2 + q_4^2) \end{bmatrix}$$

Consequently, the co-linearity equations take the form:

$$F(x) \equiv -x + x_0 - c \frac{Q_{11}(X - X_0) + Q_{12}(Y - Y_0) + Q_{13}(Z - Z_0)}{Q_{31}(X - X_0) + Q_{32}(Y - Y_0) + Q_{33}(Z - Z_0)} = -x + x_0 - c \frac{U}{W} = 0$$

$$F(y) \equiv -y + y_0 - c \frac{Q_{21}(X - X_0) + Q_{22}(Y - Y_0) + Q_{23}(Z - Z_0)}{Q_{31}(X - X_0) + Q_{32}(Y - Y_0) + Q_{33}(Z - Z_0)} = -y + y_0 - c \frac{V}{W} = 0 \quad (\text{A.1})$$

Equations (2.1) describe the fundamental mathematical model for photogrammetric mapping, where it reveals the relationship between the image and the object coordinate systems. With this model, one can solve the basic problems of photogrammetric mapping, namely: resection and intersection, which when merged together form the photogrammetric triangulation also known as Bundle adjustment.

In photogrammetry, two terms are distinguished: interior and exterior orientation. The first term embraces the focal length and the coordinates of the projection of the perspective centre to the image plane: c, x_0, y_0 . The exterior orientation parameters (EOP), on the other hand, is a set of the coordinates of the perspective centre in the object frame and the three rotation angles: $X_0, Y_0, Z_0, \omega, \phi, \kappa$; but since the quaternions are used, the EOP is the set of the coordinates of the perspective centre in the object frame and the four quaternions: $X_0, Y_0, Z_0, q_1, q_2, q_3, q_4$.

In this chapter, all the vectors and matrices (**Bold**) headed by a prime (e.g., \mathbf{X}') refer to the resection and all those headed by two primes (e.g., \mathbf{X}'') refer to the intersection.

Resection

With the problem of resection (Fig. 2-2), the position and attitude (EOP) of an image are determined by having at least a set of four points whose coordinates are known in the object frame as well as in the image frame; these points are called Ground Control Points (GCP). Therefore, the known, unknowns and measurements are:

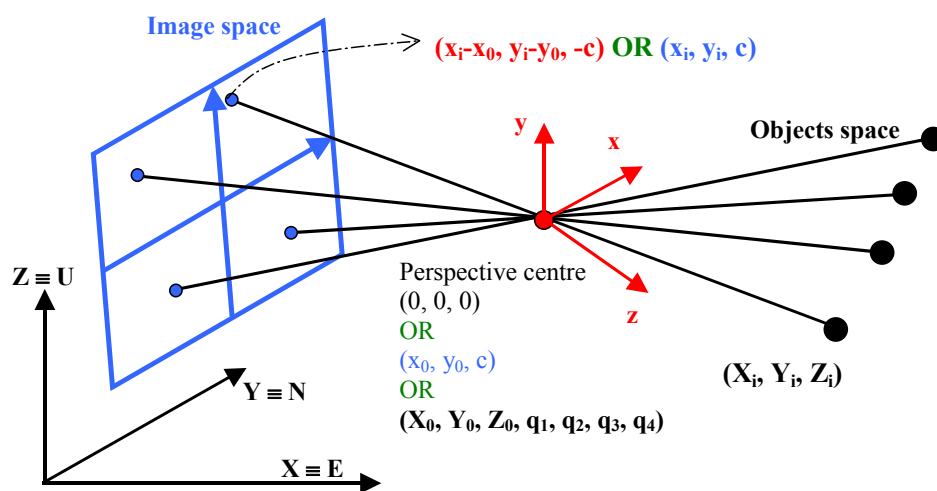


Figure A-7-1: Resection Problem

Measurements: $X_i, Y_i, Z_i, x_i, y_i, i = 1 \dots n$; **Unknowns:** $X_0, Y_0, Z_0, q_1, q_2, q_3, q_4$

In resection, there are seven unknowns; for the system of equation to be solved, seven equations are needed. In most cases, resection is handled in the frame of LSA. A minimum set of eight equations is used through measuring the photo-coordinates, (x_i, y_i) , of four GCPs. In addition to this, a constraint is forced here: $g \equiv q_1^2 + q_2^2 + q_3^2 + q_4^2$ has to be equal to one.

Resection Least-Squares Adjustment with Constraints

To solve resection, we consider the following vectors. The vector of the unknowns:

$$\mathbf{x}' = [X_0 \ Y_0 \ Z_0 \ q_1 \ q_2 \ q_3 \ q_4]^T \quad (\text{A.2})$$

is computed by:

$$\mathbf{x}' = \overset{\circ}{\mathbf{x}'} + \delta\mathbf{x}' \quad (\text{A.3})$$

where $\overset{\circ}{\mathbf{x}'}$ is the vector of the approximate values of \mathbf{x}' :

$$\overset{\circ}{\mathbf{x}'} = \left[\overset{\circ}{X}_0 \ \overset{\circ}{Y}_0 \ \overset{\circ}{Z}_0 \ \overset{\circ}{q}_1 \ \overset{\circ}{q}_2 \ \overset{\circ}{q}_3 \ \overset{\circ}{q}_4 \right]^T \quad (\text{A.4})$$

and $\delta\mathbf{x}'$ is the computed vector of corrections:

$$\delta\mathbf{x}' = [\delta X_0 \ \delta Y_0 \ \delta Z_0 \ \delta q_1 \ \delta q_2 \ \delta q_3 \ \delta q_4]^T \quad (\text{A.5})$$

The vector of measurements is:

$$\mathbf{y}' = [x_1 \ y_1 \ X_1 \ Y_1 \ Z_1 \ \dots \ x_n \ y_n \ X_n \ Y_n \ Z_n]^T \quad (\text{A.6})$$

Having the above vectors, $\delta\mathbf{x}'$ is computed through solving the following equations:

$$\mathbf{A}'\delta\mathbf{x}' + \mathbf{B}'\mathbf{v}' + \mathbf{w}' = \mathbf{0} \quad \text{and} \quad \mathbf{H}\delta\mathbf{x}' = \mathbf{z} \quad (\text{A.7})$$

\mathbf{v}'' is the vector of errors. The misclosure vector $\mathbf{w}' = F \begin{pmatrix} 0 \\ \mathbf{x}', \mathbf{y}' \end{pmatrix}$. The LSA solution of equations (A.8) is:

$$\delta \mathbf{x}' = \mathbf{N}'^{-1} \mathbf{U}' + \mathbf{N}'^{-1} \mathbf{H}'^T (\mathbf{H} \mathbf{N}'^{-1} \mathbf{H}'^T)^{-1} (\mathbf{z} - \mathbf{H} \mathbf{N}'^{-1} \mathbf{U}'), \quad (\text{A.8})$$

$$\text{with } \mathbf{N}' = \mathbf{A}'^T \mathbf{M}'^{-1} \mathbf{A}', \quad \mathbf{U}' = \mathbf{A}'^T \mathbf{M}'^{-1} \mathbf{w}', \quad \mathbf{M}' = \mathbf{B}' \mathbf{C}'_y \mathbf{B}'^T$$

The constraints are introduced through vector \mathbf{z} and matrix \mathbf{H} . Vector \mathbf{z} is computed as:

$$\mathbf{z} = 1 - \begin{pmatrix} 0 \\ q_1 \end{pmatrix}^2 - \begin{pmatrix} 0 \\ q_2 \end{pmatrix}^2 - \begin{pmatrix} 0 \\ q_3 \end{pmatrix}^2 - \begin{pmatrix} 0 \\ q_4 \end{pmatrix}^2 \quad (\text{A.9})$$

The stochastic model for the measurements is included in matrix \mathbf{C}'_y , the variance-covariance matrix, and it takes the following form:

$$\mathbf{C}'_y = \begin{bmatrix} \sigma_{x_1}^2 & 0 & 0 & 0 & 0 & \dots & 0 & 0 & 0 & 0 & 0 \\ & \sigma_{y_1}^2 & 0 & 0 & 0 & \dots & 0 & 0 & 0 & 0 & 0 \\ & & \sigma_{x_1}^2 & \sigma_{x_1 y_1} & \sigma_{x_1 z_1} & \dots & 0 & 0 & \sigma_{x_1 x_n} & \sigma_{x_1 y_n} & \sigma_{x_1 z_n} \\ & & & \sigma_{y_1}^2 & \sigma_{y_1 z_1} & \dots & 0 & 0 & \sigma_{y_1 x_n} & \sigma_{y_1 y_n} & \sigma_{y_1 z_n} \\ & & & & \sigma_{z_1}^2 & \dots & 0 & 0 & \sigma_{z_1 x_n} & \sigma_{z_1 y_n} & \sigma_{z_1 z_n} \\ & & & & & \ddots & \vdots & \vdots & \vdots & \vdots & \vdots \\ & & & & & & \sigma_{x_n}^2 & 0 & 0 & 0 & 0 \\ & & & & & & & \sigma_{y_n}^2 & 0 & 0 & 0 \\ & & & & & & & & \sigma_{x_n}^2 & \sigma_{x_n y_n} & \sigma_{x_n z_n} \\ & & & & & & & & & \sigma_{y_n}^2 & \sigma_{y_n z_n} \\ & & & & & & & & & & \sigma_{z_n}^2 \end{bmatrix}_{5n \times 5n} \quad (\text{A.10})$$

Matrix \mathbf{A}' is the first design matrix (Jacobi matrix) and it contains the derivatives of the measurement model (Eq. A.1) with respect to the Unknowns.

$$\mathbf{A}' = \begin{bmatrix} \frac{\partial F(x)_1}{\partial X_0} & \frac{\partial F(x)_1}{\partial Y_0} & \frac{\partial F(x)_1}{\partial Z_0} & \frac{\partial F(x)_1}{\partial q_1} & \frac{\partial F(x)_1}{\partial q_2} & \frac{\partial F(x)_1}{\partial q_3} & \frac{\partial F(x)_1}{\partial q_4} \\ \frac{\partial F(y)_1}{\partial X_0} & \frac{\partial F(y)_1}{\partial Y_0} & \frac{\partial F(y)_1}{\partial Z_0} & \frac{\partial F(y)_1}{\partial q_1} & \frac{\partial F(y)_1}{\partial q_2} & \frac{\partial F(y)_1}{\partial q_3} & \frac{\partial F(y)_1}{\partial q_4} \\ \vdots & \vdots & \vdots & \vdots & \vdots & \vdots & \vdots \\ \frac{\partial F(x)_n}{\partial X_0} & \frac{\partial F(x)_n}{\partial Y_0} & \frac{\partial F(x)_n}{\partial Z_0} & \frac{\partial F(x)_n}{\partial q_1} & \frac{\partial F(x)_n}{\partial q_2} & \frac{\partial F(x)_n}{\partial q_3} & \frac{\partial F(x)_n}{\partial q_4} \\ \frac{\partial F(y)_n}{\partial X_0} & \frac{\partial F(y)_n}{\partial Y_0} & \frac{\partial F(y)_n}{\partial Z_0} & \frac{\partial F(y)_n}{\partial q_1} & \frac{\partial F(y)_n}{\partial q_2} & \frac{\partial F(y)_n}{\partial q_3} & \frac{\partial F(y)_n}{\partial q_4} \\ \frac{\partial X_0}{\partial X_0} & \frac{\partial Y_0}{\partial Y_0} & \frac{\partial Z_0}{\partial Z_0} & \frac{\partial q_1}{\partial q_1} & \frac{\partial q_2}{\partial q_2} & \frac{\partial q_3}{\partial q_3} & \frac{\partial q_4}{\partial q_4} \end{bmatrix}_{2n \times 7} \quad (\text{A.11})$$

with the following elements:

$$\frac{\partial F(x)}{\partial X_0} = -\frac{c}{W^2} (Q_{31}U - Q_{11}W), \quad \frac{\partial F(x)}{\partial Y_0} = -\frac{c}{W^2} (Q_{32}U - Q_{12}W), \quad \frac{\partial F(x)}{\partial Z_0} = -\frac{c}{W^2} (Q_{33}U - Q_{13}W)$$

$$\frac{\partial F(y)}{\partial X_0} = -\frac{c}{W^2} (Q_{31}V - Q_{21}W), \quad \frac{\partial F(y)}{\partial Y_0} = -\frac{c}{W^2} (Q_{32}V - Q_{22}W), \quad \frac{\partial F(y)}{\partial Z_0} = -\frac{c}{W^2} (Q_{33}V - Q_{23}W)$$

$$\frac{\partial F(x)}{\partial q_1} = -2 \frac{c}{W^2} [(X_0 - X)(q_1W - q_3U) + (Y_0 - Y)(q_2W - q_4U) + (Z_0 - Z)(q_3W + q_1U)]$$

$$\frac{\partial F(x)}{\partial q_2} = -2 \frac{c}{W^2} [(X_0 - X)(-q_2W + q_4U) + (Y_0 - Y)(q_1W - q_3U) + (Z_0 - Z)(q_4W + q_2U)]$$

$$\frac{\partial F(x)}{\partial q_3} = -2 \frac{c}{W^2} [(X_0 - X)(-q_3W - q_1U) + (Y_0 - Y)(-q_4W - q_2U) + (Z_0 - Z)(q_1W - q_3U)]$$

$$\frac{\partial F(x)}{\partial q_4} = -2 \frac{c}{W^2} [(X_0 - X)(q_4W + q_2U) + (Y_0 - Y)(-q_3W - q_1U) + (Z_0 - Z)(q_2W - q_4U)]$$

$$\frac{\partial F(y)}{\partial q_1} = -2 \frac{c}{W^2} [(X_0 - X)(q_2W - q_3V) + (Y_0 - Y)(-q_1W - q_4V) + (Z_0 - Z)(-q_4W + q_1V)]$$

$$\frac{\partial F(y)}{\partial q_2} = -2 \frac{c}{W^2} [(X_0 - X)(q_1W + q_4V) + (Y_0 - Y)(q_2W - q_3V) + (Z_0 - Z)(q_3W + q_2V)]$$

$$\frac{\partial F(y)}{\partial q_3} = -2 \frac{c}{W^2} [(X_0 - X)(q_4W - q_1V) + (Y_0 - Y)(-q_3W - q_2V) + (Z_0 - Z)(q_2W - q_3V)]$$

$$\frac{\partial F(y)}{\partial q_4} = -2 \frac{c}{W^2} [(X_0 - X)(q_3 W + q_2 V) + (Y_0 - Y)(q_4 W - q_1 V) + (Z_0 - Z)(-q_1 W - q_4 V)]$$

Matrix **B'** is the second design matrix and it contains the derivatives of the measurement model (Equation A.1) with respect to the vector of measurements. It has the following form:

$$\mathbf{B}' = \begin{bmatrix} \frac{\partial F(x)_1}{\partial x_1} & \frac{\partial F(x)_1}{\partial y_1} & \frac{\partial F(x)_1}{\partial X_1} & \frac{\partial F(x)_1}{\partial Y_1} & \frac{\partial F(x)_1}{\partial Z_1} & \dots & 0 & 0 & 0 & 0 & 0 \\ \frac{\partial F(y)_1}{\partial x_1} & \frac{\partial F(y)_1}{\partial y_1} & \frac{\partial F(y)_1}{\partial X_1} & \frac{\partial F(y)_1}{\partial Y_1} & \frac{\partial F(y)_1}{\partial Z_1} & \dots & 0 & 0 & 0 & 0 & 0 \\ \vdots & \vdots & \vdots & \vdots & \vdots & \ddots & \vdots & \vdots & \vdots & \vdots & \vdots \\ 0 & 0 & 0 & 0 & 0 & \dots & \frac{\partial F(x)_n}{\partial x_n} & \frac{\partial F(x)_n}{\partial y_n} & \frac{\partial F(x)_n}{\partial X_n} & \frac{\partial F(x)_n}{\partial Y_n} & \frac{\partial F(x)_n}{\partial Z_n} \\ 0 & 0 & 0 & 0 & 0 & \dots & \frac{\partial F(y)_n}{\partial x_n} & \frac{\partial F(y)_n}{\partial y_n} & \frac{\partial F(y)_n}{\partial X_n} & \frac{\partial F(y)_n}{\partial Y_n} & \frac{\partial F(y)_n}{\partial Z_n} \end{bmatrix}$$

$$= \begin{bmatrix} -1 & 0 & \frac{\partial F(x)_1}{\partial X_1} & \frac{\partial F(x)_1}{\partial Y_1} & \frac{\partial F(x)_1}{\partial Z_1} & \dots & 0 & 0 & 0 & 0 & 0 \\ 0 & -1 & \frac{\partial F(y)_1}{\partial X_1} & \frac{\partial F(y)_1}{\partial Y_1} & \frac{\partial F(y)_1}{\partial Z_1} & \dots & 0 & 0 & 0 & 0 & 0 \\ \vdots & \vdots & \vdots & \vdots & \vdots & \ddots & \vdots & \vdots & \vdots & \vdots & \vdots \\ 0 & 0 & 0 & 0 & 0 & \dots & -1 & 0 & \frac{\partial F(x)_n}{\partial X_n} & \frac{\partial F(x)_n}{\partial Y_n} & \frac{\partial F(x)_n}{\partial Z_n} \\ 0 & 0 & 0 & 0 & 0 & \dots & 0 & -1 & \frac{\partial F(y)_n}{\partial X_n} & \frac{\partial F(y)_n}{\partial Y_n} & \frac{\partial F(y)_n}{\partial Z_n} \end{bmatrix}_{2n \times 5n} \quad (\text{A.12})$$

The other elements of matrix **B'** are:

$$\frac{\partial F(x)}{\partial X} = \frac{c}{W^2} (Q_{31}U - Q_{11}W), \quad \frac{\partial F(x)}{\partial Y} = \frac{c}{W^2} (Q_{32}U - Q_{12}W), \quad \frac{\partial F(x)}{\partial Z} = \frac{c}{W^2} (Q_{33}U - Q_{13}W)$$

$$\frac{\partial F(y)}{\partial X} = \frac{c}{W^2} (Q_{31}V - Q_{21}W), \quad \frac{\partial F(y)}{\partial Y} = \frac{c}{W^2} (Q_{32}V - Q_{22}W), \quad \frac{\partial F(y)}{\partial Z} = \frac{c}{W^2} (Q_{33}V - Q_{23}W)$$

Matrix **H** is a Jacobi matrix with elements: $H_i = \partial g / \partial x_i$, where $g \equiv 1 - q_1^2 - q_2^2 - q_3^2 - q_4^2 = 0$; thus, it takes the following form:

$$\mathbf{H} = \begin{bmatrix} 0 & 0 & 0 & -2\overset{\circ}{q}_1 & -2\overset{\circ}{q}_2 & -2\overset{\circ}{q}_3 & -2\overset{\circ}{q}_4 \end{bmatrix} \quad (\text{A.13})$$

The approximate values are used to compute the matrices \mathbf{A}' , \mathbf{B}' and \mathbf{H} .

The precision estimation of the parameters, residuals and measurements are computed, respectively, as:

$$\mathbf{C}'_{\hat{\mathbf{x}}} = \mathbf{N}'^{-1} \left[\mathbf{I} - \mathbf{H}^T (\mathbf{H} \mathbf{N}'^{-1} \mathbf{H}^T)^{-1} \mathbf{H} \mathbf{N}'^{-1} \right] \quad (\text{A.14})$$

$$\mathbf{C}'_{\mathbf{v}} = \mathbf{C}'_{\mathbf{y}} \mathbf{B}'^T \mathbf{M}'^{-1} \mathbf{B}' \mathbf{C}'_{\mathbf{y}} - \mathbf{C}'_{\mathbf{y}} \mathbf{B}'^T \mathbf{M}'^{-1} \mathbf{A}' \left(\mathbf{N}'^{-1} - \mathbf{N}'^{-1} \mathbf{H}^T (\mathbf{H} \mathbf{N}'^{-1} \mathbf{H}^T)^{-1} \mathbf{H} \mathbf{N}'^{-1} \right) \mathbf{A}'^T \mathbf{M}'^{-1} \mathbf{B}' \mathbf{C}'_{\mathbf{y}} \quad (\text{A.15})$$

$$\mathbf{C}'_{\hat{\mathbf{y}}} = \mathbf{C}'_{\mathbf{y}} - \mathbf{C}'_{\mathbf{v}} \quad (\text{A.16})$$

The a-posteriori variance factor is:

$$\hat{\sigma}_0^2 = \frac{\mathbf{v}^T \mathbf{P} \mathbf{v}}{2n - 7 + 1} \quad (\text{A.17})$$

where $2n$ is the number of measurements, 7 is the number of the unknowns and 1 is the number of constraints.

Intersection

By the problem of intersection (Figure A-2), two images, whose EOP are known, are used to determine the coordinates in the object frame of features found on the two images simultaneously, employing the principle of stereovision; so, known, unknowns and measurements (R and L designate the Right and Left camera/image) are:

Measurements: $X_{0L/R}, Y_{0L/R}, Z_{0L/R}, q_{1L/R}, q_{2L/R}, q_{3L/R}, q_{4L/R}, x_{ij}, y_{ij}$; **Unknowns:** X_i, Y_i, Z_i
 $i = 1 \dots n, j = R, L$

Intersection is always handled in the frame of LSA because the measurements ($4n$) are always more than the unknowns ($3n$).

Intersection Least-Squares Adjustment

To solve resection, we consider the following vectors. The vector of the unknowns:

$$\mathbf{x}'' = [X_1 \ Y_1 \ Z_1 \ \dots \ X_n \ Y_n \ Z_n]^T \quad (\text{A.18})$$

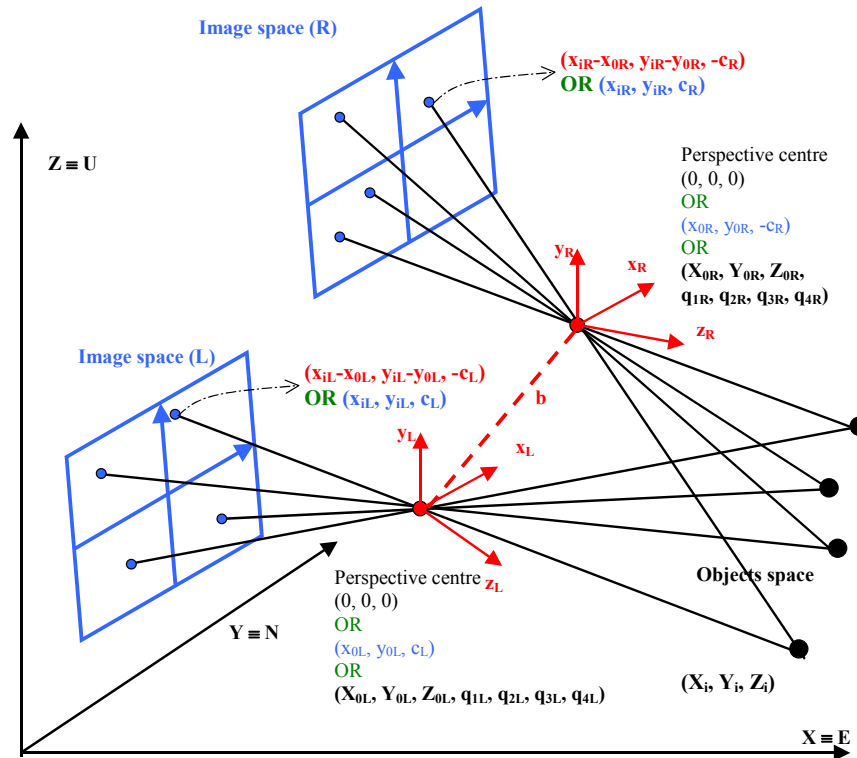


Figure A-7-2: Intersection Problem

is computed by:

$$\mathbf{x}'' = \overset{\circ}{\mathbf{x}}'' + \delta \mathbf{x}'' \quad (\text{A.19})$$

where $\overset{\circ}{\mathbf{x}}''$ is the vector of the approximate values of the unknowns:

$$\overset{\circ}{\mathbf{x}}'' = \left[\overset{\circ}{X}_1 \quad \overset{\circ}{Y}_1 \quad \overset{\circ}{Z}_1 \quad \cdots \quad \overset{\circ}{X}_n \quad \overset{\circ}{Y}_n \quad \overset{\circ}{Z}_n \right]^T \quad (\text{A.20})$$

and $\delta \mathbf{x}''$ is the computed vector of corrections:

$$\delta \mathbf{x}'' = [\delta X_1 \quad \delta Y_1 \quad \delta Z_1 \quad \cdots \quad \delta X_n \quad \delta Y_n \quad \delta Z_n]^T \quad (\text{A.21})$$

The vector of measurements is:

$$\mathbf{y}'' = \left[\begin{array}{cccccccccccc} x_{L1} & y_{L1} & \cdots & x_{Ln} & y_{Ln} & X_{L0} & Y_{L0} & Z_{L0} & q_{L1} & q_{L2} & q_{L3} & q_{L4} \\ x_{R1} & y_{R1} & \cdots & x_{Rn} & y_{Rn} & X_{R0} & Y_{R0} & Z_{R0} & q_{R1} & q_{R2} & q_{R3} & q_{R4} \end{array} \right]^T \quad (\text{A.22})$$

Having the above vectors, $\delta \mathbf{x}''$ is computed through solving the following equation:

$$\mathbf{A}'' \delta \mathbf{x}'' + \mathbf{B}'' \mathbf{v}'' + \mathbf{w}'' = \mathbf{0} \tag{A.23}$$

\mathbf{v}'' is the vector of errors. The misclosure vector $\mathbf{w}'' = \mathbf{F} \begin{pmatrix} 0 \\ \mathbf{x}'', \mathbf{y}'' \end{pmatrix}$.

The LSA solution of Eq. (A.24) is:

$$\delta \mathbf{x}'' = \mathbf{N}''^{-1} \mathbf{U}'' \tag{A.24}$$

where $\mathbf{N}'' = \mathbf{A}''^T \mathbf{M}''^{-1} \mathbf{A}''$, $\mathbf{U}'' = \mathbf{A}''^T \mathbf{M}''^{-1} \mathbf{w}''$, $\mathbf{M}'' = \mathbf{B}'' \mathbf{C}_y'' \mathbf{B}''^T$

The error information of the measurements \mathbf{C}_y'' is included in the variance-covariance matrix:

$$\mathbf{C}_y'' = \begin{bmatrix} \mathbf{C}_{Ly}'' & \mathbf{C}_{LRy}'' \\ \mathbf{C}_{LRy}''^T & \mathbf{C}_{Ry}'' \end{bmatrix}_{(4n+14) \times (4n+14)} \tag{A.25}$$

$$\mathbf{C}_{jy}'' = \begin{bmatrix} \sigma_{x_{j1}}^2 & 0 & \dots & 0 & 0 & 0 & 0 & 0 & 0 & 0 & 0 & 0 & 0 \\ & \sigma_{y_{j1}}^2 & \dots & 0 & 0 & 0 & 0 & 0 & 0 & 0 & 0 & 0 & 0 \\ & & \ddots & \vdots & \vdots & \vdots & \vdots & \vdots & \vdots & \vdots & \vdots & \vdots & \vdots \\ & & & \sigma_{x_{jn}}^2 & 0 & 0 & 0 & 0 & 0 & 0 & 0 & 0 & 0 \\ & & & & \sigma_{y_{jn}}^2 & 0 & 0 & 0 & 0 & 0 & 0 & 0 & 0 \\ \hline & & & & & \sigma_{X_{L0}}^2 & \sigma_{X_{j0}Y_{j0}} & \sigma_{X_{j0}Z_{j0}} & \sigma_{X_{j0}q_{j1}} & \sigma_{X_{j0}q_{j2}} & \sigma_{X_{j0}q_{j3}} & \sigma_{X_{j0}q_{j4}} \\ & & & & & & \sigma_{Y_{j0}}^2 & \sigma_{Y_{j0}Z_{j0}} & \sigma_{Y_{j0}q_{j1}} & \sigma_{Y_{j0}q_{j2}} & \sigma_{Y_{j0}q_{j3}} & \sigma_{Y_{j0}q_{j4}} \\ & & & & & & & \sigma_{Z_{j0}}^2 & \sigma_{Z_{j0}q_{j1}} & \sigma_{Z_{j0}q_{j2}} & \sigma_{Z_{j0}q_{j3}} & \sigma_{Z_{j0}q_{j4}} \\ & & & & & & & & \sigma_{q_{j1}}^2 & \sigma_{q_{j1}q_{j2}} & \sigma_{q_{j1}q_{j3}} & \sigma_{q_{j1}q_{j4}} \\ & & & & & & & & & \sigma_{q_{j2}}^2 & \sigma_{q_{j2}q_{j3}} & \sigma_{q_{j2}q_{j4}} \\ & & & & & & & & & & \sigma_{q_{j3}}^2 & \sigma_{q_{j3}q_{j4}} \\ & & & & & & & & & & & \sigma_{q_{j4}}^2 \end{bmatrix} \tag{A.26}$$

$$\mathbf{C}_{LRy}'' = \left[\begin{array}{cccc|cccccccc}
 0 & 0 & \dots & 0 & 0 & 0 & 0 & 0 & 0 & 0 & 0 & 0 & 0 \\
 0 & \dots & 0 & 0 & 0 & 0 & 0 & 0 & 0 & 0 & 0 & 0 & 0 \\
 & & \ddots & \vdots & \vdots & \vdots & \vdots & \vdots & \vdots & \vdots & \vdots & \vdots & \vdots \\
 & & & 0 & 0 & 0 & 0 & 0 & 0 & 0 & 0 & 0 & 0 \\
 & & & & 0 & 0 & 0 & 0 & 0 & 0 & 0 & 0 & 0 \\
 \hline
 & & & & \sigma_{X_{L0}X_{R0}} & \sigma_{X_{L0}Y_{R0}} & \sigma_{X_{L0}Z_{R0}} & \sigma_{X_{L0}q_{R1}} & \sigma_{X_{L0}q_{R2}} & \sigma_{X_{L0}q_{R3}} & \sigma_{X_{L0}q_{R4}} & & \\
 & & & & & \sigma_{Y_{L0}Y_{R0}} & \sigma_{Y_{L0}Z_{R0}} & \sigma_{Y_{L0}q_{R1}} & \sigma_{Y_{L0}q_{R2}} & \sigma_{Y_{L0}q_{R3}} & \sigma_{Y_{L0}q_{R4}} & & \\
 & & & & & & \sigma_{Z_{L0}Z_{R0}} & \sigma_{Z_{L0}q_{R1}} & \sigma_{Z_{L0}q_{R2}} & \sigma_{Z_{L0}q_{R3}} & \sigma_{Z_{L0}q_{R4}} & & \\
 & & & & & & & \sigma_{q_{L1}q_{R1}} & \sigma_{q_{L1}q_{R2}} & \sigma_{q_{L1}q_{R3}} & \sigma_{q_{L1}q_{R4}} & & \\
 & & & & & & & & \sigma_{q_{L2}q_{R2}} & \sigma_{q_{L2}q_{R3}} & \sigma_{q_{L2}q_{R4}} & & \\
 & & & & & & & & & \sigma_{q_{L3}q_{R3}} & \sigma_{q_{L3}q_{R4}} & & \\
 & & & & & & & & & & \sigma_{q_{L4}q_{R4}} & & \\
 \hline
 \text{SYM.} & & & & & & & & & & & &
 \end{array} \right] \tag{A.27}$$

Matrix \mathbf{A}'' is the first design matrix (Jacobi matrix) and it contains the derivatives of the measurement model (Eq. A.1) with respect to the Unknowns.

$$\mathbf{A}'' = \begin{bmatrix} \mathbf{A}''_L \\ \mathbf{A}''_R \end{bmatrix}_{4n \times 3n} \tag{A.28}$$

With,

$$\mathbf{A}''_{j=(L,R)} = \begin{bmatrix} \frac{\partial F(x)_{j1}}{\partial X_1} & \frac{\partial F(x)_{j1}}{\partial Y_1} & \frac{\partial F(x)_{j1}}{\partial Z_1} & \dots & \frac{\partial F(x)_{j1}}{\partial X_n} & \frac{\partial F(x)_{j1}}{\partial Y_n} & \frac{\partial F(x)_{j1}}{\partial Z_n} \\
 \frac{\partial F(y)_{j1}}{\partial X_1} & \frac{\partial F(y)_{j1}}{\partial Y_1} & \frac{\partial F(y)_{j1}}{\partial Z_1} & \dots & \frac{\partial F(y)_{j1}}{\partial X_n} & \frac{\partial F(y)_{j1}}{\partial Y_n} & \frac{\partial F(y)_{j1}}{\partial Z_n} \\
 \vdots & \vdots & \vdots & \ddots & \vdots & \vdots & \vdots \\
 \frac{\partial F(x)_{jn}}{\partial X_1} & \frac{\partial F(x)_{jn}}{\partial Y_1} & \frac{\partial F(x)_{jn}}{\partial Z_1} & \dots & \frac{\partial F(x)_{jn}}{\partial X_n} & \frac{\partial F(x)_{jn}}{\partial Y_n} & \frac{\partial F(x)_{jn}}{\partial Z_n} \\
 \frac{\partial F(y)_{jn}}{\partial X_1} & \frac{\partial F(y)_{jn}}{\partial Y_1} & \frac{\partial F(y)_{jn}}{\partial Z_1} & \dots & \frac{\partial F(y)_{jn}}{\partial X_n} & \frac{\partial F(y)_{jn}}{\partial Y_n} & \frac{\partial F(y)_{jn}}{\partial Z_n} \\
 \vdots & \vdots & \vdots & \ddots & \vdots & \vdots & \vdots \end{bmatrix}_{2n \times 3n} = \begin{bmatrix} \frac{\partial F(x)_{j1}}{\partial X_1} & \frac{\partial F(x)_{j1}}{\partial Y_1} & \frac{\partial F(x)_{j1}}{\partial Z_1} & \dots & 0 & 0 & 0 \\
 \frac{\partial F(y)_{j1}}{\partial X_1} & \frac{\partial F(y)_{j1}}{\partial Y_1} & \frac{\partial F(y)_{j1}}{\partial Z_1} & \dots & 0 & 0 & 0 \\
 \vdots & \vdots & \vdots & \ddots & \vdots & \vdots & \vdots \\
 0 & 0 & 0 & \dots & \frac{\partial F(x)_{jn}}{\partial X_n} & \frac{\partial F(x)_{jn}}{\partial Y_n} & \frac{\partial F(x)_{jn}}{\partial Z_n} \\
 0 & 0 & 0 & \dots & \frac{\partial F(y)_{jn}}{\partial X_n} & \frac{\partial F(y)_{jn}}{\partial Y_n} & \frac{\partial F(y)_{jn}}{\partial Z_n} \end{bmatrix}_{2n \times 3n} \tag{A.29}$$

with the following elements:

$$\frac{\partial F(x)}{\partial X} = \frac{c}{W^2} (Q_{31}U - Q_{11}W), \quad \frac{\partial F(x)}{\partial Y} = \frac{c}{W^2} (Q_{32}U - Q_{12}W), \quad \frac{\partial F(x)}{\partial Z} = \frac{c}{W^2} (Q_{33}U - Q_{13}W)$$

$$\frac{\partial F(y)}{\partial X} = \frac{c}{W^2} (Q_{31}V - Q_{21}W), \quad \frac{\partial F(y)}{\partial Y} = \frac{c}{W^2} (Q_{32}V - Q_{22}W), \quad \frac{\partial F(y)}{\partial Z} = \frac{c}{W^2} (Q_{33}V - Q_{23}W)$$

Matrix \mathbf{B}'' is the second design matrix and it contains the derivatives of the measurement model (Eq. 2.1) with respect to the vector of measurements. It has the following form:

$$\mathbf{B}'' = \begin{bmatrix} \mathbf{B}''_{\mathbf{L}} & \mathbf{B}''_{\mathbf{LR}} \\ \mathbf{B}''_{\mathbf{LR}}^T & \mathbf{B}''_{\mathbf{R}} \end{bmatrix}_{4n \times 4n+14}; \quad \mathbf{B}''_{\mathbf{LR}} = \mathbf{0} \quad \text{and,}$$

$$\mathbf{B}''_{\mathbf{j}} = \begin{bmatrix} \frac{\partial F(x)_{j1}}{\partial x_{j1}} & \frac{\partial F(x)_{j1}}{\partial y_{j1}} & \dots & \frac{\partial F(x)_{j1}}{\partial x_{jn}} & \frac{\partial F(x)_{j1}}{\partial y_{jn}} \\ \frac{\partial F(y)_{j1}}{\partial x_{j1}} & \frac{\partial F(y)_{j1}}{\partial y_{j1}} & \dots & \frac{\partial F(y)_{j1}}{\partial x_{jn}} & \frac{\partial F(y)_{j1}}{\partial y_{jn}} \\ \vdots & \vdots & \ddots & \vdots & \vdots \\ \frac{\partial F(x)_{jn}}{\partial x_{j1}} & \frac{\partial F(x)_{jn}}{\partial y_{j1}} & \dots & \frac{\partial F(x)_{jn}}{\partial x_{jn}} & \frac{\partial F(x)_{jn}}{\partial y_{jn}} \\ \frac{\partial F(y)_{jn}}{\partial x_{j1}} & \frac{\partial F(y)_{jn}}{\partial y_{j1}} & \dots & \frac{\partial F(y)_{jn}}{\partial x_{jn}} & \frac{\partial F(y)_{jn}}{\partial y_{jn}} \\ \frac{\partial F(x)_{j1}}{\partial x_{j0}} & \frac{\partial F(x)_{j1}}{\partial y_{j0}} & \frac{\partial F(x)_{j1}}{\partial z_{j0}} & \frac{\partial F(x)_{j1}}{\partial q_{j1}} & \frac{\partial F(x)_{j1}}{\partial q_{j2}} & \frac{\partial F(x)_{j1}}{\partial q_{j3}} & \frac{\partial F(x)_{j1}}{\partial q_{j4}} \\ \frac{\partial F(y)_{j1}}{\partial x_{j0}} & \frac{\partial F(y)_{j1}}{\partial y_{j0}} & \frac{\partial F(y)_{j1}}{\partial z_{j0}} & \frac{\partial F(y)_{j1}}{\partial q_{j1}} & \frac{\partial F(y)_{j1}}{\partial q_{j2}} & \frac{\partial F(y)_{j1}}{\partial q_{j3}} & \frac{\partial F(y)_{j1}}{\partial q_{j4}} \\ \vdots & \vdots & \vdots & \vdots & \vdots & \vdots & \vdots \\ \frac{\partial F(x)_{jn}}{\partial x_{j0}} & \frac{\partial F(x)_{jn}}{\partial y_{j0}} & \frac{\partial F(x)_{jn}}{\partial z_{j0}} & \frac{\partial F(x)_{jn}}{\partial q_{j1}} & \frac{\partial F(x)_{jn}}{\partial q_{j2}} & \frac{\partial F(x)_{jn}}{\partial q_{j3}} & \frac{\partial F(x)_{jn}}{\partial q_{j4}} \\ \frac{\partial F(y)_{jn}}{\partial x_{j0}} & \frac{\partial F(y)_{jn}}{\partial y_{j0}} & \frac{\partial F(y)_{jn}}{\partial z_{j0}} & \frac{\partial F(y)_{jn}}{\partial q_{j1}} & \frac{\partial F(y)_{jn}}{\partial q_{j2}} & \frac{\partial F(y)_{jn}}{\partial q_{j3}} & \frac{\partial F(y)_{jn}}{\partial q_{j4}} \end{bmatrix}_{2n \times 2n+7}$$

$$= \begin{bmatrix} -1 & 0 & \dots & 0 & 0 \\ 0 & -1 & \dots & 0 & 0 \\ \vdots & \vdots & \ddots & \vdots & \vdots \\ 0 & 0 & \dots & -1 & 0 \\ 0 & 0 & \dots & 0 & -1 \end{bmatrix} \begin{bmatrix} \frac{\partial F(x)_{j1}}{\partial X_{j0}} & \frac{\partial F(x)_{j1}}{\partial Y_{j0}} & \frac{\partial F(x)_{j1}}{\partial Z_{j0}} & \frac{\partial F(x)_{j1}}{\partial q_{j1}} & \frac{\partial F(x)_{j1}}{\partial q_{j2}} & \frac{\partial F(x)_{j1}}{\partial q_{j3}} & \frac{\partial F(x)_{j1}}{\partial q_{j4}} \\ \frac{\partial F(y)_{j1}}{\partial X_{j0}} & \frac{\partial F(y)_{j1}}{\partial Y_{j0}} & \frac{\partial F(y)_{j1}}{\partial Z_{j0}} & \frac{\partial F(y)_{j1}}{\partial q_{j1}} & \frac{\partial F(y)_{j1}}{\partial q_{j2}} & \frac{\partial F(y)_{j1}}{\partial q_{j3}} & \frac{\partial F(y)_{j1}}{\partial q_{j4}} \\ \vdots & \vdots & \vdots & \vdots & \vdots & \vdots & \vdots \\ \frac{\partial F(x)_{jn}}{\partial X_{j0}} & \frac{\partial F(x)_{jn}}{\partial Y_{j0}} & \frac{\partial F(x)_{jn}}{\partial Z_{j0}} & \frac{\partial F(x)_{jn}}{\partial q_{j1}} & \frac{\partial F(x)_{jn}}{\partial q_{j2}} & \frac{\partial F(x)_{jn}}{\partial q_{j3}} & \frac{\partial F(x)_{jn}}{\partial q_{j4}} \\ \frac{\partial F(y)_{jn}}{\partial X_{j0}} & \frac{\partial F(y)_{jn}}{\partial Y_{j0}} & \frac{\partial F(y)_{jn}}{\partial Z_{j0}} & \frac{\partial F(y)_{jn}}{\partial q_{j1}} & \frac{\partial F(y)_{jn}}{\partial q_{j2}} & \frac{\partial F(y)_{jn}}{\partial q_{j3}} & \frac{\partial F(y)_{jn}}{\partial q_{j4}} \end{bmatrix}_{2n \times 2n+7} \quad (\text{A.30})$$

The elements of the above two matrices, \mathbf{B}_L'' and \mathbf{B}_R'' , are computed in the same way as those of the first design matrix in resection \mathbf{A}' , after taking into account the two images, Left and Right. The approximate values are used to compute the matrices \mathbf{A}'' and \mathbf{B}'' .

In the LSA adjustment of intersection, each point is solved independently using a stereo-model. The equation of combined case LSA can take the form:

$$\mathbf{A}_{ji}'' \delta \mathbf{x}_i'' + \mathbf{B}_{ji}'' \mathbf{v}_{ji}'' + \mathbf{w}_{ji}'' = 0 \quad (\text{A.31})$$

where the subscript i denotes feature i , and j indicates Left or Right images (camera).

The solution of $\delta \mathbf{x}_i''$ is:

$$\delta \mathbf{x}_i'' = (\mathbf{N}_{Li}'' + \mathbf{N}_{Ri}'')^{-1} (\mathbf{U}_{Li}'' + \mathbf{U}_{Ri}'') \quad (\text{A.32})$$

$$\text{with} \quad \mathbf{N}_{Li}'' = \mathbf{A}_{Li}''^T (\mathbf{B}_{Li}'' \mathbf{C}_{Ly}'' \mathbf{B}_{Li}''^T)^{-1} \mathbf{A}_{Li}'' \quad \mathbf{N}_{Ri}'' = \mathbf{A}_{Ri}''^T (\mathbf{B}_{Ri}'' \mathbf{C}_{Ry}'' \mathbf{B}_{Ri}''^T)^{-1} \mathbf{A}_{Ri}''$$

$$\mathbf{U}_{Li}'' = \mathbf{A}_{Li}''^T (\mathbf{B}_{Li}'' \mathbf{C}_{Ly}'' \mathbf{B}_{Li}''^T)^{-1} \mathbf{w}_{Li}'' \quad \mathbf{U}_{Ri}'' = \mathbf{A}_{Ri}''^T (\mathbf{B}_{Ri}'' \mathbf{C}_{Ry}'' \mathbf{B}_{Ri}''^T)^{-1} \mathbf{w}_{Ri}''$$

The precision estimations are computed as in Chapter 2.

APPENDIX B: CAMERAS' CALIBRATION

For each camera (Left and Right), an independent calibration process was carried out. Photo-coordinates were measured in Socket-set® and then were input to BINGO-F® to perform the calibration.

BINGO® provides the adjusted focal length and principle point photo-coordinates, in addition to the calibration parameters.

The calibration field is located in the Geodetic Engineering Laboratory at the EPFL. A set of 15 GCPs, measured by a total-station, was used for the calibration task. In addition to the GCP, photo-coordinates of 12 tie points were also used.

Nine images for each camera were taken in the following order:

9	6	3
8	5	2
7	4	1

Calibration of the Left Camera

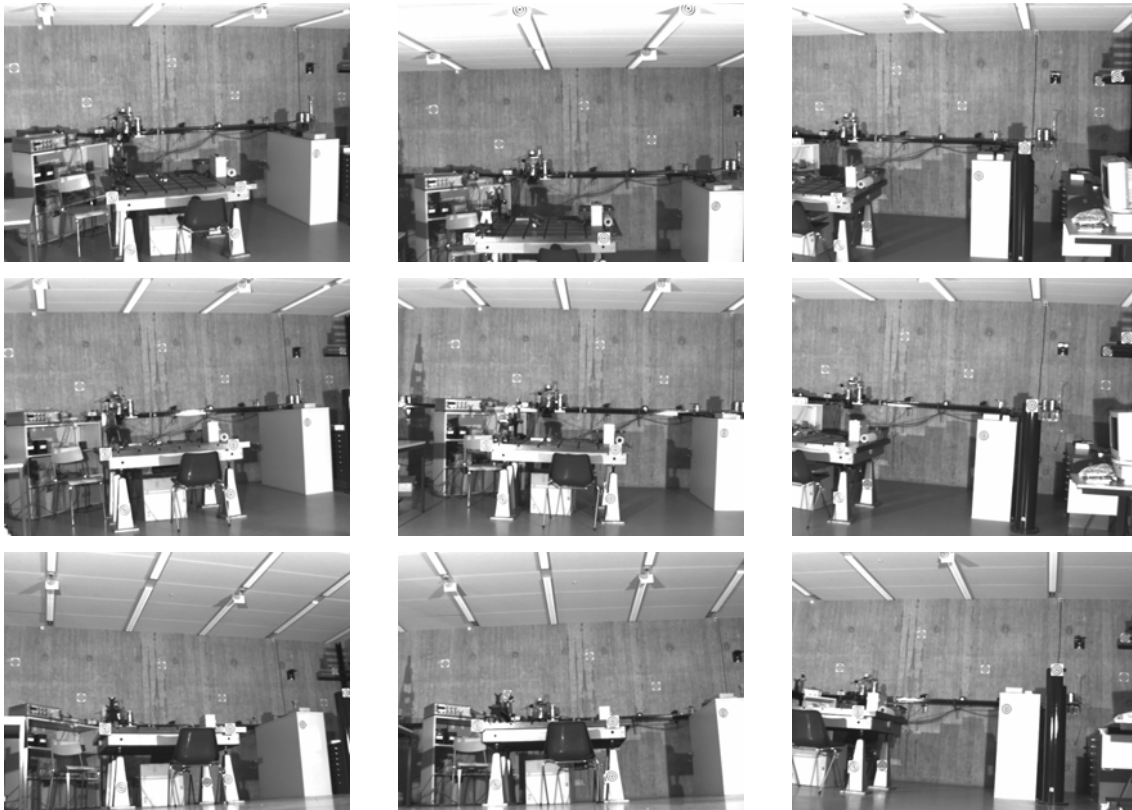
Table (B-2) shows the images that were taken from the Left camera, where the targets are clearly seen. (The different equipments are part of the Lab and have nothing to do with the calibration.)

The focal length and principle point's photo-coordinates of the Left camera are (mm):

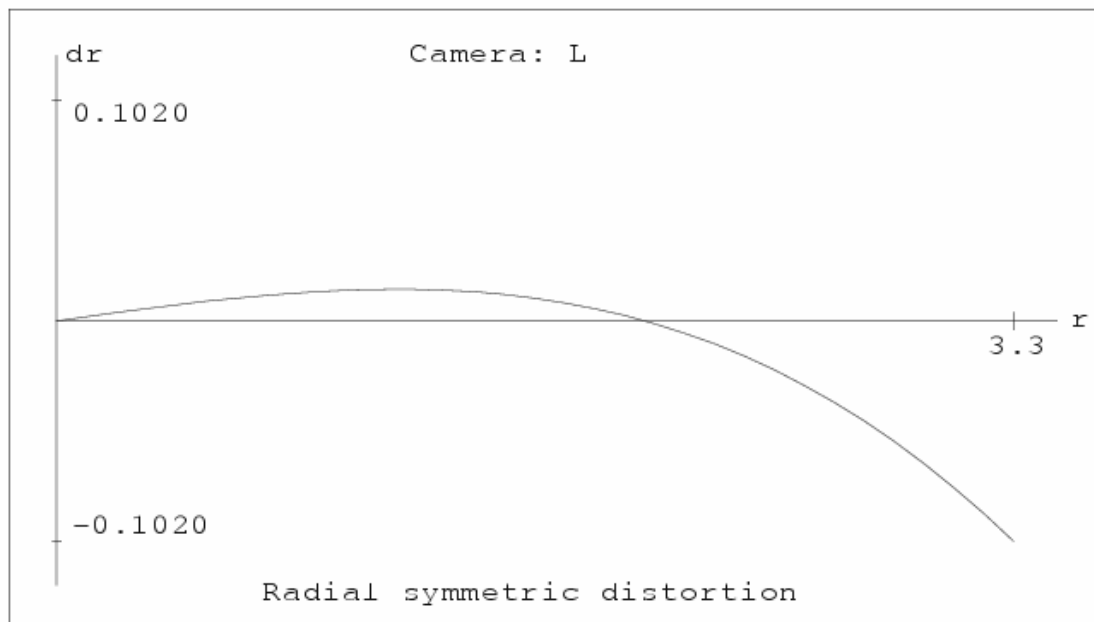
Focal length: 6.07, std = 0.009

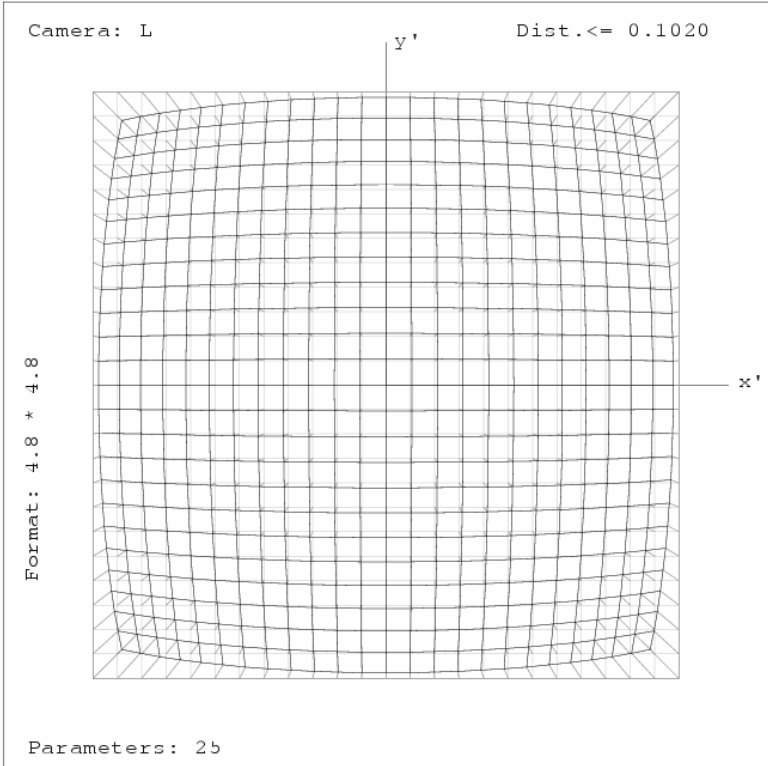
Principle point: (0.0447 , -0.0263), std(0.0065 , 0.0092)

Table B-71: Images used for the calibration of the left camera



The plots of the Radial symmetric distortion:





Calibration of the Right Camera

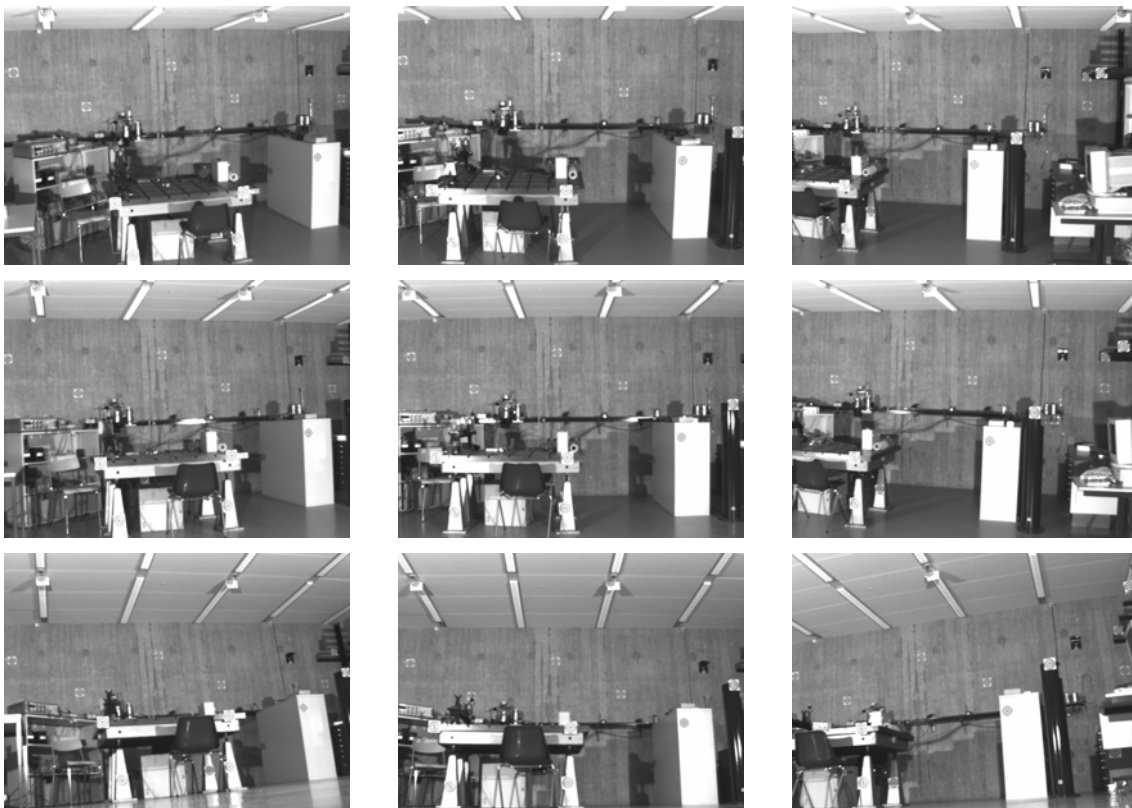
Table (B-2) shows the images that were taken from the Right camera.

The focal length and principle point's photo-coordinates of the Right camera are (mm):

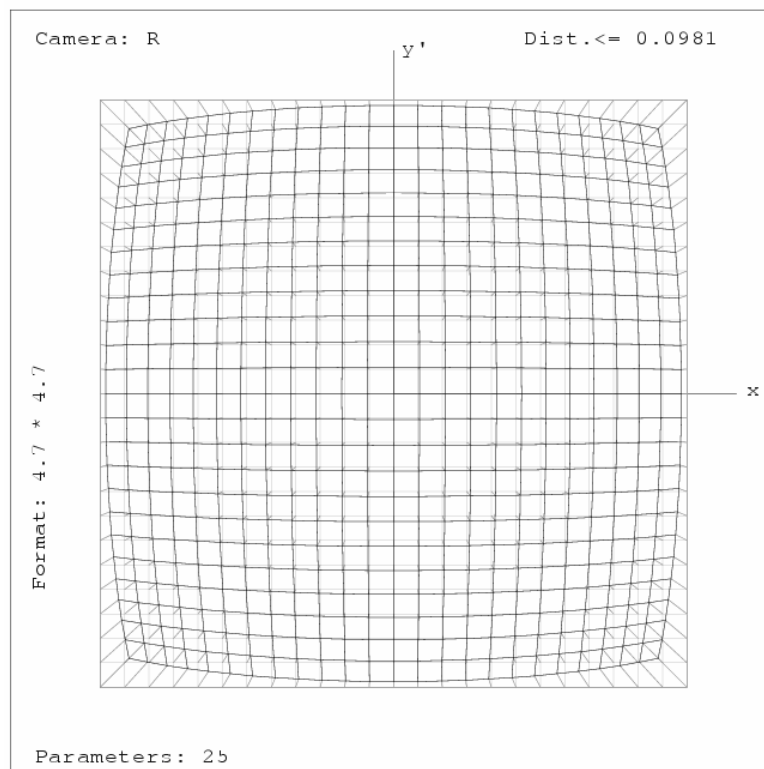
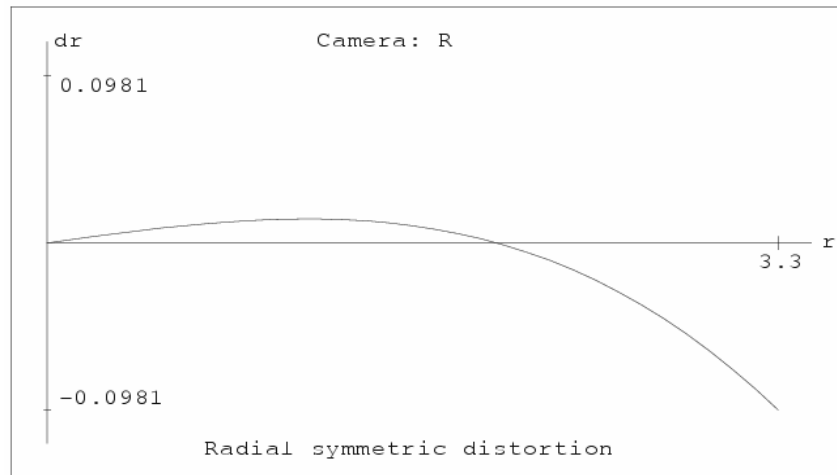
Focal length: 6.07, std = 0.007

Principle point: (-0.0330 , -0.0013), std(0.0055 , 0.0087)

Table B-2: Images used for the calibration of the right camera



The plots of the Radial symmetric distortion:



APPENDIX C: OUTDOOR IMAGES





APPENDIX D: DETAILED TABLES

Table D-1: R_p^e angles derived from INS/GPS and resection with measured GCP accuracy (degrees)

Accuracy ~ 0.01		With boresight correction			Without boresight correction		
Epoch		E_x	E_y	E_z	E_x	E_y	E_z
1	IMU/GPS	-44.7549	1.3821	-81.1443	-44.7549	1.3821	-81.1443
	L	-44.7998	1.3507	-81.2571	-46.2640	0.6866	-82.5553
	R	-44.7647	1.2773	-81.2806	-44.8828	0.8659	-82.6821
2	IMU/GPS	-44.5572	2.1910	-80.7181	-44.5572	2.1910	-80.7181
	L	-44.6433	2.2675	-80.6392	-46.1223	1.6331	-81.8993
	R	-44.5379	2.1676	-80.6837	-44.6715	1.7656	-82.077
3	IMU/GPS	-44.4795	1.9735	-80.8135	-44.4795	1.9735	-80.8135
	L	-44.5018	1.8827	-80.8411	-45.9749	1.2423	-82.1125
	R	-44.4753	1.8677	-80.8811	-44.6037	1.4673	-82.2738
4	IMU/GPS	-44.2799	5.7301	-75.3527	-44.2799	5.7301	-75.3527
	L	-44.3557	5.5887	-75.1998	-45.8844	5.0535	-76.3265
	R	-44.2344	5.5097	-75.3125	-44.4259	5.1263	-76.6853
5	IMU/GPS	-44.8479	4.6945	-77.3974	-44.8479	4.6945	-77.3974
	L	-44.9182	4.8029	-77.3213	-46.4351	4.2296	-78.4903
	R	-44.8067	4.6935	-77.4247	-44.9839	4.2884	-78.8147
6	IMU/GPS	-44.6931	2.9835	-79.0416	-44.6931	2.9835	-79.0416
	L	-44.7241	3.0605	-79.0255	-46.2152	2.445	-80.2574
	R	-44.7136	3.0127	-79.0506	-44.8617	2.6066	-80.4451
7	IMU/GPS	-44.8705	4.7685	-77.2922	-44.8705	4.7685	-77.2922
	L	-44.8944	4.8310	-77.268	-46.4117	4.2593	-78.4354
	R	-44.846	4.7821	-77.3082	-45.0246	4.3760	-78.6988
8	IMU/GPS	-44.3561	5.3890	-75.7558	-44.3561	5.3890	-75.7558
	L	-44.4041	5.5023	-75.6565	-45.9316	4.9634	-76.7875
	R	-44.3218	5.4424	-75.716	-44.5121	5.0559	-77.0911
9	IMU/GPS	-44.3675	6.6324	-74.3969	-44.3675	6.6324	-74.3969
	L	-44.3857	6.7008	-74.2828	-45.9297	6.1957	-75.3667
	R	-44.3339	6.6721	-74.3404	-44.5453	6.2891	-75.7098
10	IMU/GPS	-44.3405	6.5233	-74.453	-44.3405	6.5233	-74.4530
	L	-44.3818	6.5932	-74.3197	-45.9243	6.0852	-75.4077
	R	-44.3252	6.5956	-74.38	-44.5352	6.2127	-75.7495
11	IMU/GPS	-44.2897	5.3143	-75.1381	-44.2897	5.3143	-75.1381
	L	-44.3200	5.4066	-75.0252	-45.8462	4.8673	-76.1582
	R	-44.2272	5.3558	-75.1077	-44.4161	4.9723	-76.4810
12	IMU/GPS	-44.3826	5.6591	-75.9474	-44.3826	5.6591	-75.9474
	L	-44.3257	5.6529	-75.8071	-45.8554	5.1203	-76.9307
	R	-44.3076	5.7242	-75.8321	-44.5027	5.3391	-77.2055

Table D-2: R_b^e angles derived from INS/GPS and resection with GCP accuracy of ~ 0.05 (degrees)

Accuracy ~ 0.05		With boresight correction			Without boresight correction		
Epoch		E_x	E_y	E_z	E_x	E_y	E_z
1	IMU/GPS	-44.7549	1.3821	-81.1443	-44.7549	1.3821	-81.1443
	L	-44.8693	1.4260	-81.1615	-46.3969	0.6393	-82.6298
	R	-44.8790	1.3718	-81.1772	-45.0713	0.8613	-82.7137
2	IMU/GPS	-44.5572	2.1910	-80.7181	-44.5572	2.1910	-80.7181
	L	-44.7164	2.3421	-80.5394	-46.2620	1.5850	-81.9671
	R	-44.6423	2.2216	-80.6107	-44.8831	1.8123	-82.0545
3	IMU/GPS	-44.4795	1.9735	-80.8135	-44.4795	1.9735	-80.8135
	L	-44.5615	1.9476	-80.8127	-46.1382	1.2327	-82.4123
	R	-44.5783	1.9583	-80.7755	-44.7873	1.4548	-82.2999
4	IMU/GPS	-44.2799	5.7301	-75.3527	-44.2799	5.7301	-75.3527
	L	-44.4131	5.6549	-75.1735	-46.0597	5.0458	-76.6302
	R	-44.3176	5.5950	-75.2296	-44.6018	5.1354	-76.7094
5	IMU/GPS	-44.8479	4.6945	-77.3974	-44.8479	4.6945	-77.3974
	L	-44.9805	4.8767	-77.2330	-46.5701	4.2045	-78.5555
	R	-44.8982	4.7808	-77.3386	-45.1567	4.2942	-78.8557
6	IMU/GPS	-44.6931	2.9835	-79.0416	-44.6931	2.9835	-79.0416
	L	-44.7830	3.1257	-78.9480	-46.3436	2.4175	-80.3344
	R	-44.8162	3.0988	-78.9551	-45.0378	2.6072	-80.4908
7	IMU/GPS	-44.8705	4.7685	-77.2922	-44.8705	4.7685	-77.2922
	L	-44.9537	4.8993	-77.1863	-46.5447	4.2310	-78.5065
	R	-44.9372	4.8656	-77.2201	-45.2003	4.3783	-78.7371
8	IMU/GPS	-44.3561	5.3890	-75.7558	-44.3561	5.3890	-75.7558
	L	-44.5264	5.6528	-75.5041	-46.0626	4.9290	-76.9246
	R	-44.4163	5.5351	-75.6254	-44.6933	5.0703	-77.1157
9	IMU/GPS	-44.3675	6.6324	-74.3969	-44.3675	6.6324	-74.3969
	L	-44.4746	6.7959	-74.2961	-46.1750	6.2667	-75.6274
	R	-44.4294	6.7683	-74.2420	-44.7331	6.3086	-75.7164
10	IMU/GPS	-44.3405	6.5233	-74.453	-44.3405	6.5233	-74.453
	L	-44.4599	6.6854	-74.3332	-46.1588	6.1522	-75.6687
	R	-44.4146	6.6885	-74.2874	-44.7180	6.2304	-75.7612
11	IMU/GPS	-44.2897	5.3143	-75.1381	-44.2897	5.3143	-75.1381
	L	-44.3744	5.4689	-75.0009	-46.0196	4.8553	-76.4602
	R	-44.3164	5.4542	-75.0133	-44.5975	4.9932	-76.4915
12	IMU/GPS	-44.3826	5.6591	-75.9474	-44.3826	5.6591	-75.9474
	L	-44.4037	5.7560	-75.8124	-46.0791	5.2020	-77.1873
	R	-44.3929	5.8081	-75.7410	-44.6746	5.3345	-77.2356

Table D-3: R_b^e angles derived from INS/GPS and resection with GCP accuracy of ~ 0.10 (degrees)

Accuracy ~ 0.10		With boresight correction			Without boresight correction		
Epoch		E_x	E_y	E_z	E_x	E_y	E_z
1	IMU/GPS	-44.7549	1.3821	-81.1443	-44.7549	1.3821	-81.1443
	L	-43.7740	-0.1495	-82.7055	-46.6927	0.3424	-82.3826
	R	-43.7754	-0.2017	-82.6717	-45.3102	0.6737	-82.2632
2	IMU/GPS	-44.5572	2.1910	-80.7181	-44.5572	2.1910	-80.7181
	L	-43.6296	0.7555	-82.0917	-46.5528	1.2919	-81.7226
	R	-43.5502	0.4272	-82.2546	-44.8951	1.6454	-81.7349
3	IMU/GPS	-44.4795	1.9735	-80.8135	-44.4795	1.9735	-80.8135
	L	-43.3271	0.2544	-82.2306	-46.1187	0.7089	-82.1604
	R	-43.4845	0.3811	-82.2837	-45.0198	1.2327	-81.9148
4	IMU/GPS	-44.2799	5.7301	-75.3527	-44.2799	5.7301	-75.3527
	L	-43.3000	3.8224	-76.6621	-46.0541	4.5609	-76.3190
	R	-43.3236	3.8784	-76.8124	-44.8214	4.9842	-76.2231
5	IMU/GPS	-44.8479	4.6945	-77.3974	-44.8479	4.6945	-77.3974
	L	-43.9590	3.1801	-78.8402	-46.8843	3.9744	-78.1979
	R	-43.8595	3.0948	-78.8879	-45.4160	4.1740	-78.3105
6	IMU/GPS	-44.6931	2.9835	-79.0416	-44.6931	2.9835	-79.0416
	L	-43.7253	1.4670	-80.5113	-46.6811	2.2015	-79.9330
	R	-43.7456	1.4457	-80.4632	-45.3413	2.5070	-79.9085
7	IMU/GPS	-44.8705	4.7685	-77.2922	-44.8705	4.7685	-77.2922
	L	-43.9247	3.1967	-78.7996	-46.8736	4.0148	-78.1299
	R	-43.9036	3.1744	-78.7682	-45.4637	4.2638	-78.1837
8	IMU/GPS	-44.3561	5.3890	-75.7558	-44.3561	5.3890	-75.7558
	L	-43.3800	3.7649	-77.2275	-46.4186	4.7571	-76.6688
	R	-43.4149	3.8271	-77.1964	-44.9313	4.9376	-76.6017
9	IMU/GPS	-44.3675	6.6324	-74.3969	-44.3675	6.6324	-74.3969
	L	-43.4644	5.0330	-75.6583	-46.0281	5.6414	-75.2162
	R	-43.4564	5.0258	-75.8488	-44.9479	6.1537	-75.2390
10	IMU/GPS	-44.3405	6.5233	-74.453	-44.3405	6.5233	-74.453
	L	-43.4459	4.9217	-75.6933	-46.0076	5.5248	-75.2596
	R	-43.4382	4.9470	-75.8976	-44.9291	6.0737	-75.2875
11	IMU/GPS	-44.2897	5.3143	-75.1381	-44.2897	5.3143	-75.1381
	L	-43.2643	3.6345	-76.4968	-46.0121	4.3674	-76.1603
	R	-43.3232	3.7348	-76.6068	-44.8084	4.8324	-76.0224
12	IMU/GPS	-44.3826	5.6591	-75.9474	-44.3826	5.6591	-75.9474
	L	-43.3500	4.0029	-77.1789	-45.9337	4.5332	-76.8227
	R	-43.3885	4.0957	-77.3379	-44.9158	5.1499	-76.8095

Table D-4: R_b^e angles derived from INS/GPS and resection with GCP accuracy of ~ 0.15 (degrees)

Accuracy ~ 0.15		With boresight correction			Without boresight correction		
Epoch		E_x	E_y	E_z	E_x	E_y	E_z
1	IMU/GPS	-44.7549	1.3821	-81.1443	-44.7549	1.3821	-81.1443
	L	-44.3292	0.8740	-81.5450	-47.5145	1.3139	-81.2146
	R	-44.3230	0.8079	-81.5897	-46.0744	1.7730	-81.1052
2	IMU/GPS	-44.5572	2.1910	-80.7181	-44.5572	2.1910	-80.7181
	L	-44.1920	1.7984	-80.9147	-47.3776	2.3089	-80.5171
	R	-44.0015	1.9140	-80.9199	-45.6674	2.6176	-80.6520
3	IMU/GPS	-44.4795	1.9735	-80.8135	-44.4795	1.9735	-80.8135
	L	-44.0987	1.4547	-80.9015	-47.3948	2.0456	-80.2050
	R	-44.0346	1.4145	-81.1732	-45.8047	2.3745	-80.7122
4	IMU/GPS	-44.2799	5.7301	-75.3527	-44.2799	5.7301	-75.3527
	L	-43.9745	5.1246	-75.3020	-47.1795	6.2341	-74.1114
	R	-43.7819	4.9539	-75.7118	-45.4815	6.2442	-74.9983
5	IMU/GPS	-44.8479	4.6945	-77.3974	-44.8479	4.6945	-77.3974
	L	-44.4553	4.2331	-77.6831	-47.5957	4.9711	-77.0400
	R	-44.3460	4.1265	-77.8133	-46.0818	5.2744	-77.1636
6	IMU/GPS	-44.6931	2.9835	-79.0416	-44.6931	2.9835	-79.0416
	L	-44.2428	2.4753	-79.3936	-47.3796	3.0638	-78.8800
	R	-44.2588	2.4430	-79.4086	-45.9908	3.4786	-78.8386
7	IMU/GPS	-44.8705	4.7685	-77.2922	-44.8705	4.7685	-77.2922
	L	-44.4334	4.2543	-77.6363	-47.5748	4.9884	-76.9912
	R	-44.3850	4.2039	-77.6961	-46.1109	5.3424	-77.0514
8	IMU/GPS	-44.3561	5.3890	-75.7558	-44.3561	5.3890	-75.7558
	L	-43.9495	4.9625	-75.8214	-47.1045	5.9282	-74.8421
	R	-43.8866	4.8932	-76.0996	-45.5934	6.1482	-75.4012
9	IMU/GPS	-44.3675	6.6324	-74.3969	-44.3675	6.6324	-74.3969
	L	-44.2005	6.5064	-74.0348	-47.2567	7.4541	-73.1893
	R	-43.9124	6.1268	-74.7242	-45.6075	7.4700	-73.9766
10	IMU/GPS	-44.3405	6.5233	-74.453	-44.3405	6.5233	-74.453
	L	-44.1841	6.3958	-74.0706	-47.2334	7.3316	-73.2414
	R	-43.8950	6.0484	-74.7711	-45.5908	7.3927	-74.0238
11	IMU/GPS	-44.2897	5.3143	-75.1381	-44.2897	5.3143	-75.1381
	L	-43.9367	4.9453	-75.1223	-47.1424	6.0641	-73.9317
	R	-43.7925	4.8268	-75.4871	-45.4879	6.1458	-74.7620
12	IMU/GPS	-44.3826	5.6591	-75.9474	-44.3826	5.6591	-75.9474
	L	-44.1271	5.4237	-75.5894	-47.2269	6.1698	-74.9276
	R	-43.8604	5.1782	-76.2053	-45.6101	6.3745	-75.5636

REFERENCES

- Al-Ruzouq, R. (2004): Semi-Automatic Registration of Multi-Source Satellite Imagery with Varying Geometric Resolutions. PhD Thesis, UCGE Report No. 20190, Dept. of Geomatics Engineering, The University of Calgary, Canada.
- ASPRS (2004): Manual of Photogrammetry. American Society for Photogrammetry and Remote Sensing, Fifth Edition.
- Atkinson, K. B. E. b. (2001): Close Range Photogrammetry and Machine Vision. Whittles Publishing Services, Scotland, UK.
- Bailey, T. (2002): Mobile Robot Localisation and Mapping in Extensive Outdoor Environments. PhD Thesis, Australian Centre for Field Robotics, The University of Sydney, Australia.
- Bäumker, M. and F. J. Heimes (2001); New Calibration and Computing Method for Direct Georeferencing of Image and Scanner Data Using the Position and Angular Data of an Hybrid Inertial Navigation System. OEEPE Workshop, Integrated Sensor Orientation, Sep. 17-18, 2001; Hanover.
- Bayoud, F. A. (2001): Some Investigations on Local Geoid Determination from Airborne Gravity Data. MSc Thesis, UCGE Report No. 20154, Dept. of Geomatics Engineering, The University of Calgary, Canada.
- Beyer, H. A. (1992): Advances in Characterisation and Calibration of Digital Imaging Systems. International Archives of Photogrammetry and Remote Sensing, 29(5).
- Bjerhammar, A. (1973): Theory of Errors and Generalised Matrix Inverses. Elsevier Scientific Publishing Company, Amsterdam.
- Blais, F., J.-A. Beraldin, et al. (2001): Comparison of Pose Estimation Methods for a 3D Laser Tracking System using Triangulation and Photogrammetry Techniques. SPIE Proceedings, Electronic Imaging 2001, Videometrics and Optical Methods for 3D Shape Measurement VII, San Jose, CA. January 21–26, 2001. Vol. 4309.
- Böhm, J. J. H., D. Fritsch (2001): Towards On-line Pose Measurement for Robots. Lecture Notes in Computer Sciences, V. 2191, Springer-Verlag GmbH.
- Bosse, M. C. (1997): A Vision Augmented Navigation System for an Autonomous Helicopter. MSc Thesis, College Of Engineering, Boston University, USA.

- Britting, K. R. (1971): *Inertial Navigation System Analysis*. Wiley-Interscience, New York, USA.
- Bruton, A. M. (2000): *Improving the Accuracy and Resolution of SINS/GPS Airborne Gravimetry*. PhD Thesis, UCGE Report No. 20145, Dept. of Geomatics Engineering, The University of Calgary, Canada.
- Chaplin, B. A. (1999): *Motion Estimation from Stereo Image Sequence for a Mobile Mapping System*. MSc Thesis, UCGE Report No. 20128. Dept of Geomatics Engineering, University of Calgary, Canada. .
- Chaplin, B. A., Chapman, M. A. (1998): *A Procedure for 3D Motion Estimation from Stereo Image Sequences for a Mobile Mapping System*. *International Archives of Photogrammetry and Remote Sensing*, Vol. 32(3W1).
- Chiang, K.-W. (2005): *INS/GPS Integration Using Neural Networks for Land Vehicular Navigation Applications*. Ph.D. Thesis, UCGE Report 20209. Department of Geomatics Engineering, University of Calgary, Canada.
- Colomina, I. (1999): *GPS, INS and Aerial Triangulation: What is the Best Way for the Operational Determination of Photogrammetric Image Orientation?*. *International Archives of Photogrammetry and Remote Sensing, ISPRS Conference automatic Extraction of GIS Objects from Digital Imagery*, Vol. 32, München, pp. 121-130.
- Cox, D. B. (1980): *Integration of GPS with Inertial Navigation Systems*. *Global Positioning System, Papers Published in Navigation*, Vol. 1, Institute of Navigation, Alexandria, VA, 1980.
- Csorba, M. (1997): *Simultaneous Localisation and Map Building*. PhD Thesis, Robotics Research Group, Department of Engineering Science, University of Oxford, UK.
- Davison, A. J. (1998): *Mobile Robot Navigation Using Active Vision*. PhD, Robotics Research Group, Department of Engineering Science, University of Oxford, UK.
- Dermanis, A. (1995): *Analytical Photogrammetry*. Editions Ziti (In Greek).
- EI-Hakim, S. F., P. Boulanger, et al. (1997): *A Mobile System for Indoors 3-D Mapping and Positioning*. *Optical 3-D Measurement Techniques*, Zurich, Wichmann.
- EI-Sheimy, N. (1996): *The Development of VISAT - A Mobile Survey System for GIS Applications*. PhD Thesis, UCGE Report No. 20101, Dept. of Geomatics Engineering, The University of Calgary, Canada.
- EI-Sheimy, N. (2003): *Inertial Techniques and INS/DGPS Integration*. Lecture Notes, Dept. of Geomatics Engineering, The University of Calgary. Canada.

- Ellum, C. M. (2001): The Development of a Backpack Mobile Mapping System. MSc thesis, Dept. of Geomatics Engineering, The University of Calgary, Canada.
- Forlania, G., R. Roncellaa, F. Remondinob, (2005): Structure and Motion Reconstruction of Short Mobile Mapping Image Sequences. Proceedings of the Optical 3-D measurements Techniques 2005, Vienna, Austria.
- Gao, Y., E.J. Krakiwsky, M. Abousalem, and J. F. McLellan (1993): Comparison and Analysis of Centralized, Decentralized and Federated Filters. Journal of the Institute of Navigation, Vol. 40, No. 1., pp.69-86. .
- Gelb, A. (1974): Applied Optimal Estimation. The MIT Press, Cambridge Mass., USA.
- Grewal, M. S., L. R. Weill, et al. (2000): Global Positioning Systems, Inertial Navigation, and Integration. John Wiley & Sons.
- Groves, P., Robin J Handley, Andrew R Runnalls (2004): Optimising the Integration on Terrain Referenced Navigation with INS and GPS. Proceedings of the ION GNSS 17th International Technical Meeting of the Satellite Division, 21-24 Sep, Long Beach USA.
- Guivant, J. E. (2002): Efficient Simultaneous Localization and Mapping in Large Environments. PhD Thesis, Australian Centre for Field Robotics, Department of Mechanical and Mechatronic Engineering, The University of Sydney, Australia.
- Habib, A., M. Morgan, E. M. Kim, R. Cheng (2004): Linear Features in Photogrammetric Activities, XXth ISPRS Congress, Istanbul, Turkey, PS ICWG II/IV: Automated Geo-Spatial Data Production and Updating, pp.610, (12-23 July 2004)
- Heipke, C., K. Jacobsen , H. Wegmann (2001): The OEEPE Test on Integrated Sensor Orientation - Results of Phase I. Proceedings of the photogrammetric Week, Stuttgart.
- Hofmann-Wellenhof, B., K. Legat, M. Wieser (2003): Navigation - principles of positioning and guidance. Springer, Wien .
- Horemuz, M., K. Gajdamowicz (2005): Integration of Digital Camera with INS. Proceedings of the Optical 3-D measurements Techniques 2005, Vienna, Austria.
- Huster, A. (2003): Relative Position Sensing By Fusing Monocular Vision and Inertial Rate Sensors. PhD Thesis, Department Of Electrical Engineering, Stanford University, USA.
- Journal of Robotic Systems (2004): Volume 21, Issue 1, January 2004, <http://www3.interscience.wiley.com/cgi-bin/jissue/106592238> .
- Journal of Robotic Systems (2004): Volume 21, Issue 2, February 2004, <http://www3.interscience.wiley.com/cgi-bin/jissue/107064033> .

- Jung, I.-K. (2003): Simultaneous Localization And Mapping in 3D Environments with Stereovision. PhD Thesis, Laboratoire d'Analyse et d'Architecture des Systèmes, CNRS, Toulouse, France.
- Kalman, R. E. (1960): A New Approach to Linear Filtering and Prediction Problems. *Journal of Basic Engineering*, 82 (series D): 35-45.
- Kim J.H. and Sukkarieh S. (2003): Airborne Simultaneous Localisation and Map Building. IEEE International Conference on Robotics and Automation 15-19 September, Taiwan.
- Knickmeyer, E. T. (1990): Vector Gravimetry by a Combination of Inertial and GPS satellite Measurements. Ph.D. Thesis, Pub. # 20035. Department of Surveying, University of Calgary, Canada.
- Knight, J. (2002): Towards Fully Autonomous Visual Navigation. PhD Thesis, Robotics Research Group, Department of Engineering Science, University of Oxford, UK.
- Kuipers, Jack B. (1998): Quaternions and Rotation Sequences. Princeton University Press
- Lamon, P. (2005): 3D Position Tracking for All-terrain Robots. PhD Thesis, Autonomous Systems Lab, Ecole Polytechnique Fédérale de Lausanne, Switzerland.
- Mächler, P. (1998): Robot Positioning By Supervised and Unsupervised Odometry Correction. PhD Thesis, Département d'informatique, École Polytechnique Fédérale de Lausanne, Switzerland.
- Majumder, S. (2001): Sensor Fusion and Feature Based Navigation for Sub-Sea Robots. PhD Thesis, Australian Centre for Field Robotics, The University of Sydney, Australia.
- Martinelli, A. (2002): The Odometry Error of a Mobile Robot with a Synchronous Drive System. *IEEE Transaction on Robotics and Automation*, Vol 18, No. 3 June 2002, pp 399-405.
- Martinelli, A. and Siegwart, R. (2005): Observability Analysis for Mobile Robot Localization. In *Proceedings of the IEEE/RSJ International Conference on Intelligent Robots and Systems, IROS*, Edmonton, Canada.
- Masson, F., J. Guivant, et al. (2003): Robust Navigation and Mapping Architecture for Large Environments. *Journal of Robotic Systems* 20(10), 621-634. John Wiley & Sons, Inc.
- Mikhail, E. M. (1976): *Observations and Least Squares*. IEP, New York.
- Moritz, H. (1980): *Advanced Physical Geodesy*. Wichmann, Karlsruhe.
- Mukundan, R. (2002): Quaternions: From Classical Mechanics to Computer Graphics, and Beyond. *Proceedings of the 7th Asian Technology Conference in Mathematics*.

- Nassar, S. (2003): Improving the Inertial Navigation System (INS) Error Model for INS and INS/DGPS Applications. PhD Thesis, UCGE Report No. 20183, Dept. of Geomatics Engineering, The University of Calgary, Canada.
- Nebot, E. and H. Durrant-Whyte (1999): Initial Calibration and Alignment of Low-Cost Inertial Navigation Units for Land Vehicle Applications. *Journal of Robotic Systems* 16(2), 81-91. John Wiley & Sons, Inc.
- Newman, P. M. (1999): On the Structure and Solution of the Simultaneous Localisation and Map Building Problem. PhD Thesis, Australian Centre for Field Robotics, The University of Sydney, Australia.
- Petovello, M. (2003): Real-time Integration of a Tactical-Grade IMU and GPS for High-Accuracy Positioning and Navigation. PhD Thesis, UCGE Report No. 20173, Dept. of Geomatics Engineering, The University of Calgary, Canada.
- Peipe, j. (1995): Photogrammetric Investigation of a 3000 x 2000 Pixel High Resolution Still Video Camera. *International Archives of Photogrammetry and Remote Sensing*, 30(5W1).
- Rönnbäck, S. (2000): Development of an INS/GPS Navigation Loop for an UAV. MSc Thesis, Dept. of Computer Science and Electrical Engineering, Luleo University of Technology.
- Salychev, O. (1998): Inertial Systems in Navigation and Geophysics. Bauman MSTU Press, Moscow.
- Savage, P. G. (1978): Strapdown Sensors, Strapdown Inertial Systems. AGARD Lecture Series No. 95.
- Seitz, P., O. Vietez, T. Spirig (1995): From Pixels to Answers - Recent Development and Trends in Electronic Imaging. *International Archives of Photogrammetry and Remote Sensing*, 30(5W1).
- Schwarz, K. P. (1986): Inertial Technology for Surveying and Geodesy. Department of Surveying, University of Calgary, Canada.
- Schwarz, K. P. and M. Wei (2000): INS/GPS Integration for Geodetic Applications. Lecture Notes ENGO 623, Dept. of Geomatics Engineering, The University of Calgary. Canada.
- Shin, E.-H. (2001): Accuracy Improvement of Low Cost INS/GPS for Land Application. MSc Thesis, UCGE Report No. 20156, Dept. of Geomatics Engineering, The University of Calgary, Canada.

- Shin, E.-H. (2005): Estimation Techniques for Low-Cost Inertial Navigation. PhD Thesis, UCGE Report No. 20219, Dept. of Geomatics Engineering, The University of Calgary, Canada.
- Skaloud, J. (2002): Direct Georeferencing in Aerial Photogrammetric Mapping. *Journal of Photogrammetry and Remote Sensing*, Vol 68, No. 3: 207-210. .
- Skaloud, J., J. Vallet, G. Veyssiere, O. Koelbl (2005): HELIMAP: Rapid Large Scale Mapping Using Handheld LiDAR/CCD/GPS/INS Sensors on Helicopters. Proceedings of the ION GNSS 2005 Meeting, Long Beach, USA, 13-16 September.
- Skaloud, J. and P. Schaer (2003): Towards a More Rigorous Bore-sight Calibration. ISPRS International Workshop on Theory, Technology and Realities of Inertial/GPS/Sensor Orientation, Commission 1, WG I/5.
- Skaloud, J. and P. Viret (2004): GPS/INS Integration: From Modern Methods of Data Acquisition to New Applications. *European Journal of Navigation*, Nov. 2004: 60-64.
- Sobel (1996): Longitude: The True Story of a Lone Genius Who Solved the Greatest Scientific Problem of His Time. Penguin Group, USA.
- Smith, R. C. and P. Cheeseman (1985): On the Estimation and Presentation of Spatial Uncertainty. Technical Report TR 4760 & 7239, SRI.
- Smith, R., M. Self, P. Cheeseman (1990): Estimating Uncertain Spatial relationships in Robotics. In I.J. Cox and G.T. Wilfong, editors, *Autonomous Robot Vehicles*. Springer-Verlag.
- Sukkarieh, S. (2000): Low Cost, High Integrity, Aided Inertial Navigation Systems for Autonomous Land Vehicles. PhD Thesis, Australian Centre for Field Robotics, The University of Sydney, Australia.
- Thrun, S. (2002): Robotic Mapping: A Survey. Report published by School of Computer Science; Carnegie Mellon University, USA.
- Titterton, D. H. and J. L. Weston (1997): Strapdown Inertial Navigation Technology. Peter Peregrinus Ltd.
- Tomatis, N. (2001): Hybrid, Metric-Topological, Mobile Robot Navigation. PhD Thesis, Département d'informatique, École Polytechnique Fédérale de Lausanne, Switzerland.
- Tomé, P. (2002): Integration of Inertial and Satellite Navigation Systems for Aircraft Attitude Determination. PhD Thesis, Dept. of Applied Sciences, Faculty of Sciences, University of Oporto, Portugal.

- Triggs, B., P. McLauchlan, et al. (2000): Bundle Adjustment - A Modern Synthesis. Vision Algorithms: Theory & Practice, B. Triggs, A. Zisserman & R. Szeliski (Eds.), Springer-Verlag LNCS 1883.
- Vallet, J., J. Skaloud (2004): Development and Experiences with a Fully-Digital Handheld Mapping System Operated from a Helicopter. The International Archives of the Photogrammetry, Remote Sensing and Spatial Information Sciences, Istanbul, Vol. XXXV, Part B, Commission 5.
- Wei, M., K. P. Schwarz (1990): Testing a Decentralized Filter for GPS/INS Integration. Proc. of IEEE Positioning Location and Navigation Symposium, Orlando, Florida.
- Wheeler, M. D. (1996): Automatic Modelling and Localization for Object Recognition. PhD Thesis, School of Computer Science, Carnegie Mellon University, USA.
- Williams, S. B. (2001): Efficient Solutions to Autonomous Mapping and Navigation Problems. PhD Thesis, Australian Centre for Field Robotics, The University of Sydney, Australia.
- Ziemann, H., El-Hakim S.F. (1982): System Calibration Versus Self-Calibration. International Archives of Photogrammetry, 24(1).

CURRICULUM VITAE

I, Fadi Atef Bayoud, was born on April 04, 1976, in Jdeidet Marjeyoun, South Lebanon, and raised there facing the Biblical Haramoun Mountain that joins the sun in every morning from the East. After obtaining the Lebanese Baccalaureate in 1993, I moved to Greece on a scholarship from the Greek Government and in 1999 I obtained my Dipl.-Ing. (equivalent to a Master in Engineering) in Rural and Surveying Engineering at the Aristotle University of Thessaloniki. In September 1999, I enrolled the graduate studies program in the Department of Geomatics Engineering at the University of Calgary, Canada, and I was awarded a Master of Science in Geomatics Engineering in 2001, with a specialisation in Geodesy and Reference Systems; my research work focused on regional geoid determination using terrestrial, airborne and satellite gravity data. In 2002, I became a research associate at the Swiss Federal Institute of Technology in Lausanne in the Geodetic Engineering Laboratory, and in 2003 I registered as a PhD student to graduate at the end of 2005 with a specialisation in robotics navigation and mapping systems, INS/GPS, direct georeferencing, photogrammetry and mobile mapping systems.